Table of Contents

Tabla de Contenido

Soil Biodegradation of a Blend of Cassava Starch and Polylactic Acid

Biodegradación en suelo de una mezcla de almidón de yuca y ácido poliláctico

Margarita R. Salazar-Sánchez [1], Laura I. Delgado-Calvache[2], Juan C. Casas-Zapata [3], Héctor S. Villada-Castillo [4], and José F. Solanilla-Duque [5]

ABSTRACT

This study evaluated bio-based blended films produced from polylactic acid (PLA) and thermoplastic starch (TPS) under soil conditions for four weeks (W). The degradation of the film was evaluated in addition to thermal, structural, and morphological changes on the surface of the material. There were evident structural changes; the TPS present in the film degraded from weeks 0 to 4, exhibiting a loss of mass between 350 and 365 °C in the TGA test. This behavior was attributed to the condensation of hydroxyl groups of the cassava starch as well as to a loss of mass corresponding to the degradation of PLA between 340 and 350 °C. The addition of TPS in the PLA-containing matrix resulted in a decrease in the Tg of the PLA/TPS blends. The increase in crystallinity improved the water vapor permeability in the structure. Consequently, the incorporation of starch in these blends not only reduces the cost of the material, but it also contributes to its rapid biodegradation (68%). These results contribute and offer new alternatives to accelerate the biodegradation process of biomaterials.

Keywords: disintegration, packing, biopolymers, soil, TPS/PLA

RESUMEN

Este estudio evaluó películas de mezcla de base biológica producidas a partir de ácido poliláctico (PLA) y almidón termoplástico (TPS) bajo condiciones en suelo durante cuatro semanas (W). Se evaluó la degradación de la película, además de los cambios térmicos, estructurales y morfológicos de la superficie del material. Hubo cambios estructurales evidentes; el TPS presente en la película se degradó desde la semana 0 hasta la 4, mostrando una pérdida de masa entre 350 a 365 °C en la prueba de TGA. Este comportamiento se atribuyó a la condensación de grupos hidroxilos del almidón de yuca y a una pérdida de la masa correspondiente a la degradación del PLA entre 340 a 350 °C. La adición de TPS en la matriz que contiene PLA dio lugar a una disminución en la Tg de las mezclas de PLA/TPS. El incremento de la cristalinidad mejoró la permeabilidad al vapor de agua en la estructura. Por lo tanto, la incorporación de almidón en estas mezclas no solo reduce el coste del material, sino que también contribuye a su rápida biodegradación (68 %). Estos resultados contribuyen y ofrecen nuevas alternativas para acelerar el proceso de biodegradación de los biomateriales.

Palabras clave: desintegración, empaque, biopolímeros, suelo, TPS/PLA

Introduction

Polymers derived from plant feedstocks are increasingly replacing plastic materials, reducing their environmental impact (S. Lambert and Wagner, 2017; T. Lambert and Perga, 2019; Mierzwa-Hersztek et al., 2019). Polymers of industrial interest include cellulose, starch, alginic acids, natural polypeptides such as gelatins, and bacterial polyesters (Heidemann et al., 2019). The biodegradation of contaminated plastics under composting conditions has been reported as an effective method to reduce plastic contamination (Bher et al., 2019). However, biodegradable polymers offer the possibility of reducing the environmental impact of chemical waste from landfills, which is due to their degradation speed under composting conditions at the site of final disposal (Castro-Aguirre et al., 2018). However, some biodegradable polymers such as polylactic acid (PLA) do not biodegrade as quickly as other organic waste during composting (Lv, Zhang, et al., 2017), since their degradation depends on

1 Biologist, Universidad del Cauca; PhD in Agricultural and Agroindustrial Sciences, Universidad del Cauca. Affiliation: Assistant professor, Agro-industrial Engineering Area, Department of Engineering and Technology, Universidad Popular del Cesar, Valledupar, Colombia. Email: mdelrosariosalazar@unicesar.edu.co

2 Environmental engineer. Affiliation: Young researcher, Universidad del Cauca, Popayán, Colombia. Email: laurita@unicauca.edu.co

3 Chemical engineer, Universidad de Antioquia; PhD in Engineering, Universidad de Antioquia, Medellín, Colombia. Affiliation: Full professor, Environmental and Sanitary Engineering Area, Department of Civil Engineering, Universidad del Cauca, Popayán, Colombia. Email: jccasas@unicauca.edu.co

4 Agro-industrial engineer, Universidad La Gran Colombia, Bogotá, Colombia; Ph.D. in Engineering, Universidad del Valle, Cali, Colombia. Affiliation: Full professor, Agro-industry Area, Department of Agricultural Sciences, Universidad del Cauca, Popayán, Colombia. Email: villada@unicauca.edu.co

5 Agro-industrial engineer, Universidad La Gran Colombia, Bogotá, Colombia; Ph.D. in Science and Technology: Colloids and Interfaces, Universidad Pablo De Olavide, Sevilla, Spain. Affiliation: Associate professor, Agro-industry area, Department of Agricultural Sciences, Universidad del Cauca, Popayán, Colombia. jsolanilla@unicauca.edu.co

the action of microorganisms (Pattanasuttichonlakul et al., 2018) and hydrolysis reactions that can break lactic acid chain monomers into smaller molecules such as lactide. Consequently, the low degradability of PLA has affected its general acceptance in industrial composting. Blends of PLA with other biomolecules such as corn starch have been widely documented (Shogren et al., 2003), and blends of 4032D PLA with cassava starch (TPS) have been reported in recent years for packaging and food service applications. In these compounds, due to the effect of biodegradation, each of the components is converted into biomass, which returns to the environment in the form of carbon dioxide (CO_2), methane (CH_4), and water. During this process, the polymer or blend undergoes structural changes implying the loss of mechanical properties due to disintegration, fragmentation, and mineralization (Salazar-Sánchez et al., 2020). The objective of this work was to study the biodegradation of a blend of cassava starch and PLA under natural environmental conditions.

Materials and methods

Sample preparation

The plastic film was produced in the rheology laboratory of Universidad del Cauca. The film is a polymer obtained from renewable sources such as cassava starch (*Manihot esculenta* Crantz) and PLA. Three films were used: a film of thermoplastic starch from Cassava (TPS), a film of polylactic acid (PLA Ingeo 4032D, Mn = 88 500 g.mol⁻¹, Mw/Mn = 1,8), and one film product of a blend of the two compounds with a ratio of 72:28 (TPS-PLA) following the procedure described by Salazar-Sánchez et al. (2019).

Fourier transform spectrophotometry (ATR-FTIR) analysis

The tests were conducted in accordance with ASTM E1252-98 (ASTM International, 2013) via Fourier transform infrared spectroscopy (FT-IR) (IRAffinity-1S, Shimadzu, Inc., Shelton CT, Japan). A horizontal attenuated total reflectance (ATR) sampling accessory (ATR-8200HA) equipped with a ZnSe cell was employed for the measurement (Salazar-Sánchez et al., 2019).

Thermal properties

A thermogravimetric analysis (TGA) and a differential sweep analysis (DSC) were performed using a TGA (TGA 2050TA Instruments, USA) and a DSC (Q20 TA Instruments, New Castle, USA), respectively, according to ASTM E1131-20 and ASTM D3418-15 (ASTM International, 2015, 2020; Daza et al., 2018; Carmona et al., 2015; Frone et al., 2013).

Isotherm analysis

The sorption isotherms were determined at 10, 25, and 35 °C using a vapor sorption analyzer (Aqua Lab VSA, USA) with

an a_w range of 0,5-0,95. The equilibrium moisture content on a dry basis was plotted against the a_w in order to obtain the equilibrium moisture curves (Dutcher et al., 2011). The performance of the models (Table 1) was evaluated via the adjusted coefficient of determination (R^2_{adj}) and mean square error (MSE). The models were selected on the basis of a high R^2_{adj} and a low MSE (Andrade et al., 2011; Arslan-Tontul, 2020; Homez et al., 2018; Iglesias and Chirife, 1995; Torres et al., 2012).

Biodegradation analysis

The biodegradability test was conducted in triplicate according to ASTM D5988 (ASTM International, 2018). A mixture of coffee soils and compost (derived from agricultural residues) was used as inoculum at a ratio of 25:1, and 4% sand was added as a structuring material to improve aeration. A physicochemical analysis of the soil was performed (organic carbon, water retention capacity, cation exchange capacity, capillary electrophoresis, pulse differential polarography, and carbon/nitrogen ratio) using the Colombian Technical Standard SSLMM-42-2-92 and the 3111B standard method (APHA, 1999) to determine metals and minerals. Microbiological properties were determined by counting the colony-forming units (CFC/g) of mesophylls, thermophiles, mold, yeast, *Nematodes* and/or *Protozoa*, *Enterobacteria*, and *Salmonella* (supplementary material).

Table 1. Water activity equation models

Model	Equation	Reference
Oswin	$X = a\left(\dfrac{a_w}{1-a_w}\right)^b$	Oswin (1946)
GAB	$\dfrac{X_m C k a_w}{\left[(1-ka_w)(1-ka_w+Cka_w)\right]}$	Guggenheim (1966), Anderson (1946), de Boer (1953), van den Berg (1981)
BET	$\dfrac{X_m C a_w}{\left[(1-a_w)+(C-1)((1-a_w)a_w)\right]}$	Brunauer et al. (1938), Aguerre et al. (1989)
Hasley	$X = \left(-\dfrac{a}{\ln a_w}\right)^{\frac{1}{b}}$	Halsey (1948)

Source: Authors

The moisture content was adjusted to approximately 63%. The test material was the mixture described above (TPS/PLA), and, as a reference microcrystalline, cellulose was used for thin-layer chromatography (Merck KgaA, Germany), as well as 4032D PLA (Ingeo). The cellulose and PLA were conditioned according to ISO 10210 (ISO, 2012), and the crushed fraction with a particle diameter between 250 and 125 μm was chosen. Each reactor was loaded with 200 g of inoculum and 0,74245 ± 0,0009 g of TPS/PLA, 0,6467 ± 0,0016 g cellulose, and 1,0028 ± 0,0005 g PLA –all samples on a wet basis. The carbon mineralization in the mixtures was quantified using a respirometry assembly in a closed chamber, where $Ba(OH)_2*8H_2O$ 0,025 N (Merck KgaA,

Germany) was used as CO_2 adsorbent, and HCL 0,05 N as titrator (Merck, Germany). The titration was performed at the endpoint of a 5 ml sample of adsorbent, aided by a TITRINO PLUS (Metrohm) automatic titrator. For the statistical evaluation of the results obtained from the biodegradation process of the samples studied for 4 weeks (W), a univariate analysis of variance was performed (ANOVA and Tukey tests with a 95% reliability and minimum significant difference) and the SMD (standardized mean difference) was estimated. The differences were considered to be significant when $p < 0,05$.

Scanning electron microscopy (SEM) analysis

The samples were characterized via scanning electron microscopy (SEM) using a QUANTA 200F (FEI, The Netherlands). Each SEM sample was coated with Gold-Palladium (0,8 nm thick coating) in an EmiTech K575X Peltier Cooled (QuorumTech, United Kingdom). The samples were observed and analyzed at an accelerating voltage of 10,0 kV at different magnifications (from 50X to 2000X).

Results and discussions

ATR-FTIR analysis

The FTIR spectra were analyzed in the range of 400-4 000 cm^{-1} and are shown in Figure 1. Bands between 900 and 1 010 cm^{-1} indicate C-O-C bonds (Liu et al., 2011; Salazar-Sánchez et al., 2019). The characteristic peaks at 2 918 and 2 848 cm^{-1} correspond to CH_3, and those between 1 747 and 1 180 cm^{-1} are characteristic of 4032D PLA with C=O and C-O carbonyl group stretching, respectively (Riba et al., 2020). The peaks at 730 cm^{-1} are associated with the bending of the C=C group of the PLA's main chain. Flexure of the carbonyl group CH_3 was observed in the 1 458 and 1358 cm^{-1} peaks, and there was also a CH_3 shift in the 1 072 cm^{-1} peak. Stretching of the -C-COO (1 276 cm^{-1}) and C-O-C (872 cm^{-1}) groups was observed in the PLA spectrum. Similarly, vibrations corresponding to the stretching of the hydroxyl (O-H) group between the 3 400-2 400 cm^{-1} bands were seen.
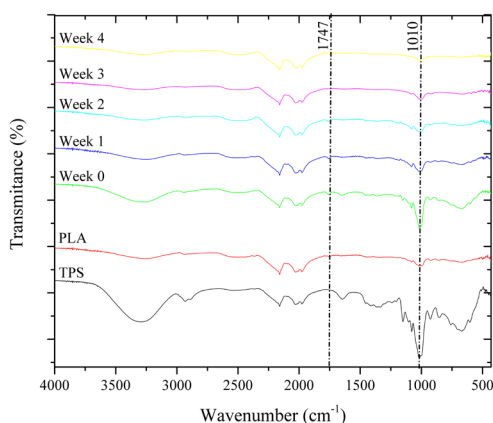
Figure 1. Fourier transform infrared (ATR-FTIR) spectra of the films
Source: Authors

Additionally, the spectra of TPS were compared because, when it blends with PLA, the mechanical, thermal, and other properties related to these mixtures (PLA/TPS) are modified. Therefore, the peaks to be analyzed were established between 750 and 1 250 cm^{-1} in order to understand the behavior of the TPS structure regarding its amylose/amylopectin composition before blending, as it is important to understand the crystalline and amorphous behavior of these molecules in the mixture. The stretching attributed to bands 1 040 cm^{-1} (C-O), 1 024 cm^{-1} (C-C), and 680 cm^{-1} (C-O-C) indicates a sensitivity to crystalline change. In other words, decreasing the crystallinity increases the 1 024 cm^{-1} band, whereas the intensity of the peak at 1 040 cm^{-1} increases with crystallinity, considering the crystalline structures of starch in this area (Cao et al., 2020). The intensity ratio between these two bands (1 046/1 024 cm^{-1}) is 1,72, thus indicating an increase in crystallinity in starch, which has a high degree of organization and is composed mainly of amylopectin (Özeren et al., 2020; Mierzwa-Hersztek et al., 2019; Homez et al., 2018; Nevoralová et al., 2019). The PLA/TPS film spectra show a stretch in the OH group in the region from 3 260 to 3 350 cm^{-1}. Likewise, the characteristic -CH peak of starch shows stretching in the 2 914 cm^{-1} band. The 1 024 cm^{-1} peak exhibited a shrinkage that could be due to starch retrogradation. When exposing the film to the biodegradation process, structural changes were evidenced; the TPS present in the film degraded from W0 to W4. These changes could be observed in the spectra and are attributed to changes in the crystallinity of starch, which is reflected by the glycosidic bonds of the TPS Neat and could be due to the fact that starch degradation occurs first in the amorphous region (amylose) as well as in the PLA, where the hydrogen bonds are very weak and more accessible to microorganisms, which degrades substantially faster compared to the crystalline part (Sedničková et al., 2018). The bands located at 1 040 cm^{-1} indicate a C-O functional group. The band located at 1 024 cm^{-1} indicates the amorphous region of starch given the presence of the C-C group. Similar observations were reported by Palai et al. (2019) and Wang et al. (2020), as well as at 680 cm^{-1} with vibrations for the C-O-C group (Gopi et al., 2019). The decrease in peak intensity at 1 178 cm^{-1} for PLA/TPS may be due to the weak chemical interaction between PLA and TPS (Muller et al., 2017).

Thermal properties

A loss of mass could be observed which reflected the condensation of hydroxyl groups (300-400 °C) (Figures 2a and b). The magnitude and location of this mass loss changed according to the degradation time (W0 to W4). In W1 and W2, the film showed a significant mass loss in the temperature range of 350-365 °C, which indicates the condensation of the hydroxyl groups of cassava starch. In W3 and W4, there was a mass loss in the range of 340-350 °C, which corresponds to the degradation of the PLA present in the blend. Similar results were reported by Nasseri et al. (2020) for mixtures of acetylated rice starch and PLA. The degradation temperatures decreased due to the

consumption of the starch content by the microorganisms (de Oliveira, Barbosa, et al., 2019; de Oliveira, de Oliveira Mota et al., 2019; Gralde, et al., 2019).

Table 2. Thermal data for PLA in their corresponding blends: samples (S), week (W), glass transition temperature (Tg), heat capacity (Cp), crystallization temperature (Tc), enthalpy of crystallization (ΔHc) melting temperature I (Tm), enthalpy of fusion (ΔHm), and crystallinity indices (Xc)

S	Tg (°C)	Cp J/g·°C	Tc (°C)	ΔHc (J/g)	Tm (°C)	ΔHm (J/g)	Xc (%)
W0	52,54	0,37	110,35	19,04	167,38	33,70	34,05
W1	56,75	0,38	109,35	18,82	167,64	31,28	33,97
W2	57,82	0,39	108,68	18,18	166,88	33,03	32,62
W3	61,18	0,39	117,93	20,83	169,65	24,81	25,84
W4	61,89	0,38	119,97	24,46	170,70	28,30	22,61
PLA W4	64,06	0,53	137,00	24,41	170,69	27,79	21,49
PLA	57,27	0,48	149,82	1,45	161,33	52,98	55,17
TPS	50,05	0,34	-	-	147	26,03	-

Source: Authors

The DSC curves show the glass transition (Tg), crystallization (Tc), and melting I (Tm) temperatures (Figure 3). The Tg is around 60 °C in the analyzed samples. It increases in W3 and W4 and has a lower value in W1 and W2, which could be due to the difference in the nature of the incidence of starch. The addition of TPS within the PLA matrix resulted in a decrease in the Tg of the PLA/TPS blends. A decrease in Tg increased the starch concentration (Li et al., 2020). This decrease in the Tg of the films can be attributed to the plastification of starch with glycerol, given the mobility of the chains caused by the migration of glycerol in the dispersed phase of TPS (Özeren et al., 2020). This effect is also attributed to the nucleation of the dispersed phase of TPS (Cai et al., 2014). The Tc of the samples (Table 2) shows a temperature decrease from 135 to 100 °C in W1, which was reflected on the weeks of biodegradation. This temperature, in comparison with that of PLA, is correlated with the TGA and FTIR results, where structural changes in the film were observed during the biodegradation process. A single endothermic peak for melting at 170 °C was observed in all weeks. Additionally, all PLA/TPS blends showed an increase in the intensity of the endothermal peak attributed to the laminar arrangement and polymorphism of the PLA's crystalline structure (Anakabe et al., 2017).

The diffusion coefficient of water in an amorphous or semi-crystalline polymer is related to the molecular dynamics of its amorphous regions (Shogren et al., 2003). If the temperature of an amorphous system (polymer-water) is above the glass transition temperature, the movement will be rapid, the free volume will increase, and the water vapor permeability will be high. Moisture penetration through the film may be due to cavities within the film that produce increased water vapor permeability, which has been linked to the two-phase morphology of PLA/TPS blends.

The isotherms show the behavior of the type I or S sigmoid form, which is indicative of physical adsorption in the
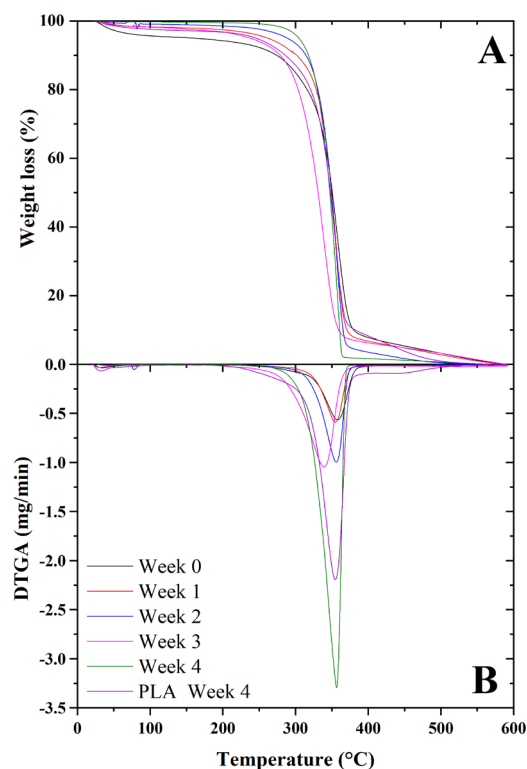
Figure 2. TGA (a) and DTG (b) curves for the biodegradation process of the TPS/PLA film
Source: Authors
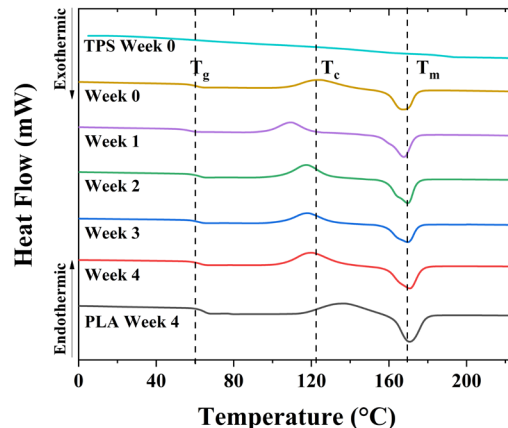
Figure 3. DSC curves for the biodegradation process of the TPS/PLA film
Source: Authors

multilayers of the material (Valsaraj, 2009). Table 3 shows the fit of the BET, GAB, Oswin, and Hasley models evaluated at different temperatures; it is evident that the model that best fits the data (MSE < 0,01) is BET, with R_{adj2} of 0,96804 at 10 °C, 0,95219 at 25 °C, and 0,97449 at 35 °C. From the prediction of the BET and GAB models, the amount of water that is strongly absorbed in the active sites of the film can be highlighted and is considered as the value at which the TPS/PLA mixture is most stable during storage (Chen et al., 2008; F. Wang et al., 2020). The addition of PLA in the blend provides a water vapor barrier, and TPS provides favorable water adsorption properties for the biodegradation

process. This is because starch is hydrophilic, unlike PLA, which tends to be completely hydrophobic (Sedničková et al., 2018). Therefore, it is possible that, in the film (TPS/PLA), the PLA prevents the starch from swelling, limiting the movement of the molecules and thus providing a part of the resistance to water permeability (Gürler et al., 2020). The variation in the water adsorption of TPS/PLA blends can be attributed to the behavior caused by the transition from the less ordered structure of starch to a higher-order structure that contains less water molecules (Lendvai et al., 2019). Consequently, the 3 300 cm^{-1} band is attributed to the stretching of the free inter- and intramolecular hydroxyl (-OH) groups of the starch chains, while the TPS exhibits a decrease in its intensity due to the interaction that occurs between starch and plasticizer by thermoplasticization (Altayan et al., 2017), which is due, in turn, to a greater interaction of the plasticizer with the polymeric chains of starch (Zdanowicz et al., 2019). On the other hand, in the region between 1 200 and 900 cm^{-1}, a band at 1 016 cm^{-1} attributed to the C-O stretching of the C-O-C group of the starch anhydroglucose ring is observed (Esmaeili et al., 2017) which is a function of the PLA concentration. The 995 cm^{-1} band, sensitive to water, is related to the intramolecular hydrogen bonding of the hydroxyl at C6, which can significantly decrease with increasing PLA.

Table 3. Water activity (a_w) models evaluated at different temperatures for a TPS/PLA blend

T (°C)	Model	Variable	Value	Standard Error	R^2_{adj}	MSE
10	BET	a	0,66208	0,04957	0,96804	0,00386
		b	0,11963			
	GAB	k	0,93128	0,06675	0,94206	0,01269
		a	-0,08992			
		b	-0,64516			
	Hasley	a	0,11001	0,04530	0,97331	0,00269
		b	0,81681			
	Oswin	a	0,09264	0,04827	0,96970	0,00347
		b	1,10053			
20	BET	a	0,660826	0,05011	0,95219	0,00571
		b	0,133906			
	GAB	k	1,03962	0,06258	0,92542	0,01416
		a	3,75515			
		b	0,05023			
	Hasley	a	0,119695	0,04987	0,95264	0,00571
		b	0,863831			
	Oswin	a	0,111984	0,05018	0,95204	0,00585
		b	1,059789			
35	BET	a	0,03633	0,04168	0,97449	0,00082
		b	1,056755			
	GAB	k	0,92990	0,04432	0.97115	0,02079
		a	3,62135			
		b	0,07296			
	Hasley	a	0,132909	0,04178	0,97436	0,00335
		b	0,906466			
	Oswin	a	0,143029	0,07425	0,91904	0,00264
		b	0,995217			

Source: Authors

This behavior has been reported by other authors working with hydrophilic polymers that have been plasticized with polyols, and it is associated with the increase in the amount of hydroxyl groups in the plasticizer. This increase causes an increase in the hygroscopicity of the material, reflected on the increase in the solubility coefficient of the samples with higher plasticizer concentration. Other authors have reported that a lower water vapor permeability is related to a lower value of the diffusion coefficient. They have also reported that the solubility coefficients of TPS/PLA blends are lower than those of TPS. This behavior is associated with a lower amount of hydroxyl groups in the blend that are available for interaction as the PLA concentration increases, which is in turn associated with the fact that each D-glucose repeat unit contains three of these groups, whereas PLA has two in each polymeric chain (Müller et al., 2012; Abdillahi et al., 2013). It is important to highlight, as mentioned by other authors (Hu and Vuillaume, 2020), that the increase in crystallinity increases the water vapor permeability in the film structure formed by PLA/TPS. This statement is validated by the data shown in the FTIR, DSC, and SEM analyses. Therefore, the incorporation of starch in these blends not only lowers the cost of the material but also contributes to its rapid biodegradation.

Biodegradation analysis

The results observed can be attributed to the dynamics of material degradation (Figure 4). Cellulose obtained a biodegradation percentage of 84%, the samples of the TPS/PLA blend 68%, and PLA 32% in 35 days. These results show that the test performed under the ASTM D5988 standard (ASTM International, 2018) is valid because there is a >20% difference between the control sample and the evaluated blend.
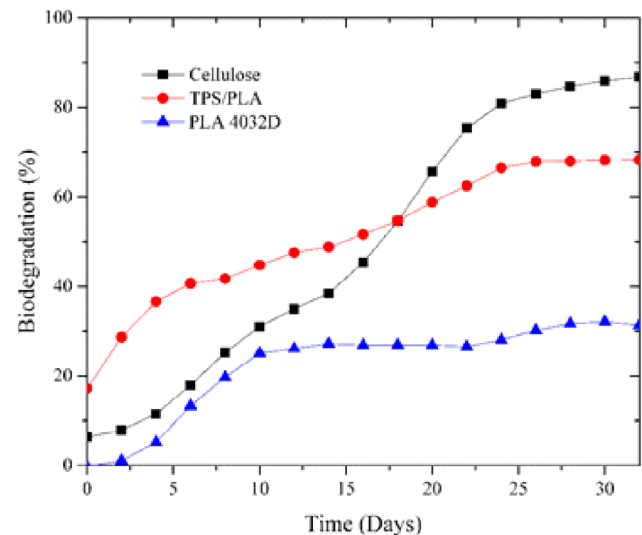
Figure 4. Biodegradability of the TPS/PLA film
Source: Authors

The reason for this is that biodegradation generally proceeds faster in the amorphous part of the polymer when compared to the crystalline ones, and the degradation rate
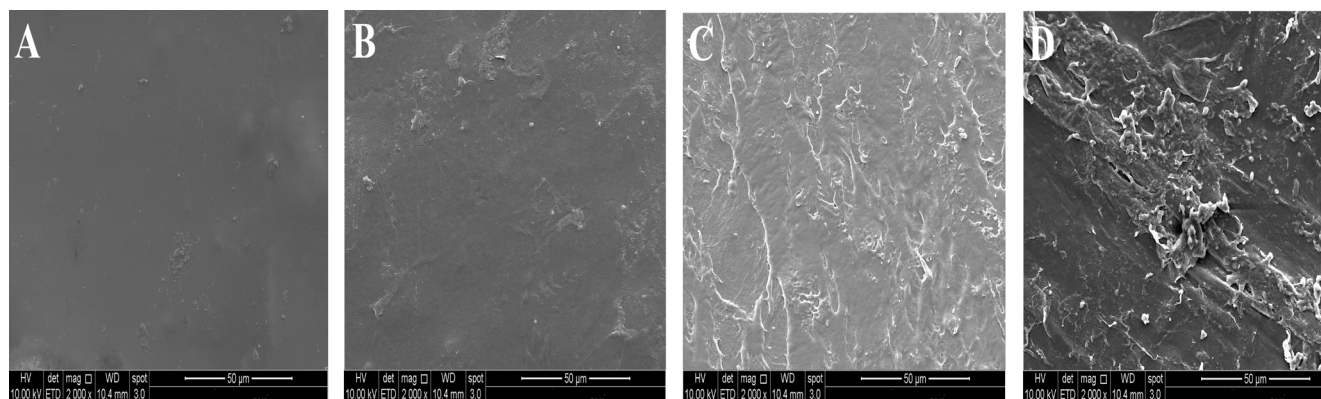
Figure 5. Surface changes in starch/PLA blends during soil degradation
Source: Authors

of polymers with higher molecular weight (PLA) is expected to be lower in comparison with shorter macromolecules (TPS), which are more easily digested by microorganisms. Consequently, the portion of PLA present in the TPS/PLA blended film containing a 72/28 ratio became more biodegradable than pure PLA (Sedničková, et al., 2018). These results are similar to those of Šerá et al., (2020), who found that cellulose obtained 91,4% of biodegradation of (25 ˚C) after 270 days, and a PBT/PLA mixture showed a percentage of 64,4%. These results are consistent with the biodegradation test performed under aerobic composting conditions, in which a 72% biodegradation percentage was found for a TPS/PLA film mixture (Bher, Auras, et al., 2018; Bher et al., 2019; Salazar-Sánchez et al., 2019). According to the results, the semi-crystalline PLA present in the mixture (TPS/PLA) reduces the amorphous regions in such a way that the molecular weight increases significantly and the crystalline regions start to decrease (Karamanlioglu and Robson, 2013; Middleton and Tipton, 2000; Weir et al., 2004), thus causing the fragmentation and disintegration of the material, as observed in the FTIR spectra and SEM micrographs, by means of the modifications to the film surface that could be noticed during the experiment. These results are similar to those reported by Olewnik-Kruszkowska et al. (2020), and they stem from the mineralization effect of the possible hydrolytic processes of microbial origin in the soil.

Scanning electron microscopy (SEM) analysis

The surface changes of the TPS/PLA blends during soil degradation (Figure 5) show that the film surfaces were smooth before degradation, and, after degrading under soil conditions during the evaluation time, they became rough; depressions and scratches appeared on the surface of these blends, similar to that reported by Lv et al. (2018) and Lv, Gu et al. (2017) for samples of 306D PLA and corn starch. After 30 days, there were fractures on the surface of each sample, cracks that would lead to the loss of mechanical strength. There were morphological changes regarding the color and shape of the film surface, which resulted from the attack of microorganisms to the PLA/TPS films (60:40) (Phetwarotai et al., 2013).

Conclusions

The addition of PLA and TPS is synergistic and significantly contributes to preservation and biodegradation processes by means of increasing or decreasing the crystallinity due to the number of amorphous phases present in the polymer. The biodegradability of the blends was confirmed by weight loss measurements with exposure time in the soil process. TPS accelerates the biodegradability of the blends in this medium due to its accessibility to microorganisms, its hydrophilic properties, and its amylose composition, which can be degraded more rapidly. The materials obtained from mixtures of TPS and PLA provide an additional advantage derived from the use of renewable sources for their manufacturing, as they provide the mixture with hydrophilic and biodegradable properties. This is an advantage over conventional plastics that must be exploited in order to obtain resistant materials which can be used in a similar way to conventional polymers.

Acknowledgements

References

Abdillahi, H., Chabrat, E., Rouilly, A., and Rigal, L. (2013). Influence of citric acid on thermoplastic wheat flour/poly(lactic acid) blends. II. Barrier properties and water vapor sorption isotherms. *Industrial Crops and Products, 50*, 104-111. https://doi.org/10.1016/j.indcrop.2013.06.028

Aguerre, R. J., Suárez, C., and Viollaz, P. E. (1989). New BET type multilayer sorption isotherms. *Lebensmittel-Wissenschaft & Technologie, 22*, 192-195.

Altayan, M. M., Al Darouich, T., and Karabet, F. (2017). On the plasticization process of potato starch: Preparation and characterization. *Food Biophysics, 12*(4), 397-403. https://doi.org/10.1007/s11483-017-9495-2

Anakabe, J., Zaldua Huici, A. M., Eceiza, A., Arbelaiz, A., and Avérous, L. (2017). Combined effect of nucleating agent and plasticizer on the crystallization behaviour of polylactide. *Polymer Bulletin, 74*(12), 4857-4886. https://doi.org/10.1007/s00289-017-1989-z

Anderson, R. B. (1946). Modifications of the Brunauer, Emmett and Teller Equation. *Journal of the American Chemical Society, 68*(4), 686-691. https://doi.org/10.1021/ja01208a049

Andrade, R. D. P., Roberto, L. M., and Pérez, C. E. C. (2011). Models of sorption isotherms for food: Uses and limitations. *Vitae, 18*(3), 325-334. https://revistas.udea.edu.co/index.php/vitae/article/view/10682

Arslan-Tontul, S. (2020). Moisture sorption isotherm, isosteric heat and adsorption surface area of whole chia seeds. *Lwt, 119*, 108859. https://doi.org/10.1016/j.lwt.2019.108859

ASTM International (2013). *ASTM E1252-98: Standard practice for general techniques for obtaining infrared spectra for qualitative analysis*. ASTM International.

ASTM International (2015). *ASTM D3418-15: Standard test method for transition temperatures and enthalpies of fusion and crystallization of polymers by differential scanning calorimetry*. ASTM International.

ASTM International (2018). *ASTM D5988-18: Standard test method for determining aerobic biodegradation of plastic materials in soil*. ASTM International.

ASTM International (2020). *ASTM E1131-20: Standard test method for compositional analysis by thermogravimetry*. ASTM International.

Bher, A., Auras, R., and Schvezov, C. E. (2018). Improving the toughening in poly(lactic acid)-thermoplastic cassava starch reactive blends. *Journal of Applied Polymer Science, 135*(15), 46140. https://doi.org/10.1002/app.46140

Bher, A., Unalan, I. U., Auras, R., Rubino, M., and Schvezov, C. E. (2018). Toughening of poly(lactic acid) and thermoplastic cassava starch reactive blends using graphene nanoplatelets. *Polymers, 10*(1), 95. https://doi.org/10.3390/polym10010095

Bher, A., Unalan, I. U., Auras, R., Rubino, M., and Schvezov, C. E. (2019). Graphene modifies the biodegradation of poly(lactic acid)-thermoplastic cassava starch reactive blend films. *Polymer Degradation and Stability, 164*, 187-197. https://doi.org/10.1016/j.polymdegradstab.2019.04.014

Brunauer, S., Emmett, P. H., and Teller, E. (1938). Adsorption of gases in multimolecular layers. *Journal of the American Chemical Society, 60*(2), 309-319. https://doi.org/10.1021/ja01269a023

Cai, J., Xiong, Z., Zhou, M., Tan, J., Zeng, F., Meihuma, Lin, S., and Xiong, H. (2014). Thermal properties and crystallization behavior of thermoplastic starch/poly(ε-caprolactone) composites. *Carbohydrate Polymers, 102*(1), 746-754. https://doi.org/10.1016/j.carbpol.2013.10.095

Cao, C., Shen, M., Hu, J., Qi, J., Xie, P., and Zhou, Y. (2020). Comparative study on the structure-properties relationships of native and debranched rice starch. *CyTA - Journal of Food, 18*(1), 84-93. https://doi.org/10.1080/19476337.2019.1710261

Carmona, V. B., Corrêa, A. C., Marconcini, J. M., and Mattoso, L. H. C. (2015). Properties of a biodegradable ternary blend of thermoplastic starch (TPS), poly(ε-caprolactone) (PCL) and poly(lactic acid) (PLA). *Journal of Polymers and the Environment, 23*(1), 83-89. https://doi.org/10.1007/s10924-014-0666-7

Castro-Aguirre, E., Auras, R., Selke, S., Rubino, M., and Marsh, T. (2018). Enhancing the biodegradation rate of poly(lactic acid) films and PLA bio-nanocomposites in simulated composting through bioaugmentation. *Polymer Degradation and Stability, 154*, 46-54. https://doi.org/10.1016/j.polymdegradstab.2018.05.017

Chen, C. H., and Lai, L. S. (2008). Mechanical and water vapor barrier properties of tapioca starch/decolorized hsian-tsao leaf gum films in the presence of plasticizer. *Food Hydrocolloids, 22*(8), 1584-1595. https://doi.org/10.1016/j.foodhyd.2007.11.006

Daza, L. D., Homez-Jara, A., Solanilla, J. F., and Váquiro, H. A. (2018). Effects of temperature, starch concentration, and plasticizer concentration on the physical properties of ulluco (Ullucus tuberosus Caldas)-based edible films. *International Journal of Biological Macromolecules, 120*(Part B), 1834-1845. https://doi.org/10.1016/j.ijbiomac.2018.09.211

American Public Health Association (APHA) (1999). *Standard methods for the examination of water and waste water* (20th ed.). APHA.

de Boer, J. H. (1953). The dynamical character of adsorption. *Soil Science, 76*(2), 166. https://doi.org/10.1097/00010694-195308000-00014

de Oliveira, T. A., Barbosa, R., Mesquita, A. B. S., Ferreira, J. H. L., de Carvalho, L. H., and Alves, T. S. (2019). Fungal degradation of reprocessed PP/PBAT/thermoplastic starch blends. *Journal of Materials Research and Technology, 9*(2), 2338-2349. https://doi.org/10.1016/j.jmrt.2019.12.065

de Oliveira, T. A., de Oliveira Mota, I., Mousinho, F. E. P., Barbosa, R., de Carvalho, L. H., and Alves, T. S. (2019). Biodegradation of mulch films from poly(butylene adipate co-terephthalate), carnauba wax, and sugarcane residue. *Journal of Applied Polymer Science, 136*(47), 48240. https://doi.org/10.1002/app.48240

Dutcher, C. S., Ge, X., Wexler, A. S., and Clegg, S. L. (2011). Statistical mechanics of multilayer sorption: Extension of the Brunauer-Emmett-Teller (BET) and Guggenheim-Anderson-de Boer (GAB) adsorption isotherms. *Journal of Physical Chemistry C, 115*(33), 16474-16487. https://doi.org/10.1021/jp203879d

Esmaeili, M., Pircheraghi, G., Bagheri, R., and Altstädt, V. (2019). Poly(lactic acid)/coplasticized thermoplastic starch blend: Effect of plasticizer migration on rheological and mechanical properties. *Polymers for Advanced Technologies, 30*(4), 839-851. https://doi.org/10.1002/pat.4517

Frone, A. N., Berlioz, S., Chailan, J. F., and Panaitescu, D. M. (2013). Morphology and thermal properties of PLA-cellulose nanofibers composites. *Carbohydrate Polymers, 91*(1), 377-384. https://doi.org/10.1016/j.carbpol.2012.08.054

Garalde, R. A., Thipmanee, R., Jariyasakoolroj, P., and Sane, A. (2019). The effects of blend ratio and storage time on thermoplastic starch/poly(butylene adipate-co-terephthalate) films. *Heliyon, 5*(3), e01251. https://doi.org/10.1016/j.heliyon.2019.e01251

Gopi, S., Amalraj, A., Jude, S., Thomas, S., and Guo, Q. (2019). Bionanocomposite films based on potato, tapioca starch

and chitosan reinforced with cellulose nanofiber isolated from turmeric spent. *Journal of the Taiwan Institute of Chemical Engineers, 96*, 664-671. https://doi.org/10.1016/j.jtice.2019.01.003

Guggenheim, E. A. (1966). *Applications of statistical mechanics*. Clarendon Press.

Halsey, G. (1948). Physical adsorption on non-uniform surfaces. *The Journal of Chemical Physics, 16*(10), 931-937. https://doi.org/10.1063/1.1746689

Gürler, N., Paşa, S., Hakkı Alma, M., and Temel, H. (2020). The fabrication of bilayer polylactic acid films from cross-linked starch as eco-friendly biodegradable materials: Synthesis, characterization, mechanical and physical properties. *European Polymer Journal, 127*, 109588. https://doi.org/10.1016/j.eurpolymj.2020.109588

Heidemann, H. M., Dotto, M. E. R., Laurindo, J. B., Carciofi, B. A. M., and Costa, C. (2019). Cold plasma treatment to improve the adhesion of cassava starch films onto PCL and PLA surface. *Colloids and Surfaces A: Physicochemical and Engineering Aspects, 580*, 123739 https://doi.org/10.1016/j.colsurfa.2019.123739

Homez, A. K., Daza, L. D., Solanilla, J. F., and Váquiro, H. A. (2018). Effect of temperature, starch and plasticizer concentrations on color parameters of ulluco (Ullucus tuberosus Caldas) edible films. *IOP Conference Series: Materials Science and Engineering, 437*, 012003. https://doi.org/10.1088/1757-899X/437/1/012003

Hu, L., and Vuillaume, P. Y. (2020). Reactive compatibilization of polymer blends by coupling agents and interchange catalysts. In A. R. Ajitha and T. Thomas (Eds.), *Compatibilization of Polymer Blends* (pp. 205-248). Elsevier. https://doi.org/10.1016/b978-0-12-816006-0.00007-4

Iglesias, H. A., and Chirife, J. (1995). An alternative to the Guggenheim, Anderson and De Boer model for the mathematical description of moisture sorption isotherms of foods. *Food Research International, 28*(3), 317-321. https://doi.org/10.1016/0963-9969(94)00002-P

ISO (2012). *10210:2012. Plastics -- Methods for the preparation of samples for biodegradation testing of plastic materials*. https://www.iso.org/standard/45851.html

Karamanlioglu, M., and Robson, G. D. (2013). The influence of biotic and abiotic factors on the rate of degradation of poly(lactic) acid (PLA) coupons buried in compost and soil. *Polymer Degradation and Stability, 98*(10), 2063-2071. https://doi.org/10.1016/j.polymdegradstab.2013.07.004

Lambert, S., and Wagner, M. (2017). Environmental performance of bio-based and biodegradable plastics: The road ahead. *Chemical Society Reviews, 46*(22), 6855-6871. https://doi.org/10.1039/c7cs00149e

Lambert, T., and Perga, M. E. (2019). Non-conservative patterns of dissolved organic matter degradation when and where lake water mixes. *Aquatic Sciences, 81*(4), 64. https://doi.org/10.1007/s00027-019-0662-z

Lendvai, L., Sajó, I., and Karger-Kocsis, J. (2019). Effect of storage time on the structure and mechanical properties of starch/bentonite nanocomposites. *Starch, 71*(1-2), 1800123. https://doi.org/10.1002/star.201800123

Li, Y., Zhang, K., Nie, M., and Wang, Q. (2020). Application of compatibilized polymer blends in packaging. In A. R. Ajitha and T. Thomas (Eds.), *Compatibilization of Polymer Blends* (pp. 539-561). Elsevier. https://doi.org/10.1016/b978-0-12-816006-0.00019-0

Liu, H., Chaudhary, D., Yusa, S. I., and Tadé, M. O. (2011). Glycerol/starch/Na+-montmorillonite nanocomposites: A XRD, FTIR, DSC and 1H NMR study. *Carbohydrate Polymers, 83*(4), 1591-1597. https://doi.org/10.1016/j.carbpol.2010.10.018

Lv, S., Gu, J., Tan, H., and Zhang, Y. (2017). The morphology, rheological, and mechanical properties of wood flour/starch/poly(lactic acid) blends. *Journal of Applied Polymer Science, 134*(16), 44743. https://doi.org/10.1002/app.44743

Lv, S., Zhang, Y., Gu, J., and Tan, H. (2017). Biodegradation behavior and modelling of soil burial effect on degradation rate of PLA blended with starch and wood flour. *Colloids and Surfaces B: Biointerfaces, 159*, 800-808. https://doi.org/10.1016/j.colsurfb.2017.08.056

Lv, S., Zhang, Y., Gu, J., and Tan, H. (2018). Physicochemical evolutions of starch/poly (lactic acid) composite biodegraded in real soil. *Journal of Environmental Management, 228*, 223-231. https://doi.org/10.1016/j.jenvman.2018.09.033

Middleton, J. C., and Tipton, A. J. (2000). Synthetic biodegradable polymers as orthopedic devices. *Biomaterials, 21*(23), 2335-2346. https://doi.org/10.1016/S0142-9612(00)00101-0

Mierzwa-Hersztek, M., Gondek, K., and Kopeć, M. (2019). Degradation of polyethylene and biocomponent-derived polymer materials: An overview. *Journal of Polymers and the Environment, 27*(3), 600-611. https://doi.org/10.1007/s10924-019-01368-4

Müller, C. M. O., Pires, A. T. N., and Yamashita, F. (2012). Characterization of thermoplastic starch/poly(lactic acid) blends obtained by extrusion and thermopressing. *Journal of the Brazilian Chemical Society, 23*(3), 426-434. https://doi.org/10.1590/S0103-50532012000300008

Müller, J., González-Martínez, C., and Chiralt, A. (2017). Poly(lactic) acid (PLA) and starch bilayer films, containing cinnamaldehyde, obtained by compression moulding. *European Polymer Journal, 95*, 56-70. https://doi.org/10.1016/j.eurpolymj.2017.07.019

Nasseri, R., Ngunjiri, R., Moresoli, C., Yu, A., Yuan, Z., and Xu, C. (Charles). (2020). Poly(lactic acid)/acetylated starch blends: Effect of starch acetylation on the material properties. *Carbohydrate Polymers, 229*, 115453. https://doi.org/10.1016/j.carbpol.2019.115453

Nevoralová, M., Koutný, M., Ujčić, A., Horák, P., Kredatusová, J., Šerá, J., Růžek, L., Růžková, M., Krejčíková, S., Šlouf, M., and Kruliš, Z. (2019). Controlled biodegradability of functionalized thermoplastic starch based materials. *Polymer Degradation and Stability, 170*, 108995. https://doi.org/10.1016/j.polymdegradstab.2019.108995

Olewnik-Kruszkowska, E., Burkowska-But, A., Tarach, I., Walczak, M., and Jakubowska, E. (2020). Biodegradation of polylactide-based composites with an addition of a compatibilizing agent in different environments. *International Biodeterioration and Biodegradation, 147*, 104840. https://doi.org/10.1016/j.ibiod.2019.104840

Oswin, C. R. (1946). The kinetics of package life. III. The isotherm. *Journal of the Society of Chemical Industry, 65*(12), 419-421. https://doi.org/10.1002/jctb.5000651216

Özeren, H. D., Olsson, R. T., Nilsson, F., and Hedenqvist, M. S. (2020). Prediction of plasticization in a real biopolymer system (starch) using molecular dynamics simulations. *Materials & Design, 187*, 108387. https://doi.org/10.1016/j.matdes.2019.108387

Palai, B., Biswal, M., Mohanty, S., and Nayak, S. K. (2019). In situ reactive compatibilization of polylactic acid (PLA) and thermoplastic starch (TPS) blends; synthesis and evaluation of extrusion blown films thereof. *Industrial Crops and Products, 141*, 111748. https://doi.org/10.1016/j.indcrop.2019.111748

Pattanasuttichonlakul, W., Sombatsompop, N., and Prapagdee, B. (2018). Accelerating biodegradation of PLA using microbial consortium from dairy wastewater sludge combined with PLA-degrading bacterium. *International Biodeterioration and Biodegradation, 132*, 74-83. https://doi.org/10.1016/j.ibiod.2018.05.014

Phetwarotai, W., Potiyaraj, P., and Aht-Ong, D. (2013). Biodegradation of polylactide and gelatinized starch blend films under controlled soil burial conditions. *Journal of Polymers and the Environment, 21*(1), 95-107. https://doi.org/10.1007/s10924-012-0530-6

Riba, J. R., Cantero, R., García-Masabet, V., Cailloux, J., Canals, T., and Maspoch, M. L. (2020). Multivariate identification of extruded PLA samples from the infrared spectrum. *Journal of Materials Science, 55*(3), 1269-1279. https://doi.org/10.1007/s10853-019-04091-6

Salazar-Sánchez, M. del R., Campo-Erazo, S. D., Villada-Castillo, H. S., and Solanilla-Duque, J. F. (2019). Structural changes of cassava starch and polylactic acid films submitted to biodegradation process. *International Journal of Biological Macromolecules, 129*, 442-447. https://doi.org/10.1016/j.ijbiomac.2019.01.187

Salazar-Sánchez, M. D. R., Cañas-Montoya, J. A., Villada-Castillo, H. S., Solanilla-Duque, J. F., Rodríguez-Herrera, R., and Avalos-Belmotes, F. (2020). Biogenerated polymers: An enviromental alternative. *DYNA, 87*(214), 75-84. https://doi.org/10.15446/dyna.v87n214.82163

Sedničková, M., Pekařová, S., Kucharczyk, P., Bočkaj, J., Janigová, I., Kleinová, A., Jochec-Mošková, D., Omaníková, L., Perdochová, D., Koutný, M., Sedlařík, V., Alexy, P., and Chodák, I. (2018). Changes of physical properties of PLA-based blends during early stage of biodegradation in compost. *International Journal of Biological Macromolecules, 113*, 434-442. https://doi.org/10.1016/j.ijbiomac.2018.02.078

Šerá, J., Serbruyns, L., de Wilde, B., and Koutný, M. (2020). Accelerated biodegradation testing of slowly degradable polyesters in soil. *Polymer Degradation and Stability, 171*, 109031. https://doi.org/10.1016/j.polymdegradstab.2019.109031

Shogren, R. L., Doane, W. M., Garlotta, D., Lawton, J. W., and Willett, J. L. (2003). Biodegradation of starch/polylactic acid/poly(hydroxyester-ether) composite bars in soil. *Polymer Degradation and Stability, 79*(3), 405-411. https://doi.org/10.1016/S0141-3910(02)00356-7

SSLMM-42-2-92. Soil Survey Laboratory Methods Manual Reporte No.42, Versión 2.0, 1992

Torres, M. D., Moreira, R., Chenlo, F., and Vázquez, M. J. (2012). Water adsorption isotherms of carboxymethyl cellulose, guar, locust bean, tragacanth and xanthan gums. *Carbohydrate Polymers, 89*(2), 592-598. https://doi.org/10.1016/j.carbpol.2012.03.055

Valsaraj, K. T. (2009). *Elements of environmental engineering: Thermodynamics and kinetics*. Taylor & Francis Group.

van den Berg, C. (1981). *Vapour sorption equilibria and other Water-starch interactions; A Physico-chemical approach* [Doctoral dissertation, Wageningen University]. http://library.wur.nl/WebQuery/wurpubs/75143

Wang, F., Lei, S., Ou, J., Li, C., and Li, W. (2019). Novel All-Natural Material for Oil/Water Separation. *Industrial & Engineering Chemistry Research, 58*(5), 1924-1931. https://doi.org/10.1021/acs.iecr.8b05535

Wang, P., Xiong, Z., Fei, P., Cai, J., Walayat, N., and Xiong, H. (2020). An approach for compatibilization of the starch with poly(lactic acid) and ethylene-vinyl acetate-glycidyl-methacrylate. *International Journal of Biological Macromolecules, 161*, 44-58. https://doi.org/10.1016/j.ijbiomac.2020.06.011

Wang, H., Wu, J., Luo, S., Zou, P., Guo, B., Liu, Y., Chen, J., and Liu, C. (2020). Improving instant properties of kudzu powder by extrusion treatment and its related mechanism. *Food Hydrocolloids, 101*, 105475. https://doi.org/10.1016/j.foodhyd.2019.105475

Weir, N. A., Buchanan, F. J., Orr, J. F., and Dickson, G. R. (2004). Degradation of poly-L-lactide. Part 1: In vitro and in vivo physiological temperature degradation. *Proceedings of the Institution of Mechanical Engineers, Part H: Journal of Engineering in Medicine, 218*(5), 307-319. https://doi.org/10.1243/0954411041932782

Zdanowicz, M., Staciwa, P., Jędrzejewski, R., and Spychaj, T. (2019). Sugar alcohol-based deep eutectic solvents as potato starch plasticizers. *Polymers, 11*(9), 1385. https://doi.org/10.3390/polym11091385

Short UV-C Treatments to Extend the Shelf-Life of Fresh-Cut Strawberries (*Fragaria x ananassa* Duch cv. Camarosa)

Tratamientos cortos con UV-C para extender la vida útil de fresas (*Fragaria x ananassa* Duch cv. Camarosa) mínimamente procesadas

Leidy C. Ortiz-Araque [1] Magalí Darré [2], Pedro M. Civello[3], and Ariel. R. Vicente[3]

ABSTRACT

In recent years, there has been a marked increase in the demand for fresh-cut fruit. Although these products have a high user convenience, they are extremely perishable, which is why they must be distributed within a very short period of time. A number of studies have shown that brief UV-C irradiation prior to storage may reduce postharvest deterioration in whole fruits. In this work, we evaluated the influence of different UV-C dosage and intensity combinations on the quality and shelf-life of fresh-cut strawberries. Fresh berries were cut in wedges and subjected to brief UV-C treatments with different combinations of radiation intensity (0, 9, or 36 W m^{-2}) and dose (0, 2, or 4 kJ m^{-2}). The treatments with the highest dosage and intensity decreased decay, juice leakage, dehydration softening, and yeasts and mold counts. UV-C-treated berries also scored better in freshness, color, and overall acceptability in consumer tests. The treatments did not affect the acidity, soluble solids, or phenolic compounds. Results suggest that a short UV-C treatment could be useful to supplement cold storage, extending the shelf-life of fresh-cut strawberries.

Keywords: berries, irradiation, fresh-cut products, postharvest

RESUMEN

En los últimos años ha habido un aumento en la demanda de frutas mínimamente procesadas. A pesar de representar una alta comodidad de usuario, estos productos son extremadamente perecederos, lo que hace que deban distribuirse en un periodo muy corto de tiempo. Algunos estudios han mostrado que la irradiación UV-C antes del almacenamiento puede retrasar el deterioro postcosecha de frutos enteros. En este trabajo evaluamos la influencia de diferentes combinaciones de dosis e intensidad de radiación UV-C en la calidad y vida útil de fresas mínimamente procesadas. Las fresas se trataron con diferentes intensidades (0, 9 o 36 W m^{-2}) y dosis (0, 2 o 4 kJ m^{-2}) de radiación UV-C. Los tratamientos con la dosis y la intensidad más altas redujeron el deterioro, el exudado de jugo, la deshidratación el ablandamiento y el recuento de mohos y levaduras. Los frutos tratados con UV-C obtuvieron además una mayor puntuación en frescura, color y aceptabilidad sensorial en paneles de consumidores. Los tratamientos no afectaron la acidez, los sólidos solubles o los fenoles totales. Los resultados sugieren que un tratamiento corto con UV-C puede ser útil para complementar los beneficios de la refrigeración y extender la vida útil de fruta mínimamente procesada.

Palabras clave: fresas, irradiación, productos frescos cortados, postcosecha

Introduction

In recent years, there has been a rapid increase in the demand for additive-free, fresh-cut fruit (Ma *et al.*, 2017). Although highly convenient, these products are extremely perishable and must be distributed within a very short time period. This has rapidly raised an interest in the search for postharvest methods that are able to maintain quality and prolong the shelf-life while reducing or avoiding the use of synthetic additives (Charles, 2018).

UV-C radiation has long been known for its germicide properties (Graça *et al.*, 2020). These treatments were initially applied for material disinfection, but they subsequently started to be evaluated for direct use on food surfaces (Vicente and Lurie, 2014). UV-C treatments have been reported to control postharvest rots, delay ripening, reduce some physiological disorders, and induce antioxidants (Romanazzi

et al., 2016). However, the effects of UV-C radiation are variable and largely dependent on the organ type, species, cultivar, ripening stage, processing degree, and irradiation conditions (Bu *et al.*, 2013; Gayán *et al.*, 2014; Abdipour *et al.*, 2019). Strawberry treatments with UV-C doses

---

[1] Center for Research and Development in Food Cryotechnology (CONICET, CIC, National University of La Plata. Argentina E-mail: leidy.ortiz@unipaz.edu.co
[2] National University of La Plata, Argentina. E-mail: magali.darre@agro.unlp.edu.ar
[3] INFIVE, Institute of Plant Physiology (CONICET-National University of La Plata, Argentina). E-mail: pmcivello@agro.unlp.edu.ar
[4] LIPA (Research Laboratory on Agro-industrial Products) (Department of Agricultural and Forest Sciences, National University of La Plata, Argentina). E-mail: arielvicente@quimica.edu.ar

ranging between 0,25 and 4,0 kJ m^{-2} have been reported to improve postharvest quality maintenance (Ortiz-Araque *et al.*, 2019). Cote *et al.* (2013) highlighted the importance of radiation intensity as a major factor, in addition to the total radiation dose applied. The relevance of considering both the treatment dosage and radiation intensity was also highlighted in UV-B-treated vegetables (Darré *et al.*, 2017), even though both process control variables were rarely reported.

Some studies have reported the benefits of UV exposure in fresh-cut fruits and vegetables (Graça *et al.*, 2020). The number of studies is much more limited when compared to unprocessed commodities. This may be due to the fact that these products are normally subjected to a wet disinfection step. While this may be speculated to decrease the potential benefits of UV-C treatments, it needs to be evaluated in a commodity-dependent manner. A recent report by Li *et al.* (2019) showed positive results in cut strawberries treated with UV-C radiation. However, in this study, the role of radiation intensity on treatment efficacy was not addressed. The aim of this work was to select the appropriate UV-C radiation dose and intensity conditions for the postharvest treatment of fresh-cut strawberries, as well as to determine their influence on the fruits' physical, chemical, microbiological, and sensory quality.

Materials and methods

Selection of optimal UV-C radiation dose and intensity combination

Strawberries cv. Camarosa produced in greenhouses in La Plata, Argentina, were harvested at commercial maturity (100% red surface color) and transported to the laboratory within 1 h. Fruit selection was performed to eliminate those with physical damage, ripening, or shape defects. The fruits were washed with chlorinated water (NaClO 100 mg L^{-1}, pH 6,5) and cut longitudinally to the main axis in quarters. After cutting, the fruits were washed again and drained to eliminate water excess. They were subjected to the following treatments:

i. Control: unexposed to UV-C light. *ii. UV-C low intensity/ low dose:* fruit treated with UV-C radiation at an intensity of 9 W m^{-2} and a dose of 2 kJ m^{-2}. *iii. UV-C low intensity/ high dose:* fruit treated with UV-C radiation at an intensity of 9 W m^{-2} and a dose of 4 kJ m^{-2}. *iv. UV-C high intensity/ low dose:* fruit treated with UV-C radiation at an intensity of 36 W m^{-2} and a dose of 2 kJ m^{-2}. *v. UV-C high intensity/ high dose:* fruit treated with UV-C at an intensity of 36 W m^{-2} and a dose of 4 kJ m^{-2}. The fruit was rotated to ensure even exposure to UV radiation. The irradiation treatments were carried out in a mobile cabinet (1,7 × 0,8 × 0,5) equipped at the top with 12 UV-C lamps (peak emission UV-C at 254 nm, TUV G30T8, 30 W, Philips, Argentina). The distance between the emitting source and the fruit was 30 cm in all cases. The dose was established by varying the treatment times and intensity and modifying the number of lamps on. The UV-C radiation dose was evaluated using a digital UV-C

radiometer (Electro Lite LC 300, United States) located at the center of the irradiation cabinet. After the treatments, the fruits were placed in polyethylene terephthalate trays (10 × 15 × 3 cm) with perforated lids (1 perforation of 1 mm diameter per cm^{-2}). Forty fruit wedges were placed per tray. Four separate trays were analyzed for each treatment, and the whole experiment was performed in duplicate. After 4 days of storage at 4 ˚C, the fruit was evaluated for decay incidence in order to select the optimal treatment condition.

Effect of selected UV-C treatment in fruit physic-chemical, microbiological, and sensory quality as well as shelf-life

Strawberries cv. Camarosa were harvested, selected, disinfected, and processed as described in the previous section. The berries were subsequently subjected to UV-C irradiation (36 W m^{-2} intensity, 4 kJ m^{-2} dose) and packed as indicated above. Forty fruit wedges were placed per tray. Fruit was stored at 4 ºC for 7 days. Corresponding controls without UV-C treatment were packaged and stored as described above. At different storage times (0, 4, and 7 days), samples were taken and used for quality evaluation. For chemical analyses, the samples were frozen in liquid nitrogen and stored at -80 ˚C until use. Three trays were utilized per treatment and storage time, and the whole experiment was performed in duplicate.

Visual Deterioration Index and juice exudate: a Visual Deterioration Index (VDI) was calculated using a hedonic five-point scale (1: no visual damage to 5: serious damage). The attributes evaluated for VDI were the presence of rot and macerated areas, as well as the loss of surface brightness. Exudate juices were determined by weighing the liquid released on each individual tray along storage. The results were expressed in grams per kilogram on a fresh weight basis. Six measurements were made for each treatment and storage time.

Weight loss: the individual trays were weighed throughout the storage period. Weight loss was calculated according to the following equation: *Weight loss (%) = 100 × (Pi-Pf)/Pi*, with *Pi* and *Pf* being the initial weight and the weight at each storage time, respectively. Six measurements were made for each treatment and storage time.

Yeasts and molds plate counts: 50 g of fruit wedges were put in pre-sterilized beakers containing 225 ml of 0,1% w/v peptone. The samples were shaken for 15 min, and two series of dilutions (10^{-2}-10^{-4}) of the washing liquid were prepared. One milliliter of each dilution was loaded on Petri dishes with a YGC medium and incubated at 20 ˚C for 5 days. The plates showing between 30 and 300 colonies were counted, and the results were expressed as log of colony forming units (CFU) per gram of fresh fruit.

Firmness: fruit firmness was determined by uniaxial puncture tests on a Texture Analyzer (TA.XT2, Stable Micro Systems Texture Technologies, NY, United States) equipped with a 3

mm diameter flat probe. The samples were compressed 2 mm at a speed of 0,5 mm s⁻¹. The initial slope of the fruit distance curve was calculated. Results were expressed in N mm⁻¹. 60 measurements were done for each treatment and storage time.

Surface color: measurements were done with a chromameter (Minolta CR-400, Japan) equipped with the CIE C illuminant and with a viewing angle of 0° in order to determine the L*, a*, and b* values. Fruit hue (tg⁻¹ b*/a*) and chroma (a*² + b*²)^{1/2} were calculated. 30 measurements were made for each treatment and storage time.

pH, acidity, and soluble solids: fruit wedges were ground in a mill, and 5 g of the resulting sample were taken to 100 mL with water. The initial pH was measured using a pH meter, and the samples were titrated with 0,1 M NaOH to a pH of 8,2 determined potentiometrically (AOAC, 1980). The results were expressed as mmol H^+ kg⁻¹ on a fresh weight basis. For soluble solid (SS) measurement, ground tissue was filtered through a cloth and measured in a self-compensated digital refractometer (HI 96801, Argentina). The results were expressed in %w/w. Six measurements were done for each treatment and storage time.

Phenolic content: fruit phenolic content, which represents the most abundant group in berries (Martinsen *et al.*, 2020), was determined spectrophotometrically in ethanolic extracts according to Singleton *et al.* (1995). Results were calculated by using chlorogenic acid (CGA) as a standard and expressed as mg CGA equivalents per kilogram on a fresh weight basis. Three extracts were analyzed for each treatment and storage time.

Sensory evaluation: a consumer sensory acceptability test was conducted for control and UV-C treated fruit stored at 4 °C for 7 days. The panel consisted of 50 consumers with an equal proportion of men and women, whose age ranged from 25 to 35 years old. The panelists were asked to score the fruit in a 9-point hedonic scale (1: poor, 9: excellent) for the following attributes: i) freshness, ii) color, and iii) overall acceptability.

Statistical analysis: The experiments were performed according to a factorial design, whose factors were the treatment (experiments 1 and 2) and storage time (experiment 2). The data were analyzed by means of an ANOVA using the InfoStat/L software, version 2018 (Di Renzo *et al.*, 2018). The model assumptions of homogeneity of variance and normality were tested by means of the Levene and Shapiro-Wilk tests, respectively, and the means were compared with the Fisher test at a significance level of p<0,05.

Results

Selection of optimal UV-C radiation dose and intensity combination

Berries are among the most perishable fruits (Pott *et al.*, 2019). Their high metabolic and softening rates, as well as their decay

susceptibility, normally lead to a very brief postharvest life, even under proper refrigeration (Panou *et al.*, 2020; Muley and Singhal, 2020). In the first experiment, the main cause of fruit deterioration during storage was the formation of discrete macerated areas on the fruit surface. This was accompanied in severely rotten fruit by signs of fungal mycelia. All four UV-C treatments significantly reduced the fruit decay relative to the control (Figure 1). The use of UV-C treatments for disease control has already been reported in whole strawberry with doses ranging between 0,25 and 4,00 kJ m⁻² (Nigro *et al.*, 2000; Pan *et al.*, 2004). In fresh-cut berries, a recent study has been conducted, with positive effects in terms of decay control in fruit subjected to a UV dose similar to that tested in this research (Li *et al.*, 2019). However, in this study, the influence of different radiation intensities for a similar dose were not evaluated; the UV-C treatments at the lowest dose already controlled rot incidence. Under this UV-C dosage, no impact of the irradiance used was found in terms of treatment efficacy. On the contrary, differences in decay control were found between UV-C doses when high radiation intensity was applied. The UV-C treatment combining high intensity and high dosage (36 W m⁻² and 4 kJ m⁻²) turned out to be the most effective condition for decay control. In strawberries, Cote *et al.* (2013) reported that a high UV-C radiation intensity improves decay control, although this work was done in unprocessed, less mature, and unwashed berries. Moreover, these authors did not assess the influence of different dose-intensity combinations. Based on the results obtained, the high dose-high intensity UV-C treatment (4 kJ m⁻² - 36 W m⁻²) was selected to further characterize the impact on fruit physicochemical, microbiological, and sensory properties during storage.
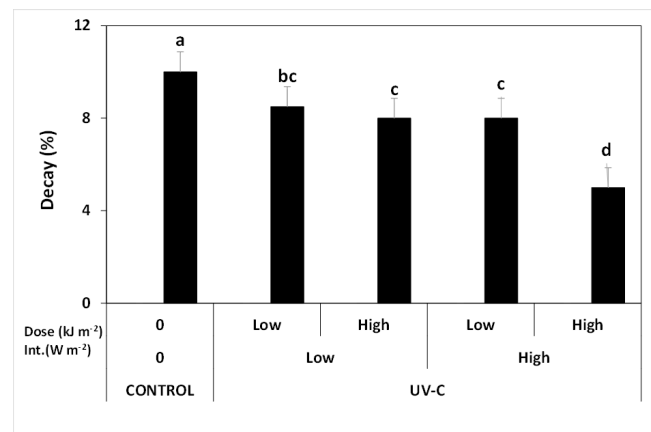
Figure 1. Selection of optimal UV-C treatment conditions (dose and intensity) based on decay control for fresh-cut strawberries stored at 4 °C for 4 d. Low intensity: 9 W m⁻²; High intensity: 36 W m⁻²; Low dose: 2 kJ/ m⁻²; High dose: 4 kJ m⁻². Different letters indicate differences according to Fisher's test with a significance level of p<0,05.
Source: Authors

Effect of selected UV-C treatment on fruit physicochemical, microbiological, and sensory quality as well as shelf-life

The most prevalent deterioration symptoms during storage were the loss of surface brightness and the formation of

rotten areas. Strikingly, tissue decay was most common in the outer zone of the receptacle (pigmented sides) than in the radial (white, pink) cutting region. This differs from what has been reported in other fresh-cut products, in which the cutting zones become the most susceptible areas (Rodoni et al., 2017). One plausible and simple explanation could be that the internal radial fruit region still contains unripe tissues, and that the protective effect of this maturity factor on decay susceptibility is more relevant and caused by the removal of natural barriers through cutting. Moreover, control and UV-C treated fruits showed clear differences regarding the Visual Deterioration Index (VDI). After 4 days of storage, the VDI was already significantly lower in UV-C-irradiated fruit (Figure 2).
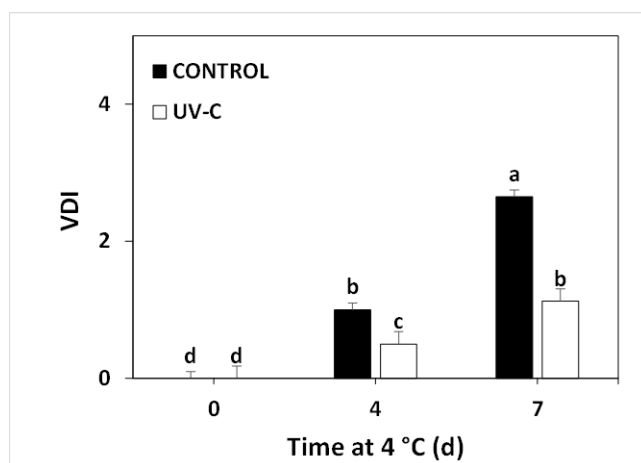
Figure 2. Visual Deterioration Index (VDI) in control or UV-C-treated (36 W m^{-2} radiation intensity and 4 kJ m^{-2} radiation dose) fresh-cut strawberry, stored at 4 °C for 0, 4, and 7 days. Different letters indicate significant differences according to Fisher's test with a significance level of p<0,05.
Source: Authors

The effect became even greater after 7 days at 4 °C. The VDI of UV-C treated berries after one week was indeed comparable to that found in control fruits stored for just 4 days. These differences are relevant for very perishable commodities such as fresh-cut strawberry, which rarely lasts more than 7 days.

Another clear difference found between control and UV-C treated fruits was the exudates of fruit juices. After 7 days of storage and indirectly indicating greater cell rupture, control fruits released 20 times more juices in the trays than the corresponding UV-C-treated berries (Figure 3).

To understand whether the responses in this case were due to a germicide response, we tested the changes in fungal CFU in control and treated fruits immediately after UV exposure as well as during storage. The main fungi that have been associated with strawberry postharvest decay include *Botrytis* and *Rhizopus* (Nigro et al., 2000; Agyare et al., 2020). Yeasts have been also reported to cause soft rots in fresh-cut commodities (Graça et al., 2020). Immediately after irradiation, no changes in yeast and mold counts were found (Figure 4).

Figure 3. Juice exudate in control or UV-C treated (36 W m^{-2} radiation intensity and 4 kJ m^{-2} radiation dose) fresh-cut strawberry, stored at 4 °C for 0, 4, and 7 days. Different letters indicate significant differences according to Fisher's test with a significance level of p<0,05.
Source: Authors
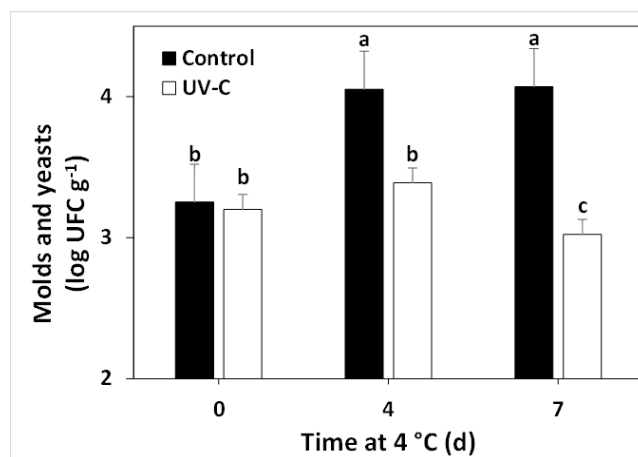
Figure 4. Molds and yeasts count in control or UV-C-treated (36 W m^{-2} radiation intensity and 4 kJ m^{-2} radiation dose) fresh-cut strawberry, stored at 4 °C for 0, 4, and 7 days. Different letters indicate significant differences according to Fisher's test with a significance level of p<0,05.
Source: Authors

However, after both 4 and 7 days of storage at 4 °C, UV-C-treated fruits presented lower CFU g^{-1} than the control. This indicates that the observed impact on fruit decay was not due to a germicidal response. Instead, it might have been caused either by germistatic effects on the pathogen side, by ripening modulation and hermetic responses on the fruit side, or by their combinations. While working with whole strawberries, Pan et al. (2004) reported that UV-C treatments at a dose similar to that used here reduced *Botrytis* and *Rhizopus* conidia germination without affecting their viability, and Pombo et al. (2010) described the induction of genes that code for antimicrobial enzymes.

UV-C-treated fruit showed lower weight loss than the control at the end of storage (Figure 5). Lamickanra et al. (2005) suggested that irradiation of fresh-cut Galia melon partially dehydrated the fruit epidermis and prevented subsequent water loss. Rodoni et al. (2012) suggested that, by favoring

the cross-linking of wall proteinaceous and phenolic components, UV exposure may increase fruit resistance to dehydration. Although further studies would be necessary to establish the mechanisms involved, results show that the UV-C treatments applied herein were also beneficial to prevent tissue dehydration.
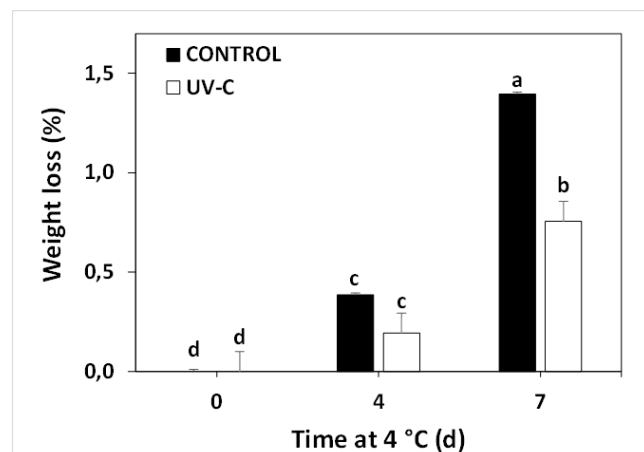
Figure 5. Weight loss in control or UV-C-treated (36 W m^{-2} radiation intensity and 4 kJ m^{-2} radiation dose) fresh-cut strawberry, stored at 4 °C for 0, 4, and 7 days. Different letters indicate significant differences according to Fisher's test with a significance level of p<0,05.
Source: Authors

Rapid softening is another relevant issue in stored berries. After 4 days of storage, control fruits already showed a drop in tissue resistance to compression (Figure 6). Higher values were found in UV-C-treated berries, also indicating a protective effect on texture deterioration. These differences were observed until the end of the storage period. The positive effect that UV-C irradiation had on fruit texture is remarkable. In fact, UV-C-treated berries showed no softening even after 7 days of storage. The greater firmness of the irradiated fruits relative to the control could be related to a retardation of cell wall disassembly. Previous works have demonstrated that UV-C radiation may delay fruit softening (Rodoni *et al.*, 2017; Bu *et al.*, 2013; Adipour *et al.*, 2019). This effect has been linked both to an inhibitory effect on fruit pectolytic enzymes (Ortiz-Araque *et al.*, 2019).

To determine if exposure to UV radiation caused modifications in other relevant quality attributes, the impact on color, acidity, soluble solids content, and phenolic content was determined (Table 1). Overall color changes throughout storage were slight since it started with fruits in a state of advanced maturity. However, on the last day of sampling, treated fruit showed a higher lightness (L*) and Hue angle, thus pointing to a delay in surface reddening. Fruit pH, acidity, soluble solids content showed no major variation throughout storage or in response to UV-C exposure. This is in line with the results reported in the literature (Cote *et al.*, 2013; Nimitkeatkai and Kulthip, 2016; Safitri *et al.*, 2015). Finally, while analyzing the content of total phenolic compounds, an increasing trend was found with storage. Regarding the impact of UV-C, after 4 days, no differences were observed between control and treated fruits. At the last day of sampling UV-C treated fruit showed a slight delay in

phenolic compound accumulation. This differs from previous works, where the use of UV-C radiation elicited antioxidant compounds (Li *et al.*, 2019; Esua *et al.*, 2019; Duarte-Sierra *et al.*, 2019; Michailidis *et al.*, 2019). The results of this research show that the inductive effect of UV-C of phenolic compound biosynthesis is highly dependent on irradiation conditions, which likely also occurs during the product processing stage. The reduction in phenolic content found in the last sampling point is of little or no relevance from an antioxidant intake point of view.

Table 1. Lightness (L*), Hue, pH, acidity, SS, and phenolic content of control and UV-C-treated (36 W m^{-2} radiation intensity and 4 kJ m-2 radiation dose) fresh-cut strawberry, stored at 4 °C for 7 days.* Different letters indicate significant differences according to Fisher's test with a significance level of p<0,05.

		0	4	7
Lightness (L*)	Control	35 a	34 a	33 b
	UV-C	36 a	35 a	35 a
Hue	Control	37 a	36 a	30 c
	UV-C	37 a	36 a	33 b
pH	Control	3,34 a	3,37 a	3,31 a
	UV-C	3,38 a	3,38 a	3,35 a
Acidity (meq H$^+$ kg^{-1})	Control	8,7 a	7,6 c	8 bc
	UV-C	8,5 ab	7,6 c	7,8 c
SS (%)	Control	6,6 a	7,3 a	6,5 a
	UV-C	6,4 a	7,4 a	6,4 a
Phenolic content (mg kg^{-1})	Control	1 245,33 c	1 234,36 c	1 459,22 a
	UV-C	1 235,39 c	1 287,92 bc	1 359,63 b

Source: Authors
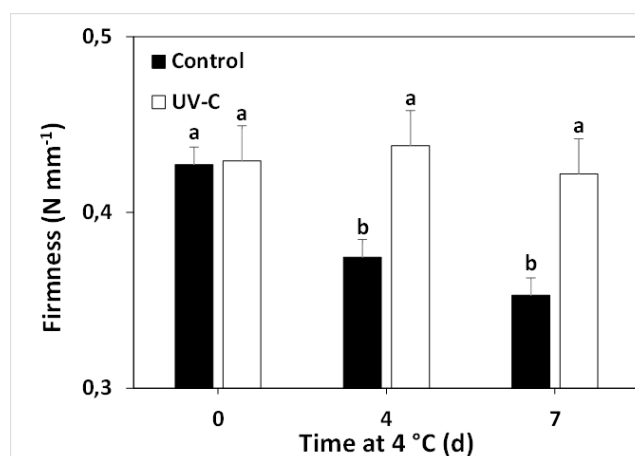
Figure 6. Firmness in control or UV-C-treated (36 W m^{-2} radiation intensity and 4 kJ m^{-2} radiation dose) fresh-cut strawberry, stored at 4 °C for 0, 4, and 7 days. Different letters indicate significant differences according to Fisher's test with a significance level of p<0,05.
Source: Authors

We finally conducted a consumer sensory test for three relevant attributes for fruit purchase (freshness, color, and overall acceptability) (Figure 7). Regardless of the attributes, UV-C-treated berries showed higher scores than the control.
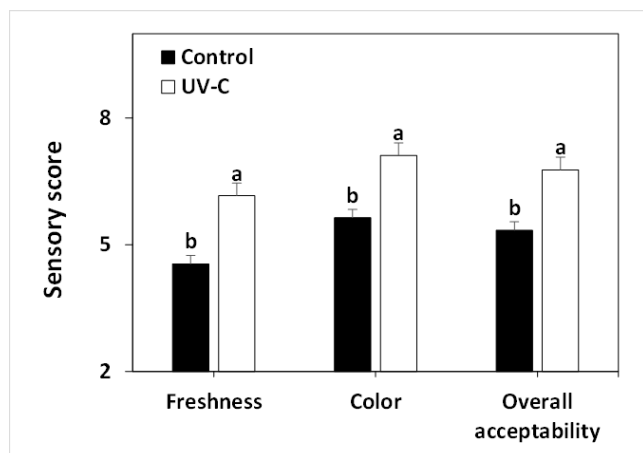
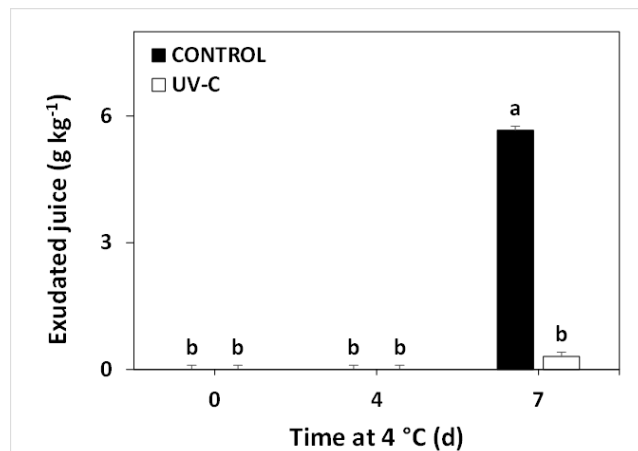**Figure 7.** Sensory scores for freshness, color, and overall acceptability in control or UV-C treated (36 W m^{-2} radiation intensity and 4 kJ m^{-2} radiation dose) fresh-cut strawberry, stored at 4 °C for 7 days. Different letters indicate significant differences according to Fisher's test with a significance level of $p < 0,05$.
**Source:** Authors

Conclusions

In this work, we first selected a proper combination of radiation dose and intensity for postharvest treatment of fresh cut strawberry. Treatments at the highest dose (4 kJ m^{-2}) and intensity (36 W m^{-2}) showed the greatest benefits in terms of fruit decay control and shelf-life extension. UV-C-treated berries showed reduced deterioration, juice exudates, weight loss, softening, and yeasts and mold counts, as well as higher scores in consumer sensory tests. The treatments did not cause major changes in fruit pH, acidity soluble solids, or phenolic compounds. After one week, UV-C-treated berries reported a similar deterioration to that of control fruit upon 4 days. The overall results suggest that short UV-C treatment could be useful to supplement cold storage, extending the shelf-life of fresh-cut strawberries.

References

Abdipour, M., Hosseinifarahi, M., and Naseri, N. (2019). Combination method of UV-B and UV-C prevents post-harvest decay and improves organoleptic quality of peach fruit. *Scientia Horticulturae, 256*, 108564. https://doi.org/10.1016/j.scienta.2019.108564

Agyare, S., Magan, N., and Xu, X. (2020). Conditions for infection of strawberry fruit by M. piriformis and *Rhizopus* spp. *European Journal of Plant Pathology, 157*, 65-75. https://doi.org/10.1007/s10658-020-01981-3

Association of Official Analytical Chemists (AOAC) (1980). *Official methods of analysis* (13 ed.). AOAC.

Bu, J., Yu, Y., Aisikaer, G., and Ying, T. (2013). Postharvest UV-C irradiation inhibits the production of ethylene and the activity of cell wall-degrading enzymes during softening of tomato (*Lycopersicon esculentum* L.) fruit. *Postharvest Biology and Technology, 86*, 337-345. https://doi.org/10.1016/j.postharvbio.2013.07.026

Charles, F. (2018). Current challenges of physical treatments to control quality and postharvest diseases of fresh fruits and vegetables. *IOP Conference Series: Earth and Environmental Science, 309*, 012003. https://doi.org/10.1088/1755-1315/309/1/012003

Civello, P. M., Vicente, A. R., and Martínez, G. A. (2007). UV-C technology to control postharvest diseases of fruits and vegetables. In R. Troncoso-Rojas, M. E. Tiznado-Hernández, and A. González-León (Eds.), *Recent advances in alternative postharvest technologies to control fungal diseases in fruits and vegetables* (pp. 1-32). Transworld Research Network. FAO.

Cote, S., Rodoni, L., Miceli, E., Concellón, A., Civello, P. M., and Vicente, A. R. (2013). Effect of radiation intensity on the outcome of postharvest UV-C treatments. *Postharvest Biology and Technology, 83*, 83-89. https://doi.org/10.1016/j.postharvbio.2013.03.009

Darré, M., Valerga, L., Ortiz Araque, L. C., Lemoine, M. L., Demkura, P. V., Vicente, A. R., and Concellón, A. (2017). Role of UV-B irradiation dose and intensity on color retention and antioxidant elicitation in broccoli florets (*Brassica oleracea* var. *Italica*). *Postharvest Biology and Technology, 128*, 76-82. https://doi.org/10.1016/j.postharvbio.2017.02.003

Di Rienzo, J.A., Casanoves, F., Balzarini, M. G., González, L., Tablada, M., and Robledo, C. W. (2018). *Infostat*. http://www.infostat.com.ar

Duarte-Sierra, A., Nadeau, F., Angers, P., Michaud, D., and Arul, J. (2019). UV-C hormesis in broccoli florets: preservation, phyto-compounds and gene expression. *Postharvest Biology and Technology, 157*, 110965. https://doi.org/10.1016/j.postharvbio.2019.110965

Esua, O. J., Chin, N. L., Yusof, Y. A., and Sukor, R. (2019). Effects of simultaneous UV-C radiation and ultrasonic energy postharvest treatment on bioactive compounds and antioxidant activity of tomatoes during storage. *Food chemistry, 270*, 113-122. https://doi.org/10.1016/j.foodchem.2018.07.031

Gayán, E., Condón, S., and Álvarez, I. (2014). Biological aspects in food preservation by ultraviolet light: A review. *Food and Bioprocess Technology, 7*(1), 1-20. https://doi.org/10.1016/j.jfoodeng.2020.110034

Graça, A., Santo, D., Pires-Cabral, P., and Quintas, C. (2020). The effect of UV-C and electrolyzed water on yeasts on fresh-cut apple at 4 °C. *Journal of Food Engineering, 282*, 110034. https://doi.org/10.1016/j.jfoodeng.2020,110034

Lamikanra, O., Kueneman, D., Ukuku, D., and Bett-Garber, K. L. (2005). Effect of processing under ultraviolet light on the shelf life of fresh-cut cantaloupe melon. *Journal of Food Science, 70*(9), C534-C539. https://doi.org/10.1111/j.1365-2621.2005.tb08301.x

Li, M., Li, X., Han, C., Ji, N., Jin, P., and Zheng, Y. (2019). UV-C treatment maintains quality and enhances antioxidant capacity of fresh-cut strawberries. *Postharvest Biology and Technology, 156*, 110945. https://doi.org/10.1016/j.postharvbio.2019.110945

Ma, L., Zhang, M., Bhandari, B., and Gao, Z. (2017). Recent developments in novel shelf-life extension technologies of fresh-cut fruits and vegetables. *Trends in Food Science and Technology, 64*, 23-38. https://doi.org/10.1016/j.tifs.2017.03.005

Martinsen, B. K., Aaby, K., and Skrede, G. (2020). Effect of temperature on stability of anthocyanins, ascorbic acid and color in strawberry and raspberry jams. *Food Chemistry, 316,* 126297. https://doi.org/10.1016/j.foodchem.2020,126297

Michailidis, M., Karagiannis, E., Polychroniadou, C., Tanou, G., Karamanoli, K., and Molassiotis, A. (2019). Metabolic features underlying the response of sweet cherry fruit to postharvest UV-C irradiation. *Plant Physiology and Biochemistry, 144,* 49-57. https://doi.org/10.1016/j.plaphy.2019.09.030

Muley, A. B., and Singhal, R. S. (2020). Extension of postharvest shelf life of strawberries (*Fragaria ananassa*) using a coating of chitosan-whey protein isolate conjugate. *Food Chemistry, 329,* 127213. https://doi.org/10.1016/j.foodchem.2020,127213

Nigro, F., Ippolito, A., Lattanzio, V., Di Venere, D., and Salerno, M. (2000). Effect of ultraviolet-C light on postharvest decay of strawberry. *Journal of Plant Pathology, 82*(1), 29-37. http://dx.doi.org/10.4454/jpp.v82i1.1142

Nimitkeatkai, H., and Kulthip, J. (2016). Effect of sequential UV-C irradiation on microbial reduction and quality of fresh-cut dragon fruit. *International Food Research Journal, 23*(4), 1818-1822. http://www.ifrj.upm.edu.my/23%20(04)%202016/(63).pdf

Ortiz-Araque, L. C., Rodoni, L. M., Darré, M., Ortiz, C. M., Civello, P. M., and Vicente, A. R. (2019). Cyclic low dose UV-C treatments retain strawberry fruit quality more effectively than conventional pre-storage single high fluence applications. *LWT - Food Science and Technology, 92,* 304-311. https://doi.org/10.1016/j.lwt.2018.02.050

Pan, J., Vicente, A. R., Martínez, G. A., Chaves, A. R., and Civello, P. M. (2004). Combined use of UV-C irradiation and heat treatment to improve postharvest life of strawberry fruit. *Journal of the Science of Food and Agriculture, 84*(14), 1831-1838. https://doi.org/10.1002/jsfa.1894

Panou, A. A., Karabagias, I. K., and Riganakos, K. A. (2020). Effect of gamma-irradiation on sensory characteristics, physicochemical parameters, and shelf life of strawberries stored under refrigeration. *International Journal of Fruit Science, 20*(2), 191-206. https://doi.org/10.1080/15538362.2019.1608890

Pombo, M. A., Dotto, M. C., Martínez, G. A., and Civello, P. M. (2009). UV-C irradiation delays strawberry fruit softening and modifies the expression of genes involved in cell wall degradation. *Postharvest Biology and Technology, 51*(2), 141-148. https://doi.org/10.1016/j.postharvbio.2008.07.007

Pott, D., de Abreu e Lima, F., Soria, C., Willmitzer, L., Fernie, A. R., Nikoloski, Z., Osorio, S., and Vallarino, J. G. (2019). Metabolite profiling of postharvest senescence in different strawberry cultivars. *Food Chemistry, 321*, 126747. https://doi.org/10.1016/j.foodchem.2020.126747

Rodoni, L. M., Concellón, A., Chaves, A. R., and Vicente, A. R. (2012). Use of UV-C treatments to maintain quality and extend the shelf life of green fresh-cut bell pepper (*Capsicum annuum* L.). *Journal of Food Science, 77*(6), C632-C639. https://doi.org/10.1111/j.1750-3841.2012.02746.x

Rodoni, L. M., Massolo, J. F., and Vicente, A. R. (2017). Evaluation of different physical treatments in minimally processed green and red pepper *Capsicum annuum* L. *Enfoque UTE, 8*(2), 33-43. https://doi.org/10.29019/enfoqueute.v8n2.154

Romanazzi, G., Smilanick, J. L., Feliziani, E., and Droby, S. (2016). Integrated management of postharvest gray mold on fruit crops. *Postharvest Biology and Technology, 113,* 69-76. https://doi.org/10.1016/j.postharvbio.2015.11.003

Safitri, A., Theppakorn, T., Naradisorn, M., and Setha, S. (2015). Effects of UV-C irradiation on ripening quality and antioxidant capacity of mango fruit cv. Nam Dok Mai Si Thong. *Journal of Food Science and Agricultural Technology, 1,* 164-170. http://rs.mfu.ac.th/ojs/index.php/jfat/article/view/47/47

Singleton, V. L., Orthofer, R., and Lamuela-Raventós, R. M. (1999). Analysis of total phenols and other oxidation substrates and antioxidants by means of Folin-Ciocalteu reagent. *Methods in Enzymology, 299,* 152-178. https://doi.org/10.1016/S0076-6879(99)99017-1

Vicente, A. R., and Lurie, S. (2014). Physical methods for preventing postharvest deterioration. *Stewart Postharvest Review, 10*(3), 12. http://hdl.handle.net/11336/10098

Development of a Bioplastic from Banana Peel

Desarrollo de un bioplástico a partir de residuos del plátano

Maura G. Alcivar-Gavilanes[1] Katiuska L. Carrillo-Anchundia[2], and María A. Riera[3]

ABSTRACT

The problems caused by synthetic plastics have motivated the use of other materials. This research consisted of utilizing banana peel and cellulose from the pseudostem of this plant to obtain a bioplastic. The flour was extracted by dry milling and cellulose via an acid-alkaline treatment. For the elaboration of the thermoplastic material, a mixture design was employed where fixed amounts of shell flour (5 g), 15% NaOH (5 mL), water (4 mL), and varying concentrations of plasticizers were used, which were glycerol and sorbitol. In two of the formulations, 0,5 g of cellulose were added as filler material. The obtained bioplastic was characterized according to its thickness, water vapor permeability (WVP), tension force (TF), break time (bt), and biodegradability. The type of plasticizer and the cellulose content did not affect the thickness of the bioplastic, but it did affect the WVP, TF, and bt. WVP decreases when glycerin is used and increases with the addition of cellulose. The best result for WVP was $1,83 \times 10^{-9}$ g/Pa.s.m in the formulation where only glycerol was used, whereas the best values for TF, bt, and biodegradability were 2,4 MPa, 17 seconds, and 37,77%, respectively, with 75% sorbitol and 25% glycerol. Expanding the study of the best formulations would allow their use as a replacement for synthetic plastics.

Keywords: agroindustrial waste, biodegradable plastic, biofilm, thermoplastic starch

RESUMEN

Las problemáticas causadas por los plásticos sintéticos han motivado el uso de otros materiales. Esta investigación consistió en el aprovechamiento de la cáscara del plátano y celulosa del pseudotallo de esta planta para obtener un bioplástico. La harina se extrajo por molienda seca y la celulosa con un tratamiento ácido-alcalino. Para la elaboración del material termoplástico se trabajó con un diseño de mezclas donde se establecieron cantidades fijas de harina de cáscara (5 g), NaOH al 15 % (5 mL), agua (4 mL) y diferentes concentraciones de plastificantes, los cuales fueron glicerol y sorbitol. En dos de las formulaciones se adicionaron 0,5 g de celulosa como material de relleno. El bioplástico obtenido se caracterizó en función de su espesor, permeabilidad al vapor de agua (PVA), fuerza de tensión (FT), tiempo de rotura (tr) y biodegradabilidad. El tipo de plastificante y el contenido de celulosa no incidieron en el espesor del bioplástico, pero sí en la PVA, la FT y el tr. La PVA disminuye cuando se utiliza glicerina y aumenta con la adición de celulosa. El mejor resultado para PVA fue de $1,83 \times 10^{-9}$ g/Pa.s.m en la formulación donde solo se utilizó glicerol, mientras que los mejores valores para FT, tr y biodegradabilidad fueron de 2,4 MPa, 17 segundos y 37,77 % respectivamente con 75 % de sorbitol y 25 % de glicerol. Ampliar el estudio de mejores formulaciones posibilitaría su uso como reemplazo de los plásticos sintéticos.

Palabras clave: residuos agroindustriales, plástico biodegradable, biopelícula, almidón termoplástico

Introduction

Plastics are a family of materials made from fossil resources and present in most sectors of the economy. Their high consumption is causing environmental problems such as prolonged permanence in landfills, greenhouse gas emissions during burning, and irreversible damage to marine ecosystems. Approximately eight million tons (Mt) of plastic reach the sea annually, with consequences from the surface to the seabed (Parker, 2018).

These materials enter the aquatic, atmospheric, and terrestrial systems, migrate among themselves, accumulate in the environment, and pass to humans through the food chain (Li *et al.*, 2020). Plastics are estimated to be responsible for emitting 400 Mt of greenhouse gases each year. If the current production rate continues, this industry alone will consume 20% of the world's oil production by 2050 (Mahapatra *et al.*, 2020). Hence the need to obtain biomaterials from plant or animal biomass that, if possible, do not compete with

the food needs of the human population. One of them is bioplastics, which can be biologically based, biodegradable in nature, or with both characteristics.

[1] Chemical Engineer, Universidad Técnica de Manabí, Ecuador. Affiliation: Department of Chemical Processes, Food, and Biotechnology. Faculty of Mathematical, Physical, and Chemical Sciences, Universidad Técnica de Manabí, Ecuador. Email: malcivar7626@utm.edu.ec

[2] Chemical Engineer, Universidad Técnica de Manabí, Ecuador. Affiliation: Department of Chemical Processes, Food, and Biotechnology. Faculty of Mathematical, Physical, and Chemical Sciences, Universidad Técnica de Manabí, Ecuador. Email: kcarrillo6947@utm.edu.ec

[3] Industrial Engineer, Universidad Yacambú. MSc in Chemical Engineer, Universidad Nacional Experimental Politécnica Antonio José de Sucre, Venezuela. Affiliation: Assistant Professor. Department of Chemical Processes, Food, and Biotechnology. Faculty of Mathematical, Physical, and Chemical Sciences, Universidad Técnica de Manabí, Ecuador. Email: maria.riera@utm.edu.ec

Agribusiness waste is a source of plant biomass from which a variety of products are obtained through chemical or microbiological treatments (Gutiérrez-Macías et al., 2017). Among them are those generated during the production and processing of plantain, where leaves, pseudostems, rachis, peels, and fruits are identified as residues (Granda et al., 2005; Mondragón-García et al., 2018). This constitutes between 20 and 30% of the available biomass used in banana harvesting (Belalcázar and Sylvio, 1991). During processing, the peel is discarded, which constitutes 30% of the weight of the fruit (Wadhwa and Bakshi, 2013).

The Ecuadorian economy has a strong agricultural participation. Among its main products are bananas, with a production of almost 750 thousand metric tons for 2019 (Ministerio de Agricultura y Ganadería, 2020). The destination of this fruit is exportation, local consumption, and processing for the production of snacks, banana flour, and vacuum-packed peeled bananas in small and medium-sized industries. The waste generated in this activity contains compounds of interest such as cellulose, hemicellulose, and starch, which is useful in the production of bioplastics.

In the Central and Latin American contexts, the possibility of applying biorefinery processes to use banana residues as raw material for the production of biofuels, nanocellulose fibers, bioplastics, and other high-value products has been evaluated (Redondo-Gómez et al., 2020). Some research works claim to have obtained biopolymers from banana peel and corn starch, banana peel, and glycerol (Kader-Sultan and Wan-Johari, 2017; Rusdi et al., 2020). In this vein, bioplastic has been made from banana peel, the pseudostem of the plant, and plasticizers. The objective of this research was to evaluate the impact that the plasticizer type has on the physical and mechanical properties of bioplastic.

Experimentation

The employed banana peels and pseudostems came from plantations and artisan factories located in the province of Manabí-Ecuador. The procedures for extracting and characterizing the residue, preparing the thermoplastic mixture, and determining its properties are described below.

Materials extraction and characterization

The flour was extracted from the banana peel via dry grinding. To this effect, twelve healthy immature bananas were selected, washed with drinking water, and disinfected by immersion in a 1% (w/v) NaClO solution for 10 min. The endocarp was removed and dehydrated in a hot air tray dryer at 40 °C for 12 h. It was ground and sieved twice on 40 and 20 µm sieves. The flour was packed in polyethylene bags until use (Mazzeo and Alzate, 2008).

The banana peel flour was characterized in terms of moisture, starch content, gelatinization temperature, water absorption index (WAI), water solubility index (WSI), swelling power (SP), amylose, and amylopectin content. The moisture was determined with a BMA 150 thermobalance (Tirado et al., 2015). The presence of starch was confirmed by means of a colorimetric analysis, applying an iodine solution stain on the sample (López et al., 2014).

The gelatinization temperature was determined by dissolving 10 g of flour on a dry basis (DB) in 100 mL of distilled water. 50 mL of the suspension were taken and immersed in a thermostatic bath at 85 °C with stirring. As the paste formed, the temperature was recorded with a thermometer until it stabilized (Grace, 1977).

The procedure for determining WAI, WSI, and SP can be described as follows. 1,25 g of flour were taken, placed in a centrifuge tube with 30 mL of distilled water at 60 °C, and stirred. The mixture was placed in a thermostatic bath at 60 °C for 30 min, stirring after the first 10 min of heating. It was centrifuged at room temperature at 4 900 RPM for 30 min. The volume (V) was measured. 10 mL of the supernatant were taken and dried in an oven at 70 °C for 14 h. Centrifuge tubes weighed the sediment and dry residue (Anderson, 1982). The calculations were made by means of Equations (1), (2), and (3).

$$WAI = \frac{\text{Gel weight}(g)}{\text{Sample weight}(g)} \qquad (1)$$

$$WSI = \frac{\text{Soluble weight}(g) \times V \times 10}{\text{Sample weight}(g)} \qquad (2)$$

$$SP = \frac{\text{Gel weight}(g) \times V \times 10}{\text{Sample weight}(g) - \text{Soluble weight}(g)} \qquad (3)$$

Amylose was quantified by spectrophotometry with a wavelength of 620 nm, using the calibration curve for the standard solution (Galicia et al., 2012). The amylopectin content was determined by difference using Equation (4).

$$\%Amylopectin = 100\% - \%Amylose \qquad (4)$$

Cellulose was extracted from the pseudostem of the banana. To this effect, the fruit was cut into sections, washed with distilled water, separated by layers, and washed again. It was dried to constant weight and degreased using Soxhlet extraction. It was submitted to an acid treatment with a solution of CH3(COOH) at 80% (w/v) and HNO$_3$ at 65% (w/v) with stirring. Then, it was shaken with a 10% (w/v) NaOH solution, washed, and dried at 55 °C. The obtained pulp was ground and sieved to reduce its size (Romero-Viloria et al., 2014). The cellulose content was determined with the Kurschner and Hoffer method, holocellulose by applying the TAPPI T-21 method, lignin with the Klason method, and hemicellulose through Equation (5) (Romero-Uscanga et al., 2014).

$$\%Hemicellulose = \%Holocellulose - \%Cellulose \qquad (5)$$

Preparation of the thermoplastic mixture

Before defining the experimental design, a preliminary test of 16 formulations was carried out with different compositions of banana peel flour, cellulose, water, glycerin, sorbitol, and 5 and 15% NaOH solutions (w/v) in order to identify the mixtures that form the film. In each plastic mixture, the pH was measured with a potentiometer. Based on the results, a mixture design was elaborated, with fixed amounts of banana peel flour (5 g), 15% NaOH (5 mL), and water (4 mL), varying the concentrations of the plasticizers used, which were glycerol and sorbitol (0 to 2 g) (Table 1).

Table 1. Design of mixtures for experimentation

Formulation	Sorbitol (%)	Glycerol (%)
F1	100	0
F2	75	25
F3	50	50
F4	25	75
F5	0	100

Source: Authors

The procedure consisted of mixing the banana peel flour with the water and the NaOH solution at 20 °C. The mix was stirred at 400 RPM for 10 min and placed in a thermostatic bath. Then, the selected plasticizer was added, and the temperature was increased to 65 °C with constant stirring. The obtained gel was cooled to 20 °C in order to eliminate bubbles, and it was deposited on Petri dishes to form the plastic films via the casting method. It was dried at room temperature for 24 h and then demolded. After determining the characteristics of the obtained bioplastic, the formulations with the best physical appearance and resistance were selected. 0,50 g of cellulose were added to the selected formulations, and then the effect caused by this filler material on the physical, chemical, and mechanical properties of the material was determined.

Bioplastic properties

The following characteristics were evaluated in the obtained film: thickness, water vapor permeability (WVP), biodegradability, and tension force at the break. The thicknesses were measured directly on the film in three different sections with a precision 25 x 1 mm linear vernier C4.svg micrometer (Anchundia et al., 2016). The WVP was measured according to the modified E96-80 ASTM standard as described by Joaqui and Villada-Castillo (2013), for which samples of the material were sectioned into 2 x 2 cm pieces and used to seal a hole at the top of a 1 x 1 cm plastic cuvette containing distilled water. The cuvette was placed in a desiccator for 24 h. The initial and final weights of the film were determined, as well as the moisture percentage. To calculate the WVP, Equations (6) and (7) were used.

$$WVP = \frac{WVTR \times T}{Pw \times \Delta RH} \tag{6}$$

$$WVTR = \frac{m}{t \times A} \tag{7}$$

where WVP is the water vapor permeability (g/Pa.sm), and WVTR is the water vapor transmission rate (g/s.m^2) calculated from the mass m (g), the time t (s) corresponding to the duration of the experiments (24 h), and the area A of the film exposed to the transfer of humidity (m^2). T is the average thickness of the film (m), Pw is the partial pressure of pure water vapor (3 160 Pa at 25 °C), and ΔRH is the relative humidity gradient between the container (0%) and the medium (41%).

Biodegradability was measured through the weight loss of the thermoplastic material, based on a soil burial test (Saffian et al., 2016). The natural soil was collected free of composting material. The samples were weighed, placed with soil in polyethylene bags, and kept at room temperature with a relative humidity of approximately 43% for 40 days. Every ten days, the samples were removed, rinsed with water to remove soil residues, dried for one hour at room temperature to remove moisture, and finally weighed. The biodegradability percentage of the bioplastic for the evaluated environment was determined via weight difference with Equation (8).

$$Weight\ loss\,(\%) = \frac{Initial\ weight - Final\ weight}{Initial\ weight} \times 100\% \tag{8}$$

Tensile tests were carried out to measure the tensile strength and break time of the film. To this effect, a Nestor universal machine was used according to the method described in the modified ASTM D-882 standard (ASTM International, 2018). The diameter, area, and thickness of three samples of the films were measured. They were then placed between the clamping presses of the equipment and subjected to tension until they broke.

Experiments were conducted in triplicate for each variable.

Statistical processing

For the statistical analysis, the R Studio software version 4.0.3 was used.

Results and discussion

The colorimetric determination of the banana peel flour confirmed the presence of starch because it took a blue color when in contact with iodine. The rest of the results obtained from the analysis carried out for the characterization in terms of humidity, gelatinization temperature, WAI, WSI, SP, amylose, and amylopectin, is presented in Table 2.

The moisture in the banana peel flour was 14,80 ± 0,40, higher than that reported in similar studies for banana flour and starch, respectively, which reported values of 9,26 and 9,45% (Montoya et al., 2014) and 8 and 9,27% (Pelissari et al.,

Table 2. Characterization of residual flour

Variable	Value $\pm$ σ
Moisture (%)	14,80 $\pm$ 0,40
Gelatinization temperature (°C)	62,70 $\pm$ 1,50
Water Absorption Index (g gel / g sample)	4,73 $\pm$ 0,19
Water Solubility Index (%)	3,12 $\pm$ 0,56
Swelling power (%)	4,81 $\pm$ 0,18
Amylose (%)	8,59 $\pm$ 0,82
Amylopectin (%)	91,41 $\pm$ 0,82

Source: Authors

2012). This variation in the moisture content of the flour could be affected by the environmental conditions of the laboratory where the analysis was carried out (Lucas et al., 2013).

Banana starch gelatinizes within a temperature range similar to cereal starch (Montoya et al., 2014). In this research, the gelatinization temperature was lower than the value reported for flour (68 °C) and banana starch (66,41 °C) (Lucas et al., 2013). Pozo (2019) recorded a temperature of 65 °C for green banana starch. The differences in the values obtained for the gelatinization temperature can be attributed to the genetic conditions of the fruit, the climatic conditions of the crop, and the weeks of harvest (Montoya et al., 2014).

The quality of the starch subsequently affects the properties of the bioplastic. Water resistance is an important property for biodegradable films, especially when used as a protective barrier for food, where water activity and the possibility of film breakage are high (Moro et al., 2017).

The water absorption, solubility, and swelling power indices serve as indicators of the functional properties of starch (Rodríguez-Sandoval et al., 2012). The WAI, WSI, and SP values were 4,73 $\pm$ 0,19 g gel/g sample, 3,12 $\pm$ 0,56%, and 4,81 $\pm$ 0,18% respectively. Solubility and swelling power depend on the fruit's state of ripeness. High starch content and high viscosity entail low solubility, high water absorption, and high swelling power (Aristizábal and Sánchez, 2007).

The amylose and amylopectin contents for the banana peel flour were 8,59 $\pm$ 0,82% and 91,41 $\pm$ 0,82%, respectively. Pelissari et al., (2012) registered 23,10 and 35% for the amount of amylose in banana flour and starch. In the same way, Contreras-Pérez et al. (2018) obtained values between 23,5 and 31,3% for banana starch from four different varieties. The contents of amylose and amylopectin in starch are determining factors for the quality of finished foods. High values in amylose content favor greater solubility and a greater tendency to retrograde gels (Aristizábal and Sánchez, 2007). Amylose retrogrades faster than amylopectin because, due to its linear and highly polar nature, it tends to form hydrogen bonds between hydroxyl groups of adjacent molecules, thus causing a partial shrinkage of the starch (Salinas-Moreno et al., 2003). Therefore, the higher the content of amylopectin, the lower the retrogradation and, therefore, the better the properties of the bioplastic material formed.

The characterization of the extracted cellulose pulp is in Table 3.

Table 3. Characterization of cellulose pulp

Variable	Value $\pm$ σ
Cellulose (%)	58,89 $\pm$ 0,76
Hemicellulose (%)	3,47 $\pm$ 0,76
Lignin (%)	18,99 $\pm$ 0,19

Source: Authors

The results obtained for cellulose were compared with those indicated for a wheat straw with 57,09% (Romero-Uscanga et al., 2014), which was used as a reinforcement material in thermoplastic materials, providing mechanical properties similar to those of composites of wood flour (Mishra and Sain, 2009). Similar experiences show satisfactory results when using other agro-industrial residues such as cocoa pod husk (Lubis et al., 2018) and rice straw (Bilo et al., 2018) as sustainable fillers in bioplastics.

With thermoplastic mixtures, the film was formed at basic pH (8,11-13,15) but not at neutral pH values (7,3). The increase in the concentration of the NaOH solution favored the consistency and durability of the material. Díaz et al. (2019) characterized chickpea flour films and found that film-forming solutions at pH 10 had better results than solutions at neutral pH.

In the mechanical test, only formulations 1, 2, and 3 (F1-3) showed no breakage. In the rest of the formulations, the tensile strength and the breaking time could not be determined (ND). Therefore, to evaluate the incidence of the filler material on the characteristics of the bioplastic, 0,50 g of cellulose were added to F1 and F2 (F6 and F7, respectively), as they were the ones that exhibited the best appearance.

The results of the thickness, WVP, tensile strength and, break time tests for each formulation are shown in Table 4.

Table 4. Properties of the bioplastic obtained

Formulation	Variable			
	Thickness (mm)	WVP x 10⁻⁹ (g/ Pa.s.m)	Tensile force (MPa)	Break time (s)
F1	1,61 $\pm$ 0,05	1,83 $\pm$ 0,21	1,90	11
F2	1,53 $\pm$ 0,21	1,86 $\pm$ 0,41	2,40	17
F3	1,64 $\pm$ 0,02	2,67 $\pm$ 0,18	2,00	13
F4	1,71 $\pm$ 0,19	2,32 $\pm$ 0,02	ND	ND
F5	1,55 $\pm$ 0,13	0,69 $\pm$ 0,03	ND	ND
F6	1,68 $\pm$ 0,09	2,68 $\pm$ 0,18	ND	ND
F7	1,67 $\pm$ 0,04	4,12 $\pm$ 0,82	ND	ND

Source: Authors

The thickness of the biodegradable films was between 1,55 and 1,71 mm, showing different results regardless of the type of plasticizer used. In a study involving edible films,

a thickness of 0,11 mm was reported when using 0,5% banana peel and a 0,17 mm thickness with 1,5% banana peel (Anchundia *et al.*, 2016). The permeability to water vapor showed values between 0,69 and $4,12 \times 10^{-9}$ g/Pa.sm. However, in all cases, they were higher than $2,41 \times 10^{-11}$ g/Pa.sm, which was recorded for a film made with a banana skin and salicylic acid (Anchundia *et al.*, 2016). The addition of cellulose favors the passage of water vapor and, according to Wang *et al.* (2018), this occurs because cellulosic materials absorb or desorb the humidity from the surrounding air until they reach an equilibrium moisture content.

According to the results, both plasticizers reduce the passage of water vapor, but sorbitol does so to a lesser extent when it is not mixed with glycerol. F2 showed the best mechanical properties, with a tensile strength of 2,40 MPa and a break time of 17 seconds. The mechanical behavior of the material obtained in this research was better than that of bioplastics made with cassava starch, fique fiber, and glycerol, whose tensile stress was less than 2 MPa (Navia-Porras and Bejarano-Arana, 2014). On the other hand, it is lower than that reported for banana films, bark, and acetylsalicylic acid, whose tensile strength was between 4,43 and 10,80 MPa (Anchundia *et al.*, 2016).

The influence of the plasticizer on the properties of the bioplastic was verified with an analysis of variance (ANOVA). The Shapiro-Wilk test was used to verify the normality of the data. For WVP and thickness, p-values of 0,105 and 0,9185 were obtained, respectively, in compliance with the normality assumption. The Bartlett test was also applied to verify the homoscedasticity of the variances. For thickness and WVP, p-values of 0,2787 and 0,4593 were obtained, respectively, satisfying the assumption of the equality of variances. In both tests, both the tensile strength and the breaking time had a p-value<0,05. For the tensile strength and the breaking time, given the characteristics of the data, the Kruskal-Wallis test was conducted.

The above-mentioned procedure was repeated to determine the influence exerted by cellulose on the characteristics of the material obtained. Fisher's test was used for the thickness and WVP variables. The corresponding results for both factors (plasticizer used and addition of cellulose) are shown in Table 5.

Table 5. ANOVA for bioplastic properties

Factor	Variable	p-value
Plasticizer	Thickness	0,733
	Water vapor permeability, WVP	$4,78 \times 10^{-5}$
	Tension force	0,01431
	Break time	0,01431
Cellulose	Thickness	0,18700
	Water vapor permeability, WVP	0,00389

Source: Authors

The ANOVA and the non-parametric test carried out for the plasticizer factor indicate, with a p-value<0,05, that there are significant differences in water vapor permeability, tensile strength, and break time, thus confirming the influence exerted by the type of plasticizer on the behavior of these variables. In similar studies, it was concluded that the concentration of the plasticizer affects the WVP and that it is positively correlated with the concentration of glycerol (Díaz *et al.*, 2019; Faradilla *et al.*, 2018). In other related research works, it was determined that plasticizers influence the physical properties of soy-based bioplastics (Tummala *et al.*, 2006) since they increase the tensile modulus and tensile strength when using sorbitol instead of glycerol and when using a mixture of these intermediate values, in comparison with the results obtained when the plasticizers are used independently. For the cellulose addition factor, there was a p-value<0,05 in the WVP, indicating that the variable is affected when cellulose is added to the bioplastic film, as it was experimentally verified. On the contrary, the thickness did not show significant results, that is, it is not affected by the type of plasticizer used or by the addition of cellulose.

In the biodegradability test, information was only obtained for five of the formulations. At the end of the test, the samples were fragmented, thus making them difficult to review. To compare the behavior of the bioplastic produced against other materials, a positive control (filter paper) was taken as well as a negative control (PET plastic bottle). The weight loss during the 40 days of the biodegradability test are presented in Figure 1. Likewise, the total weight loss percentage of the bioplastics at the end of the test is shown in Table 6.

Table 6. Percentage of weight lost by the bioplastic in the biodegradability test

Formulation	Days		
	10	**20**	**40**
F1	8,14	11,05	14,53
F2	20,60	28,76	37,77
F3	17,43	19,92	35,27
F6	0,55	0,83	8,29
F7	0,38	8,46	11,92
Control +	0	-1,69	-16,95
Control -	0	0	-2,22

Source: Authors

A decrease in the weight of the bioplastics was observed throughout testing, being more evident during the first ten days. The best result was for F2 with a weight loss of 37,77%, and the lowest value corresponded to F6 with 8,28%. The negative value in both the positive and negative controls implies a weight gain, probably due to the presence of moisture or traces of dirt. In a similar study, a weight loss of 64,21% was reported after 90 days in compost for a bioplastic made with potato starch (Meza *et al.*, 2016). On the other hand, in the evaluation of a bioplastic based on a banana peel for agricultural purposes, 65,10% of the initial
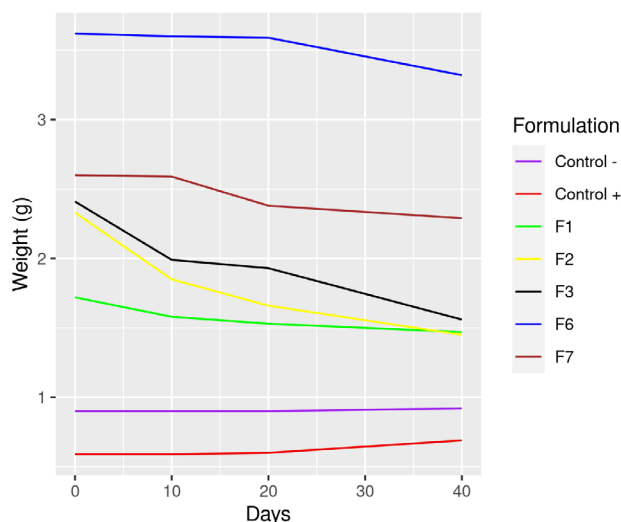
Figure 1. Biodegradability expressed in weight loss
Source: Authors

weight was lost in a period of eight weeks; its degradation process is much faster compared to other commercial plastics intended for sowing (Huzaisham and Marsi, 2020).

Conclusions

Bioplastics made from plant or animal biomass represent an alternative to replace synthetic plastics. In this research, banana residues were used to obtain thermoplastic starch. To extract starch and cellulose from the residues, physical, and chemical methods were applied. According to the results obtained during experimentation, it was concluded that starch has characteristics similar to those reported in previous works. The plasticizer used affected the WVP and the mechanical properties of the material. Although cellulose is used as a filler material to add strength, in this case, it increased the WVP, an unwanted characteristic in packaging materials. The biodegradability test showed that the material degrades for the evaluated conditions. The formulation with the lowest WVP was obtained when using glycerol, which works as a reference in food packaging applications. Regarding the mechanical properties, the best results were obtained when mixing glycerol and sorbitol. Although the developed formulations do not conclusively constitute a replacement for currently existing synthetic plastics, the results of this research serve as a reference for future work, where other formulations are evaluated, aimed at obtaining bioplastics capable of competing with synthetic plastics.

References

Anchundia, K., Santacruz, S., and Coloma, J. (2016). Caracterización física de películas comestibles a base de cáscara de plátano (*Musa Paradisiaca*). *Revista Chilena de Nutricion, 43*(4), 394-399. https://doi.org/10.4067/S0717-75182016000400009

Anderson, R. (1982). Water absortion and solubility and amilograph characteristics of roll-cooked small grain products. *Cereal Chemistry,* 59(4), 123-127.

Aristizábal, J., and Sánchez, T. (2007). *Guía técnica para producción y análisis de almidón de yuca.* FAO. http://www.fao.org/3/a-a1028s.pdf

ASTM International (2018). *D882-18: Standard test method for tensile properties of thin plastic sheeting.* ASTM Standards. https://doi.org/10.1520/D0882-18

Belalcázar, S., and Sylvio, L. (1991). *El cultivo del plátano (Musa AAB Simmonds) en el trópico.* Instituto Colombiano Agropecuario. http://hdl.handle.net/20.500.12324/12434

Bilo, F., Pandini, S., Sartore, L., Depero, L. E., Gargiulo, G., Bonassi, A., Federici, S., and Bontempi, E. (2018). A sustainable bioplastic obtained from rice straw. *Journal of Cleaner Production, 200,* 357-368. https://doi.org/10.1016/j.jclepro.2018.07.252

Contreras-Pérez, R. K., de la Torre- Gutiérrez, L., González-Cortés, N., Jiménez-Vera, R. (2018). Caracterización funcional de almidones de plátano cuadrado (*Musa balbisiana* Colla). *European Scientific Journal, 14*(30), 82-97. https://doi.org/10.19044/esj.2018.v14n30p82

Díaz, O., Ferreiro, T., Rodríguez-Otero, J. L., and Cobos, Á. (2019). Characterization of chickpea (*Cicer arietinum* L.) flour films: Effects of pH and plasticizer concentration. *International Journal of Molecular Sciences, 20*(5), 1246. https://doi.org/10.3390/ijms20051246

Faradilla, R. H. F., Lee, G., Roberts, J., Martens, P., Stenzel, M., and Arcot, J. (2018). Effect of glycerol, nanoclay and graphene oxide on physicochemical properties of biodegradable nanocellulose plastic sourced from banana pseudo-stem. *Cellulose, 25,* 399-416. https://doi.org/10.1007/s10570-017-1537-x

Galicia, L., Miranda, A., Gutiérrez, M. G., Custodio, O., Rosales, A., Ruíz, N., Surles, R., and Palacios, N. (2012). *Laboratorio de calidad nutricional de maíz y análisis de tejido vegetal: protocolos de laboratorio.* CIMMYT.

Grace, M. (1977). *Elaboración de la yuca.* FAO.

Granda R., D., Mejía G., A. I., and Jiménez T., G. (2005). Utilización de residuos de plátano para la producción de metabolitos secundarios por fermentación en estado sólido con el hongo *Lentinus Crinitus. Vitae, 12*(2), 13-20. https://www.redalyc.org/articulo.oa?id=169813259002

Gutiérrez-Macías, P., Hernández de Jesús, M. de L., and Barragán-Huerta, B. (2017). The production of biomaterials from agro-industrial waste. *Fresenius Environmental Bulletin, 26*(6), 4128-4152.

Huzaisham, N. A., and Marsi, N. (2020). Utilization of banana (Musa Paradisiaca) peel as bioplastic for planting bag application. *International Journal of Advanced Research in Engineering and Technology, 11*(4), 108-118. https://papers.ssrn.com/sol3/papers.cfm?abstract_id=3598064

Joaqui, D., and Villada-Castillo, H. S. (2013). Propiedades ópticas y permeabilidad de vapor de agua en películas producidas a partir de almidón. *Biotecnología en el Sector Agropecuario y Agroindustrial, 2,* 59-68. https://revistas.unicauca.edu.co/index.php/biotecnologia/article/view/1229

Kader-Sultan, N. F., and Wan-Johari, W. L. (2017). The development of banana peel/corn starch bioplastic film: A preliminary study. *Bioremediation Science and Technology Research, 5*(1), 12-17. https://doi.org/10.54987/bstr.v5i1.352

Li, P., Wang, X., Su, M., Zou, X., Duan, L., and Zhang, H. (2020). Characteristics of plastic pollution in the environment: A review. *Bulletin of Environmental Contamination and Toxicology*, *107*, 577–584. https://doi.org/10.1007/s00128-020-02820-1

López, J., Cuarán, J., Arenas, L., and Flórez, L. (2014). Usos potenciales de la cáscara de banano: elaboración de un bioplástico. *Revista Colombiana de Investigaciones Agroindustriales, 1*(1), 7-21. https://doi.org/10.23850/24220582.109

Lubis, M., Gana, A., Maysarah, S., Ginting, M. H. S., and Harahap, M. B. (2018). Production of bioplastic from jackfruit seed starch (*Artocarpus heterophyllus*) reinforced with microcrystalline cellulose from cocoa pod husk (*Theobroma cacao* L.) using glycerol as plasticizer. *IOP Conference Series: Materials Science and Engineering, 309,* 012100. https://doi.org/10.1088/1757-899X/309/1/012100

Lucas, J. C., Quintero, V. D., and Valencia, C. A. C. (2013). Caracterización de harina y almidón obtenidos a partir de plátano guineo AAAea (*Musa sapientum* L.). *Acta Agronomica*, *62*(2), 83-96. http://www.scielo.org.co/scielo.php?pid=S0120-28122013000200001&script=sci_abstract&tlng=es

Mahapatra, P. C., Sahu, B. K., and Mohanty, A. K. (2020). Plastic waste, health and climate change: Issues and challenges of Odisha. *Indian Journal of Public Health Research and Development, 11*(6), 735-741. https://doi.org/10.37506/ijphrd.v11i6.9873

Mazzeo MM, Alzate GA, M. M. (2008). Obtención de Almidón a partir de residuos poscosecha del platano dominico harton (*Musa AAB* Simmonds). *Vector*, *3*, 57-69. http://vector.ucaldas.edu.co/downloads/Vector3_6.pdf

Meza, P., Quipuzco U, L., and, Meza C, V. (2016). Elaboración de bioplásticos y determinación de su biodegradabilidad - Proyecto de laboratorio. *Revista del Instituto de Investigación FIGMMG-UNMSM, 22*(43), 67-80. https://doi.org/10.15381/iigeo.v22i43.16691

Montoya, J., Quintero, V., and Lucas, J. (2014). Evaluación fisicotérmica y reológica de harina y almidón de plátano dominico hartón (Musa Paradisiaca ABB). *Temas agrarios, 19*(2), 214-233. https://doi.org/10.21897/rta.v19i2.736

Ministerio de Agricultura y Ganadería (2020). *Panorama Agroestadístico*. http://sipa.agricultura.gob.ec/descargas/panorama_estadistico/panorama_estadistico.pdf

Mishra, S., and Sain, M. (2009). Commercialization of wheat straw as reinforcing filler for commodity thermoplastics. *Journal of Natural Fibers, 6*(1), 83-97. https://doi.org/10.1080/15440470802703851

Mondragón-García, J. M., Serna-Jiménez, J. A., García-Alzate, L. S., and Jaramillo-Echeverry, L. M. (2018). Caracterización fisicoquímica de los subproductos cáscara y vástago del plátano Dominico hartón. *Revista ION, 30*(2), 21-24. https://doi.org/10.18273/revion.v31n1-2018003

Montoya, J., Quintero, V. D., and Lucas, J. C. (2014). Evaluacion fisicotermica y reologica de harina y almidón de plátano dominico hartón (Musa Paradisiaca AAB). *Temas Agrarios, 19*(2), 214-233. https://doi.org/10.21897/rta.v19i2.736

Moro, M. A., Ascheri, J. L. R., Ortiz, J. A. R., Carvalho, C. W. P., and Meléndez-Arévalo, A. (2017). Bioplastics of native starches reinforced with passion fruit peel. *Food and Bioprocess Technology, 10*, 1798-1808. https://doi.org/10.1007/s11947-017-1944-x

Navia-Porras, D., and Bejarano-Arana, N. (2014). Evaluación de propiedades físicas de bioplásticos termo-comprimidos elaborados con harina de yuca. *Biotecnología en el Sector Agropecuario y Agroindustrial, 12*(2), 40-48. https://revistas.unicauca.edu.co/index.php/biotecnologia/article/view/346

Parker, L. (2018). Planet or Plastic? *The National Geographic Magazine, 42*(6), 2-51. https://www.nationalgeographic.com/magazine/2018/06/plastic-planet-waste-pollution-trash-crisis/

Pelissari, F. M., Andrade-Mahecha, M. M., Sobral, P. J. D. A., and Menegalli, F. C. (2012). Isolation and characterization of the flour and starch of plantain bananas (Musa paradisiaca). *Starch, 64*(5), 382-391. https://doi.org/10.1002/star.201100133

Pozo, L. (2019). *Extracción y caracterización del almidón de plátano verde (Musa paradisiaca) producido en el sector Untal, parroquia El Chical, y su potencial uso como aditivo en la elaboración de pan blanco*. [Unpublished tesis, Universidad Politécnica Estatal del Carchi].

Redondo-Gómez, C., Quesada, M. R., Astúa, S. V., Zamora, J. P. M., Lopretti, M., and Vega-Baudrit, J. R. (2020). Biorefinery of biomass of agro-industrial banana waste to obtain high-value biopolymers. *Molecules 25*(17), 3829. https://doi.org/10.3390/molecules25173829

Rodríguez-Sandoval, E., Lascano, A., and Sandoval, G. (2012). Influencia de la sustitución parcial de la harina de quinoa y papa en las propiedades termomecánicas y de panificación de masas. *Revista UDCA. Actualidad & Divulgación Científica, 15*(1), 199-207. https://doi.org/10.31910/rudca.v15.n1.2012.817

Romero-Uscanga, E., Montero-Alpírez, G., Toscano-Palomar, L., Pérez-Pelayo, L., Torres-Ramos, R., and Beleño-Cabarcas, M. T. (2014). *Determinación de los principales componentes de la biomasa ligonocelulósica; celulosa, hemicelulosa y lignina de la paja de trigo para su posterior pretratamiento biológivo* [Conference presentation]. XVII Congreso Internacional en Ciencias Agrícolas. Agricultura sustentable: Uso eficiente del agua, suelo y fertilizantes, Mexicali, México.

Romero-Viloria, P., Marfisi, S., Oliveros-Rondón, P., Rojas-de Gáscue, B., and Peña, G. (2014). Obtención de celulosa microcristalina a partir de desechos agrícolas del Cambur (*Musa sapientum*). Síntesis de celulosa microcristalina. *Revista Iberoamericana de Polímeros, 15*(6), 286-300. https://reviberpol.files.wordpress.com/2019/07/2014-romero.pdf

Rusdi, S., Destian, R. A., Rahman, F., and Chafidz, A. (2020). Preparation and characterization of bio-degradable plastic from banana Kepok peel waste. *Materials Science Forum, 981*, 132-137. https://doi.org/10.4028/www.scientific.net/MSF.981.132

Saffian, H. A., Abdan, K., Hassan, M. A., Ibrahim, N. A., and Jawaid, M. (2016). Characterisation and biodegradation of poly(lactic acid) blended with oil palm biomass and fertil-

iser for bioplastic fertiliser composites. *BioResources, 11*(1), 2055-2070. https://doi.org/10.15376/biores.11.1.2055-2070

Salinas-Moreno, Y., Pérez-Herrera, P., Castillo-Merino, J., and Álvarez-Rivas, L. (2003). Relación amilosa: amilopectina en el almidón de harina nixtamalizada de maíz y su efecto en la calidad de la tortilla. *Revista Fitotecnia Mexicana, 26*(2), 115-121. https://revistafitotecniamexicana.org/documentos/26-2/7a.pdf

Tirado, D., Montero, P., Acevedo, D. (2015). Estudio comparativo de métodos empleados para la determinación de humedad de varias matrices alimentarias. *Información Tecnológica, 26*(2), 3-10. https://doi.org/10.4067/S0718-07642015000200002

Tummala, P., Liu, W., Drzal, L. T., Mohanty, A. K., and Misra, M. (2006). Influence of plasticizers on thermal and mechanical properties and morphology of soy-based bioplastics. *Industrial and Engineering Chemistry Research, 45*(22), 7491-7496. https://doi.org/10.1021/ie060439l

Wadhwa, M., and Bakshi, S. P. M. (2013). *Utilization of fruit and vegetable wastes as livestock feed and as substrates for generation of other value-added products*. FAO.

Wang, J., Gardner, D. J., Stark, N. M., Bousfield, D. W., Tajvidi, M., and Cai, Z. (2018). Moisture and oxygen barrier properties of cellulose nanomaterial-based films. *ACS Sustainable Chemistry and Engineering, 6*(1), 49-70, https://doi.org/10.1021/acssuschemeng.7b03523

Influence of Agitator Geometry in the Dissolution Kinetics of a Spherical Solid

Influencia de la geometría del agitador en la cinética de disolución de un sólido esférico

Gustavo A. Orozco [1], Clara T. González-Hidalgo[2], and Fabio Fajardo[3]

ABSTRACT

An experimental study was conducted with the purpose of establishing the effect of both agitator geometry and agitation rate on the dissolution kinetics of spherical candies. To this effect, the dissolution constants were determined in aqueous solutions by way of the Hixson-Crowell model for three types of agitators, namely a paddle agitator with two blade, and two turbine agitators with four and six blades, respectively. Subsequently, for a fixed agitation rate, the temperature was varied in order to experimentally determine the activation energy of each agitator. It was found that, while the geometry of the agitator has an effect on the pre-exponential factors of the dissolution constant, the activation energy remains constant. Finally, differences in the dissolution constants as a function of the angular frequency of the agitator were also found.

Keywords: solid dissolution constant, activation energy, agitator geometry, agitation rate

RESUMEN

Se realizó un estudio experimental con el fin de establecer el efecto de la geometría de un agitador y su tasa de agitación en la cinética de disolución de dulces esféricos. Para ello se determinaron las constantes de disolución en soluciones acuosas usando el modelo de Hixson-Crowell en tres tipos de agitadores, a saber: un agitador de paleta de dos aspas, y dos agitadores tipo turbina de cuatro y seis aspas respectivamente. Posteriormente, para una tasa fija de agitación, se varió la temperatura con el propósito de determinar experimentalmente la energía de activación de cada agitador. Se encontró que, mientras la geometría del agitador tiene un efecto en el factor pre-exponencial de la constante de disolución, la energía de activación permanece constante. Finalmente, también se encontraron diferencias en las constantes de disolución en función de la frecuencia angular del agitador.

Palabras clave: constante de disolución de sólidos, energía de activación, geometría del agitador, tasa de agitación

Introduction

The dissolution phenomenon plays an important role in several industrial and biological processes such as drug delivery via mucosal surfaces (Jug *et al.*, 2018), water treatment (Pham, Sedlak and Doyle, 2012), or controlled release of inhibitors from coatings (Pham *et al.*, 2012), among others. Once a solute is introduced in a solvent, it is expected to engage in a dynamical process where the solute particles migrate from the highest to the lowest concentration regions. This phenomenon is strongly dependent on thermodynamic variables such as pressure, temperature, and the nature of the solvent.

From a mathematical point of view, the dissolution rate can be accounted for by using the Noyes-Whitney equation: (Noyes and Whitney, 1897)

$$-\frac{dm}{dt} = \frac{DS}{h}(C_s - C_t) \qquad (1)$$

where m is the solid mass at a given time t, S is the solid surface area, h is the diffusion layer thickness, C_s is the solute solubility, C_t is the solute concentration at a time t, and D is the diffusion coefficient. It is known that the diffusion coefficient characterizes the ease with which each particle moves into a given solute and depends on many factors such as the size and shape of the solute, solvent viscosity, and temperature.

[1] Chemical Engineer, Universidad de América, Colombia. Physicist, Universidad Nacional de Colombia, Colombia. MSc Chemical Engineering, Universidad Nacional de Colombia, Colombia. PhD Chemical Engineering, Universitat Rovira i Virgili, Spain. Affiliation: Assistant Professor, Universidad Nacional de Colombia, Colombia. E-mail: gaorozcoa@unal.edu.co

[2] Physicist, Universidad Nacional de Colombia, Colombia. MSc Physics, Universidad Nacional de Colombia, Colombia. PhD Chemical Engineering, Universitat Rovira i Virgili, Spain. Affiliation: Assistant Professor, Pontificia Universidad Javeriana, Colombia. E-mail: gonzalezclara@javeriana.edu.co

[3] Physicist, Universidad Nacional de Colombia, Colombia. PhD Physics, Universidade Estadual de Campinas, Brasil. Affiliation: Associate Professor, Universidad Nacional de Colombia, Colombia. E-mail: fefajardot@unal.edu.co

If a solute with a spherical geometry is considered, it is possible to see that the integration of Equation (1) results in the Hixson-Crowell model (Hixson and Crowell, 1931). Details about the procedure can be found in the literature (Beauchamp, 2001; Hixson and Crowell, 1931; Hixson and Baum, 1942).

$$m^{1/3} = m_0^{1/3} - kt \tag{2}$$

where k represents the constant kinetic of dissolution given by

$$k = \frac{D}{h}\left(\frac{4\pi}{3}\right)^{1/3}\left(\frac{1}{p}\right)^{2/3} C_{s.} \tag{3}$$

It can be observed that k depends on density (ρ), diffusivity (D), and solubility parameters (Cs). k is also explicitly dependent on temperature through an Arrhenius-like law given by the following Equation:

$$k = Ae^{-E_a/RT} \tag{4}$$

where A is the pre-exponential factor, E_a is the activation energy, R is the ideal gas constant, and T is the temperature.

Although the dissolution constants of spherical solids have been previously reported, to the best of our knowledge, the effect of the agitator geometry on it has not yet been considered. This effect is of great importance to understand the dissolution dynamics in stirred tanks where additional variables need to be considered, such as the type of impeller device and the proportions of the tank, deflectors, and agitators (Mc Cabe et al,. 2007). Previous works have been carried out on the effect of different impeller features on different processes. For instance, (Mangwandi et al., 2010) showed that, for a high-shear granulator, impeller speed has an effect on granule size distribution, as well as on structure and shape, which in turn affects the dissolution rate measured by means of the time a certain percentage of granules takes to dissolve. (Legendre et al., 2016) simulated bubble dissolution in a fluid tower to optimize the process of CO_2 mineralization. Using a specific impeller geometry, they calculated the Hatta number, demonstrating that the effect of the chemical reaction is minimal in contrast to the mass transfer process, as well as presenting the dissolution of mass over time. Kravtchenko et al. (1999) studied the dissolution of food hydro-colloids, for which they empirically found a certain configuration between stirrer and container in order to overcome the issue with lump formation. They were able to quantify dissolution kinetics by assessing the mass dissolved over time. (Jirout et al,. 2011) showed that mixing system aspect ratios have an effect on the mixing of suspensions calculated through the Froud number and dimensionless power consumption

necessary for off-bottom particle suspension. (Thakur et al., 2004) demonstrated that, in complex fluids (Newtonian and non-Newtonian), the column-to-impeller distance has an effect on mixing, which was evidenced by means of computing the effective shear rate and the power consumption. (Akrap et al., 2012) studied the effect of variation in the ratio of the impeller diameter to tank diameter, on the nucleation rate of borax decahydrate and crystal growth, but they did not examine dissolution. (Abreu-Lopez et al., 2017) numerically computed the effect of different impeller designs in a batch reactor for aluminum degassing, estimating pressure fields and dimensionless oxygen concentration with respect to time. (Alok et al., 2014) analyzed the effect of different kinds of impeller on mixing in an aerobic stirred tank fermenter, determining the volumetric mass transfer coefficient. They reported a particular kind of impeller to be the most efficient in regards to mass transfer in comparison with the others by measuring the turbulent dissipation rate, which, according to the authors, represents the volumetric mass transfer rate. (Ćosić et al., 2016) studied the influence of the impeller blade angle on the crystallization kinetics of borax. Some of the findings were that the flow pattern of the liquid charge changes significantly with the blade angle, the rate of nucleation increases as the blade angle decreases, and increasing the impeller blade angle significantly impacts the crystal growth rate constant. By means of electrical resistance tompgraphy and computational fluid dynamics, (Kazemzadeh et al, 2020) analyzed the effect of impeller type on the mixing of highly concentrated large-particle slurries. Using three types of axial impellers, they found that the impeller type has impact on the homogeneity of the mixture, the average particle velocity along the tank, and the energy dissipation, which therefore affects power consumption. (Gu et al., 2020) studied floating particle drawdown and dispersion in a stirred tank with four pitched-blade impellers using computational fluid dynamics simulation. The type of impeller can reduce the power consumption at the same impeller speed, and it can also enhance the solid integrated velocity and the level of homogeneity for the floating particle dispersion process under constant power consumption. (Liu et al., 2021) investigated gas-liquid mass transfer and power consumption in jet-flow high-shear mixers. They found that gas-liquid mass transfer performance and power consumption are significantly affected by structural parameters, among them rotor blade angle and rotor blade arc. They also found the gas-liquid mass transfer performance is improved with increasing blade angle and that power consumption is reduced by decreasing the blade angle.

This work aims to experimentally study the effect of impeller geometry on the dissolution rate of spherical candy. In order to do that, the dissolution constant rate will be evaluated considering variations in the geometry of the stirrers, their agitation angular frequency, and the solvent temperature. The activation energy of the

dissolution is determined, as well as the pre-exponential factors for every agitator.

Experimental development

Inside a mixing cylindrical tank, it is possible to distinguish three velocity components: the radial component, which acts perpendicularly to the stirrer axis; the longitudinal component, which acts parallel to the axis; and the rotational component, which acts tangentially to the circular trajectory around the axis.

Impellers can be divided into two types: those which generate currents parallel to the axis, called axial flow impellers; and those which generate currents in the radial or tangential direction, called radial flow impellers. The main impeller types for liquids are propellers, paddles, and turbines (Mc Cabe *et al.*, 2007).

In this work, three different impellers were used to generate diverse flow patterns inside the system and observe the effect of different geometries on the dissolution process. The types of conventional agitators used were:

- *Agitator 1*: This agitator is a paddle which consists of two blades (Figure 1); it mainly produces radial and tangential flow currents, as well as intense shear stresses.

- *Agitator 2*: This agitator is a turbine type which consists of four blades (Figure 1) pitched at 45 °. It produces both axial and radial flow, as well as high shear stresses.

- *Agitator 3*: This agitator is also a turbine type which consists of six straight blades (Figure 1). It produces radial and tangential flow, as well as a higher shear stress than agitator 2.

Empirical geometric proportions of the tank and agitator, which are illustrated in Figure 2, were taken into account for the paddle-type and turbine-type agitators shown in Table 1, where D_a is the propeller diameter, D_t is the water tank diameter, W is the width of the propeller blade, H is the water tank height, and E is the height of the propeller with respect to the water tank bottom. Dimensions were measured using a caliper with an error of $\pm$.

Table 1. Ratios used between tank and agitator size

	Paddle-type	**Turbine-type**
D_a/D_t	0, 9	0, 7
H/D_t	0, 8	0, 8
E/D_t	0, 3	0, 3
W/D_a	0, 2	0, 3
L/D_a	0, 4	0, 4
W/L	0, 4	0, 7

Source: Authors
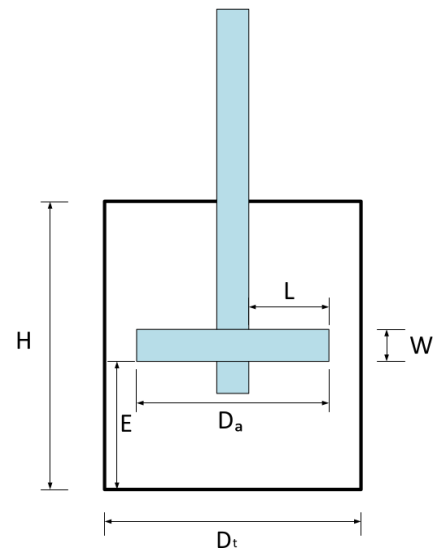
Figure 2. Geometric factors considered in the blade design of the agitators

Source: Authors
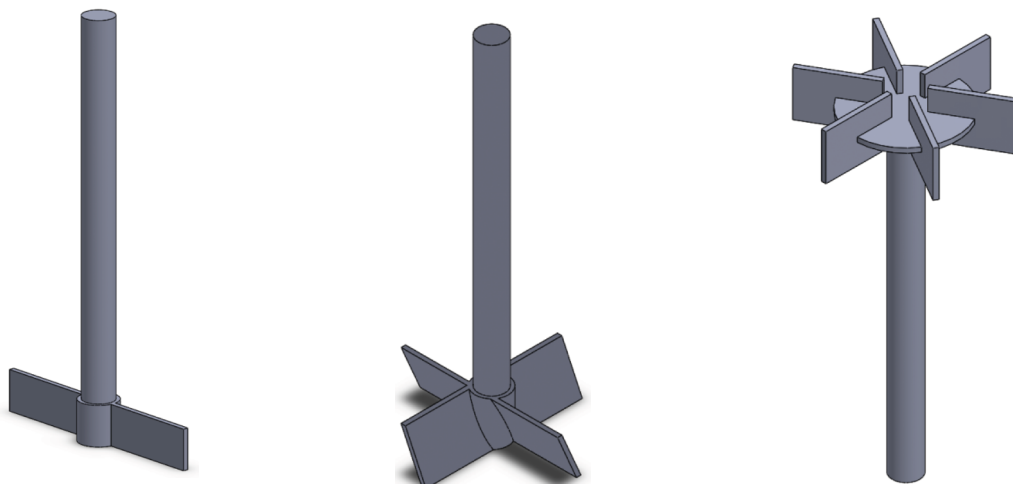
Figure 1. Agitator 1: paddle agitator, two blades; agitator 2: turbine agitator, four inclined blades; agitator 3: turbine agitator, six disk straight blades

Source: Authors

A sketch of the experimental set-up is shown in Figure 3. It consisted of a 1 000 ml beaker filled with 700 ml of water and a candy sphere (solute) immersed in it. The agitation was provided by means of an agitator coupled to a DC motor, whose angular frequency (ω) was controlled using a variable DC voltage source. The rotational speed was practically achieved as soon as the motor is started. Therefore, by changing ω, modifications of the flow pattern inside the tank were obtained.
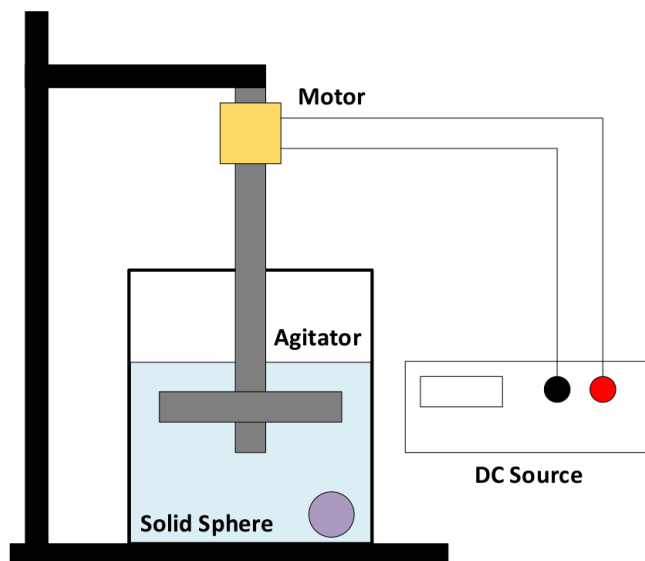
Figure 3. Sketch of the experimental setup

Source: Authors

The spherical mass was initially measured using a precision digital balance (OHAUS) with an accuracy of 0,01 g. Averaging ten candies, the initial mass of the candy was 10,01 g $\pm$ 0,49 g. Although the radius was not used, the candy spheres had an average diameter of 17,07 mm $\pm$ 0,25 mm. The solid was introduced into the beaker, and the solution was stirred for 2 min under a fixed voltage applied to the motor, which corresponds to a given angular velocity. Afterwards, the candy sphere was taken out and dried. Then, its mass was measured again. This process was repeated 10 times in 2 min intervals at room temperature (20 °C). Time was measured using a digital chronometer with an accuracy of 0,01 s. Five variations in the stirring frequency were chosen for each agitator. The described procedure was performed for the three types of agitators illustrated in Figure 1. Each measurement was repeated five times with different candies. It is important to clarify that, while the agitation occurred, there were no collisions between the candy spheres and the agitator paddles, and no changes in their spherical shape were observed. The candy was introduced and taken out with a strainer in a very short time with the agitator at rest, and it was put on a napkin so water was absorbed the mass was measured, which is why measurement errors in this regard were not significant.

As a second stage of the study, the experimental setup was placed inside a thermal bath under a controlled temperature (Thermo HAAKE Phoenix II circulator). The voltage applied to the motor was kept at 7 V (632 rpm) 0,1 V, and temperature variations between 20 and 70 1°C were implemented and measured with a mercury thermometer. Because the solid dissolution rate and mass loss increased at higher temperatures, it was necessary to take mass measurements more often during this stage (they were taken every minute).

The angular velocity of the agitator was controlled by the voltage applied to the motor and measured using a tachometer with an accuracy of 0,1 rpm. The motor calibration curve is shown in Figure 4, which evidences a direct relation between the voltage applied to the motor and the rotational speed. The results were very similar for the different agitators coupled to the motor because all of them have a small moment of inertia. Numerical values of the calibration curve can be consulted in the Supplementary Information section.

Results and discussion

Dissolution constants at room temperature

For Figures 4 to 11, dots represent the average of five measurements, and error bars are not included since they are smaller than the symbol size.
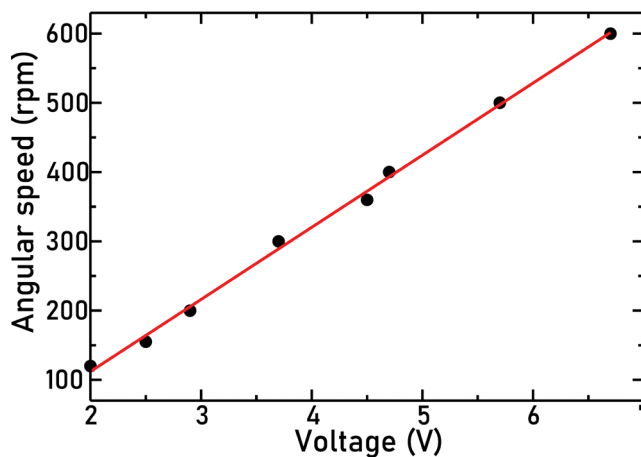
Figure 4. Motor calibration curve

Source: Authors

Figure 5 represents the cube root of mass as a function of time and at room temperature. Dots correspond to experimental points and lines to a linear fit. Although several angular frequencies were considered, for this Figure only, the lowest and the highest angular frequencies are shown for every agitator.

It can be observed that, at all frequencies, the three types of agitators follow a linear relation between the cube root of mass and time, which agrees with the Hixson-Crowell model. From the slope of these curves, and considering Equation (2), it was possible to determine the value of the dissolution constant k.
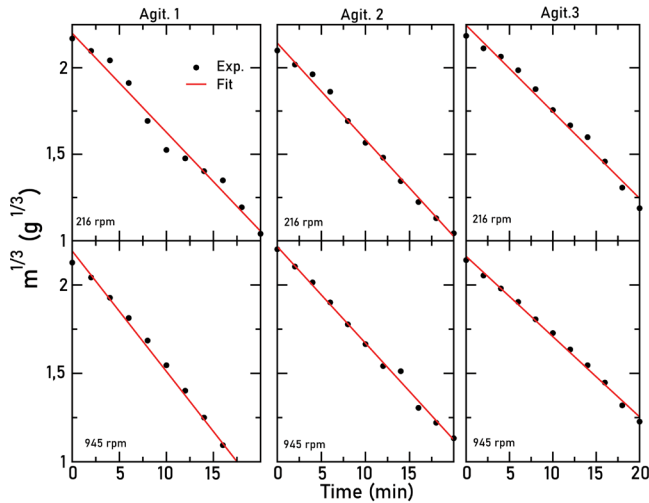
Figure 5. Cube root solid mass as a function of time for several angular frequencies of the three agitators
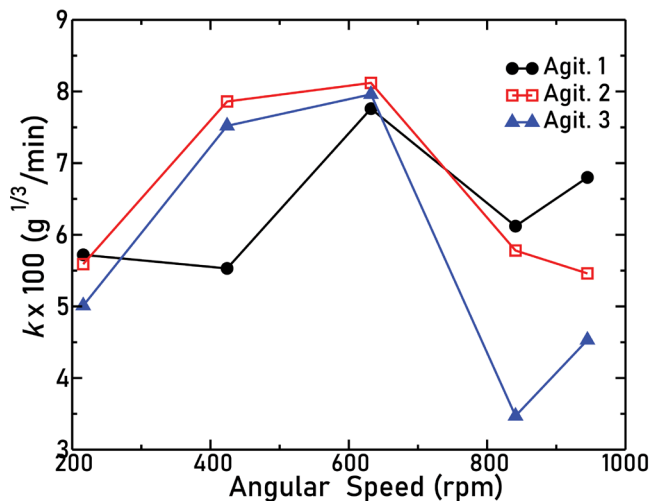
Source: Authors

Figure 6. Solid dissolution constant as a function of the angular frequency for the three agitators

Source: Authors

The relation between the angular frequency ω of the agitators and the solid dissolution constant k is represented by Figure 6.

Note how, for $\omega \leqslant 632$ rpm, the value of k increases. For agitator 1, the difference between the two first dissolution constant values is so small (around 3%) that we can assume that the k remained constant. However, for higher values of ω, a decrease with respect to the maximum achieved dissolution constant is found, which is a characteristic of the three types of agitators. This behavior can be attributed to the fact that, for $\omega > 650$ rpm, vortex and high turbulence inside the beaker were experimentally observed, especially for agitator 3, which showed the highest drop in k. The combination of these effects could make the mass transfer between solute and solvent difficult and therefore produce a decrease in mass transfer during the diffusion process. From Figure 6, it is also possible to infer how, for $\omega \leqslant 632$

rpm, the higher values of dissolution constants are obtained with agitator 2, which is the one that actually has its blades pitched, thus allowing an axial flow. For $\omega > 632$ rpm, agitator 1 attains the highest rates of dissolution, presumably since it is the one which reported the least of turbulence. This led us to infer that the dissolution constant depends indeed on the geometry used in the agitation system.

Dissolution constants under different temperatures

Figures 7, 8, and 9 show the cube root of mass as a function of time for agitators 1, 2, and 3, respectively, for different temperatures as indicated in each Figure. Lines correspond to the fit to the experimental points. In all cases, the angular frequency was held at 632 rpm.
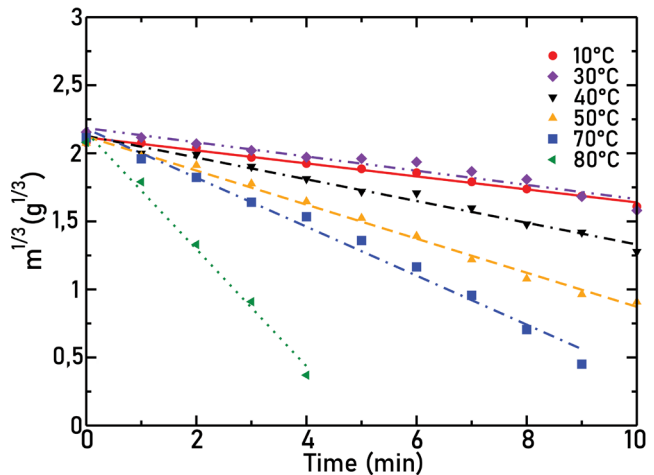
Figure 7. Cube root of mass as a function of time for agitator 1 at different temperatures, $\omega = 632$ rpm
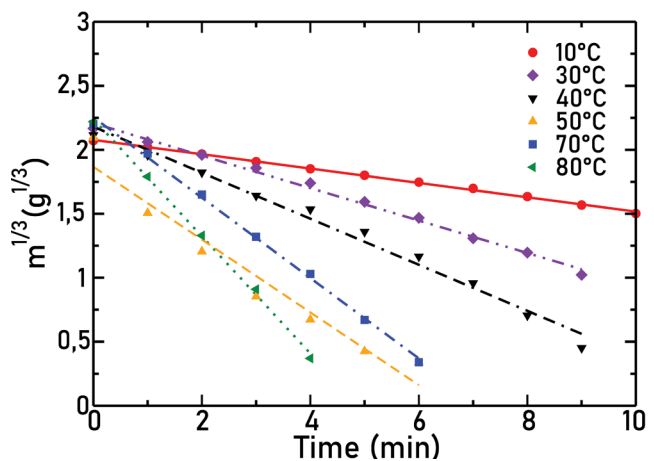
Source: Authors

Figure 8. Cube root of mass as a function of time for agitator 2 at different temperatures, $\omega = 632$ rpm

Source: Authors

In these Figures, it is observed how, as the temperature increases, there is an increase in the slope absolute value and therefore in the solid dissolution constant. This was expected, since, when temperature increases, there is also an increase in the solubility of particles.
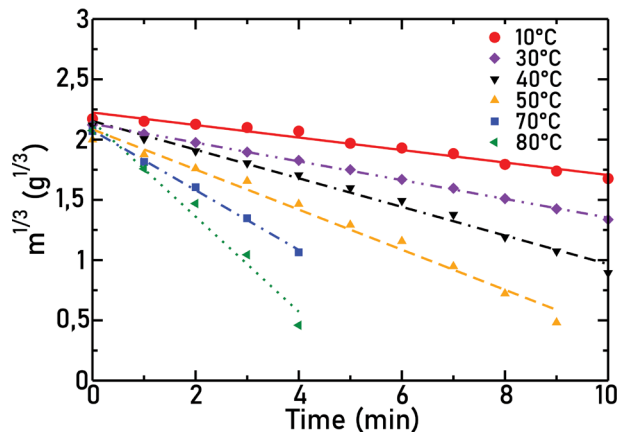
Figure 9. Cube root of mass as a function of time for agitator 3 at different temperatures, ω = 632 rpm

Source: Authors

Figure 10 shows the dependence of the solid dissolution constant as a function of temperature for the different agitators used in this experiment. As predicted by Equation (4), there is an increase in the solid dissolution constant as the temperature increases. It is also possible to observe that the dissolution constant is remarkably dependent on the type of agitator, and it is again the agitator 2 which attains the highest dissolution constants for all temperatures. For the highest temperature studied, the difference between the constants decreases, possibly due to the effect of temperature, which exerts a greater influence on the dissolution process than the agitator geometry. Still, agitator 2 keeps attaining the highest constant. Therefore, taking into consideration the results shown in Figure 6, we can say that agitator 2, which produces both axial and radial flow, also induces the highest solid dissolution constants.
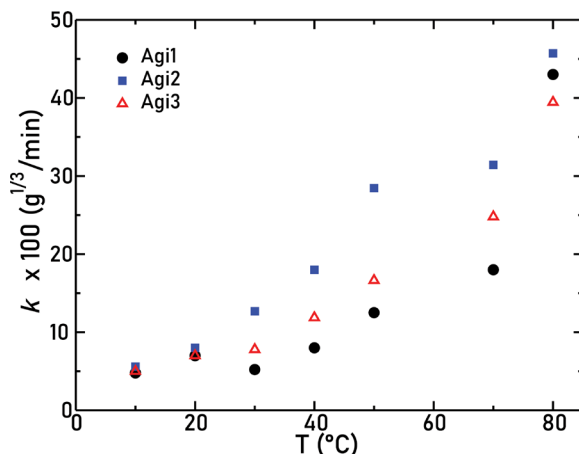
Figure 10. Variation of the dissolution constant as a function of temperature for the three types of agitators

Source: Authors

Activation energies

Activation energies E_a for the dissolution process are determined by taking the natural logarithm of Equation (4), so that

$$\ln k = \ln A - \frac{E_a}{RT} \qquad (5)$$

where A represents the pre-exponential constant.

Figure 11 shows the natural logarithm of the solid dissolution constant as a function of the inverse of the temperature for the three types of agitators used in this work. In this Figure, it is possible to observe how every straight line has approximately the same slope (Table 2). Differences between them are about 6% at most. Therefore, it is possible to conclude that the activation energy is approximately the same for all cases and is independent of the agitator geometry. This activation energy is similar to the 23 kJ/mol value reported by (Beauchamp, 2001). However, in Table 3, which summarizes the pre-exponential factors (A), some remarkable variations appear, since line intercepts in Figure 11 are different in each situation.
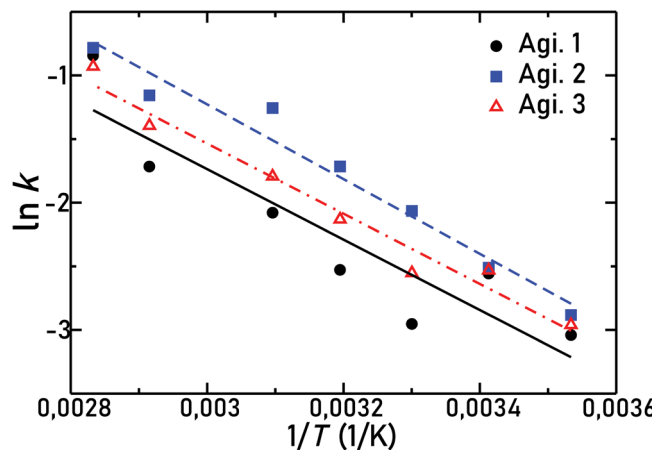
Figure 11. Relation between logarithm of dissolution constant, for all the agitators, and the inverse of temperature

Source: Authors

This leads us to conclude that the agitation phenomenon is modified specifically in the pre-exponential factor of the dissolution constant, while the activation energy of the process remains practically constant.

Table 2. Activation energy for the different agitators

	E_a (kJ/mol)
Agi 1	$23,0 \pm 1,0$
Agi 2	$24,4 \pm 1,0$
Agi 3	$22,9 \pm 1,0$

Source: Authors

Table 3. Pre-exponential factors for the different agitators

	A (g$^{1/3}$/min)
Agi 1	712 ± 14
Agi 2	1947 ± 16
Agi 3	843 ± 17

Source: Authors

Conclusions

Hixson-Crowell model appropriately predicts the kinetics of the dissolution of solids with spherical geometry. By using this model, it was possible to determine both the kinetic constants and activation energy necessary in the dissolution process. Additionally, the results showed that the agitation rate and agitator geometries affect the kinetic dissolution constant. Therefore, it is important to consider these variables when conducting a dissolution experiment.

Values of the solid dissolution constant are affected at constant temperature by the angular frequency of the agitator in all the studied geometries. The highest values in the constants were obtained for the turbine- type agitator 2, which produces axial and radial flow. However, for higher angular frequency values, the constant decreases, which can be explained in terms of the high turbulence manifested in the formation of vortices.

The activation energy was approximately the same for the three types of agitators used, regardless of their geometry. For the pre-exponential factors, a remarkable difference appeared among the agitators, which leads us to conclude that the geometry of the agitator can affect the kinetic constant specifically in the pre-exponential factor.

References

Abreu-López, D., Amaro-Villeda, A., Acosta-González, F., González-Rivera, C., and Ramírez-Argaez, M. (2017). Effect of the impeller design on degasification kinetics using the impeller injector technique assisted by mathematical modeling. *Metals, 7*(4), 132. https://doi.org/10.3390/met7040132

Akrap, M., Kuzmanić, N., and Kardum, J. P. (2012). Impeller geometry effect on crystallization kinetics of boraxdecahydrate in a batch cooling crystallizer. *Chemical Engineering Research and Design, 90*(6), 793-802. https://doi.org/10.1016/j.cherd.2011.09.015

Alok, S. (2014). Effect of different impellers and baffles on aerobic stirred tank fermenter using computational fluid dynamics. *Journal of Bioprocessing & Biotechniques, 4*(7), 1000184. https://doi.org/10.4172/2155-9821.1000184

Beauchamp, G. (2001). Dissolution kinetics of solids: Application with spherical candy. *Journal of Chemical Education, 78*(4), 523. https://doi.org/10.1021/ed078p523

Ćosić, M., Kaćunić, A., and Kuzmanić, N. (2016).The investigation of the influence of impeller blade inclination on borax nucleation and crystal growth kinetics. *Chemical Engineering Communications, 203*(11), 1497-1506. https://doi.org/10.1080/00986445.2016.1212023

Gu, D., Shi, X. and Liu, Z. (2020). Intensification on drawdown process of floating particles by circle package fractal impellers. *Journal of the Taiwan Institute of Chemical Engineers, 106*, 62-73. https://doi.org/10.1016/j.jtice.2019.09.028

Hixson, A., and Baum, S. (1942). Power requirement of turbine agitators. *Industrial and Engineering Chemistry, 34*(2), 194-208. https://doi.org/10.1021/ie50386a013

Hixson, A., and Crowell, J. (1931). Dependence of reaction velocity upon surface and agitation I – Theorical considerations. *Industrial and Engineering Chemistry, 23*(8), 923-931. https://doi.org/10.1021/ie50260a018

Jirout, T., and Rieger, F. (2011). Impeller design for mixing of suspensions. *Chemical Engineering Research and Design, 89*(7), 1144-1151. https://doi.org/10.1016/j.cherd.2010.12.005

Jug, M. Hafner, A., Lovrić, J., Kregar, M. L., Pepić, I., Vanić, Ž., Cetina-Čižmek, B., and Filipović-Grčić, J. (2018). An overview of *in vitro* dissolution/release methods for novel mucosal drug delivery systems. *Journal of Pharmaceutical and Biomedical Analysis, 147*, 350-366. https://doi.org/10.1016/j.jpba.2017.06.072

Kazemzadeh, A., Ein-Mozaffari, F., and Lohi, A. (2020). Effect of impeller type on mixing of highly concentrated slurries of large particles. *Particuology, 50*, 88-99. https://doi.org/10.1016/j.partic.2019.07.004

Kravtchenko, T., Renoir, J., Parker, A., and Brigand, G. (1999). A novel method for determining the dissolution kinetics of hydrocolloid powders. *Food Hydrocolloids, 13*(3), 219-225. https://doi.org/10.1016/S0268-005X(99)00002-8

Legendre, D., and Zevenhoven, R. (2016). A numerical Euler-Lagrange method for bubble tower CO_2 dissolution modeling. *Chemical Engineering Research and Design, 111*, 49-62. https://doi.org/10.1016/j.cherd.2016.04.010

Liu, Y., Guo, J., Li, W., Li, W., and Zhang, J. (2021). Investigation of gas-liquid mass transfer and power consumption characteristics in jet-flow high shear mixers. *Chemical Engineering Journal, 411*, 128580. https://doi.org/10.1016/j.cej.2021.128580

Mangwandi, C., Adams, M. J., Hounslow, M. J., and Salman, A. D. (2010). Effect of impeller speed on mechanical and dissolution properties of high-shear granules. *Chemical Engineering Journal, 164*(2-3), 305-315. https://doi.org/10.1016/j.cej.2010.05.039

McCabe, W., Smith, J., and Harriott, P. (2007). *Unit operations of chemical engineering*. McGraw-Hill.

Noyes, A., and Whitney, W. (1897). The rate of solution of solid substances in their own solutions. *Journal of the American Chemical Society, 19*(12), 930-934. https://doi.org/10.1021/ja02086a003

Pham, A. L. T., Sedlak, D. L., and Doyle, F. M. (2012).Dissolution of mesoporous silica supports in aqueous solutions: Implications for mesoporous silica-based water treatment processes. *Applied Catalysis B: Environmental, 126*, 258-264. https://doi.org/10.1016/j.apcatb.2012.07.018

Tabor, Z., and Warszyński, P. (2014). Modeling dissolution controlled release of inhibitor from a damaged coating. *Corrosion Science, 82*, 290-296. https://doi.org/10.1016/j.corsci.2014.01.026

Thakur, R. K., Vial, C., Djelveh, G., and Labbafi, M. (2004). Mixing of complex fluids with flat-bladed impellers: Effect of impeller geometry and highly shear-thinning behavior. *Chemical Engineering and Processing: Process Intensification, 43*(10), 1211-1222. https://doi.org/10.1016/j.cep.2003.11.005

Application of a Mathematical Model for Sludge Reduction in Pharmaceutical Wastewater

Aplicación de un modelo matemático para la reducción de lodos de aguas residuales farmacéuticas

Yongqiang Zhu[1], Shengqi Yan[2], and Min Zhu[3]

ABSTRACT

Excess sludge treatment is indispensable in sewage treatment plants. This study aims to reduce the excess material from activated sludge and establish a mathematical model. Sludge dissolution rates were calculated by measuring the total chemical oxygen demand (TCOD) and the soluble COD (SCOD) with regard to water quality before and after pretreatment. Then, sludge reduction effects were obtained by means of the suspended solid (SS) changes. The major impact factors on sludge dissolution rates were evaluated, such as pH, temperature, potassium ferrate amount, and reaction time, among others. The response surface method of the Design-Expert V8.0.6.1 software was adopted to analyze the sludge dissolution rate, which represents the sludge reduction effect. By regulating the different constraint factors, the Design-Expert model showed that the sludge dissolution rate reached the highest value of 54,36% at a temperature of 21,58 °C and a pH of 4, as well with a potassium ferrate dosage of 1 mg/g SS and a reaction time of 4,07 hours with constant stirring. A mathematical model for the sludge dissolution rate that considers temperature, pH, potassium ferrate dosage, reaction time, and stirring condition was established, and the simulated R2 value of 0,72 indicated a relatively acceptable fitting effect.

Keywords: response surface model, sludge reduction, sludge dissolution rate, pharmaceutical wastewater

RESUMEN

El tratamiento de lodos sobrantes es indispensable en las plantas de tratamiento de aguas residuales. Este estudio tiene como objetivo reducir el exceso de material en lodos activados y establecer un modelo matemático. Las tasas de disolución de lodo se calcularon midiendo la demanda química total de oxígeno (DQO) y la DQO soluble (DQOS) con respecto a la calidad del agua antes y después del pretratamiento. Luego se obtuvieron los efectos de reducción de lodos por los cambios en sólidos suspendidos (SS). Se evaluaron los principales factores de impacto en las tasas de disolución de lodos, tales como pH, temperatura, cantidad de ferrato potásico y tiempo de reacción, entre otros. Se adoptó el método de superficie de respuesta del software Design-Expert V8.0.6.1 para analizar la velocidad de disolución del lodo, que representa el efecto de reducción del lodo. Mediante la regulación de los diferentes factores de restricción, el modelo Design-Expert mostró que la velocidad de disolución del lodo alcanzó el valor más alto de 54,36 % a una temperatura de 21,58 oC y un pH de 4, así como con una dosis de ferrato de potasio de 1 mg/g SS y un tiempo de reacción de 4,07 horas con agitación constante. Se estableció un modelo matemático para la velocidad de disolución del lodo que considera la temperatura, el pH, la dosis de ferrato de potasio, el tiempo de reacción y la condición de agitación. El valor R2 simulado de 0,72 indicó un efecto de ajuste relativamente aceptable.

Palabras clave: modelo de superficie de respuesta, reducción de lodos, tasa de disolución de lodos, aguas residuales farmacéuticas

Introduction

With the development of industry and manufacture, the amount of toxic and harmful substances in wastewater has gradually increased. The activated sludge method is the most widely used treatment technique for municipal and industrial sewage around the world. At present, more than 90% of the municipal wastewater is treated using the activated sludge method (Xiao *et al.*, 2017; Yuan *et al.*, 2019; Zheng *et al.*, 2019). However, the main drawback of this approach is that it produces a huge amount of surplus sludge, which contains a lot of toxic substances and excess nutrients, including pathogenic microorganisms, parasite ova, viruses, synthetic organics, heavy metal ions, salts, nitrogen, phosphorous, potassium, *etc*. (Fei *et al.*, 2019;

[1] Professorate senior engineer, Shanghai Institute of Technology, Shanghai, China. Affiliation: Dean of Environmental Engineering Department Shanghai Institute of Technology, Shanghai, China. Email: zhuyq@sit.edu.cn

[2] Graduate student, Shanghai Institute of Technology, Shanghai, China. Affiliation: School of Chemical and Environmental Engineering, Shanghai Institute of Technology, Shanghai, China. Email: 1021784885@qq.com

[3] Master's degree in Environmental Engineering, Tongji University, Shanghai, China. Affiliation: Senior engineer from Comprehensive Department, Fengxian Environmental Monitoring Station of Shanghai, Fengxian, China. Email: brag2005@126.com

Mazeed *et al.*, 2020; Poot *et al.*, 2016; Xia *et al.*, 2019). The organic materials in the remaining sludge are easy to spoil and release a foul odor that pollutes the environment and causes discomfort to the senses. The pathogens in sludge, including various pathogenic bacteria, parasites, and viruses, can spread disease and pose a potential threat to human and animal health (Chakraborty *et al.*, 2020; Zeng *et al.*, 2019). Excess nutrients in the remaining sludge, such as nitrogen, phosphorus, and potassium can cause eutrophication and lead to algae blooms once they enter surface water bodies, which negatively impacts the environment (Fang *et al.*, 2020; Hu and Gao, 2020; Zittel *et al.*, 2020).

Nowadays, researchers are paying more attention to sludge reduction with modern techniques, such as physical, chemical, and biological methods, promoting the hydrolysis of sludge, which improves the efficiency of acid and methane production. However, sludge hydrolysis is a rate-limiting step in anaerobic digestion. Lysis-Recessive Growth (LRG) is a method for improving hydrolysis, which is easy to operate, simple to implement, and relatively mature. It involves breaking the cell membrane and solid cell wall of the microorganisms in the sludge, thus releasing organic matter into the liquid phase, increasing the organic load of sludge (F/M), and shortening the anaerobic digestion time of the sludge. LRG requires adding the pretreatment sludge to an anaerobic reactor for fermentation.

Heating excess sludge can effectively foster the dissolution of a large number of organic substances in microbial cells, making the microbe cells bigger and increasing the pore size of the cell membranes, which facilitates the transfer of a large amount of organic matter in microbial cells to the liquid phase for it to become soluble organic matter (Wu *et al.*, 2020). When the alkali is added, the hydroxyl ion (OH^-) plays a key role in destroying sludge flocs. In addition, it can also hydrolyze some proteins and nucleic acids, so that the original insoluble organic matter in the sludge turns into soluble substances transferred to the liquid phase. The addition of alkali can also reduce the resistance of the cell wall to temperature and accelerate the release of substances in the sludge (Feria-Díaz *et al.*, 2016). Zheng *et al.* (2019) used a thermal-alkali pretreatment to treat straw and fermentation waste, and they found that a cumulative gas production above 80 °C can be increased by more than 40% when compared to a heat treatment only 80 °C, as well as by 72% in comparison with no-heat treatments (room temperature). The thermal-alkali method can effectively crack the sludge, which has some advantages in the process of anaerobic fermentation to produce acid. Furthermore, the addition of potassium ferrate can oxidize the surface film of the sludge micelle and destroy the structure of the film layer to release the material within it (Pabón and Gelvez, 2009). Furthermore, high temperatures could change the sludge structure, reduce the shear resistance capacity of flocculate, and make the organic suspended solids in water more soluble. Agitation has a positive effect on cell dissolution rate, as it enhances mixing between sludge and acid, alkali, and potassium ferrate.

In this study, the impact of temperature, pH, potassium ferrate dosage, reaction time, and stirring conditions on the dissolution of residual sludge was explored via the response surface methodology in order for the sludge cell dissolution rate to reach optimal conditions. With these optimal conditions, the model can efficiently guide the sludge reduction of pharmaceutical wastewater.

Materials and Methods

Experimental samples

The wastewater and sludge used in this study were taken from a solid-liquid separation tank in a pharmaceutical wastewater treatment plan in Shanghai, China, which mainly deals with high concentrations of pharmaceutical wastewater and has a daily processing capacity of 150 m^3 in addition to a hydraulic retention time of 6 h. The sampled sludge was black with no serious bad odor. The composition of the sludge is shown in Table 1.

Table 1. Source sludge composition

Composition	TCOD	SCOD	pH	NH$_3$-N	TN	TP
Value (mg/L)	27 560	3 820	7,2	480	1 427	546

Source: Authors

Experimental procedures and measurement methods

The experiment was conducted in a common laboratory. Samples from the pharmaceutical wastewater treatment plant were stored in plastic bottles and used for experiments either right away or after 5 h of being kept in a refrigerator at 4 °C. The wastewater sample was first evenly shaken, and about 300 mL of wastewater were poured into a 500 ml beaker. The pH value was adjusted using the 1:9 ratio of hydrochloric acid or 4 M of sodium hydroxide solution, and its value was obtained with a pH meter. Next, potassium ferrate was added into the wastewater sample, which was put in a blender for full mixing. The heating mode of the blender was also switched on in order to achieve the designated temperatures and start reactions. The 46 detailed test parameters are listed in Table 2. After the pretreatment, three wastewater samples of equal volume were put in a centrifuge for 30 min with a rotation rate of 1 500 rpm.

To measure the soluble chemical oxygen demand (SCOD), the supernatant was filtered through a 0,45 μm filter paper and diluted in a ratio of 1:20 using deionized water. The solution was then injected into a digestion tube filled with a solution of 6 ml of silver sulfate (10 g/L) and 1 ml of potassium dichromate. The digestion tube was mixed well and digested for 15 min in a microwave digestion instrument (Lanzhou Lianhua Environmental Protection Technology co., LTD, 5B-1B). The absorbance value of the solution was measured using an ultraviolet spectrophotometer (L6) and recorded to compute for supernatant COD values.

The total chemical oxygen demand (TCOD) was measured by following the SCOD procedure, albeit without filtration, and the diluted wastewater samples (1:20) were directly injected into the digestion tubes.

Three equal pretreated sludge samples were injected into centrifuge tubes and were centrifuged for 30 min at 1 500 rpm. The precipitate in the centrifugal tube was filtered using a suction filter machine (Bonsi Instrument Technology co. LTD), and dried to a constant weight in a crucible (Shaoxing Galaxy Machinery Instrument co. LTD, 101-0B) at 105 ˚C. The suspended solids (SS) value was finally obtained by weighing the dried samples on an analytic balance (Shanghai Yueping Science Instrument Co. LTD, FA2004B).

Data analysis

The equation for calculating the sludge dissolution rate (W) is expressed below:

$$W = \frac{SCOD_t - SCOD_0}{TCOD_0 - SCOD_0} \times 100\% \quad (1)$$

where $SCOD_t$ is the supernatant COD value after pretreatment, $SCOD_0$ is the original supernatant COD value, and $TCOD_0$ is the original TCOD value.

The data was analyzed by the response surface method of the Design-Expert V8.0.6.1 software. There were four main types of response surface designs, as well as a Box-Behnken design. A three-level, second-order response surface version of the Box-Behnken design was adopted in this research. The Box-Behnken design combined mathematical and statistical methods to determine the test design scheme according to its contents and purposes. The experiment was optimized by means of an analysis of variance, the estimation of the standard deviation and the signal ratio, and a regression analysis.

Results and discussion

Response surface optimization analysis

The synergistic effect of temperature and pH on the sludge dissolution rate is shown in Figures 1a and 1b for a reaction time of 6,5 h and a potassium ferrate dose of 5,5 mg/g SS with stirring. There were two regions (green) with a cell dissolution rate greater than 20%. In zone 1, the cell dissolution rate was more than 20% when the temperature ranged from 20 to 44 ˚C and the pH value was between 4 and 4,6. In zone 2, the cell dissolution rate was also greater than 20% when the temperature was between 32 and 80 ˚C and the pH value between 8 and 12. When the temperature ranged from 68 to 80 ˚C and the pH was between 11,5 and 12, the cell dissolution rate was above 40%. As shown in Figures 2a 2b, when the pH

value was fixed at 8 and the potassium ferrate dose was 5,5 mg/g SS with stirring, the cell dissolution rate of the sludge did not significantly increase with temperature and time. The cell dissolution rate of the sludge was up to 18% when the temperature was between 50 and 68 ˚C and the reaction time was between 3,5 and 7,5 h. Therefore, the effect of the reaction time on the cell dissolution rate was not significant.
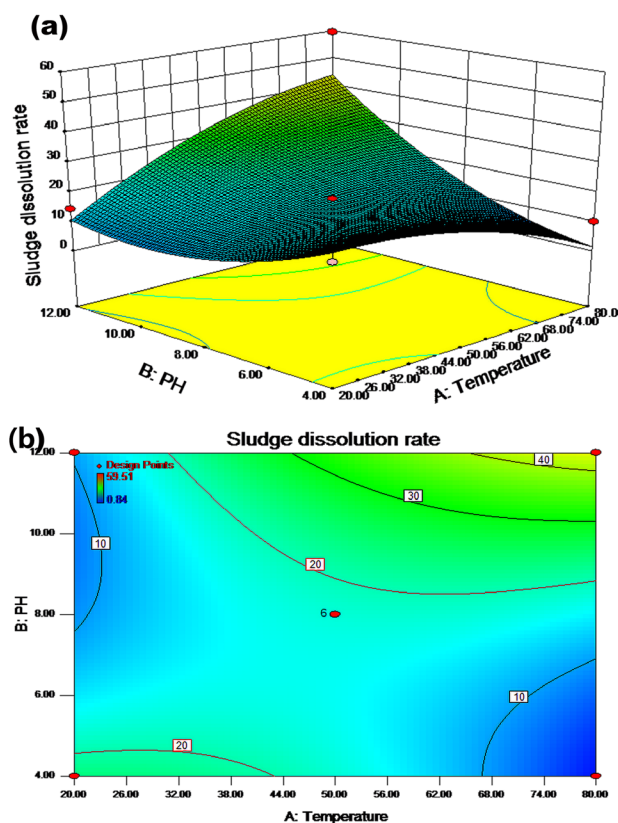
Figure 1. Response surface (a) and contour (b) maps: pH value and temperature
Source: Authors

The synergistic effect of temperature and potassium ferrate dosage on the sludge dissolution rate is shown in Figures 3a and 3b for a pH value of 8 and a reaction time of 6,5 h with agitation. The sludge dissolution rate was more than 15% when the temperature was between 24 and 80 ˚C and the potassium ferrate dose ranged from 1 to 8 mg/g SS. The cell dissolution rate was above 20% when the temperature was between 37 and 80 ˚C, with a potassium ferrate dose between 1 and 4 mg/g SS. The results show that the rate of sludge dissolution did not always increase as the potassium ferrate did. As shown in Figures 4a and 4b, the dissolution rate of sludge was more than 20% when the pH value ranged from 9 to 12 and the reaction time was between 1 and 12 h. The cell dissolution rate was above 30% when the pH value was in the range of 11,5-12 and the reaction time was between 1 and 12 h. These results show that the effect of the reaction time on the cell dissolution rate was not significant in this case.

Table 2. Experimental groups of sludge cell dissolution rate

No.	Reaction temperature χ_1 /°C	pH value χ_2	Stirring time χ_3 / h	Potassium ferrate dosage χ_4 /mg	Agitation conditions χ_5
1	80,00	8,00	6,50	5,50	1,00
2	50,00	12,00	6,50	10,00	0,50
3	80,00	4,00	6,50	5,50	0,50
4	20,00	8,00	6,50	5,50	0,00
5	20,00	8,00	6,50	5,50	1,00
6	50,00	8,00	1,00	5,50	1,00
7	50,00	4,00	6,50	5,50	0,00
8	50,00	12,00	6,50	1,00	0,50
9	50,00	8,00	12,00	1,00	0,50
10	50,00	12,00	1,00	5,50	0,50
11	50,00	8,00	6,50	5,50	0,50
12	20,00	8,00	12,00	5,50	0,50
13	50,00	8,00	6,50	1,00	0,00
14	80,00	8,00	1,00	5,50	0,50
15	50,00	4,00	1,00	5,50	0,50
16	50,00	8,00	12,00	5,50	1,00
17	50,00	8,00	6,50	5,50	0,50
18	20,00	8,00	6,50	10,00	0,50
19	50,00	8,00	6,50	5,50	0,50
20	80,00	8,00	6,50	5,50	0,00
21	20,00	8,00	6,50	1,00	0,50
22	50,00	8,00	1,00	1,00	0,50
23	50,00	12,00	6,50	5,50	0,00
24	50,00	8,00	12,00	10,00	0,50
25	50,00	8,00	6,50	1,00	1,00
26	50,00	4,00	6,50	10,00	0,50
27	50,00	8,00	12,00	5,50	0,00
28	50,00	8,00	6,50	5,50	0,50
29	50,00	12,00	6,50	5,50	1,00
30	80,00	8,00	12,00	5,50	0,50
31	80,00	12,00	6,50	5,50	0,50
32	50,00	8,00	1,00	10,00	0,50
33	50,00	8,00	1,00	5,50	0,00
34	50,00	8,00	6,50	10,00	1,00
35	50,00	4,00	6,50	5,50	1,00
36	50,00	12,00	12,00	5,50	0,50
37	20,00	4,00	6,50	5,50	0,50
38	80,00	8,00	6,50	10,00	0,50
39	50,00	8,00	6,50	5,50	0,50
40	20,00	12,00	6,50	5,50	0,50
41	50,00	4,00	12,00	5,50	0,50
42	50,00	4,00	6,50	1,00	0,50
43	50,00	8,00	6,50	5,50	0,50
44	50,00	8,00	6,50	10,00	0,00
45	80,00	8,00	6,50	1,00	0,50
46	20,00	8,00	1,00	5,50	0,50

Source: Authors
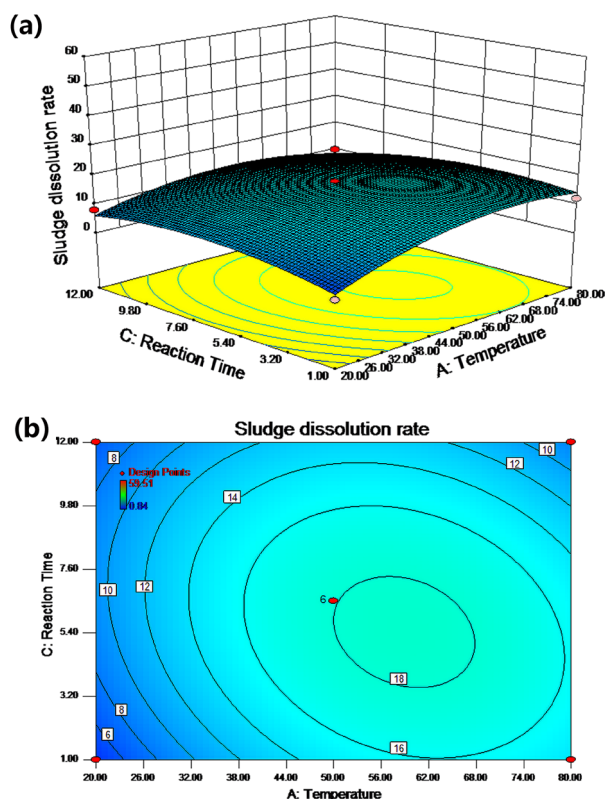
Figure 2. Response surface (a) and contour (b) maps: reaction time and temperature
Source: Authors
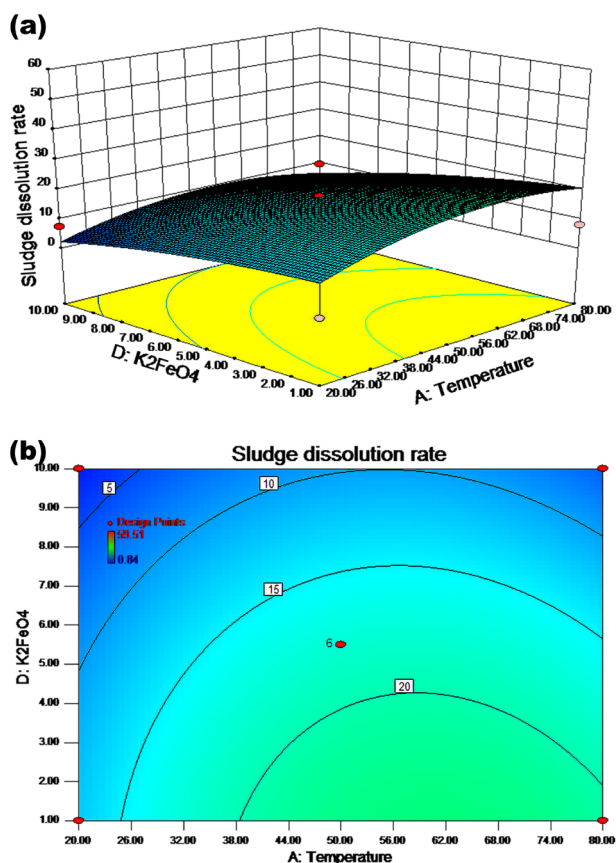
Figure 3. Response surface (a) and contour (b) maps: potassium ferrate dosage and temperature
Source: Authors
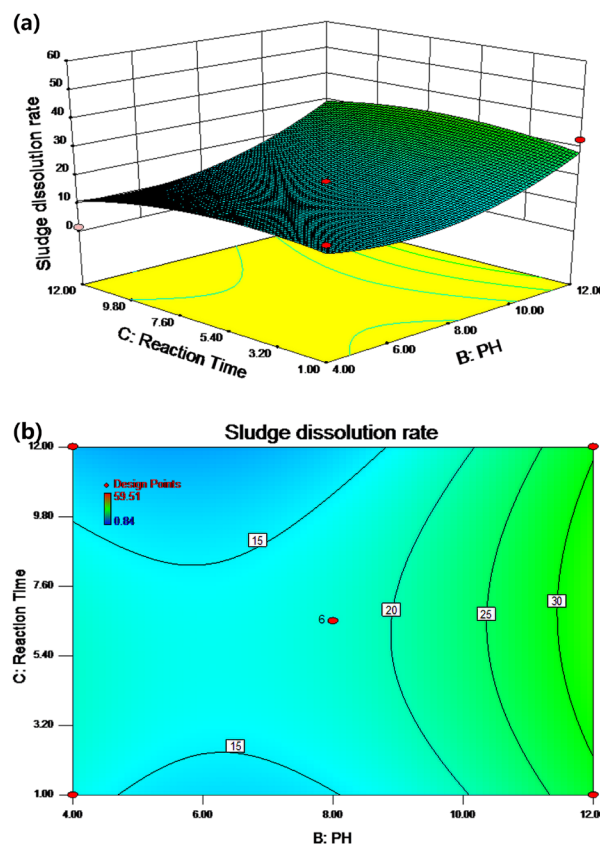
Figure 4. Response surface (a) and contour (b) maps: reaction time and pH value
Source: Authors

The synergistic effect of the pH value and the potassium ferrate dosage on the sludge dissolution rate is shown in Figures 5a and 5b for a temperature of 50 °C and a reaction time of 6,5 h with stirring. There were two regions with relatively high cell dissolution rate. In zone 1, the cell dissolution rate was more than 20% when the pH value changed from 4 to 8 and the potassium ferrate dose varied from 1 to 3,5 mg/g SS. In zone 2, the cell dissolution rate was greater than 20% when the pH value increased from 8 to 12 and the potassium ferrate dose increased from 1 to 10 mg/g SS. When the pH value was between 11,5 and 12 and the potassium ferrate dose was within the range of 1-10 mg/g SS, the cell dissolution rate was above 30%.

The synergistic effect of the reaction time and the stirring conditions on the sludge dissolution rate is shown in Figures 6a and 6b for a temperature of 50 °C, a pH of 8, and a potassium ferrate dose of 5,5 mg/g SS. According to the results, the cell dissolution rate improved; it increased by about 10% with stirring.

Fitting results and regression equation

Experimental data points were randomly scattered on both sides of the predicted straight line (Figure 7a), thus indicating an acceptable fit. The following quadratic multinomial regression equation for the sludge cell dissolution rate was obtained via Design-Expert for experimental design and multivariate analysis:

$$P = 0,01\chi_1 - 11,13\chi_2 + 1,91\chi_3 - 1,05\chi_4 + 70,58\chi_5 + 0,11\chi_1\chi_2 - 0,01\chi_1\chi_3 - 0,14\chi_1\chi_5 + 0,07\chi_2\chi_3 + 0,29\chi_2\chi_4 - 4,46\chi_2\chi_5 - 0,61\chi_3\chi_5 - 2,64\chi_4\chi_5 + 0,47\chi_2^2 - 0,14\chi_3^2 - 0,09\chi_4^2 + 1,29\chi_5^2 + 32,89 \quad (2)$$

where P is the sludge dissolution rate, χ_1 is the reaction temperature, χ_2 is the solution pH value, χ_3 is the reaction time, χ_4 is the potassium ferrate dosage, and χ_5 is the agitation condition (0 for no stirring or 1 for stirring). An F-value of 3,16 with a p-value (Prob>F, less than 0,5) was obtained from the statistical test using the aforementioned model, which indicates a nonlinear relationship between the four factors and a significant difference among them. Said factors had a significant effect on the residual sludge dissolution rate, and there was some interaction between them. The R^2 value regarding the fit of the regression model was 0,72, which was acceptable. The signal ratio was represented via Adeq Precision, which could be used for simulation purposes when it is greater than 4. In this study, Adeq Precision showed a value of 7,20, which was large enough to simulate the design.

Three repetitive experiments were conducted at 21,58 °C as well as with a pH = 4, a potassium ferrate dose of 1 mg/g SS, a reaction time of 4,07 h, and stirring, which are the optimal conditions given by the mathematical model. The obtained residual sludge cell dissolution rates were 52,78, 55,12, and 51,02%, which is listed in Table 3. The results showed a standard deviation of 2,06 and were very close to the 54,36% predicted by the software. Therefore, the reliability of this model was as expected, and the fitting diagram of the predicted values *vs.* the actual ones is shown in Figure 7b. According to Table 3, the real value under the best experimental conditions was very close to the simulation value obtained by the software, with a low error rate, thus indicating the reliability of the model.

Table 3. Sludge cell dissolution rate mode validation

No.	Simulation value	Actual value	Error value	Rate of deviation
1	54,36%	51,78%	2,58%	$5,0\times10^{-2}$
2	54,36%	57,12%	2,76%	$4,8\times10^{-2}$
3	54,36%	48,02%	6,34%	$1,32\times10^{-1}$

Source: Authors

Mechanism analysis

Changes in the residual sludge cell dissolution rate could be clearly observed, which are represented by color changes in Figures 1-6 (Capela *et al.*, 2017). The strength of the interaction between two factors is represented by the change in the contour line. An ellipse indicates that two factors interacted significantly, whereas a circle means the opposite. All seven diagrams in this study had ellipse shapes, thus indicating significant interaction effects between factors.

The interaction effect of the temperature and pH values on the residual sludge cell dissolution rate is shown in Figures

1a and 1b. The results in Figures 4a and 5a show that the effect of the pH value on the residual sludge dissolution rate was significant. A positive linear relationship was observed, where an increased pH value caused an increase in the cell dissolution rate. Like the pH, increasing the temperature improved the dissolution rate.
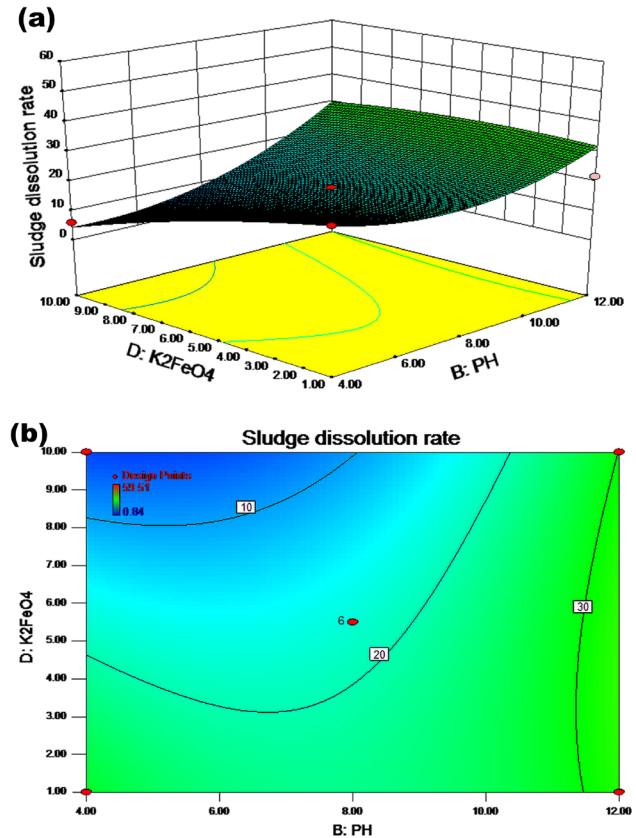
Figure 5. Response surface (a) and contour (b) maps: potassium ferrate and pH value
Source: Authors

As shown in Figures 1-6, two factors had a synergistic effect and could achieve the optimal treatment conditions, albeit within a specific range. There was an interaction between pH and temperature, and an optimal region of cell dissolution rate was observed in the 3D diagram. On the lower left corner of Figure 1b, the cell dissolution rate was relatively high (more than 20%). The correlation of SCOD with the low alkaline condition was relatively small, but there was a quite high correlation under high alkaline conditions. A possible explanation could be that only the flocculation structure of the sludge could be destroyed when the amount of alkaline was low, unlike the cellular structure of the microorganisms. However, both structures could be destroyed simultaneously under high alkalinity to produce organic materials such as hydrolyzed proteins and carbohydrates. Originally insoluble organic matter in the sludge were also released from microbial cells and became soluble substances, so the SCOD concentration of the sludge increased (Wilson and Novak, 2009).

A large amount of dissolved total sugars, soluble proteins, and other organic substances were released when cells lysed after the residual sludge was heated. Some highly hydrophilic substances such as proteins, carbohydrates, and nucleic acids became other, likely smaller compounds during heating. For instance, the proteins prevalent in EPS can lose their normal shapes and even precipitate. Furthermore, high temperatures could change the sludge structure, reducing the shear resistance capacity of the flocculate and allowing the organic suspended solids to be more soluble in water.
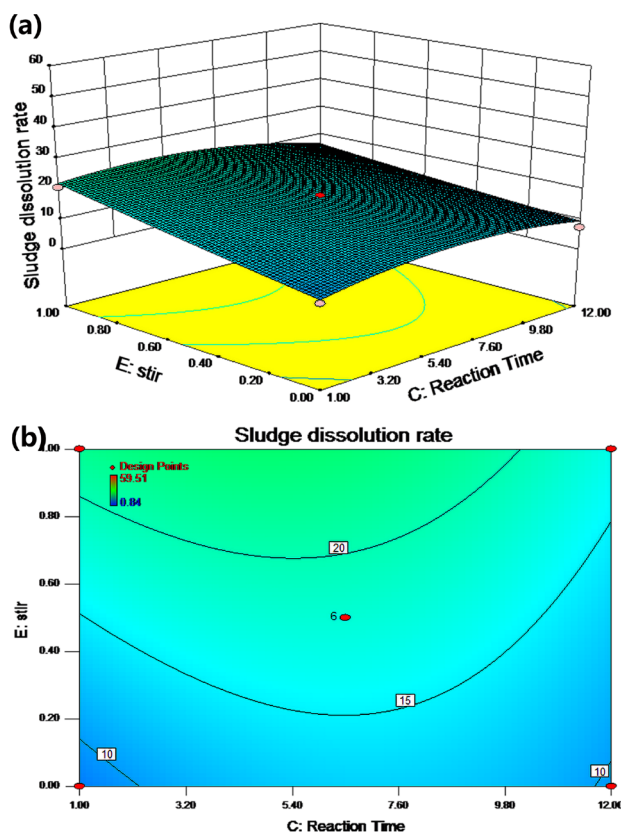
Figure 6. Response surface (a) and contour (b) maps: agitation conditions and reaction time
Source: Authors

Figures 2a and 2b show the effect of the interaction between temperature and reaction time on the residual sludge cell dissolution rate. A linear relationship with a relatively small slope between the cell dissolution rate and the reaction time was observed in the contour map. This indicated the insignificance of time, which was regarded as a secondary factor. A possible reason could be the dynamic equilibrium between the growth and decay of microorganisms over a relatively long period of time (Wang *et al.*, 2013). A weak interaction between temperature and reaction time can be observed in Figures 3 and 4, and an elliptic region indicates a cell dissolution rate of more than 18%, when the temperature was between 50 and 68 ˚C and the reaction time between 3,5 and 7,2 h.

The results indicate that the addition of a moderate amount of potassium ferrate could improve the cell dissolution

rate of sludge according to Figures 3a and 5a. However, based on the experimental observations, further addition of potassium ferrate (> 4 mg/g SS) does not increase the SCOD values. There were two possible mechanisms: (1) potassium ferrate oxidized the extracellular polymers of the sludge; or (2) potassium ferrate oxidized the cell membrane and reacted with some of the dissolved materials. When the oxidation and reaction processes were completed, the remaining potassium ferrate had nothing to react with. This explains why an excess dosage had no effect. Therefore, the optimal dosage of potassium ferrate was 4 mg/g SS when combined with other factors, such as temperature, pH, and reaction time.
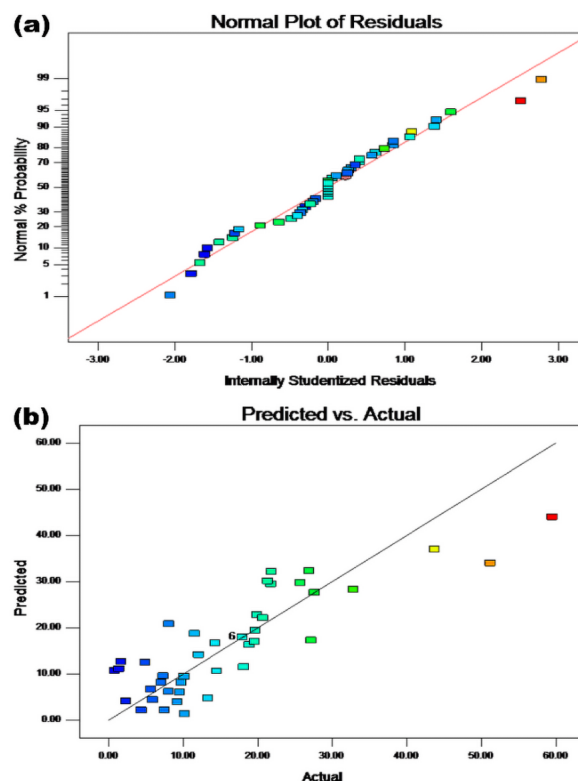
Figure 7. Residual plot (a) and fitting diagram of predicted *vs.* actual values (b)
Source: Authors

The effect of the interaction between the reaction time and the pH value on residual sludge cell dissolution rate is shown in Figure 2b. The results showed that the cell dissolution rate of the residual sludge increased with an increased pH value. The cell dissolution rate was above 20%, as shown in Figure 5a, when the pH value was relatively low and the amount of potassium ferrate additive was lower than 4,5 mg/g SS. The cell dissolution rate was not affected by the amount of potassium ferrate and the reaction time when the pH value was over 10. The rate was more than 30% according to Figures 2b and 5a. The influence of the reaction time on the excess sludge cell dissolution rate was not significant, which was similar to the results shown in Figures 1b and 6a. From the contour map and 3D diagram, the effect of the interaction between pH and reaction time was not significant –based on the numbers and color change. Therefore, the pH value played a vital role in this reaction process.

pH adjustment is one of the key procedures during the sludge pretreatment process because it can break flocculate and cells in the sludge within a very short period. When hydroxyl was added (the pH value was increased), lipids, carbohydrates, and proteins were degraded into small molecules, such as fatty acids, polysaccharides, and amino acids, thus reducing the solid parts of sludge. EPS could be dissolved under high alkalinity, and the process not only involved chemical degradation, but also the ionization of OH⁻, which caused EPS to swell and dissolve greatly (Zhang *et al.*, 2021). The microbial cell wall was destroyed when EPS was dissolved by strong alkalis, and a saponification process continued to react between the alkali and the lipids of the cell membrane. After the cell membrane dissolved, the intracellular materials and water were released from the cells. These could be utilized by other microbes. As a result, a higher pH value had an obvious effect on the cell dissolution rate, and the biochemical properties of the sludge improved (Chen *et al.*, 2013; Hong and Li, 2011; Kelessidis and Stasinakis, 2012).

Although there are few studies that explore the reduction of sludge via response surface models, especially with regard to pharmaceutical wastewater, this model involved five factors, which was much more than that of the solar photo-Fenton process, which has an error value of 6,91(Kavitha *et al.*, 2015). The mathematical model is helpful to find the optimal operation control conditions for the sludge reduction process. In addition, the error between the theoretical simulation value and the actual one was less than 6,34% with few dosages of potassium ferrate (1 mg/g SS), which meets the requirements of engineering applications. Therefore, this mathematical model can provide a processing method to reduce other kinds of sludge.

Conclusions

The sludge from a pharmaceutical wastewater treatment plant was treated in this study. The effects of temperature, pH adjustment, addition of potassium ferrate, time control, and stirring on sludge reduction were studied. By using the response surface method, a mathematical model was established. Based on the experimental data, the optimum experimental conditions were obtained by means of the mathematical model. At a temperature of 21,58 °C, as well as with a pH value of 4, a potassium ferrate dose of 1 mg/g SS, and a reaction time of 4,07 h with stirring, the cell dissolution rate of sludge reached 54,36% as predicted by the mathematical model. The triplicate cell dissolution rates of the residual sludge were 52,78, 55,12, and 51,02%. Thus, a high cell dissolution rate and a good sludge reduction effect were achieved in this study, and a relatively reliable mathematical model was established.

Acknowledgements

References

Capela, D., Ratola, N., Alves, A., and Homem, V. (2017). Volatile methylsiloxanes through wastewater treatment plants - A review of levels and implications. *Environment International, 102*, 9-29. https://doi.org/10.1016/j.envint.2017.03.005

Chakraborty, T., Balusani, D., Smith, S., Santore, D., Walton, J., Nakhla, G., and Ray, M. B. (2020). Reusability of recovered iron coagulant from primary municipal sludge and its impact on chemically enhanced primary treatment. *Separation and Purification Technology, 231*, 115894. https://doi.org/10.1016/j.seppur.2019.115894

Chen, M., Blanc, D., Gautier, M., Mehu, J., and Gourdon, R. (2013). Environmental and technical assessments of the potential utilization of sewage sludge ashes (SSAs) as secondary raw materials in construction. *Waste Management, 33*(5), 1268-1275. https://doi.org/10.1016/j.wasman.2013.01.004

Fang, C., Huang, R., Dykstra, C. M., Jiang, R., Pavlostathis, S. G., and Tang, Y. (2020). Energy and nutrient recovery from sewage sludge and manure via anaerobic digestion with hydrothermal pretreatment. *Environmental Science & Technology, 54*(2), 1147-1156. https://doi.org/10.1021/acs.est.9b03269

Fei, Y.-H., Zhao, D., Liu, Y., Zhang, W., Tang, Y.-Y., Huang, X., Wu, Q., Wang, Y.-X., Xiao, T., and Liu, C. (2019). Feasibility of sewage sludge derived hydrochars for agricultural application: Nutrients (N, P, K) and potentially toxic elements (Zn, Cu, Pb, Ni, Cd). *Chemosphere, 236*, 124841. https://doi.org/10.1016/j.chemosphere.2019.124841

Feria-Díaz, J. J., Polo-Corrales, L., and Hernández-Ramos, E. J. (2016). Evaluation of coagulation sludge from raw water treated with Moringa oleifera for agricultural use. *Ingeniería e Investigación, 36*(2), 14-20. https://doi.org/10.15446/ing.investig.v36n2.56986

Hong, J., and Li, X. (2011). Environmental assessment of sewage sludge as secondary raw material in cement production--a case study in China. *Waste Management, 31*(6), 1364-1371. https://doi.org/10.1016/j.wasman.2010.12.020

Hu, Y., and Gao, Z. (2020). Sewage sludge in microwave oven: A sustainable synthetic approach toward carbon dots for fluorescent sensing of para-Nitrophenol. *Journal of Hazardous Materials, 382*, 121048. https://doi.org/10.1016/j.jhazmat.2019.121048

Kavitha, S., Karthika, P., Rajesh Banu, J., Yeom, I. T., and Adish Kumar, S. (2015). Enhancement of waste activated sludge reduction potential by amalgamated solar photo-Fenton treatment. *Desalination and Water Treatment, 57*(28), 13144-13156. https://doi.org/10.1080/19443994.2015.1055810

Kelessidis, A., and Stasinakis, A. S. (2012). Comparative study of the methods used for treatment and final disposal of sewage sludge in European countries. *Waste Management, 32*(6), 1186-1195. https://doi.org/10.1016/j.wasman.2012.01.012

Mazeed, A., Lothe, N. B., Kumar, A., Sharma, S. K., Srivastav, S., and Verma, R. K. (2020). Evaluation of phytoaccumulation potential of toxic metals from sewage sludge by high-value aromatic plant geranium. *Journal of Environmental Biology, 41*(4), 761-769. https://doi.org/10.22438/jeb/41/4/MRN-1210

Pabón, S. L., and Gelvez, J. H. S. (2009). Starting-up and operating a full-scale activated sludge system for slaughterhouse wastewater. *Ingeniería e Investigación, 29*(2), 53-58. https://doi.org/10.15446/ing.investig.v29n2.15161

Poot, V., Hoekstra, M., Geleijnse, M. A. A., van Loosdrecht, M. C. M., and Pérez, J. (2016). Effects of the residual ammonium concentration on NOB repression during partial nitritation with granular sludge. *Water Research, 106*, 518-530. https://doi.org10.1016/j.watres.2016.10.028

Wang, Z., Yu, H., Ma, J., Zheng, X., and Wu, Z. (2013). Recent advances in membrane bio-technologies for sludge reduction and treatment. *Biotechnology Advances, 31*(8), 1187-1199. https://doi.org/10.1016/j.biotechadv.2013.02.004

Wilson, C. A., and Novak, J. T. (2009). Hydrolysis of macromolecular components of primary and secondary wastewater sludge by thermal hydrolytic pretreatment. *Water Research, 43*(18), 4489-4498. https://doi.org/10.1016/j.watres.2009.07.022

Wu, P., Pi, K., Shi, Y., Li, P., Wang, Z., Zhang, H., Liu, D., and Gerson, A. R. (2020). Dewaterability and energy consumption model construction by comparison of electro-dewatering for industry sludges and river sediments. *Environmental Research, 184*, 109335. https://doi.org/10.1016/j.envres.2020.109335

Xia, H., Wu, Y., Chen, X., Huang, K., and Chen, J. (2019). Effects of antibiotic residuals in dewatered sludge on the behavior of ammonia oxidizers during vermicomposting maturation process. *Chemosphere, 218*, 810-817. https://doi.org/10.1016/j.chemosphere.2018.11.167

Xiao, K., Chen, Y., Jiang, X., Seow, W. Y., He, C., Yin, Y., and Zhou, Y. (2017). Comparison of different treatment methods for protein solubilisation from waste activated sludge. *Water Research, 122*, 492-502. https://doi.org/10.1016/j.watres.2017.06.024

Yuan, Y., Yu, Y., Xi, H., Zhou, Y., and He, X. (2019). Comparison of four test methods for toxicity evaluation of typical toxicants in petrochemical wastewater on activated sludge. *Science of the Total Environment, 685*, 273-279. https://doi.org/10.1016/j.scitotenv.2019.05.389

Zeng, Q., Zan, F., Hao, T., Biswal, B. K., Lin, S., van Loosdrecht, M. C. M., and Chen, G. (2019). Electrochemical pretreatment for stabilization of waste activated sludge: Simultaneously enhancing dewaterability, inactivating pathogens and mitigating hydrogen sulfide. *Water Research, 166*, 115035. https://doi.org/10.1016/j.watres.2019.115035

Zhang, W., Tang, M., Li, D., Yang, P., Xu, S., and Wang, D. (2021). Effects of alkalinity on interaction between EPS and hydroxy-aluminum with different speciation in wastewater sludge conditioning with aluminum based inorganic polymer flocculant. *Journal of Environmental Sciences, 100*, 257-268. https://doi.org/10.1016/j.jes.2020.05.016

Zheng, M., Li, Y., Ping, Q., and Wang, L. (2019). MP-UV/CaO2 as a pretreatment method for the removal of carbamazepine and primidone in waste activated sludge and improving the solubilization of sludge. *Water Research, 151*, 158-169. https://doi.org/10.1016/j.watres.2018.11.086

Zittel, R., da Silva, C. P., Domingues, C. E., Seremeta, D. C. H., da Cunha, K. M., and de Campos, S. X. (2020). Availability of nutrients, removal of nicotine, heavy metals and pathogens in compounds obtained from smuggled cigarette tobacco compost associated with industrial sewage sludge. *Science of the Total Environment, 699*, 134377. https://doi.org/10.1016/j.scitotenv.2019.134377

Devolatilization of African Palm (*Elaeis guineensis*) Husk Catalyzed by Ferrous Sulfate Studied by TG-MS

Devolatilización del cuesco de palma (*Elaeis Guineensis*) catalizado con sulfato ferroso estudiado por TG-MS

Alberto R. Albis-Arrieta [1], María C. Romero-Castilla [2], Ever Ortiz-Muñoz [3], Ismael E. Piñeres-Ariza [4], and Edgar F. Donado-Medina [3]

ABSTRACT

By means of a thermogravimetric analysis coupled with mass spectroscopy, the catalytic effect of ferrous sulfate on the pyrolysis of African Palm husk (APH) was studied. Thermogravimetric data were adjusted to the distributed activation energy model (DAEM) with four pseudo-components. Ferrous sulfate had a strong influence on the decomposition parameters of the second and fourth pseudo-components of the DAEM, which are identified as hemicellulose and lignin, respectively. The profiles of the signal intensity curves for the selected m/z ratios were successfully modeled using the kinetic parameters obtained by adjusting the thermogravimetric data. It was found that ferrous sulfate promotes the formation of fragments of m/z = 64, 95, and 96, corresponding to molecules, such as SO_2, hydrocarbon ions of general formula $[CnH2n-3]+$, and furfural, respectively.

Keywords: TG-MS, catalytic pyrolysis, ferrous sulfate, African Palm husk

RESUMEN

Mediante el análisis termogravimétrico acoplado a espectroscopía de masas, se estudió el efecto catalítico del sulfato ferroso sobre pirólisis del cuesco de Palma Africana (APH). Los datos termogravimétricos se ajustaron al modelo de energía de activación distribuida (DAEM, por sus siglas en inglés) con cuatro pseudocomponentes. El sulfato ferroso tuvo una fuerte influencia en los parámetros de descomposición del segundo y cuarto pseudocomponente del DAEM, que se identifican como hemicelulosa y lignina respectivamente. Los perfiles de las curvas de intensidad de la señal para las relaciones m/z seleccionadas se modelaron con éxito utilizando los parámetros cinéticos obtenidos del ajuste de los datos termogravimétricos. Se encontró que el sulfato ferroso promueve la formación de fragmentos de m/z = 64, 95 y 96, que corresponden a moléculas como SO_2, iones hidrocarburos de fórmula general $[CnH2n-3]+$ y furfural respectivamente.

Palabras clave: TG-MS, pirólisis catalítica, sulfato ferroso, cuesco de Palma Africana

Introduction

Global energy consumption has increased considerably in recent years due to the substantial growth of the global population and industrial development. As a result, the demand for transportation fuels has significantly increased (Bhoi *et al.*, 2020). The development of renewable energy has played an important role in meeting demands and mitigating the dependence on fossil fuels, as they are non-renewable and unsustainable and their use increases the emissions of greenhouse gases (GHG) into the atmosphere, which causes global climate change. Residual biomass has great potential for use in the synthesis of renewable energies because it is found in large quantities, it is available and cheap, and it is ecological and sustainable (Rasid *et al.*, 2020).

Several mechanisms exist through which biomass can be converted into renewable energy sources, such as gasification to produce gaseous fuels or pyrolysis or hydrothermal liquefaction to generate liquid fuels. Pyrolysis can be carried out at ambient pressure. As a result, biomass transformation

[1] Chemical engineer, Universidad Nacional de Colombia, Colombia. Dr. Sc. Chemistry, Universidad Nacional de Colombia, Colombia. Affiliation: Associate Professor, Universidad del Atlántico, Colombia. E-mail: albertoalbis@uniatlantico.edu.co

[2] Chemical engineer, Universidad del Atlántico. E-mail: mceciliaromero@mail.uniatlantico.edu.co

[3] Physics graduate, Universidad Pedagógica de Colombia, Colombia. M.Sc. Physics, Universidad del Valle, Colombia. Dr.Sc. Physics, Universidad del Valle, Colombia. Affiliation: Full Professor, Universidad del Atlántico, Colombia. E-mail: everortiz@uniatlantico.edu.co

[4] Physics graduate, Universidad del Atlántico, Colombia. M.Sc. Physics, Universidad del Atlántico, Dr.Sc. Physics, Universidad del Atlántico, Colombia. Affiliation: Assistant Professor, Universidad del Atlántico, Colombia. E-mail: ismaelpineres@mail.uniatlantico.edu.co

[5] Chemical Engineer, Universidad del Atlántico. E-mail: edgardonado@ingenieros.com.

into liquid fuels through pyrolysis has become very attractive (Hu and Gholizadeh, 2019). Pyrolysis is the thermochemical decomposition of biomass in the absence of oxygen at temperatures between 300 and 700 °C. From this process, liquid bio-oil, non-condensable gases, and solid biochar are obtained (Brassard et al., 2017). Non-condensable gases can be used to provide energy to the pyrolysis process. Catalytic Fast Pyrolysis (CFP) is commonly used to transform biomass into high-quality bio-oil, deoxygenating the H_2O, CO, and CO_2 vapors formed during the process (Chen et al., 2019).

Oil palm (Elaeis guineensis) is the world's main source of vegetable oil, and it is produced principally by Malaysia and Indonesia. Oil palm industry residues constitute the biggest source of biomass in Malaysia, produced in large quantities throughout the year, but only a small fraction is converted into value-added products. Colombia is the second largest producer outside Southeast Asia and the largest producer in South and Central America (Onoja et al., 2019; Rivera-Méndez et al., 2017). African Palm Husk (APH) is produced as a result of the extraction of palm oil and is a biomass available in large quantities to be transformed. Many efforts have been made to take advantage of solid waste from the palm oil industry. Some studies involve the pyrolysis of this biomass using TG-MS, catalytic pyrolysis with low-cost catalysts, conversion of oil palm biomass to hydrogen via gasification reaction in supercritical water, metal oxide-catalyzed hydrothermal liquefaction of oil palm biomass, among others (Salema et al., 2019; Ro et al., 2018; Kelly-Yong et al., 2007; Yim et al., 2017).

It has become essential to know the effect of heavy metals as catalysts in the pyrolysis of metal-impregnated biomass, as well as their distribution in pyrolysis products, in order to find a suitable way of using them (Han et al., 2018). The effect of metallic salts as catalysts in this process has been studied by several authors (Zhao et al., 2017; Cao et al., 2020). Moreover, metal (Ru/Fe) impregnated banana pseudo-stem (Kumar et al., 2019), and copper and iron salts as additives in wood pyrolysis (Edye et al., 1992) have been studied.

Due to its advantages, biomass has gained interest as a green renewable energy. Lignocellulosic biomass is composed of cellulose (32-45%), hemicellulose (19-25%), and lignin (14-26%), which usually makes for very complex thermal decomposition profiles (Kaur et al., 2018; Han et al., 2018). The combination of thermogravimetric analysis coupled with mass spectrometry (TGA-MS) appears to provide a deeper insight into the identification and quantification of devolatilization products. One of the main advantages of TGA-MS is that it can afford real-time and sensitive detection of evolved gases, which is an important and often difficult task in many thermal applications (Malika et al., 2016).

In this work, the effect of $FeSO_4$ as a catalyst on the devolatilization kinetics of APH and its product distribution at 10 and 100 K/min heating rates were studied using the TG-MS simultaneous analysis technique, as a continuation

of a previous study on APH devolatilization by TG-MS in the absence of a catalyst (Albis et al., 2018). Kinetics parameters obtained using TGA were fitted to the Distributed Activation Energy Model (DAEM).

Methodology

Materials

The APH was obtained from a biodiesel plant in the municipality of Santa Marta, Magdalena, Colombia. Biomass was ground (particle size < 200 mm) and stored in a desiccator for further use.

Sample preparation

An aqueous solution of $FeSO_4$ was prepared by dissolving 2 000 g of the salt at 75% in 100 ml of water to obtain a final concentration of 15 mg Fe/ml. The prepared APH was added to the solution in the adequate volume, and the suspension was stirred for 2 h. Then, the sample was dried at 80 °C for 2 h, and thereafter for 2 h at 105 °C. The final concentration of $FeSO_4$ in the biomass was 1,5% by weight.

Thermogravimetric Analysis (TGA)

Thermogravimetric analysis was performed using a TA instruments TGA 2950 thermogravimetric analyzer. Control and acquisition of experimental data were carried out via the Universal Analysis software. The procedure for this analysis was the same as that used in the previous study (Albis et al., 2018).

Distributed Activation Energy Model

The DAEM is a multiple reaction model widely used in the pyrolysis of lignocellulosic biomass. This model assumes that the decomposition mechanism takes a large number of independent, parallel, first-order, or n^{th}-order reactions with different activation energies, reflecting variations in species' bond strengths. The difference in activation energies can be represented by a continuous distribution function (Cai et al., 2014). As described in Albis et al. (2018), in this model, the mass conversion rate is represented by several numbers of reactions that share the same frequency factor (A_j), with an activation energy distributed in Gaussian form. A media activation energy E_{0j} and a standard deviation of the activation energy (σ_j) are part of the model represented by Equations (1) and (2).

$$Y^{calc}(t) = -\sum_{j=1}^{M} c_j \frac{dx_j}{dt} \qquad (1)$$

Where, according to Albis et al. (2018):

Y^{calc} represents the conversion rate of the sample or signal strength, M is the number of reactions or pseudo-

components of the sample, c_j is a proportionality constant, x_j is the unreacted fraction of the material represented by the j-th kinetic equation, and $\frac{dx_j}{dt}$ is the rate of production or consumption of j, which can be calculated as:

$$\frac{dx_j}{dt}(t) = \frac{1}{2\sqrt{\pi}} \int_{-\infty}^{\infty} exp\left[\mu_j^2\right] exp\left[0,75\left|\,\left|\mu_j^2\right|\right.\right] \frac{dx_j(t,\mu_j)}{dt} d\mu_j \quad (2)$$

where $\mu_j = 2\left(E - E_{0j}\right)/\left(\sqrt{2}\sigma_j\right)$ and $X_j(t,\mu_j)$ are the solution for dx_j/dt at time t, and the value of the energy of activation is E.

Equation (2) was solved using MATLAB, as described by Albis *et al.* (2014).

Results

Thermogravimetric Analysis (TGA)

The TG and DTG of the samples of APH and APH + 1% FeSO$_4$ at temperature rates of 10 and 100 K/min are shown in Figures 1a and 1b, respectively. In Figure 1, four events are observed: the first is related with water release at temperatures below 393 K; the second, at temperatures between 393 and 475 K, which approximately corresponds to the first thermal decomposition; followed by the main pyrolytic event, which shows two peaks; and, finally, the last event is a slow-rate decomposition.

In Figure 1a, a displacement to the right with increased heating rate from 10 to 100 K/min is noted in the thermogram in both cases, *i.e.*, in the absence and presence of the catalyst, related to a small increase in sample weight loss. A similar percentage of char reported in the absence of the catalyst (Albis *et al.*, 2018) was also observed in its presence, which is within the limits of experimental uncertainty. This means that the presence of the catalyst does not affect the percentage of carbonization at either of the two heating rates evaluated.

In the main pyrolytic event, the first peak is associated with hemicellulose decomposition, and the second one with the disintegration of cellulose. In Figure 1b, a difference in the formation of peaks in the presence of FeSO$_4$ is observed, which is related to an increase in the second pseudo-component (corresponding to hemicellulose) within the DTG peak. This peak is higher in the pyrolytic event than the hemicellulose peak for the APH pyrolysis in the absence of the catalyst at the heating rates studied.

The presence of FeSO$_4$ leads to a hemicellulose reduction in the DTG peak temperature at heating rates of 10 and 100 K/min. This behavior suggests a catalytic effect that causes the pyrolytic process to start earlier. In previous studies, it was found that the promoting effects of FeSO$_4$ were noticeable in the hydrolysis of microcrystalline cellulose –an 84,14% conversion was obtained. It was also found that

the depolymerization and hydrolysis of biomass remains active in the presence of metals that lower the degradation temperature of the biomass (Tao *et al.*, 2010). This shows the capability of catalysts of initiating pyrolysis reactions at lower temperatures.
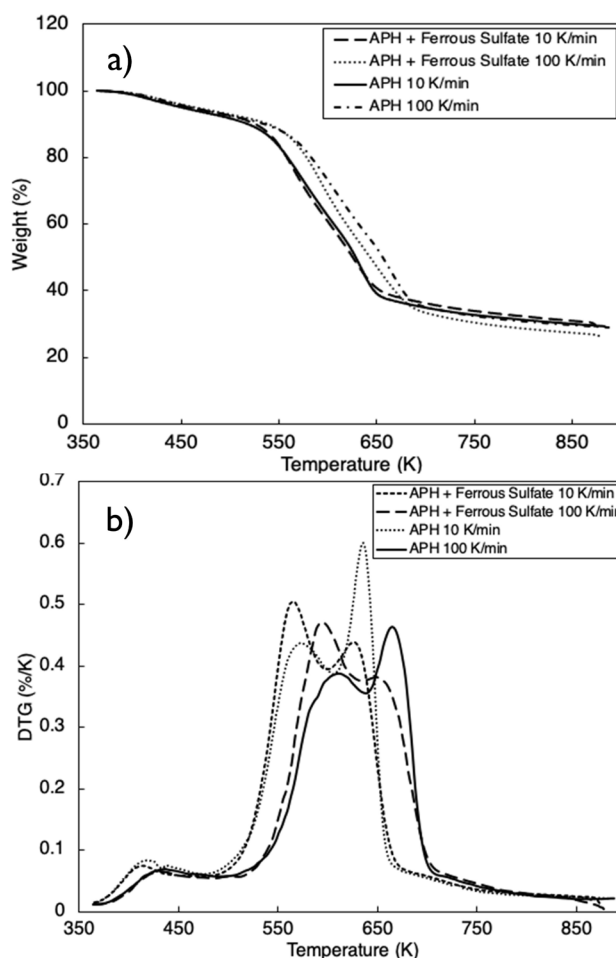
Figure 1. a) TG and b) DTG thermograms of APH and APH + 1% FeSO$_4$ at heating rates of 10 and 100 K/min, respectively
Source: Authors

Fitting to the DAEM

In Figure 2, the fitting of the DAEM in the presence of the catalyst at heating rates of 10 and 100 K/min is shown. Given the number of peaks, Figure 1b suggests the use of at least four pseudo-components. Consequently, the DAEM with four pseudo-components is used to illustrate the experimental data in this study.

The fitting of the data regarding the conversion rate to the DAEM with four pseudo-components for pyrolysis of APH with FeSO$_4$ heated at 10 and 100 K/min is shown in Table 1. In comparison with a previous study (Albis *et al.*, 2018), the results in Table 1 show that the catalytic effect of FeSO$_4$ affects mainly the second and fourth pseudo-components, identified as hemicellulose and lignin, reducing their average activation energies and their corresponding standard deviations. This behavior explains the reduced starting

temperature for the pyrolysis process of APH in the presence of a catalyst: reduction of the activation energy increases the decomposition rate of these compounds, and reduction in the standard deviations of the activation energy causes these components to have a narrow temperature range. For the third pseudo-component, identified as cellulose, the catalytic effect of $FeSO_4$ enhances the standard deviation of the activation energy, which produces a broad temperature range. Moreover, the proportionality constant decreased for the first, second, and third pseudo-components, but increased for the fourth one. On the other hand, the values of the frequency factors remained within the range of values reported for all pseudo-components. Prior studies have reported the catalytic effects of $FeSO_4$ in the decomposition of lignin in wood pyrolysis (Edye et al., 1992), as well as the catalytic effects of ferric sulfate in hemicellulose pyrolysis (Albis et al., 2018).

Table 1. DAEM parameters with four pseudo-components for APH + 1,5% $FeSO_4$ at heating rates of 10 and 100 K/min

DAEM Parameter	Heating Rates	
	$\beta = 10\ K/min$	$\beta = 100\ K/min$
C_1	0,166	0,179
A_1	1,270E+15	1,270E+15
E_{01}	1,380E+05	1,380E+05
S_1	1,900E+04	1,900E+04
C_2	5,767E-01	6,864E-01
A_2	1,274E+14	1,274E+14
E_{02}	1,739E+05	1,733E+05
S_2	8,550E+03	1,082E+04
C_3	5,161E-01	3,964E-01
A_3	7,987E+14	7,987E+14
E_{03}	2,023E+05	2,013E+05
S_3	8,518E+03	6,269E+03
C_4	6,474E-01	6,573E-01
A_4	1,064E+14	1,064E+14
E_{04}	1,864E+05	1,863E+05
S_4	3,832E+04	3,833E+04
SE	4,359E-05	2,396E-04

Source: Authors

Figure 2. Fitting of the DAEM with four pseudo-components for APH + 1% $FeSO_4$ at a) 10 K/min and b) 100 K/min
Source: Authors

It was found that, in comparison with the previous study (Albis et al., 2018), the activation energy for the first pseudo-component (Ea = 1,38E+5 kJ/mol), identified as extractives, remained the same in the absence and presence of the catalyst for the heating rates studied. The activation energy for the second pseudo-component, identified as hemicellulose, went from Ea = 1,77E+05 kJ/mol in the absence of the catalyst to Ea = 1,739E+05 kJ/mol and Ea = 1,733E+05 kJ/mol in the presence of $FeSO_4$ at heating rates of 10 and 100 K/min, respectively. Furthermore, the activation energy for the third pseudo-component, identified as cellulose, went from Ea = 2,04E+05 kJ/mol in the absence of the catalyst to Ea = 2,023E+05 kJ/mol and Ea = 2,013E+05 kJ/mol in the presence of $FeSO_4$ at 10 and 100 K/min, respectively. The activation energy for the fourth pseudo-component, identified as lignin, went from Ea = 1,95E + 05 kJ/mol in the absence of the catalyst to Ea = 1,864E+05 kJ / mol and Ea = 1,863E+05 kJ/mol in the presence of $FeSO_4$ at 10 and 100 K/min, respectively. The decreased activation energy shows the catalytic effect of $FeSO_4$ on APH pyrolysis.

A previous study on pyrolysis of banana pseudo-stem found that, in comparison with raw biomass (Ea =116,22 kJ/mol), samples impregnated with $FeSO_4$ have a lower activation energy (Ea = 86,78 kJ/mol). The catalytic effect lowers the activation energy, thus enhancing the reaction rate with modified reaction pathways (Kumar et al., 2019).
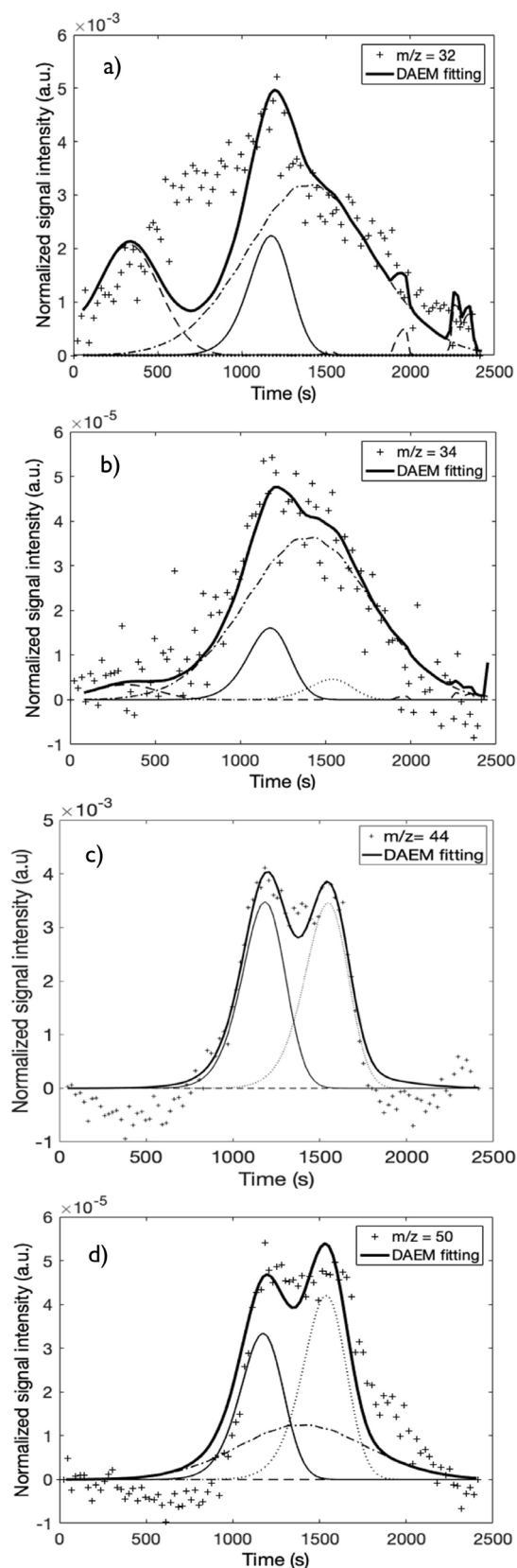
Figure 3. Fitting of the DAEM with four pseudo-components of selected m/z signal intensities: a) m/z = 32, b) m/z = 34, c) m/z = 44, d) m/z = 50 of APH + 1% $FeSO_4$ at a 10 K/min heating rate
Source: Authors
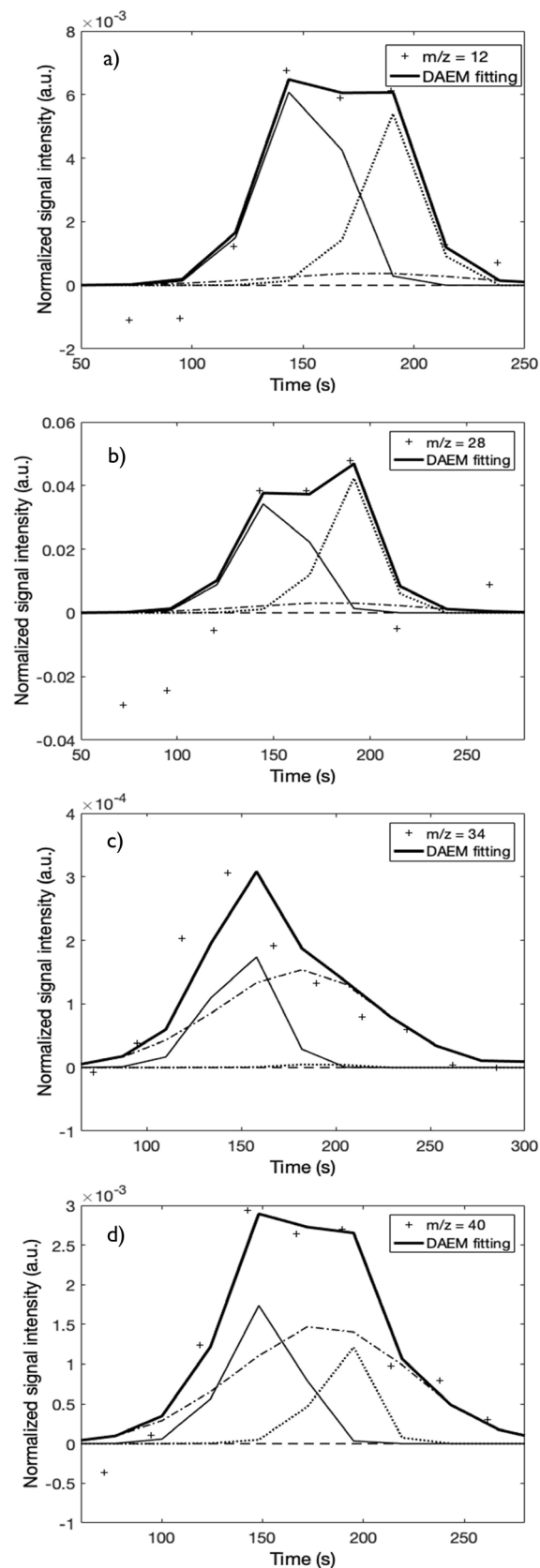
Figure 4. Fitting of the DAEM with four pseudo-components of selected m/z signal intensities: a) m/z = 12, b) m/z = 28, c) m/z = 34, d) m/z = 40 of APH + 1% $FeSO_4$ at a 100 K/min heating rate
Source: Authors

Mass spectrometry

Figures 3 and 4 show the fitting of the DAEM with four pseudo-components for some of the m/z ratios at heating rates of 10 and 100 K/min, respectively. The fit for all the m/z curves at the heating rates studied is supplied in the complementary material.

To analyze the effect of the catalyst, the data obtained at the 10-K/min heating rate is used because, due to the high speed, very few points were obtained in the areas of interest at 100 K/min (Figure 4). Table 2 shows the mass spectrometric intensities selected for kinetic evaluation and its presence in the main thermal events at heating rates of 10 and 100 K/min.

At the heating rate of 10 K/min, the fragments associated with m/z = 2, 16, 28, and 40 did not evolve during pyrolysis in the presence of the catalyst. The signal intensities m/z = 12, 14, 17, 32, 34, 44, 50, 51, 55, 58, 60, and 98 for APH pyrolysis in the presence of $FeSO_4$ were lower than the signals corresponding to the absence of the catalyst (Albis *et al.*, 2018). These signals were assigned to methane (m/z =12 and 14), water (m/z = 17), methanol (m/z = 32), hydrogen sulfide (m/z = 34), and carbon dioxide (m/z = 44). The fragments associated with m/z = 50 and 51 were assigned to furfural and benzene. m/z = 55 was assigned to cyclohexanone, 2(5H)-furanone, or 1,4-dimethylcyclohexane, C_3H3O^+. m/z = 58 was assigned to isobutane, propanal, acetone, or propanol. m/z = 60 was assigned to acetic acid, dodecanoic acid, hexadecanoic acid, or octadecanoic acid, and m/z = 98 was assigned to 1,2-cyclopentanedione, 4-methyl-5H-furan-2-one, 3-furanmethanol, or cyclohexanone.

In addition, the signal intensities of the m/z = 64, 95, and 96 ratios for APH pyrolysis in the presence of $FeSO_4$ were greater than those corresponding to the absence of the catalyst. This behavior suggests that $FeSO_4$ promotes the formation of these compounds. Signals were assigned to the production of $[SO_2]^+$ or $[SONH_2]^+$ (m/z = 64) (Kuehl and Rozynov, 2003), hydrocarbon ions of general formula $[C_nH_{2n-3}]^+$ (m/z = 95) (Mjøs, 2004), and furfural (m/z = 96) (Shen *et al.*, 2015). It has been reported that Fe, as a catalyst, removes the oxygenated compounds from the pyrolysis process, thus, improving bio-oil quality and, consequently, increasing the formation of hydrocarbons. Also, the aqueous solution contains aldehydes (Kumar *et al.*, 2019; Ansari and Gaikar, 2019).

Fitting mass spectrometry data to the DAEM

Tables 3 and 4 show the proportionality constant values (c_i) for the DAEM with four pseudo-components for the m/z signals detected regarding the pyrolysis of APH + 1% $FeSO_4$ at heating rates of 10 and 100 K/min.

When comparing these results to those of a previous study (Albis *et al.*, 2018), several observations can be made. In the absence of the catalyst, at a heating rate of 10 K/min, the fragments associated with m/z = 12, 17, 18, 60, and 95 were associated with the thermal decomposition of

hemicellulose, cellulose, and lignin. However, in the presence of the catalyst, these fragments were associated only with the thermal decomposition of hemicellulose and cellulose, with the contribution of the thermal decomposition of lignin being almost negligible. In the case of the fragments associated with m/z = 51, 55, and 96, the gases evolved were associated with hemicellulose, cellulose, and lignin decomposition with and without the catalyst. For the m/z ratios described, in the absence of the catalyst, the peak corresponding to the decomposition rate of hemicellulose is lower than that corresponding to the decomposition rate of cellulose. In contrast, in the presence of the catalyst, the peak corresponding to the decomposition rate of hemicellulose is higher than that corresponding to the decomposition rate of cellulose. This, except for m/z = 55, whose main event is associated with the thermal decomposition of lignin. This behavior coincides with the results obtained in the DTG curves described.

Table 2. m/z obtained for the kinetic study and its presence in the main thermal event at heating rates of 10 and 100 K/min

m/z	Component/ Fragment-molecule	10 K/min				100 K/min			
	Heating Rate	E	H	C	L	E	H	C	L
2	H_2	NA	NA	NA	NA	NA	NA	NA	NA
12	C	-	+	+	-	-	+	+	+
14	CH_4	-	+	-	+	-	+	+	+
16	CH_4	NA	NA	NA	NA	-	-	+	+
17	H_2O	-	+	+	-	-	+	+	+
18	H_2O	-	+	+	-	-	+	+	+
28	CO	NA	NA	NA	NA	-	+	+	+
30	formaldehyde	NA	NA	NA	NA	-	+	+	+
32	Methanol	+	+	-	+	+	+	-	+
34	H_2S	+	+	+	+	-	+	-	+
40	Furfural	NA	NA	NA	NA	-	+	+	+
42	Acetonitrile	NA	NA	NA	NA	-	+	+	+
44	CO_2	-	+	+	-	-	+	+	+
46	NO_2	NA	NA	NA	NA	+	+	+	+
50	Furfural; benzene	-	+	+	+	-	+	+	+
51	Furfural; benzene	-	+	+	+	-	+	+	+
52	Benzene	-	+	+	+	-	+	+	+
53	2-Furanmethanol; 5- Methyl-2-furancarboxaldehyde	-	+	+	+	-	+	+	+
54	4,4-dimethylcyclohexene	-	+	+	+	NA	NA	NA	NA
55	Cyclohexanone; 2(5H)-Furanone; 1,4-Dimethylcyclohexane,C3H3, O+	-	+	+	+	NA	NA	NA	NA
56	4,4-dimethylcyclohexene	-	+	+	+	-	+	+	+
58	Isobutane, propanal, acetone, propanol	-	+	+	+	-	+	-	+
60	Acetic acid; dodecanoic acid; hexadecanoic acid; octadecanoic acid	-	+	+	-	-	+	+	+
64	$[SO2]^+$ or $[SONH2]^+$	-	+	+	-	-	+	-	+
95	Hydrocarbon ions of general formula $[C_nH_{2n-3}]^+$	-	+	+	+	-	+	+	+
96	Furfural	-	+	+	+	-	+	+	+
98	1,2-Cyclopentanedione; 4- Methyl-5H-furan-2-one; 3- Furanmethanol; cyclohexanone	-	+	+	+	-	+	+	+

E= Extractives ; H= Hemicellulose ; C= Cellulose ; L= Lignin ; NA= Not-Applicable

Source: Authors

Table 3. Proportionality constants regarding the DAEM with four pseudo-components for m/z signals detected related with the pyrolysis of APH + 1% $FeSO_4$ at a 10 K/min heating rate

m/z	c_1	c_2	c_3	c_4
2	2,293E-01	8,275E-07	1,842E-01	3,901E-01
12	3,787E-07	1,657E-01	2,273E-01	1,078E-01
14	2,755E-07	9,183E-01	3,570E-02	2,531E
16	7,661E-08	1,509E-02	5,647E-02	6,413E-02
17	5,532E-08	1,270E-01	2,035E-01	1,331E-01
18	3,526E-06	6,935E-01	1,085E+00	7,248E-01
28	7,050E-01	5,420E-07	3,711E-01	1,583E+01
32	1,850E+00	1,394E+00	9,926E-07	5,853
34	3,026E-03	1,001E-02	2,905E-03	6,657E-02
40	1,003E-07	5,584E-02	7,001E-02	4,878E-02
44	8,693E-07	3,546E-04	6,111E-03	3,373E-03
50	2,910E-09	2,077E-02	2,652E-02	2,283E-02
51	7,650E-07	1,808E-02	2,421E-02	2,309E-02
52	9,952E-07	1,970E-02	2,564E-02	2,239E-02
53	4,267E-07	1,325E-02	4,181E-02	3,160E-02
54	4,776E-07	2,517E-02	3,990E-02	4,574E-02
55	3,458E-07	6,714E-02	5,892E-02	1,009E-01
56	3,370E-07	1,769E-02	3,343E-02	3,711E-02
58	5,504E-08	2,835E-02	5,870E-02	4,267E-02
60	1,240E-07	3,829E-01	1,204E-01	1,246E-04
64	2,974E-07	3,006E-02	5,171E-02	3,224E-04
95	1,588E-07	4,337E-02	1,397E-02	1,099E-02
96	1,263E-04	5,084E-02	1,748E-02	7,193E-03
98	9,529E-05	4,995E-04	4,085E-03	1,110E-02

Source: Authors

Table 4. Proportionality constants regarding the DAEM with four pseudo-components for m/z signals detected related with the pyrolysis of APH + 1% $FeSO_4$ at a 100 K/min heating rate

m/z	c_1	c_2	c_3	c_4
12	7,774E-07	5,769E-01	3,691E-01	8,162E-02
14	2,458E-07	1,917E	3,587E-01	1,971
16	1,830E-07	7,087E-03	5,504E-01	2,162
17	1,739E-06	4,934E	1,134	8,902
18	1,007E-05	1,816E+01	8,453	4,014E+01
28	3,953E-07	3,185	2,866	6,740E-01
32	4,660E-01	2,545E-01	1,649E-07	3,016
34	6,479E-08	1,563E-02	4,466E-04	3,253E-02
40	4,538E-07	1,503E-01	8,201E-02	3,152E-01
44	7,678E-06	4,174	2,958	4,253
50	5,237E-08	3,332E-02	1,433E-02	3,581E-02
51	2,871E-07	2,081E-02	8,129E-03	5,866E-02
52	1,321E-08	2,399E-02	8,875E-03	5,640E-02
53	1,187E-07	3,023E-02	2,094E-02	6,537E-02
54	2,888E-07	1,870E-02	1,912E-02	7,988E-02
55	6,239E-08	2,523E-02	1,166E-02	1,722E-01
56	3,994E-04	2,605E-02	5,213E-03	8,258E-02
58	7,451E-04	6,835E-02	7,989E-07	6,423E-02
60	2,261E-07	3,386E-01	7,752E-02	5,932E-02
64	1,177E-03	1,029E-01	2,436E-08	8,370E-02
95	9,348E-08	4,438E-02	8,566E-03	1,231E-02
96	1,557E-07	4,771E-02	9,458E-03	1,521E-02
98	1,150E-07	2,171E-03	8,642E-04	4,755E-03

Source: Authors

Moreover, in the absence of the catalyst, the fragments associated with the m/z = 14, 32, 34, 50, 64, and 98 were associated with the thermal decomposition of all major biomass components, extractives, hemicellulose, cellulose, and lignin. Similarly, in the presence of the catalyst, m/z = 32 was associated with the thermal decomposition of extractives, hemicellulose, cellulose, and lignin. However, for m/z = 64, the presence of $FeSO_4$ changed the m/z signal intensity profiles, and the evolution of this fragment was only associated with the thermal decomposition of hemicellulose and cellulose. In the presence of $FeSO_4$, m/z = 50, 34, and 98 were associated with the thermal decomposition of hemicellulose, cellulose, and lignin, but not extractives. Finally, the evolution of the fragment of ratio m/z = 14 was associated with the thermal decomposition only of hemicellulose and lignin in the presence of $FeSO_4$. For the aforementioned m/z ratios, in the absence of the catalyst, the peak corresponding to the decomposition rate of cellulose is higher than that corresponding to the decomposition of hemicellulose, which was higher than the peak corresponding to the decomposition of lignin. In contrast, in the presence of the catalyst, the peak corresponding to lignin decomposition is higher than those corresponding to hemicellulose and cellulose decomposition, with the contribution of the thermal decomposition of cellulose being smaller or negligible in some cases, except for m/z = 64 for which the contribution of the thermal decomposition of lignin is negligible.

For all m/z ratios, the catalytic effect of $FeSO_4$ on hemicellulose and lignin can be evidenced as a displacement to the left of the DAEM fit for the thermal decomposition of hemicellulose and lignin: the peaks go from being broad in the absence of the catalyst to becoming narrow in its presence. This means that decomposition occurs at lower temperatures (increasing the decomposition rate), and in a shorter period of time. Additionally, the thermal decomposition of cellulose in the absence of the catalyst occurs in a short period of time and it takes longer in its presence.

Conclusions

This work studied the effect of $FeSO_4$ on the APH pyrolysis process. It was found that the catalyst mainly affects the thermal decomposition of hemicellulose and lignin and that $FeSO_4$ promotes the formation of compounds for ratios m/z = 64, 95, and 96 –corresponding to fragments of molecules, such as SO_2, hydrocarbon ions of general formula $[C_nH_{2n-3}]^+$, and furfural, respectively– due to the iron deoxygenation effect, which improves hydrocarbon formation. The m/z ratios of the gases evolved in the presence of the catalyst were compared with the signals corresponding to its absence. A difference in the formation of peaks shows an effect on the rate of production in the presence of $FeSO_4$, thus increasing the decomposition rate in the case of hemicellulose and lignin, and decreasing it in the case of cellulose.

References

Albis A., A. R., Muñoz, E. O., Ariza, I. P., Suárez-Escobar, A. F., and Ariza-Barraza, C. S. (2018). TG characterization of pyrolysis of cassava starch residues catalyzed by ferric sulfate. *Contemporary Engineering Sciences*, *11*(72), 3587-3597. https://doi.org/10.12988/ces.2018.87365

Albis, A., Ortiz, E., Piñeres, I., Suárez, A., and Vanegas, M. (2018). Devolatilization of African Palm (*Elaeis guineensis*) Husk studied by TG-MS. *Ingeniería e Investigación*, *38*(2), 9. https://doi.org/10.15446/ing.investig.v38n2.67743

Albis, A., Ortiz, E., Suárez, A., and Piñeres, I. (2014). TG/MS study of the thermal devolatization of Copoazú peels (*Theobroma grandiflorum*). *Journal of Thermal Analysis and Calorimetry*, *115*(1), 275-283. https://doi.org/10.1007/s10973-013-3227-8

Ansari, K. B., and Gaikar, V. G. (2019). Investigating production of hydrocarbon rich bio-oil from grassy biomass using vacuum pyrolysis coupled with online deoxygenation of volatile products over metallic iron. *Renewable Energy*, *130*, 305-318. https://doi.org/10.1016/j.renene.2018.06.052

Bhoi, P. R., Ouedraogo, A. S., Soloiu, V., and Quirino, R. (2020). Recent advances on catalysts for improving hydrocarbon compounds in bio-oil of biomass catalytic pyrolysis. *Renewable and Sustainable Energy Reviews*, *121*, 109676. https://doi.org/10.1016/j.rser.2019.109676

Brassard, P., Godbout, S., Raghavan, V., Palacios, J. H., Grenier, M., and Zegan, D. (2017). The production of engineered biochars in a vertical auger pyrolysis reactor for carbon sequestration. *Energies*, *10*(3), 288. https://doi.org/10.3390/en10030288

Cai, J., Wu, W., and Liu, R. (2014). An overview of distributed activation energy model and its application in the pyrolysis of lignocellulosic biomass. *Renewable and Sustainable Energy Reviews, 36*, 236-246. https://doi.org/10.1016/j.rser.2014.04.052

Cao, Z., Niu, J., Gu, Y., Zhang, R., Liu, Y., and Luo, L. (2020). Catalytic pyrolysis of rice straw: Screening of various metal salts, metal basic oxide, acidic metal oxide and zeolite catalyst on products yield and characterization. *Journal of Cleaner Production*, *269*, 122079. https://doi.org/10.1016/j.jclepro.2020.122079

Chen, X., Che, Q., Li, S., Liu, Z., Yang, H., Chen, Y., Wang, X., Shao, J., and Chen, H. (2019). Recent developments in lignocellulosic biomass catalytic fast pyrolysis: Strategies for the optimization of bio-oil quality and yield. *Fuel Processing Technology*, *196*, 106180. https://doi.org/10.1016/j.fuproc.2019.106180

Edye, L. A., Richards, G. N., and Zheng, G. (1992). Transition metals as catalysts for pyrolysis and gasification of biomass. In M. Rashid Khan (Ed.), *Clean Energy from Waste and Coal* (pp. 90-101). ACS Publications. https://doi.org/10.1021/bk-1992-0515.ch008

Han, Z., Guo, Z., Zhang, Y., Xiao, X., Xu, Z., and Sun, Y. (2018). Pyrolysis characteristics of biomass impregnated with cadmium, copper and lead: Influence and distribution. *Waste and Biomass Valorization*, *9*(7), 1223-1230. https://doi.org/10.1007/s12649-017-0036-5

Hu, X., and Gholizadeh, M. (2019). Biomass pyrolysis: A review of the process development and challenges from initial researches up to the commercialisation stage. *Journal of Energy Chemistry*, *39*, 109-143. https://doi.org/10.1016/j.jechem.2019.01.024

Kaur, R., Gera, P., Jha, M. K., and Bhaskar, T. (2018). Pyrolysis kinetics and thermodynamic parameters of castor (*Ricinus communis*) residue using thermogravimetric analysis. *Bioresource Technology*, *250*, 422428. https://doi.org/10.1016/j.biortech.2017.11.077

Kelly-Yong, T. L., Lee, K. T., Mohamed, A. R., and Bhatia, S. (2007). Potential of hydrogen from oil palm biomass as a source of renewable energy worldwide. *Energy Policy*, *35*(11), 5692-5701. https://doi.org/10.1016/j.enpol.2007.06.017

Kuehl, D. W., and Rozynov, B. (2003). Chromatographic and mass spectral studies of perfluorooctanesulfonate and three perfluorooctanesulfonamides. *Rapid Communications in Mass Spectrometry, 17*(20), 2364-2369. https://doi.org/10.1002/rcm.1181

Kumar, A., Mylapilli, S. V. P., and Reddy, S. N. (2019). Thermogravimetric and kinetic studies of metal (Ru/Fe) impregnated banana pseudo-stem (*Musa acuminate*). *Bioresource Technology*, *285*, 121318. https://doi.org/10.1016/j.biortech.2019.121318

Malika, A., Jacques, N., Jaafar, E. F., Fatima, B., and Mohammed, A. (2016). Pyrolysis investigation of food wastes by TG-MS-DSC technique. *Biomass Conversion and Biorefinery*, *6*(2), 161-172. https://doi.org/10.1007/s13399-015-0171-9

Mjøs, S. A. (2004). The prediction of fatty acid structure from selected ions in electron impact mass spectra of fatty acid methyl esters. *European Journal of Lipid Science and Technology*, *106*(8), 550-560. https://doi.org/10.1002/ejlt.200401013

Onoja, E., Chandren, S., Abdul Razak, F. I., Mahat, N. A., and Wahab, R. A. (2019). Oil Palm (*Elaeis guineensis*) biomass in Malaysia: The Present and Future Prospects. *Waste and Biomass Valorization*, *10*(8), 2099-2117. https://doi.org/10.1007/s12649-018-0258-1

Rasid, N. S. A., Asadullah, M., Malek, N. H., and Amin, N. A. S. (2020). Fast pyrolysis of oil palm empty fruit bunch in an auger reactor: Bio-oil composition and characteristics. *IOP Conference Series: Materials Science and Engineering*, *736*(3), 1-11. https://doi.org/10.1088/1757-899X/736/3/032021

Rivera-Méndez, Y. D., Rodríguez, D. T., and Romero, H. M. (2017). Carbon footprint of the production of oil palm (*Elaeis guineensis*) fresh fruit bunches in Colombia. *Journal of Cleaner Production*, *149*, 743-750. https://doi.org/10.1016/j.jclepro.2017.02.149

Ro, D., Kim, Y. M., Lee, I. G., Jae, J., Jung, S. C., Kim, S. C., and Park, Y. K. (2018). Bench scale catalytic fast pyrolysis of empty fruit bunches over low cost catalysts and HZSM-5 using a fixed bed reactor. *Journal of Cleaner Production*, *176*, 298-303. https://doi.org/10.1016/j.jclepro.2017.12.075

Salema, A. A., Ting, R. M. W., and Shang, Y. K. (2019). Pyrolysis of blend (oil palm biomass and sawdust) biomass using TG-MS. *Bioresource Technology*, *274*, 439-446. https://doi.org/10.1016/j.biortech.2018.12.014

Shen, D., Zhang, L., Xue, J., Guan, S., Liu, Q., and Xiao, R. (2015). Thermal degradation of xylan-based hemicellulose under oxidative atmosphere. *Carbohydrate Polymers*, *127*, 363-371. https://doi.org/10.1016/j.carbpol.2015.03.067

Tao, F., Song, H., and Chou, L. (2010). Hydrolysis of cellulose by using catalytic amounts of FeCl2 in Ionic liquids. *ChemSusChem*, *3*(11), 1298-1303. https://doi.org/10.1002/cssc.201000184

Yim, S. C., Quitain, A. T., Yusup, S., Sasaki, M., Uemura, Y., and Kida, T. (2017). Metal oxide-catalyzed hydrothermal liquefaction of Malaysian oil palm biomass to bio-oil under supercritical condition. *Journal of Supercritical Fluids*, *120*(Part 2), 384-394. https://doi.org/10.1016/j.supflu.2016.05.044

Zhao, S., Liu, M., Zhao, L., and Lu, J. (2017). Effects of organic and inorganic metal salts on thermogravimetric pyrolysis of biomass components. *Korean Journal of Chemical Engineering*, *34*(12), 3077-3084. https://doi.org/10.1007/s11814-017-0209-8

Correlation between Electrical Conductivity and the Percentage of Fermented Beans for Peruvian CCN 51 Cocoa Beans

Correlación entre la conductividad eléctrica y el porcentaje de granos fermentados de granos de cacao peruano CCN 51

Jorge L.M. Loo-Miranda[1], Gabriela C. Chire-Fajardo [ID][2], and Milber O. Ureña-Peralta[3]

ABSTRACT

The objective of this study was to determine whether there is a relationship between electrical conductivity (EC) and the percentage of fermented beans (FB) of the CCN 51 cocoa bean cultivar. To this effect, the FB of three lots of cocoa beans fermented from 0 to 6 days was evaluated via the cut test method. In addition, the effect of the number of beans (15, 20, 25), the days of fermentation (0, 1, 2, 3, 4, 5, 6), and production lots (1, 2, 3) on the EC of whole and cut beans was evaluated ($p<0,05$). Then, EC values of 15, 20, and 25 of each presentation (whole or cut) of cocoa beans were correlated with their FB. An increase in FB from 0,00 to 89,70% was observed after six days of fermentation. The EC increased from 6,86 to 42,73 µS cm-1 g-1 in whole beans and from 38,45 to 63,16 µS cm^{-1} g^{-1} for cut beans as the fermentation progressed. There were no significant differences ($p<0,05$) between the EC of 15, 20, and 25 whole beans. On the other hand, there was a significant different ($p<0,05$) in EC of 15 cut beans in comparison to EC of 20 and 25 cut beans. Finally, it was concluded that there is a directly proportional linear relationship between the EC and the FB of cocoa beans, which is stronger for whole beans, with correlation coefficients of 0,963, 0,967, and 0,959 for 15, 20, and 25 beans, respectively.

Keywords: cocoa beans for chocolate, mathematical model, fermentation

RESUMEN

La presente investigación tuvo como objetivo determinar si existe alguna relación entre la conductividad eléctrica (CE) y el porcentaje de granos fermentados (GF) de granos de cacao varietal CCN 51. Para ello se evaluó el GF de tres lotes de granos de cacao con 0 a 6 días de fermentación mediante la prueba de corte. Además, se evaluó el efecto del número de granos (15, 20, 25), los días de fermentación (0, 1, 2, 3, 4, 5, 6) y los lotes producidos (1, 2, 3) en la CE de granos de cacao enteros y cortados ($p<0,05$). Luego se correlacionaron los valores de CE con 15, 20, 25 granos de cacao para cada presentación (cortados o enteros) con su GF. Se observó un incremento de GF de 0,00 a 89,70 % tras seis días de fermentación. La CE se incrementó desde 6,86 hasta 42,73 µS cm^{-1} g^{-1} en granos enteros y desde 38,45 hasta 63,16 µS cm-1 g-1 en granos cortados con el avance de la fermentación. No hubo diferencias significativas ($p<0,05$) entre la CE de 15, 20 y 25 granos enteros. En cambio, hubo una diferencia significativa ($p<0,05$) en la CE de 15 granos cortados en comparación con las de 20 y 25 granos. Finalmente se concluyó que existe una relación linear directamente proporcional entre la CE y el GF del grano de cacao, siendo más fuerte en los granos enteros, con índices de correlación de 0,963, 0,967 y 0,959 en 15, 20 y 25 granos, respectivamente.

Palabras clave: grano de cacao para chocolate, modelo matemático, fermentación

Introduction

Cocoa beans are the main raw material in chocolate manufacturing. The beans originate as seeds in fruit pods of the tree *Theobroma cacao,* which is cultivated in plantations in tropical regions around the world (Ardhana and Fleet, 2003). The quality of the cocoa beans determines their price: the better the quality, the higher the price. This quality is defined by a set of physical, chemical, and hygienic qualities, as well as those perceived by the senses (sensory qualities, such as the flavor and odor of the beans), which make them acceptable to the chocolate industry and the consumers (Aguilar, 2016).

[1] Food engineer, Universidad Nacional Agraria La Molina (UNALM), Faculty of Food Industry (FIAL), Peru. Cocoa and chocolate specialized professional. Email: jloomiranda@gmail.com

[2] Researcher and associate professor, Universidad Nacional Agraria La Molina (UNALM), Faculty of Food Industry (FIAL), Peru. Email: gchire@lamolina.edu.pe

[3] Researcher and full professor, Universidad Nacional Agraria La Molina (UNALM), Faculty of Food Industry (FIAL), Peru. Email: moup@lamolina.edu.pe

The fermentation of cocoa beans consists of heaping them together for several days in order to allow microorganisms to decompose the mucilage (the white sweet pulp surrounding the beans), increasing the temperature to produce the death of the embryo and initiate the biochemical changes and enzymatic reactions inside it, which will be responsible for the formation of the precursor compounds of chocolate flavor (Cubillos *et al.*, 2008). The higher the percentage of fermented beans and the lower the number of violet, slaty, and over-fermented beans, the better the flavor of the cocoa, which will also be more pleasant. This results in cocoa that is less acidic, less astringent, and less bitter or free of undesirable flavors (Aguilar, 2016). To evaluate the degree of fermentation and determine the percentage of fermented beans (FB), a cut test is carried out. 300 beans are opened or cut lengthwise through the middle, so as to expose the maximum cut surface of cotyledons. Both halves of each bean are visually examined in full daylight or equivalent artificial light. Each defective type of bean is counted separately, and the result for each kind of defect is expressed as a percentage of the 300 beans examined (INACAL, 2016). This test identifies beans that are visibly moldy, slaty (*i.e.*, unfermented), infested, germinated, or flat (*i.e.*, containing no nib or cotyledon) (Beckett, 2017). However, the cut test is considered to have a low precision, as it depends on lighting quality and the evaluator's knowledge and visual perception of color. In addition, the color can change due to factors that favor oxidation such as storage time and prior moniliasis attacks (Aguilar, 2016).

Several methods to measure the degree of fermentation of cocoa beans have been proposed, such as the use of spectrophotometry (Gourieva and Tzerevitinov, 1979; Afoakwa *et al.*, 2012), the application of ^{1}H NMR spectroscopy combined with chemometrics (Caligiani *et al.*, 2014), the determination of ammonia nitrogen contents by near infrared spectroscopy or NIRS (Hue *et al.*, 2014), and a cocoa quality index (CQI) based on adaptations of the quality index developed for soils (Araujo *et al.*, 2014).

Electrical conductivity through an ionic solution is determined by means of the movement of ions. There are different factors that may affect electrical conductivity tests, namely the seed moisture content, which influences the leakage rate of the compounds; the soaking temperature, which greatly influences the amount of solutes leaking from seeds soaked in water; the length of the soaking period, since the leakage from the seeds first increases rapidly and then levels off; and the presence of empty seeds, given that abnormal seeds leak as much (or as little) as normal ones (Sorensen *et al.*, 1996). Some reports and conditions to measure electrical conductivity (EC) in seeds are: *Ricinus communis* L. with 220 μS/cm using distilled water with a 20-hour soaking time (Cárdenas-Ruiz, 2020); *Chenopodium quinoa* Wild from 227,8 to 298,0 uS cm^{-1}g^{-1} using 50 ml deionized water with a 2-hour soaking time (Farias-Menegaes, 2021); and *Solanum melongena* L. with electrolyte releases of 0,48 μScm^{-1}g^{-1} per hour for 100 seeds with a 6-hourimbibition time (Aramendiz-Tatis *et al.*, 2017).

This method can be adapted because it is based on checking the level of integrity of the cell membranes in the tissues that constitute the seeds. As the fermentation of the cocoa beans progresses, electrolytes develop, and these suffer a loss of cellular content when exposed to an aqueous medium, which produces an increase in the EC of the leachate.

To justify the use of the EC test, the main objective of this research was to determine whether there is a relationship between the EC values of cocoa bean leakage and their fermentation index.

Methodology

Ripe and healthy cocoa pods of the CCN 51 cultivar were used. These samples were obtained from the Uchiza district of the Tocache province in the region of San Martín. The ripe cocoa pods were harvested manually by making a clean cut through the stalk with a well sharpened blade. Then, the harvested pods were carefully cut with a machete while avoiding damaging the cocoa beans. The wet beans were removed from the cut pods by hand, separating the damaged beans. The healthy wet cocoa beans were placed in plastic containers and transported to wooden boxes, covering them in order to avoid external contaminants (dust, soil, leaves, insects, *etc.*)

The fermentation was carried out by filling a wooden box with 300 kg of wet cocoa beans, covering them with banana leaves and leaving them to ferment for six days. The bean mass was turned by transferring it from one box to another at 48, 72, 96, and 120 hours. 2 kg samples of beans were taken for each day of fermentation. The fermentation temperature was controlled by placing a thermometer 10 cm deep into the bean mass. The end of the fermentation was determined by measuring the pH of the grain (final pH = 5,5) which, added to the decrease in the fermentation temperature, indicated the end of the process (Portillo *et al.*, 2011). The fermentation was carried out in triplicate for each lot.

After each sampling time, the cocoa bean samples with 0, 1, 2, 3, 4, 5, and 6 days of fermentation were dried in the sun using wooden pallets with a polypropylene cover in order to avoid direct sunlight exposure. The thickness of the cocoa bean layer was 5 cm, and it was stirred with a wooden rake once every hour (so that the beans would not stick together) until the moisture content was between 6 and 7% (5-7 days). The samples of the dry cocoa beans with 0, 1, 2, 3, 4, 5, and 6 days of fermentation were packed in polyethylene bags and labeled, indicating the duration of fermentation and lot number.

Percentage of fermented beans (FB)

The FB was determined via the cut test, according to the Peruvian Technical Standard NTP - ISO 1114: 2011 (INACAL, 2016). A total of 300 beans were cut lengthwise through the middle in order to expose the maximum cut surface of

the cotyledons. Both halves were examined in full daylight and placed in one of the following categories: purple, pale purple, brown, slaty, germinated, and moldy. The value of the FB that represents the ratio of well-fermented (brown) beans with respect to the 300 beans analyzed in the cut test was calculated by means of Equation (1).

$$FB = \frac{number \quad of \quad brown \quad beans}{300 \quad beans} x \ 100 \quad (1)$$

Electrical conductivity (EC)

The EC test, adapted from Sorensen et al. (1996), was conducted on two presentations (whole and cut) and three quantities (15, 20, and 25) of cocoa beans. Cocoa beans were weighed in an analytical balance with a 0,01 g precision. Then, the beans were washed in deionized water for 10 s, placed into containers holding 400 ml of deionized water, and left to soak for a period of 24 h at 25 ˚C. As for the cut beans, a longitudinal cut was made with a scalpel before soaking. A control with 400 ml of deionized water accompanied each battery. The containers were covered during soaking in order to avoid the evaporation and contamination of deionized water. After soaking, the solution was homogenized, and the EC was measured with an Inolab Cond Level 2P conductivity meter. Finally, the EC of the cocoa beans was determined via Equation (2):

$$EC_B = \frac{EC_L - EC_C}{w} \quad (2)$$

where EC_B is the EC of cocoa bean ($\mu S \ cm^{-1} g^{-1}$), EC_L is the EC of the soak solution ($\mu S \ cm^{-1}$), EC_C is the EC of the deionized water ($\mu S \ cm^{-1}$), and w is the weight of the beans in grams.

Statistical analysis and experimental design

Statistical analysis was performed using the Statgraphics® Centurion XVII software. In the first phase, the effect of the duration of fermentation on the FB and EC of cocoa beans was studied. For FB, a randomized complete block design (RCBD) was used, where each lot (1, 2, and 3) represented a block. The study factor was the fermentation time (0, 1, 2, 3, 4, 5, and 6 days). Three replicates were carried out with a p-value < 0,05. The study of the EC of whole and cut beans was performed using a 3 x 7 x 3 factorial design with experimental factors such as the number of beans (15, 20, and 25), the days of fermentation (0, 1, 2, 3, 4, 5, and 6), and the lot number (1, 2, and 3). Three replicates were carried out with a p-value < 0,05. The data were subjected to the Tukey test for comparing the means between the number of beans, the days of fermentation, and the production lots.

In the second phase of this research, the data obtained for 15, 20, and 25 whole and cut beans of the three lots were studied, analyzing the correlation between the FB and EC of the cocoa beans. Here, the FB was defined as an independent or predictor variable, and the EC as a dependent or response variable. The EC values of the cocoa beans were subjected to an analysis of variance (ANOVA) in order to verify the existence of a statistically significant relationship with the FB, using a p-value < 0,05.

Results and discussion

The FB values of cocoa beans for each day of fermentation are presented in Figure 1. It can be observed that the FB increase has two stages. The first one stands out for a rapid increase from 0,00 to 46,37% in beans fermented for two days, possibly because the first two or three days of fermentation are characterized by a successive growth of various microorganisms (Ardhana and Fleet, 2003), whose intense metabolic activity causes biochemical reactions leading to a considerable increase in the percentage of fermented beans (Rivera et al., 2012). The second stage was characterized by a slow increase in the FB, from 46,37 to 89,70%, as the beans were fermented for more days. According to Schwan and Wheals (2004), on the third day of fermentation, the high temperatures reached by the cocoa mass cause the inhibition of acetic acid bacteria, resulting in a decrease in microbial activity.
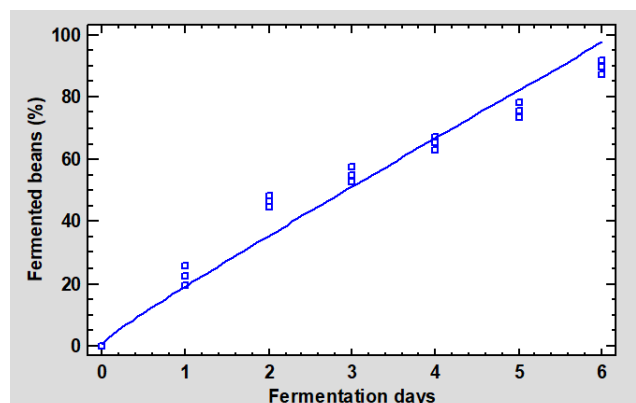
Figure 1. Variation of the FB of cocoa beans for each day of fermentation
Source: Authors

The beans fermented for four or more days reached a FB above 60%, which guarantees a good cocoa flavor development (Afoakwa et al., 2012). Otherwise, the products made with these beans would be bitter, astringent, or lacking the chocolate flavor (Jalil and Ismail, 2008).

The effect of the duration of fermentation on the EC value of cocoa beans, either whole or cut, was also evaluated. As seen in Figure 2, the EC of cocoa beans showed significant differences according to the duration of fermentation. In whole beans, the EC value increased from 6,86 $\mu S \ cm^{-1} g^{-1}$ (unfermented beans) to 42,73 $\mu S \ cm^{-1} g^{-1}$ (six days of fermentation), while, in cut beans, this value increased from 38,45 $\mu S \ cm^{-1} g^{-1}$ (unfermented beans) to 63,16 $\mu S \ cm^{-1} g^{-1}$ (six days of fermentation). Figure 3 shows a relationship between the EC of whole and cut cocoa beans and the FB. As the beans absorb water during imbibition, there is a rapid release of solutes such as sugars, organic

acids, ions, amino acids, and proteins into the surrounding medium (Ouyang *et al.*, 2002; Fessel *et al.*, 2006). In this sense, the amount of leached ions is inversely proportional to the integrity of the grain cell membranes (Arámendiz *et al.*, 2017). Therefore, the increase in the EC of cocoa beans indirectly reflects the extent of the damage caused to the cell membranes of the beans as a result of deterioration (Abreu *et al.*, 2011).
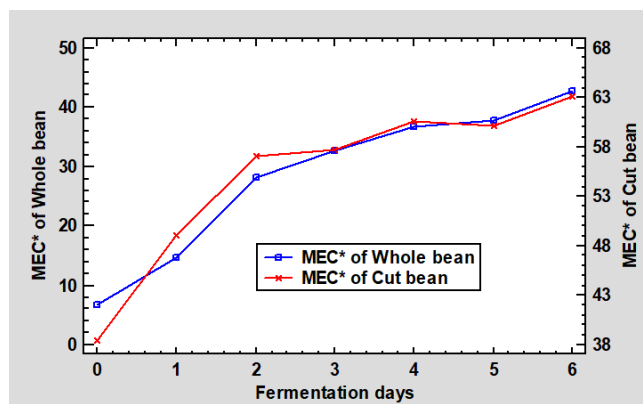
Figure 2. Variation of the EC of whole and cut cocoa beans for each day of fermentation. MEC* = Mean Electrical Conductivity (μS cm^{-1} g^{-1}).
Source: Authors
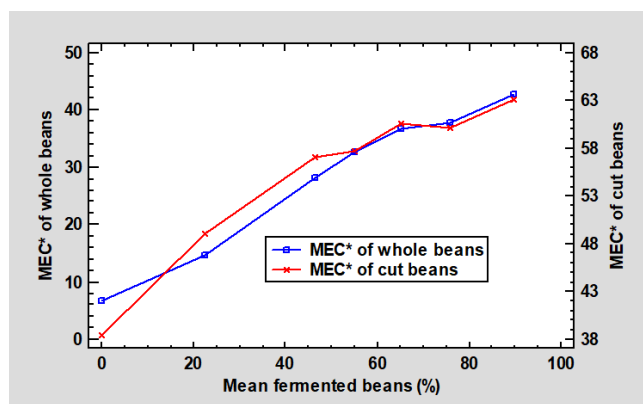
Figure 3. Variation of the EC of whole and cut cocoa beans regarding the FB. MEC* = Mean Electrical Conductivity (μS cm^{-1} g^{-1})
Source: Authors

The deterioration of the cotyledon of cocoa beans is a consequence of fermentation, since it contributes to structural changes such as the removal of the compartmentalization of enzymes and substrates with notable swelling and key changes in cell membranes which facilitate enzyme and substrate movements through the cocoa cotyledon (Afoakwa *et al.*, 2008). During drying, intracellular spaces (pores) previously occupied by water are replaced by air or are compressed as result of shrinkage (Zabalaga *et al.*, 2016), thus causing an increase in the number of damaged cells (de Brito *et al.*, 2000). Koua *et al.* (2017) report an increase in cocoa bean porosity from 15,82 to 24,67% with a decrease in moisture content. In other words, the volume of water removed was greater than the cocoa bean volume reduction during drying.

Everything seems to confirm that the increase in the EC value of cocoa beans is due to the rupture of the cotyledon cell walls as the fermentation progresses, which is consolidated with the increase in porosity during drying. As reported by Zambrano *et al.* (2010), regardless of whether it is a Criollo, Trinitario, or Forastero cocoa bean, if it is well fermented, the cotyledon will have cracked, which implies an increase in its permeability, and therefore in the number of leached electrolytes (dos Santos and de Paula, 2005).

The EC values of the cut beans were higher than whole beans since the maximum surface of cut beans cotyledons were exposed to deionized water. In addition, splitting cocoa beans in halves implies the rupture of their shell, which plays a fundamental role, given that its microstructure, thickness, and number of pores may affect the levels of leakage during imbibition, and therefore the value of EC (Borji *et al.*, 2007).

The effect of the number of beans used in the EC test was also evaluated for the same fermentation days (0 to 6). As shown in Table 1, the ANOVA demonstrated that there are statistically significant differences between using 15, 20, and 25 whole or cut cocoa beans. According to the results, increasing the number of beans slightly reduces the EC value. In fact, Brouwer and Mulder (1982) assure that, in a conventional conductivity test, a bean was surrounded by other leaching beans, which increased the local concentration of the leachate to high levels, thus slowing down the leaching process. Artola and Carrillo-Castañeda (2005) evaluated the effect of the number of birdsfoot trefoil seeds on the EC value without finding conclusive results, as increasing this number from 50 to 100 seeds caused an increase in the EC. However, when increasing the number from 200 to 1 000 seeds, there was a reduction in EC.

By means of Tukey's HSD test, it was determined that using 20 whole beans in EC test is statistically ($p<0,05$) equal to using 15 or 25 beans. In the case of cut beans, no statistically significant differences ($p<0,05$) were found between using 20 and 25 beans, unlike using 15 beans.

Table 1. Variation in the EC of whole and cut cocoa beans according to the number of beans used

Number of beans	Electrical conductivity (μS cm^{-1} g^{-1})	
	Whole bean	Cut bean
15	29,33 ± 12,75b	57,11 ± 8,47b
20	28,51 ± 12,78ab	54,72 ± 9,10a
25	27,77 ± 12,25a	53,67 ± 8,30a

Different letters in each column indicate significant differences ($p < 0,05$)
Source: Authors

It has been shown that the FB and EC of beans are influenced by the duration of fermentation. With the objective of obtaining a general model for each presentation (whole and cut) and the quantity of beans (15, 20, and 25) the reported values of the three lots were integrated. The linear models

obtained for whole and cut beans are presented in Table 2. The relationship between FB and EC was significant in all cases (p<0,05); it was strongly positive (0,8 ≤ r < 1) according to the classification established by Nieves and Domínguez (2009). The models describe a different increase in the EC of whole and cut beans as the fermentation progresses, perhaps because whole beans have a relatively intact husk at the beginning of the process, which limits the migration of ions to the solution, and, as deterioration progresses, the number of ions in the solution increases. In the case of cut beans, the migration of ions to the solution is more accentuated because the interior is more exposed, which results in a high EC value.

Table 2. Models of the correlation of the FB and the EC of cocoa beans with each presentation and number of beans

Bean presentation	Beans number	Intercept (a)	Slope (b)	Standard error	R	Significance (p<0,05)
	15	7,90	0,4232	3,48	0,963	*
Whole	20	6,93	0,4261	3,29	0,967	*
	25	7,25	0,4051	3,51	0,959	*
	15	43,85	0,2618	3,79	0,896	*
Cut	20	40,55	0,2798	4,16	0,891	*
	25	40,58	0,2585	3,59	0,903	*

Source: Authors

The standard statistical error obtained in whole bean models is lower (3,29-3,51) than that of cut bean models (3,59-4,16). Moreover, it expresses the deviation that the EC can have for an FB value in upper and lower limits.

It is worth mentioning that the variability left explained by the regression models is due to chance or the existence of hidden variables that influence the response variable (Nieves and Domínguez, 2009). In this research, the difference in the proportion of slate and purple beans at the same FB, as well as the difference in the degree of fermentation of each bean, could constitute some of these hidden variables.

There is a linear relationship between the EC of the beans and the FB, being stronger in the case of whole beans, which have a higher correlation coefficient and a lower standard error. Thus, the existence of a mathematical relationship between these two variables represents an opportunity to develop a quick and more analytical method to evaluate the degree of fermentation of cocoa beans.

Conclusions

Finding the number of whole and cut cocoa beans necessary for the determination of electrical conductivity in aqueous solutions –as well as the relationship between this electrical property and the percentage of fermented beans– opens the possibility of establishing a more effective method to determine the degree of fermentation reached, which surpasses the current cutting method.

References

Abreu, L. A. S., de Carvalho, M. L. M., Pinto, C. A. G., and Kataoka, V. Y. (2011). Teste de condutividade elétrica na avaliação de sementes de girassol armazenadas sob diferentes temperaturas. *Revista Brasileira de Sementes, 33*(4), 635-642. https://doi.org/10.1590/S0101-31222011000400005

Afoakwa, E.O., Paterson, A., Fowler, M., and Ryan, A. (2008). Flavor formation and character in cocoa and chocolate: A critical review. *Critical Reviews in Food Science and Nutrition, 48*(9), 840-857. https://doi.org/10.1080/10408390701719272

Afoakwa, E. O., Quao, J., Budu, A. S., Jemmy, S. T., and Saalia, F. K. (2012). Influence of pulp-preconditioning and fermentation on fermentative quality and appearance of Ghanaian cocoa (*Theobroma cacao*) beans. *International Food Research Journal, 19*(1), 127-133.

Aguilar, H. (2016). *Manual para la evaluación de la calidad del grano de cacao*. FHIA.

Arámendiz-Tatis, H., Cardona-Ayala, C., and Alzate-Román, K. (2017). Prueba de conductividad eléctrica en la evaluación de la calidad fisiológica de semillas en berenjena (*Solanum melongena* L.). *Scientia Agropecuaria, 8*(3), 225-231. https://doi.org/10.17268/sci.agropecu.2017.03.05

Araujo, Q. R., Fernandes, C. A. F., Ribeiro, D. O., Efraim, P., Steinmacher, D., Lieberei, R., Bastide, P., and Araujo, T. G. (2014). Cocoa Quality Index – A proposal. *Food Control, 46*, 49-54. https://doi.org/10.1016/j.foodcont.2014.05.003

Ardhana, M. M., and Fleet, G. H. (2003). The microbial ecology of cocoa bean fermentations in Indonesia. *International Journal of Food Microbiology, 86*(1-2), 87-99. https://doi.org/10.1016/S0168-1605(03)00081-3

Artola, A., and Carrillo-Castañeda, G. (2005). The bulk conductivity test for birdsfoot trefoil seed. *Seed Science and Technology, 33*(1), 231-236. https://doi.org/10.15258/sst.2005.33.1.23

Beckett, S. T. (2017). *Industrial chocolate manufacture and use*. John Wiley & Sons Inc.

Borji, M., Ghorbanli, M., and Sarlak, M. (2007). Some seed traits and their relationships to seed germination, emergence rate electrical conductivity in common bean (*Phaseolus vulgaris* L.). *Asian Journal Plant Sciences, 6*(5), 781-787. https://doi.org/10.3923/ajps.2007.781.787

Brouwer, H. M., and Mulder, J. C. (1982). Reduced steeping time for the conductivity vigor test of *Phaseolus vulgaris* L. seed. *Journal of Seed Technology, 7*(1), 84-96.

Caligiani, A., Palla, L., Acquotti, D., Marseglia, A., and Palla, G. (2014). Application of 1H NMR for the characterization of cocoa beans of different geographical origins and fermentation levels. *Food Chemistry, 157*, 94-99. https://doi.org/10.1016/j.foodchem.2014.01.116

Cárdenas-Ruiz, P. M. (2020). *Rangos de conductividad eléctrica para el análisis del poder germinativo de semillas provenientes de la colección de higuerilla (Ricinus communis L.)* [Undergraduate thesis, Universidad Central del Ecuador]. http://www.dspace.uce.edu.ec/handle/25000/21474

Cubillos, G., Merizalde, G. J., and Correa, E. (2008). *Manual del Beneficio del Cacao 2008 para: técnicos, profesionales del sector agropecuario y productores*. Secretaria de Agricultura de Antioquía.

de Brito, E. S., Pezoa, N. H., Gallão, M. I., Cortelazzo, A. L., Fevereiro, P. S., and Braga, M. R. (2000). Structural and chemical changes in cocoa (*Theobroma cacao* L.) during fermentation, drying and roasting. *Journal of the Science of Food and Agriculture, 81*(2), 281-288. https://doi.org/10.1002/1097-0010(20010115)81:2<281::AID-JSFA808>3.0.CO;2-B

dos Santos, S. R., and de Paula, R. C. (2005). Teste de condutividade elétrica para avaliação da qualidade fisiológica de sementes de Sebastiania commersoniana (bail) Smith & Downs –Euphorbiaceae. *Revista Brasileira de Sementes, 27*(2), 136-145. https://doi.org/10.1590/S0101-31222005000200020

Farias Menegaes, J., Denardi Munareto, J., Petter Medeiros , S. L., Russi Nunes, U., and Soares de Vasconcelos, E. (2021). Electrical conductivity test to assess vigor in quinoa seeds. *Research, Society and Development*, *10*(5), 14682. https://doi.org/10.33448/rsd-v10i5.14682

Fessel, S. A., Vieira, R. D., da Cruz, M. C. P., de Paula, R. C., and Panobianco, M. (2006). Electrical conductivity testing of corn seeds as influenced by temperature and period of storage. *Pesquisa Agropecuária Brasileira, 41*(10), 1551-1559. https://doi.org/10.1590/S0100-204X2006001000013

Gourieva, K. B., and Tzerevitinov, O. B. (1979). *Method of evaluating the degree of fermentation of cocoa beans* (*USSR Patent no. 646254*). https://patents.google.com/patent/SU646254A1/en

Hue, C., Gunata, Bergounhou, Z., A., Assemat, S., Boulanger, R., Sauvage, F. X., and Davrieux, F. (2014). Near infrared spectroscopy as a new tool to determine cocoa fermentation levels through ammonia nitrogen quantification. *Food Chemistry, 148*, 240-245. https://doi.org/10.1016/j.foodchem.2013.10.005

Jalil, A. M. M., and Ismail, A. (2008). Polyphenols in cocoa and cocoa products: Is there a link between antioxidant properties and health? *Molecules, 13*(9), 2190-2219. https://doi.org/10.3390/molecules13092190

Koua, B. K., Ekoun, P. M., and Gbaha, P. (2017). Evolution of shrinkage, real density, porosity, heat and mass transfer coefficients during indirect solar drying of cocoa beans. *Journal of the Saudi Society of Agricultural Sciences, 18*(1), 72-82. https://doi.org/10.1016/j.jssas.2017.01.002

Nieves, A., and Domínguez, F. (2009). *Probabilidad y estadística para ingeniería. Un enfoque moderno.* McGraw Hill Latinoamérica.

INACAL (2016). *NTP–ISO 1114:2016. Granos de cacao. Prueba de corte*. INACAL.

Ouyang, X., van Voorthuysen, T., Toorop, P. E., and Hilhorst, H. W. M. (2002). Seed vigor, aging, and osmopriming affect anion and sugar leakage during imbibition of maize (*Zea mays* L.) caryopses. *International Journal of Plant Sciences, 163*(1), 107-112. https://doi.org/10.1086/324550

Portillo, E., Labarca, M., Grazziani, L., Cros, E., Assemat, S., Davrieux, F., and Boulager, R. (2011). Influencia de las condiciones del tratamiento poscosecha sobre la temperatura y acidez en granos de cacao criollo (*Theobroma cacao* L.). *Revista de la Facultad de Agronomía, 28*(1), 646-660. https://produccioncientificaluz.org/index.php/agronomia/article/view/27036

Rivera, R. D., Mecías, F. W., Guzmán, A. M., Peña, M. M., Medina, H. N., Casanova, L. M., Barrera, A. E., and Nivela, P. E. (2012). Efecto del tipo y tiempo de fermentación en la calidad física y química del cacao (*Theobroma cacao* L.) tipo nacional. *Revista Ciencia y Tecnología, 5*(1), 7-12. https://doi.org/10.18779/cyt.v5i1.120

Schwan, R. F., and Wheals, A. E. (2004). The microbiology of cocoa fermentation and its role in chocolate quality. *Critical Reviews in Food Science and Nutrition, 44*(4), 205-221. https://doi.org/10.1080/10408690490464104

Sorensen, A., Brask, E., and Thomsen, K. (1996). Electrical conductivity test. *Danida Forest Seed Centre Technical Notes, 45*(45), 1-19. https://curis.ku.dk/ws/files/20710854/tn45.pdf

Zabalaga, R. F., la Fuente, C. I. A., and Tadini, C. C. (2016). Experimental determination of thermophysical properties of unripe banana slices (*Musa cavendishii*) during convective drying. *Journal of Food Engineering, 187*, 62-69. https://doi.org/10.1016/j.jfoodeng.2016.04.020

Zambrano, A., Gómez, A., Ramos, G., Romero, C., Lacruz, C., and Rivas, E. (2010). Caracterización de parámetros físicos de calidad en almendras de cacao criollo, trinitario y forastero durante el proceso de secado. *Agronomía Tropical, 60*(4), 389-396. http://sian.inia.gob.ve/revistas_ci/Agronomia%20Tropical/at6004/at6004_zambrano.pdf

Study of a Semi-Active Control System to Reduce Lateral Displacement in Framed Structures under Seismic Load

Estudio de un sistema de control semi-activo para reducir los desplazamientos laterales en estructuras aporticadas bajo cargas sísmicas

Luis A. Lara-Valencia [1] Yamile Valencia-González[2], and David M. Bedoya-Zambrano [3]

ABSTRACT

This study presents the numerical implementation of a semi-active control system used to reduce lateral displacements in framed structures under seismic loads. To manage forces in the structures, two controllable fluid devices called magnetorheological (MR) dampers were used together with a fuzzy logic (FL) algorithm to determine the optimal control forces. The FL controller was programmed based on a set of 49 inference rules using two input parameters: displacement and velocity of the first story of the uncontrolled structure. The voltage applied to the MR dampers was the output parameter of the control algorithm, thus altering the damping forces in the system. To evaluate the performance of the proposed controller, three plane frame structures with different geometric configurations were modeled and subjected to four different real ground acceleration records. The results obtained in this study show a considerable reduction in the displacement, acceleration, and inter-story drift for all the studied structures, demonstrating the effectiveness and efficiency of the controller at improving the damping characteristics in structures.

Keywords: magnetorheological dampers, structure control, earthquake load, reduction of lateral displacements

RESUMEN

Este estudio presenta el desarrollo numérico de un sistema de control semiactivo empleado para reducir los desplazamientos en estructuras aporticadas bajo cargas sísmicas. Para administrar las fuerzas en las estructuras se usaron dos dispositivos de fluido controlable llamados amortiguadores magnetoreológicos (MR) junto con un algoritmo de control basado en lógica difusa (FL), con el fin de determinar las fuerzas de control óptimas. El controlador FL fue programado con base en un conjunto de 49 reglas de inferencia, para las cuales se emplearon dos parámetros de entrada: desplazamiento y velocidad del primer piso de la estructura no controlada. El voltaje aplicado a los amortiguadores MR fue el parámetro de salida del algoritmo de control, modificando de esta manera las fuerzas de amortiguamiento del sistema. Para evaluar el desempeño del controlador propuesto, se modelaron tres pórticos planos con diferente configuración geométrica, sometiéndolos a cuatro registros reales y diferentes de aceleraciones del suelo. Los resultados obtenidos indican una considerable reducción en el desplazamiento, la aceleración y las derivas de entrepiso en todas las estructuras estudiadas, demostrando la eficacia y eficiencia del controlador para mejorar las características de amortiguamiento en estructuras.

Palabras clave: amortiguadores magnetoreológicos, control estructural, carga sísmica, reducción de desplazamientos laterales

Introduction

Structural control can be successful through different methodologies, among which is the modification of the structural system's stiffness, mass, shape, or damping (Housner *et al.*, 1997; Kaveh *et al.*, 2020; Shih and Sung, 2021). This can also be classified in up to four different control groups: active control (Bitaraf *et al.*, 2012; Gutiérrez and Navarro, 2013; Kannan *et al.*, 1995; Khodabandolehlou *et al.*, 2018; Mohammadi *et al.*, 2021; Pourzeynali *et al.*, 2007; Smanchai and Yao, 1978), passive control (Arzeytoon *et al.*, 2017; Basili and de Angelis, 2007; Chowdhury *et al.*, 2021; Constantinou, 1994; Lara-Valencia *et al.*, 2020; Selmani, 2020; Zhang and Balendra, 2013; Zhao *et al.*, 2020), hybrid control (Kim and Adeli, 2005; Omidi and Mahmoodi, 2015; Subramaniam *et al.*, 1996; Taniguchi *et al.*, 2016; Yang *et al.*, 1992; Zhou and Zheng, 2020), and semi-active control (Amini *et al.*, 2015; Bathaei *et al.*, 2018;

Behrooz *et al.*, 2014; Cha and Agrawal, 2017; K-Karamodin and H-Kazemi, 2010; Kori and Jangid, 2008; Madhekar and Jangid, 2009; Singh *et al.*, 1997; Xu *et al.*, 2003).

---
1 Civil engineer, Universidad Nacional de Colombia, Colombia. Ph.D. in Structures and Civil Construction, Universidade de Brasília, Brasil. Affiliation: Associate Professor, Universidad Nacional de Colombia, Medellín branch, Colombia. E-mail: lualarava@unal.edu.co

2 Civil engineer, Universidad Nacional de Colombia, Colombia. Ph.D. in Geotechnical Engineering, Universidade de Brasília, Brasil. Affiliation: Associate Professor, Universidad Nacional de Colombia, Medellín branch, Colombia. E-mail: yvalenc0@unal.edu.co

3 Civil engineer, Universidad Nacional de Colombia, Colombia. Master's student in Structures, Universidad Nacional de Colombia, Medellín branch, Colombia. E-mail: dmbedoyaz@unal.edu.co

Today, semi-active controllers are probably the most popular family of structural control systems, which is mainly due to their potential to safeguard structural systems through sophisticated mechanisms, with the ability to operate and reduce the response of the monitored structures by using small portable external energy sources. This characteristic causes semi-active devices to show similar results to those of active control systems, due to the fact that the former devices use just a fraction of the energy required by the latter, which makes them safe, reliable, and ideal devices to face the great magnitude of natural hazards.

In the last decades, the study of semi-active controllers has been the focus of interest for many researchers, who have made various contributions to the development and refinement of control devices and algorithms in order to improve the performance of structures subjected to dynamic solicitations. In this way, devices such as controllable fluid dampers (Cruze *et al.*, 2018; Cruze *et al.*, 2021; Pahlavan and Rezaeepazhand, 2007), semi-active stiffness dampers (SASD)and semi-active tuned liquid column dampers (TLCD) (Kataria and Jangid, 2016), piezoelectric dampers (Zamani *et al.*, 2017), friction variable dampers (Downey *et al.*, 2016), and semi-active tuned mass dampers (Sun and Nagarajaiah, 2014) stand out as attractive alternatives to developing control systems to reduce lateral displacements in structures.

Magnetorheological dampers (MR dampers) are semi-active devices used for structural control. MR dampers and electrorheological dampers (ER dampers) are classified in the literature as controllable fluid dampers, mainly due to the special characteristics of the fluid that works in the tube of the absorber. MR dampers use magnetorheological fluid, which owes its name to the fact that micron-sized, magnetizable particles are randomly dispersed in an appropriate carrier liquid. Thus, when the fluid is exposed to a magnetic field, the magnetizable particles form parallel linear chains to the field, thus changing the fluid state, restricting the piston movement of the device, and increasing the flow resistance. This particularity allows magnetorheological dampers to develop variable non-linear damping forces, which depend on the voltage applied to the device, thus obtaining an energy dissipation mechanism with the potential to control the responses in real structural systems.

A numerical study to determine the structural behavior and performance of three plane frame buildings equipped with a semi-active control strategy based on MR dampers is carried out in this work. Four different ground motion earthquakes excite these buildings in order to analyze the potential use of this type of device. To this effect, a controller that uses two MR dampers governed by a fuzzy logic algorithm is used. This algorithm is responsible for managing the damping forces required by the structural system, so that the energy of the ground motion is rapidly and optimally dissipated, aiming at the reduction of the structure's response at all stories. A comparative analysis is also performed to compare the response of controlled and uncontrolled structural

systems. It assesses the effectiveness of the controller used and its relevance in reducing the lateral displacement in the analyzed structures.

Methodology

Three different plane frame buildings have been discretized to set up the numerical model required to simulate the conditions of the controlled and uncontrolled systems. Each of these structures has been equipped with and without a control system based on MR dampers governed by a fuzzy logic algorithm (Lara-Valencia *et al.*, 2015; Lara-Valencia, 2011; Liu *et al.*, 2001; Wilson, 2005). To examine the effectiveness of the proposed controller, the uncontrolled and controlled configurations of the buildings are subjected to four different earthquake acceleration records. In this way, the results obtained allow comparing the behavior of each structure in its uncontrolled and controlled states in order to establish the impact of semi-active controllers in the reduction of lateral displacements.

The controlled structural systems are equipped with MR dampers partially based on the RD-1005-3 reference damper manufactured by the Lord Corporation (Lord Company, 2006). The location and number of devices used is the same in all the numerical models, prioritizing the installation of the MR dampers on the lower stories of the buildings. It should be noted that the performance of MR dampers is sensitive to the ground motion acting on the structure. The control system adapts according to the inputs (*i.e.*, the displacements and velocities of the structure), thus determining the optimal damping forces required to reduce the structural response.

The ground motion records used to excite the structures corresponds to the North-South component of El Centro earthquake, which occurred in United States in 1940; the ground motion known as Christchurch-Lyttelton that took place in New Zealand in 2011; the acceleration record of Mistrato in Colombia, which occurred in 1979; and the earthquake ground motion that occurred in Algarrobo, Chile in 1985.

Modeled structural systems

Three buildings discretized as plane frames were the structures chosen to be studied in this work, assuming the rigid diaphragm hypothesis as valid. Each developed model has the following dimensions: 2,8 m of floor-to-floor height and 6 m of column spacing. The maximum heights of the structural systems are 5,6, 22,4, and 30,8 m, which are related to buildings with two (model A), eight (model B), and eleven stories (model C), respectively. The two- and eight-floor buildings consist of a single span, while the eleven-floor building consists of four spans with variable heights. Concrete with a compressive strength (f''_c) of 28 MPa is assumed to be the material used for the construction of the frames. The sections of beams and columns are

assumed to be square, with cross-sectional areas of 30 and 40 cm, respectively. The fundamental frequencies of the structures are 36,32, 7,48, and 7,19 rad/sec for models A, B, and C, respectively. The damping matrix is calculated as a Rayleigh damping matrix proportional to the stiffness and mass matrices, assuming a critical damping ratio of 5% for the first and last modes of vibration. Figure 1 illustrates the frames used.
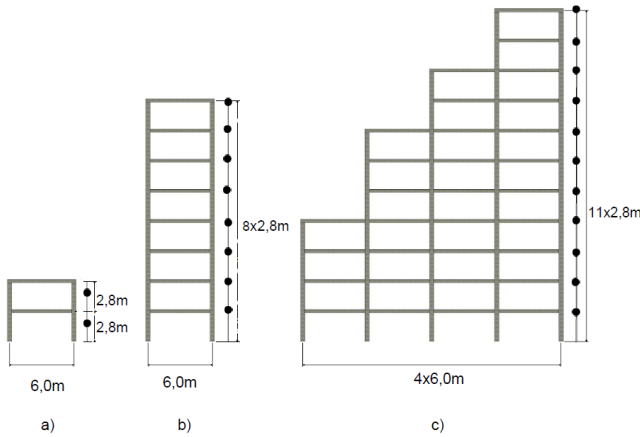
Figure 1. (a) Model A: two-floor building; (b) model B: eight-floor building; (c) model C: eleven-floor building
Source: Authors

MR dampers

The devices used to dissipate the energy generated in the structures as a consequence of the accelerations of the soil where buildings are founded are modified dissipators based on the MR damper type RD 1005-3 built by the Lord Corporation (Lord Company, 2006). This reference needs an adjustment to be able to reduce the response of the structures used in the numerical study. This adjustment consists of an increase in the damping forces generated by the device. In this way, the MR dampers produced damping forces of 2 224 N at factory settings. After modification, the device produces ten times more damping forces according to the scale of the modeled structures.

Two dampers were used for all the modeled buildings. The first one was installed on the first story and the second one on the second. The numerical model used to simulate the behavior of this type of dampers is known as the phenomenological model, which was proposed by Spencer Jr. et al. (1997). This model works based on a modified hysteresis Bouc-Wen model. The force f generated by the MR damper is calculated using Equation (1):

$$f = \alpha z + c_0 \left(\dot{x} - \dot{y} \right) + k_0 \left(x - y \right) + k_1 \left(x - x_0 \right) \quad (1)$$

where z is the evolutionary variable of the Bouc-Wen model that is calculated through Equation (2):

$$z = -\gamma \left| \dot{x} - \dot{y} \right| z \left| z \right|^{n-1} - \beta \left(\dot{x} - \dot{y} \right) \left| z \right|^n + A \left(\dot{x} - \dot{y} \right) \quad (2)$$

$$\dot{y} = \frac{1}{\left(c_0 + c_1 \right)} \left[\alpha z + c_0 \dot{x} + k_0 \left(x - y \right) \right] \quad (3)$$

In the above Equations, the parameters γ, β, and A are constant setting parameters; k_1 is the stiffness of the MR damper; c_0 is the viscous damping observed at higher velocities; c_1 is the damping coefficient of the device; k_0 x_0 is a parameter to control stiffness at high velocities; and x_0 is the initial displacement of the device associated with nominal damper force due to accumulation.

The general properties of these devices can be seen in Table 1. The parameters that describe the behavior of the dampers are defined by Basili (2006).

Table 1. Properties of the MR damper used

General Properties	Values
Compressed length (mm)	155
Extended length (mm)	208
Body diameter (mm)	41,4
Damper forces (N)	22 240
Operating temperature (°C)	Max 71
Input voltage (V)	12 DC
Response time (ms)	< 15

Source: Authors

Proposed structural control

The proposed structural control works based on a fuzzy-logic algorithm that manages the control forces generated by the MR dampers. This algorithm uses heuristic knowledge obtained from the real data of the structural systems studied in order to produce an optimal control action through a set of functions and classification parameters. The algorithm produces the optimal control action by introducing variable forces over time from the manipulation of the voltage to be induced in the MR dampers. An outline of the control project proposed for this work can be seen in Figure 2.
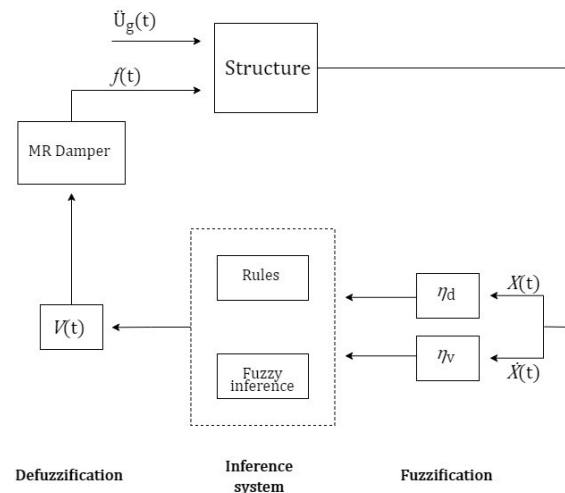
Figure 2. Structural control based on fuzzy-logic
Source: Authors

The controller uses the displacement $X(t)$ and velocitiy $\dot{X}(t)$ response functions of the building's first story. These variables must be normalized through a set of linear functions, since the range of study in the fuzzy universe is defined by the interval [-1, 1]. The normalization functions and scaling factors used in this work correspond to those defined by Liu *et al*. (2001) and Wilson (2005). Equations (4) and (5) describe the normalization functions for the displacement (η_d) and the velocity (η_v), respectively.

$$\eta_d = k_d \cdot x \qquad (4)$$

$$\eta_v = k_v \cdot \dot{x} \qquad (5)$$

where k_d is the displacement scaling factor, and k_v is the velocity scaling factor, both defined by Liu *et al*. (2001). Moreover, η_d and η_v are the first story values of displacement and velocity, respectively.

The controller's single output parameter is the voltage required by the MR damper to generate the optimal structural control forces. The output value of this variable is defined in the universe [0, 1], and it is defuzzified using the centroid method. The scaling factor that was used to determine the output voltage *V* in the real universe is described by Equation (6):

$$V = V_{max}\left(\frac{5}{3}s - \frac{1}{3}\right) \qquad (6)$$

where V_{max} is the maximum voltage that can be provided to the MR damper, and s is the numerical output value obtained during defuzzification.

The input and output membership functions used in the fuzzification and defuzzification processes are composed of identical triangles with a 50% overlap. Figure 3 presents the input membership functions (displacement or velocity), whereas Figure 4 presents the output membership functions (voltage).
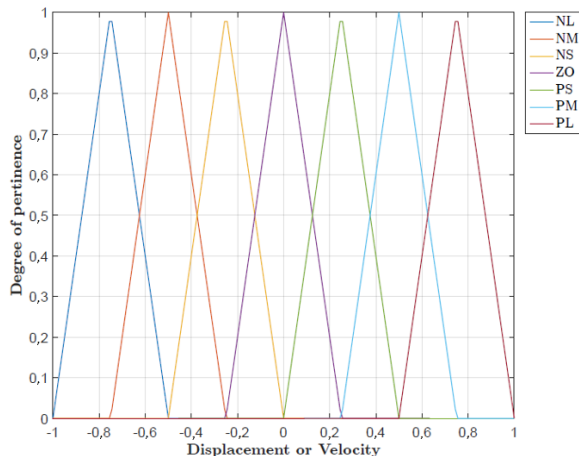
Figure 3. Input membership functions used in the fuzzification process
Source: Authors
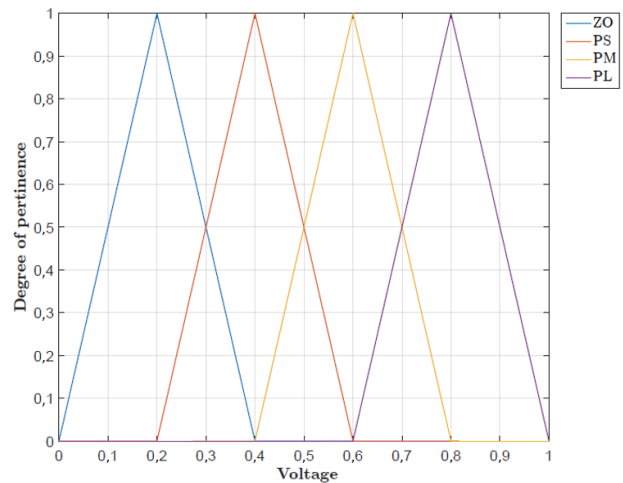
Figure 4. Output membership functions used in the defuzzification process
Source: Authors

Table 2 shows the controller inference system defined by Liu *et al*. (2001). The linguistic fuzzy values NL, NM, NS, ZO, PS, PM, and PL mean Negative Large, Negative Medium, Negative Small, Zero, Positive Small, Positive Medium, and Positive Large, respectively.

Table 2. Fuzzy inference system

$X(t)$ \ $\dot{X}(t)$	NG	NM	NP	ZO	PP	PM	PG
NG	PG	PG	PG	PM	ZO	ZO	ZO
NM	PG	PG	PG	PP	ZO	ZO	PP
NP	PG	PG	PG	ZO	ZO	PP	PM
ZO	PG	PM	PP	ZO	PP	PM	PG
PP	PM	PP	ZO	ZO	PG	PG	PG
PM	PP	ZO	ZO	PP	PG	PG	PG
PG	ZO	ZO	ZO	PM	PG	PG	PG

Source: Authors

The generation of optimal voltages, which allow the injection of damping forces with the capacity to dissipate a significant amount of energy caused by the ground motions, depends exclusively on the displacements and velocities of the first floor in each model. To adjust these parameters to the proposed set of fuzzy linguistic values, linear functions are used to normalize the responses of the structures in the universe of the defined pertinence functions.

The structural control implementation and the numerical simulations carried out to verify the performance of the controlled and uncontrolled frames were executed in the programming and numeric computing platform Matlab.

Results and discussion

As mentioned above, each model, in its uncontrolled and controlled configuration, was excited by four different seismic records, and their respective numerical responses

were determined. Every controlled structure was equipped with two MR dampers installed in the two first stories of the frames. The MR dampers were managed by the classic fuzzy-logic algorithm described above, which calculates the optimal damping forces to be provided by the MR dampers in order to reduce the structural response. A comparative response analysis for the controlled and uncontrolled systems was carried out to evaluate the performance of the developed controller.

Figure 5 shows the behavior of the absolute maximum displacement of each story for all the studied structures, considering the uncontrolled and controlled configurations. In this graph, the first, second, and third columns represent the maximum lateral displacement of each floor for models A, B, and C, respectively, when the structures are subjected to the El Centro, Christchurch-Lyttelton, Mistrato, and Algarrobo ground motions.

The greatest reductions in the peak displacements always occur in the two highest stories of the structures. It is also possible to affirm that the use of the fuzzy-logic-based controllers in the different models does not ensure a uniform trend in the lateral displacement reduction for all the stories of the structural systems. For instance, in model A, it is possible to get reductions of up to 78% in the lateral displacement of each story of the structure when it is subjected to the ground acceleration caused by El Centro
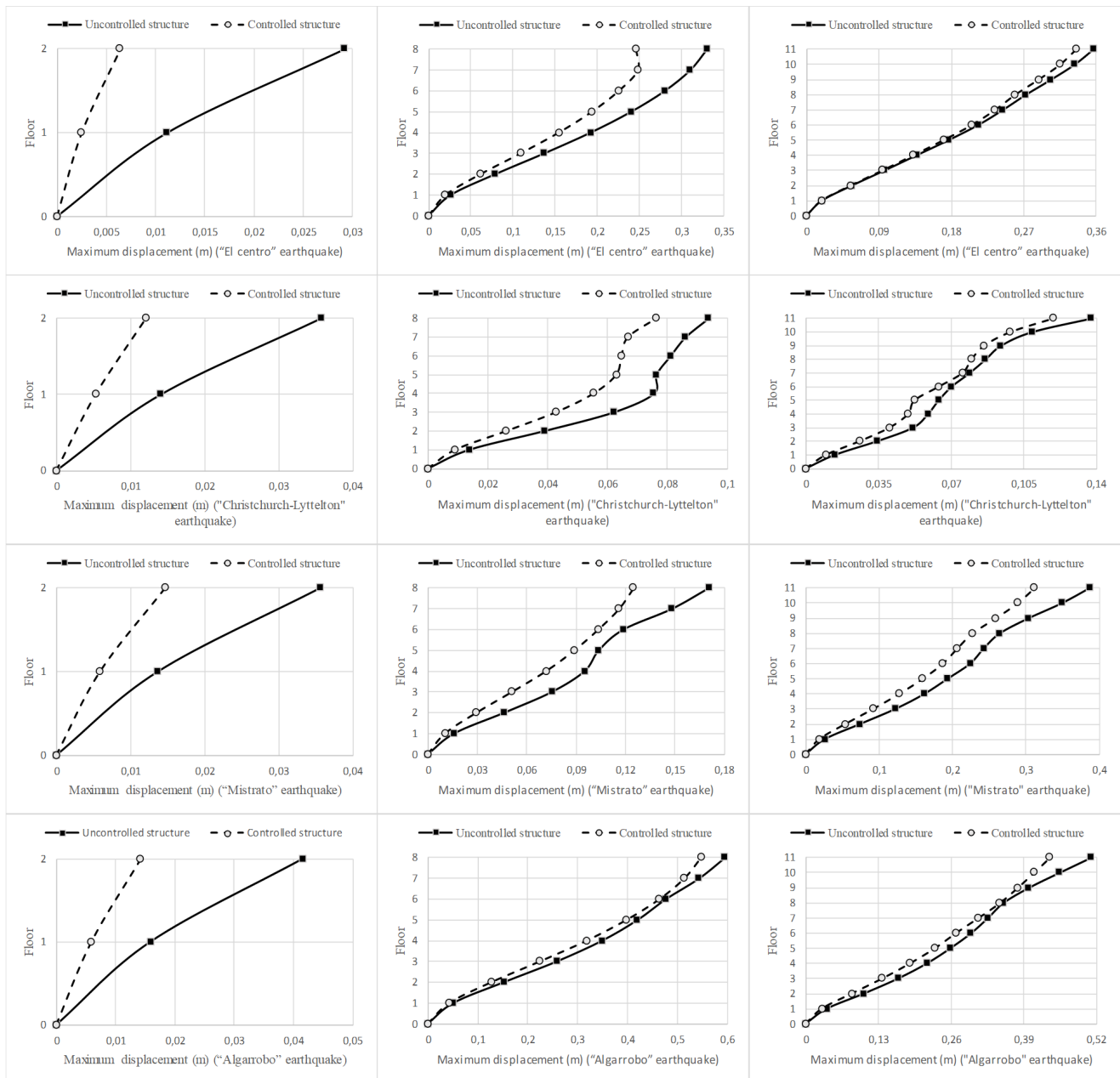
Figure 5. Absolute maximum displacements for the uncontrolled and controlled structures
Source: Authors

earthquake. On the other side, the reductions of the lateral displacements of each floor of model A when it is subjected to the Mistrato ground motion are up to 62%.

The analysis of the reduction of the lateral displacements of models B and C have some characteristics that can be generalized and allow inferring some interesting aspects about the performance of the controller used. First, the structures in models B and C are 4 and 5,5 times higher, respectively, than the structure discretized in the model A, so the lateral displacements of models B and C have higher displacement magnitudes. In spite of this, it is possible to see that the percentages of lateral displacement reduction for the controlled structures with eight and eleven levels are lower than those corresponding to model A, thus obtaining maximum reduction percentages of up to 27% in model B and up to 20% in model C.

Although the decrease in the reduction percentages may lead to consider that the configuration used in the controller loses its effectiveness in high structures, a deeper analysis allows deducing that the reduction in the lateral displacement magnitudes of the structures in models B and C are similar or even higher than those obtained for model A. An example of this is the response of the three modeled structures when excited by the acceleration produced by the Algarrobo earthquake. For this case, a maximum lateral displacement reduction of 2,78 cm was reached on the second floor of model A. On the other hand, the magnitude of the maximum lateral displacement reductions for the discretized structures in models B and C reached values of 6,57 and 7,54 cm on floors eight and eleven, respectively. These results reaffirm that the control system is a valid strategy to be used in the reduction of lateral displacement in low- and medium-height buildings.

The Algarrobo ground motion caused the maximum responses in the uncontrolled models among all the studied cases. As expected, these maximum responses took place at the top story of each structure. In model A, the maximum lateral displacement, velocity, and acceleration were 0,0416 m, 1,46 m/s, and 55,12 m/s², respectively. The control system's operation reduces these response parameters to 0,0138 m, 0,54 m/s, and 30,04 m/s², implying reductions of 66,83, 63,01, and 45,50%, respectively.

For the uncontrolled models B and C, the maximum lateral displacement at the top story was 0,5952 and 0,5104 m, respectively. The same parameters for the controlled configurations of models B and C were 0,5295 and 0,4350 m, which represents response decreases of 11,04 and 14,77%. It is remarkable that the maximum displacement of model B is larger than that of model C. The main reason for this is that model C, despite being taller, is stiffer than the idealized structure in model B. Likewise, the maximum velocity of models B and C were 5,28 and 5,87 m/s for the uncontrolled configurations and 4,39 and 4,42 m/s for the controlled configurations, thus consolidating velocity parameter reductions of 16,86% for model B and 24,70% for model C. The peak accelerations for the uncontrolled

models B and C were 62,81 and 97,94 m/s², respectively. These values drop to 57,18 and 56,60 m/s² when the MR damper-based control system is installed on the structures. The achieved acceleration reductions were 8,96 and 42,21% for models B and C, respectively.

Table 3 presents a summary with the maximum lateral displacement values and RMS (Root Mean Square) values for the displacements of the uncontrolled and controlled structures for all the ground motions used. This Table also shows the corresponding percentages of the response reductions achieved in the controlled structures.

It is interesting to note the general behavior of the RMS displacement response in the studied structures. According to the results, the semi-active controller was able to reduce the RMS displacement values for the first and second stories of the discretized structure in case A by up to 96%. On the other hand, when the structure was subjected to the Mistrato earthquake, the smallest reductions in the RMS displacement response was evidenced, namely 34 and 38% for the first and second floor, respectively. The variation in the lateral displacement on the top story of model A when El Centro and Mistrato earthquakes excite the structure is shown in Figures 6 and 7, respectively.

Figure 6. Displacement of the second floor of model A when the structure is subjected to El Centro ground motion record
Source: Authors

Figure 7. Displacement of the second floor of model A when the structure is subjected to the Mistrato ground motion record.
Source: Authors

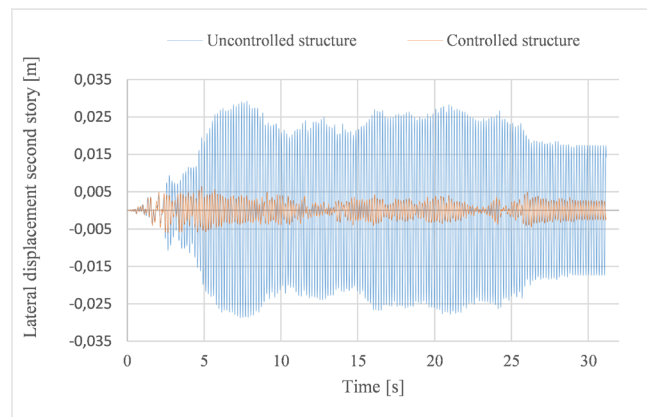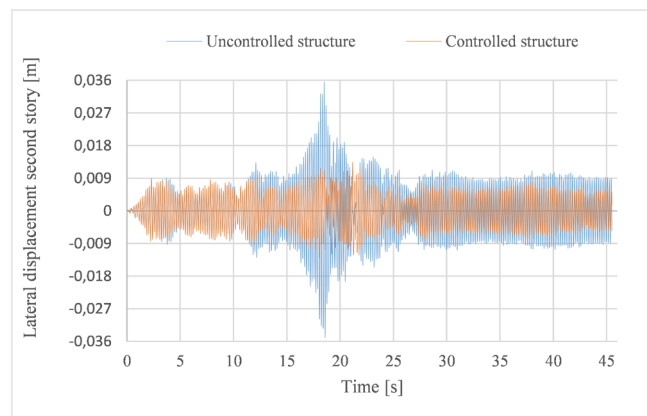**Table 3.** Summary of the response for the analyzed uncontrolled and controlled structures

Model A

| | El Centro, 1940 | | | | Christchurch-Lyttelton, 2011 | | | | Mistrato, 1979 | | | | Algarrobo, 1985 | | | |
| | Maximum displacement (m) | | RMS value of displacement (m) | | Maximum displacement (m) | | RMS value of displacement (m) | | Maximum displacement (m) | | RMS value of displacement (m) | | Maximum displacement (m) | | RMS value of displacement (m) | |
	1st Story	2nd Story	1st Story	2nd Story	1st Story	2nd Story	1st Story	2nd Story	1st Story	2nd Story	1st Story	2nd Story	1st Story	2nd Story	1st Story	2nd Story
Uncontrolled structure	0,0112	0,0292	0,0059	0,0154	0,0141	0,0357	0,0065	0,0170	0,0137	0,0356	0,0029	0,0076	0,0159	0,0416	0,0043	0,0112
Controlled structure	0,0026	0,0065	0,0008	0,0021	0,0057	0,0128	0,0014	0,0035	0,0056	0,0135	0,0019	0,0047	0,0057	0,0138	0,0021	0,0054
Reduction (%)	76,79	77,74	86,44	86,36	59,57	64,15	78,46	79,41	59,12	62,08	34,48	38,16	64,15	66,83	51,16	51,79

Model B

| | El Centro, 1940 | | | | Christchurch-Lyttelton, 2011 | | | | Mistrato, 1979 | | | | Algarrobo, 1985 | | | |
| | Maximum displacement (m) | | RMS value of displacement (m) | | Maximum displacement (m) | | RMS value of displacement (m) | | Maximum displacement (m) | | RMS value of displacement (m) | | Maximum displacement (m) | | RMS value of displacement (m) | |
	7th Story	8th Story	7th Story	8th Story	7th Story	8th Story	7th Story	8th Story	7th Story	8th Story	7th Story	8th Story	7th Story	8th Story	7th Story	8th Story
Uncontrolled structure	0,3102	0,3301	0,1733	0,1848	0,0739	0,0937	0,0288	0,0350	0,1482	0,1706	0,0469	0,0518	0,5433	0,5952	0,2352	0,2513
Controlled structure	0,2470	0,2624	0,1269	0,1353	0,0663	0,0756	0,0237	0,0256	0,1155	0,1244	0,0405	0,0436	0,4984	0,5295	0,2118	0,2260
Reduction (%)	20,37	20,51	26,77	26,79	10,28	19,32	17,71	26,86	22,06	27,08	13,65	15,83	8,26	11,04	9,95	10,07

Model C

| | El Centro, 1940 | | | | Christchurch-Lyttelton, 2011 | | | | Mistrato, 1979 | | | | Algarrobo, 1985 | | | |
| | Maximum displacement (m) | | RMS value of displacement (m) | | Maximum displacement (m) | | RMS value of displacement (m) | | Maximum displacement (m) | | RMS value of displacement (m) | | Maximum displacement (m) | | RMS value of displacement (m) | |
	10th Story	11th Story	10th Story	11th Story	10th Story	11th Story	10th Story	11th Story	10th Story	11th Story	10th Story	11th Story	10th Story	11th Story	10th Story	11th Story
Uncontrolled structure	0,3334	0,3567	0,1704	0,1794	0,1089	0,1375	0,0347	0,0442	0,3490	0,3867	0,1247	0,1335	0,4538	0,5104	0,1676	0,1783
Controlled structure	0,3140	0,3346	0,1590	0,1672	0,0993	0,1195	0,0250	0,0289	0,2882	0,3110	0,1118	0,1187	0,4062	0,4350	0,1488	0,1572
Reduction (%)	5,82	6,20	6,69	6,80	8,82	13,09	27,95	34,62	17,42	19,58	10,34	11,09	10,49	14,77	11,22	11,83

Source: Authors

The data obtained from the analysis of the RMS displacement response for models B and C ratify the reductions obtained using the developed controller. In model B, the highest reduction of the RMS displacement response for the controlled structure was reached when the structure was excited by El Centro earthquake, obtaining reductions of up to 27% for the last two stories of the building. On the other hand, when the Algarrobo earthquake excited the structure, the RMS displacement responses were lower, with decreased up to 10% in the last two stories of the modeled building. The reduction in the RMS values of displacement in the last two stories of the controlled model C was up to 34%.

This occurred when the structure was excited by the ground motion record of Christchurch-Lyttelton. On the contrary, the lower performance of the controlled model C occurred when it was subjected to the acceleration record of El Centro earthquake, in which the reduction in the RMS value of displacement was around 7%. Figures 8 and 9 present the last story's time histories of models B and C in their uncontrolled and controlled configurations for the El Centro and Christchurch-Lyttelton records, respectively. These figures clearly show the performance of the controller based on MR dampers acting to reduce the lateral displacement of the last story of the structure.

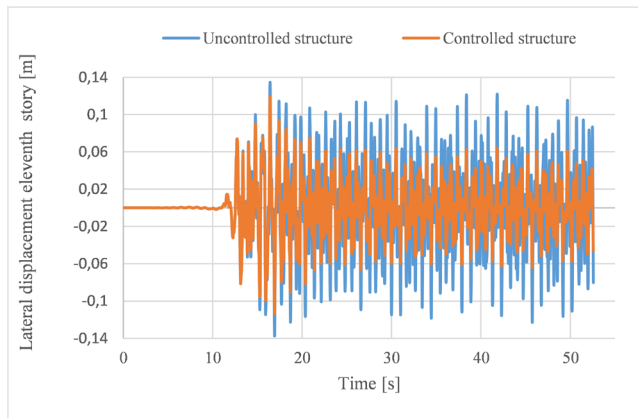**Figure 8.** Displacement of the eight floor of model B when the structure is subjected to El Centro ground motion record
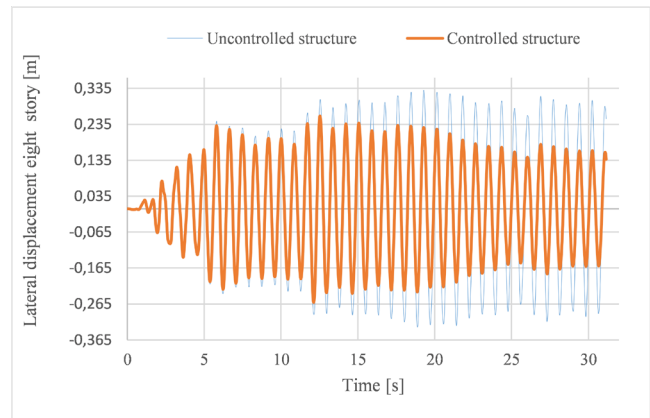**Source:** Authors

Figure 9. Displacement of the eleventh floor of model C when the structure is subjected to the Christchurch-Lyttelton ground motion record
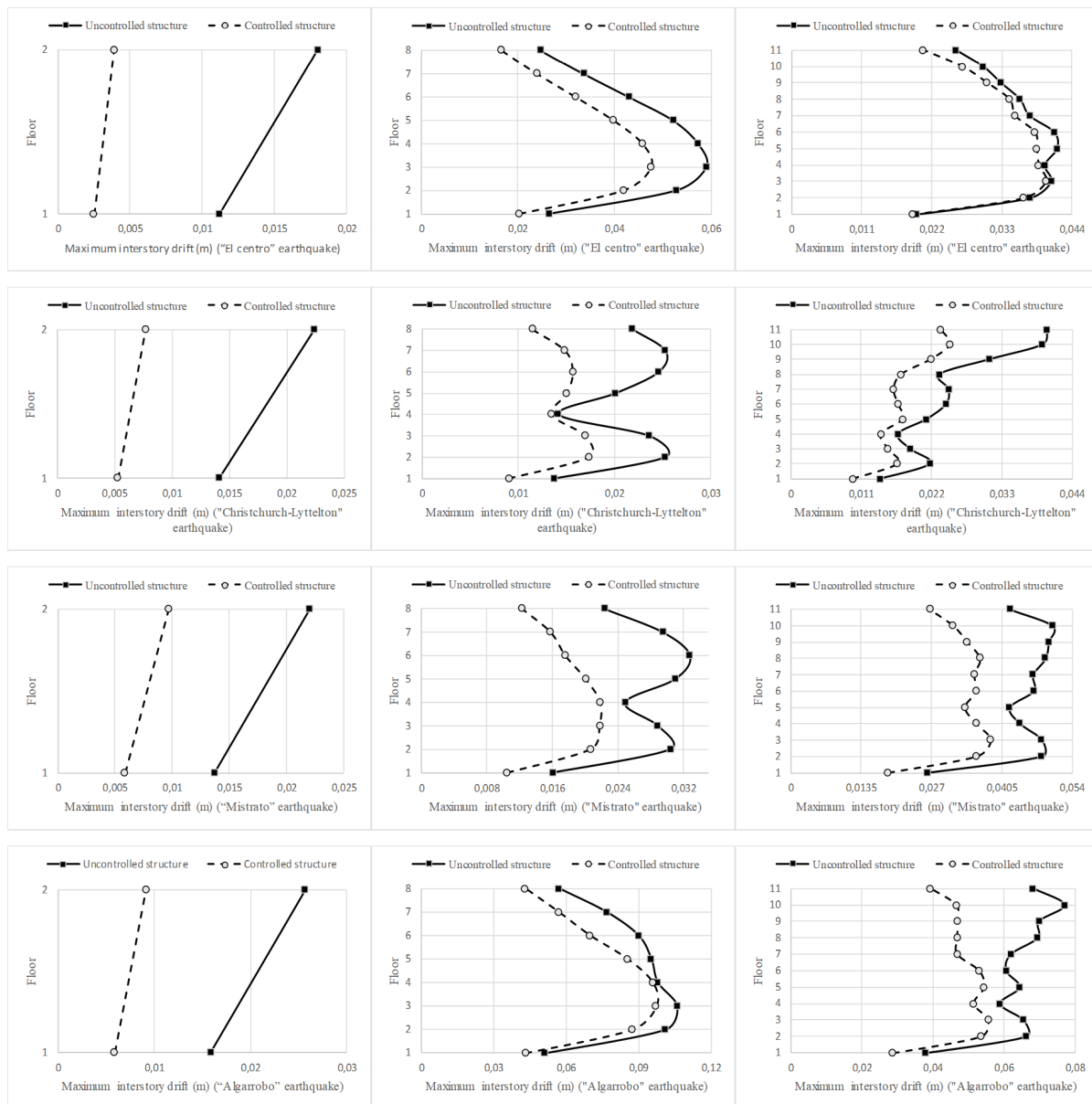**Source:** Authors

Figure 10. Interstory drift graphs for the uncontrolled and controlled structures
Source: Authors

Figure 10 presents the graphs of the maximum relative lateral displacements between consecutive floors of the three buildings in their controlled and uncontrolled configurations. Based on the analysis of this Figure, it is possible to demonstrate the effect of drift reduction in the controlled structures. For instance, in the study of models A and C, higher reductions were observed on the drifts of the last floors of the structures. Maximum horizontal interstory displacements of up to 1,65 cm (64,20% equivalent reduction) and up to 2,89 cm (42,31% equivalent reduction) were obtained for models A and C, respectively. On the other hand, in model B, the highest drift decrease was obtained for the middle stories of the building, with the sixth story generally being the level where the highest reductions were found, obtaining reduction values of up to 2,01 cm (equivalent reduction of 22,33%). All these reductions were reached when the excitation affecting the structures was the Algarrobo earthquake.

There is another important result, which is obtained by analyzing the story drifts graphs: all the inter-story drifts showed improvements with the control system proposed in this work. This means, that the control device works adequately in reducing the structure's interstory drifts, thus decreasing the magnitude of this parameter in the three models, regardless of the height of the next considered story. In addition, these data confirm that there are effective reductions in the lateral displacements of all the stories of the structures studied when using the controller based on MR dampers.

Conclusions

This study investigated the implementation of an MR damper-based control system to reduce the structural response in three different plane frame buildings subjected to diverse soil accelerations. An algorithm based on fuzzy logic was used to calculate the voltage required by the MR damper to generate the optimal damping forces, depending on the input parameters of displacement and the velocity of the first floor of the structures. Based on the numerical results obtained, it is concluded that the semi-active controller based on the set of MR dampers and the fuzzy logic control algorithm is an effective tool to reduce the lateral displacements of framed low- and medium-height buildings. The performance obtained in the three controlled models shows reductions for the lateral displacement of up to 78, 27, and 20%, as well as reduction percentages of the interstory drift of up to 78, 47, and 42% for models A, B, and C, respectively. Furthermore, the estimation of the evolution of the horizontal displacements over time in terms of the RMS values demonstrates the success of the controller system in achieving reductions of up to 86% for both floors of model A. In the case of models B and C, reduction rates for the RMS value of displacement of up to 26 and 34% were determined for the last levels of the buildings. Thus, the effectiveness of the developed controller was demonstrated, which opens the way for future efforts in the actual implementation of this type of technology, as well as in the optimization of MR damper configurations to make them more efficient.

References

Amini, F., Mohajeri, S. A., and Javanbakht, M. (2015). Semi-active control of isolated and damaged structures using online damage detection. *Smart Materials and Structures*, *24*(10), 105002. https://doi.org/10.1088/0964-1726/24/10/105002

Arzeytoon, A., Golafshani, A. A., Toufigh, V., and Mohammadi, H. (2017). Seismic performance of ribbed bracing system in passive control of structures. *Journal of Vibration and Control*, *23*(18), 2926-2941. https://doi.org/10.1177/1077546315623876

Basili, M., and de Angelis, M. (2007). Optimal passive control of adjacent structures interconnected with nonlinear hysteretic devices. *Journal of Sound and Vibration*, *301*(1), 106-125. https://doi.org/10.1016/j.jsv.2006.09.027

Bathaei, A., Zahrai, S. M., and Ramezani, M. (2018). Semi-active seismic control of an 11-DOF building model with TMD+MR damper using type-1 and -2 fuzzy algorithms. *Journal of Vibration and Control*, *24*(13), 2938-2953. https://doi.org/10.1177/1077546317696369

Behrooz, M., Wang, X., and Gordaninejad, F. (2014). Modeling of a new semi-active/passive magnetorheological elastomer isolator. *Smart Materials and Structures*, *23*(4), 45013. https://doi.org/10.1088/0964-1726/23/4/045013

Bitaraf, M., Hurlebaus, S., and Barroso, L. R. (2012). Active and semi-active adaptive control for undamaged and damaged building structures under seismic load. *Computer-Aided Civil and Infrastructure Engineering*, *27*(1), 48-64. https://doi.org/10.1111/j.1467-8667.2011.00719.x

Cha, Y.-J., and Agrawal, A. K. (2017). Seismic retrofit of MRF buildings using decentralized semi-active control for multi-target performances. *Earthquake Engineering and Structural Dynamics*, *46*(3), 409-424. https://doi.org/10.1002/eqe.2796

Chowdhury, S., Banerjee, A., and Adhikari, S. (2021). Enhanced seismic base isolation using inertial amplifiers. *Structures*, *33*, 1340-1353. https://doi.org/10.1016/j.istruc.2021.04.089

Constantinou, M. C. (1994). Passive energy dissipation development in U.S. In M.C. Constantinou (Ed.), *Passive and Active Structural Vibration Control in Civil Engineering* (pp. 255-269). Springer. https://doi.org/10.1007/978-3-7091-3012-4

Cruze, D., Hemalatha, G., Magdalene, A., Tensing, D., and Sundar Manoharan, S. (2018). Magnetorheological damper for performance enhancement against seismic forces. In H. Rodrigues, A. Elnashai, and G. M. Calvi (Eds.), *Facing the Challenges in Structural Engineering* (pp. 104-117). Springer International Publishing.

Cruze, D., Hemalatha, G., Noroozinejad, F. E., Arnab, B., Sarala, L., and Manoharan, S. S. (2021). Seismic performance evaluation of a recently developed magnetorheological damper: experimental investigation. *Practice Periodical on Structural Design and Construction*, *26*(1), 4020061. https://doi.org/10.1061/(ASCE)SC.1943-5576.0000544

Downey, A., Cao, L., Laflamme, S., Taylor, D., and Ricles, J. (2016). High capacity variable friction damper based on band brake technology. *Engineering Structures*, *113*, 287-298. https://doi.org/10.1016/j.engstruct.2016.01.035

Gutiérrez, M. R., and Navarro, G. S. (2013). Control activo de vibraciones en estructuras tipo edificio usando actuadores piezoeléctricos y retroalimentación positiva de la aceleración. *Dyna*, *80*(179), 116-125. https://repositorio.unal.edu.co/handle/unal/41449

Housner, G. W., Bergman, L. A., Caughey, T. K., Chassiakos, A. G., Claus, R. O., Masri, S. F., Skelton, R. E., Soong, T. T., Spencer, B. F., and Yao, J. T. P. (1997). Structural control: Past, present, and future. *Journal of Engineering Mechanics*, *123*(9), 897-971. https://doi.org/10.1061/(ASCE)0733-9399(1997)123:9(897)

K-Karamodin, A., and H-Kazemi, H. (2010). Semi-active control of structures using neuro-predictive algorithm for MR dampers. *Structural Control and Health Monitoring*, *17*(3), 237-253. https://doi.org/10.1002/stc.278

Kannan, S., Uras, H. M., and Aktan, H. M. (1995). Active control of building seismic response by energy dissipation. *Earthquake Engineering and Structural Dynamics*, *24*(5), 747-759. https://doi.org/10.1002/eqe.4290240510

Kataria, N. P., and Jangid, R. S. (2016). Seismic protection of the horizontally curved bridge with semi-active variable stiffness damper and isolation system. *Advances in Structural Engineering*, *19*(7), 1103-1117. https://doi.org/10.1177/1369433216634477

Kaveh, A., Javadi, S. M., and Moghanni, R. M. (2020). Optimal structural control of tall buildings using tuned mass dampers via chaotic optimization algorithm. *Structures*, *28*, 2704-2713. https://doi.org/10.1016/j.istruc.2020.11.002

Khodabandolehlou, H., Pekcan, G., Fadali, M. S., and Salem, M. M. A. (2018). Active neural predictive control of seismically isolated structures. *Structural Control and Health Monitoring*, *25*(1), e2061. https://doi.org/10.1002/stc.2061

Kim, H., and Adeli, H. (2005). Hybrid control of irregular steel highrise building structures under seismic excitations. *International Journal for Numerical Methods in Engineering*, *63*, 1757-1774. https://doi.org/10.1002/nme.1336

Kori, J. G., and Jangid, R. S. (2008). Semiactive control of seismically isolated bridges. *International Journal of Structural Stability and Dynamics*, *08*(04), 547-568. https://doi.org/10.1142/S021945540800279X

Lara-Valencia, L. A., Farbiarz-Farbiarz, Y., and Valencia-González, Y. (2020). Design of a tuned mass damper inerter (tmdi) based on an exhaustive search optimization for structural control of buildings under seismic excitations. *Shock and Vibration*, *2020*, 8875268. https://doi.org/10.1155/2020/8875268

Lara-Valencia, L. A., Valencia-González, Y., and de Brito, J. L. V. (2015). Use of fuzzy logic for the administration of a structural control system based on magnetorheological dampers. *Revista Facultad de Ingeniería*, *74*(1), 151-164. https://revistas.udea.edu.co/index.php/ingenieria/article/view/16461?articlesBySimilarityPage=71

Lara-Valencia, L. A. (2011). *Estudo de algorítimo de controle semi-ativo aplicados a amortecedores* [Doctoral thesis, Universidade de Brasilia]. https://repositorio.unb.br/handle/10482/9389

Liu, Y., Gordaninejad, F., Evrensel, C. A., and Hitchcock, G. H. (2001, July 30). *Experimental study on fuzzy logic vibration control of a bridge using fail-safe magnetorheological fluid dampers* [Conference presentation]. SPIE's 8th Annual International Symposium on Smart Structures and Materials, Newport beach, CA, USA. https://doi.org/10.1117/12.434135

Lord Company (2006). *Products and solutions*. https://www.lord.com/products-and-solutions

Madhekar, S. N., and Jangid, R. S. (2009). Variable dampers for earthquake protection of benchmark highway bridges. *Smart Materials and Structures*, *18*(11), 115011. https://doi.org/10.1088/0964-1726/18/11/115011

Mohammadi, R. K., Ghamari, H., and Farsangi, E. N. (2021). Active control of building structures under seismic load using a new uniform deformation-based control algorithm. *Structures*, *33*, 593-605. https://doi.org/10.1016/j.istruc.2021.04.054

Omidi, E., and Mahmoodi, N. (2015). Hybrid positive feedback control for active vibration attenuation of flexible structures. *IEEE/ASME Transactions on Mechatronics*, *20*(4), 1790-1797. https://doi.org/10.1109/TMECH.2014.2354599

Pahlavan, L., and Rezaeepazhand, J. (2007). Dynamic response analysis and vibration control of a cantilever beam with a squeeze-mode electrorheological damper. *Smart Materials and Structures*, *16*(6), 2183-2189. https://doi.org/10.1088/0964-1726/16/6/021

Pourzeynali, S., Lavasani, H. H., and Modarayi, A. H. (2007). Active control of high rise building structures using fuzzy logic and genetic algorithms. *Engineering Structures*, *29*(3), 346-357. https://doi.org/10.1016/j.engstruct.2006.04.015

Selmani, F. H. (2020, October 31). Passive control of structures – The dynamic case. *UBT International Conference, 239*, 165-174. https://doi.org/10.33107/ubt-ic.2020.82

Shih, M.-H., and Sung, W.-P. (2021). Structural control effect and performance of structure under control of impulse semi-active mass control mechanism. *Iranian Journal of Science and Technology, Transactions of Civil Engineering*, *45*(2), 1211-1226. https://doi.org/10.1007/s40996-020-00387-9

Singh, M. P., Matheu, E. E., and Suárez, L. E. (1997). Active and semi-active control of structures under seismic excitation. *Earthquake Engineering and Structural Dynamics*, *26*(2), 193-213. https://doi.org/10.1002/(SICI)1096-9845(199702)26:2%3C193::AID-EQE634%3E3.0.CO;2-%23

Smanchai, S., and Yao, J. (1978). Active control of building structures. Journal of the engineer-ing mechanics division. *Journal of the Engineering Mechanics Division, 104*(2), 335-350. https://doi.org/10.1061/JMCEA3.0002335

Spencer Jr, B., Dyke, S. J., Sain, M. K., and Carlson, J. D. (1997). Phenomenological model for magnetorheological dampers. *Journal of Engineering Mechanics*, *123*(3), 230-238. https://doi.org/10.1061/(ASCE)0733-9399(1997)123:3(230)

Subramaniam, R. S., Reinhorn, A. M., Riley, M. A., and Nagarajaiah, S. (1996). Hybrid control of structures using fuzzy logic. *Computer-Aided Civil and Infrastructure Engineering*, *11*(1), 1-17. https://doi.org/10.1111/j.1467-8667.1996.tb00305.x

Sun, C., and Nagarajaiah, S. (2014). Study on semi-active tuned mass damper with variable damping and stiffness under seismic excitations. *Structural Control and Health Monitoring*, *21*(6), 890-906. https://doi.org/10.1002/stc.1620

Taniguchi, M., Fujita, K., Tsuji, M., and Takewaki, I. (2016). Hybrid control system for greater resilience using multiple isolation and building connection. *Frontiers in Built Environment*, *2,* 26. https://doi.org/10.3389/fbuil.2016.00026

Wilson, C. M. D. (2005). *Fuzzy control of magnetorheological dampers for vibration reduction of seismically excited structures* [Doctoral thesis, The Florida State University].

Xu, Z.-D., Shen, Y.-P., and Guo, Y.-Q. (2003). Semi-active control of structures incorporated with magnetorheological dampers using neural networks. *Smart Materials and Structures*, *12*(1), 80-87. https://doi.org/10.1088/0964-1726/12/1/309

Yang, J. N., Li, Z., Danielians, A., and Liu, S. C. (1992). Aseismic hybrid control of nonlinear and hysteretic structures I. *Journal of Engineering Mechanics*, *118*(7), 1423-1440. https://doi.org/10.1061/(ASCE)0733-9399(1992)118:7(1423)

Zamani, A. A., Tavakoli, S., and Etedali, S. (2017). Control of piezoelectric friction dampers in smart base-isolated structures using self-tuning and adaptive fuzzy proportional-derivative controllers. *Journal of Intelligent Material Systems and Structures*, *28*(10), 1287-1302. https://doi.org/10.1177/1045389X16667561

Zhang, Z., and Balendra, T. (2013). Passive control of bilinear hysteretic structures by tuned mass damper for narrow band seismic motions. *Engineering Structures*, *54*, 103-111. https://doi.org/10.1016/j.engstruct.2013.03.044

Zhao, Z., Zhang, R., Wierschem, N. E., Jiang, Y., and Pan, C. (2020). Displacement mitigation–oriented design and mechanism for inerter-based isolation system. *Journal of Vibration and Control*, *27*(17-18), 1991-2003. https://doi.org/10.1177/1077546320951662

Zhou, Y., and Zheng, S. (2020). Machine-learning based hybrid demand-side controller for high-rise office buildings with high energy flexibilities. *Applied Energy*, *262*, 114416. https://doi.org/10.1016/j.apenergy.2019.114416

Ensemble Kalman Filter for Hourly Streamflow Forecasting in Huaynamota River, Nayarit, México

Filtro de Kalman de Conjuntos para pronóstico de caudales horarios en el río Huaynamota, Nayarit, México

Ildefonso Narváez-Ortiz [1], Laura Ibáñez-Castillo [2], Ramon Arteaga-Ramírez [3], and Mario Vázquez-Peña [4]

ABSTRACT

Hydrological phenomena are characterized by the formation of a non-linear dynamic system, and streamflows are not unrelated to this premise. Data assimilation offers an alternative for flow forecasting using the Ensemble Kalman Filter, given its relative ease of implementation and lower computational effort in comparison with other techniques. The hourly streamflow of the Chapalagana station was forecasted based on that of the Platanitos station in northwestern México. The forecasts were made from one to six steps forward, combined with set sizes of 5, 10, 20, 30, 50, and 100 members. The Nash-Sutcliffe coefficients of the Discrete Kalman filter were 0,99 and 0,85 for steps one and six, respectively, achieving the best fit with a tendency to shift the predicted series, similar to the persistent forecast. The Ensemble Kalman Filter (EnKF) obtained 0,99 and 0,05 in steps one and six. However, it converges on the observed series with the limitation of considerable overestimation in higher steps. All three algorithms have equal statistical adjustment values in step one, and there are progressive differences in further steps, where ARX and DKF remain similar and EnKF is differentiated by the overestimation. EnKF enables capturing non-linearity in sudden streamflow changes but generates overestimation at the peaks.

Keywords: Ensemble Kalman Filter, autoregressive models, short-term streamflow forecasting, data assimilation

RESUMEN

Los fenómenos hidrológicos se caracterizan por conformar un sistema dinámico no lineal, y los caudales no son ajenos a esta premisa. La asimilación de datos ofrece una alternativa para el pronóstico de caudales mediante el Filtro de Kalman de Conjuntos, dada su relativa facilidad de implementación y menor esfuerzo computacional en contraste con otras técnicas. Se pronosticó el caudal horario de la estación Chapalagana en función del de la estación Platanitos en el noroeste de México. Los pronósticos se realizaron de uno a seis pasos hacia adelante, combinados con tamaños de conjunto de 5, 10, 20, 30, 50 y 100 miembros. Los coeficientes de Nash-Sutcliffe para el Filtro de Kalman Discreto fueron de 0,99 y 0,85 en los pasos uno y seis respectivamente, logrando el mejor ajuste con tendencia a desplazar la serie pronosticada, similar al pronóstico persistente. El Filtro de Kalman de Conjuntos (EnKF) obtuvo 0,99 y 0,05 en los pasos uno y seis. No obstante, este converge sobre la serie observada con la limitante de sobrestimación considerable en pasos superiores. Los tres algoritmos tienen igual valor de ajuste estadístico en el paso uno, y se dan diferencias progresivas en pasos sucesivos, donde ARX y DKF se mantienen similares y EnKF se diferencia por la sobrestimación. EnKF permite captar la no linealidad en los cambios bruscos de caudal, pero genera sobrestimación en los picos.

Palabras clave: Filtro de Kalman de Conjuntos, modelos autorregresivos, pronósticos de caudales a corto plazo, asimilación de datos

Introduction

Climate variability has intensified the incidence of extreme precipitation events that can generate sudden changes in streamflow and lead to floods and landslides (IPCC, 2012). Having advance information on streamflow behavior becomes an indispensable tool for the administration of dams and disaster risk management (IPCC, 2012; Singh and Zommers, 2014). Different methods have been used for streamflow forecasting, such as autoregressive methods, neural networks (Box *et al.*, 2016; Shmueli and Lichtendahl, 2016), and, more recently, data assimilation methods such as Kalman filters (Abaza *et al.*, 2015; Alvarado-Hernández *et al.*, 2020; González-Leiva *et al.*, 2015; Morales-Velázquez *et al.*, 2014). In hydrological studies, the Ensemble Kalman

[1] PhD in Agricultural Engineering and Integral Water Use at Universidad Autónoma de Chapingo, Texcoco, México. Affiliation: International University of American Tropics – Unitrópico, Casanare Colombia. Email: ildenarvaez@unitropico.edu.co

[2] PhD in Civil Engineering from Texas A&M University. Affiliation: Universidad Autónoma de Chapingo, Texcoco, México. Email: libacas@gmail.com

[3] PhD in Hydrosciences from Colegio de Postgraduados. Affiliation: Universidad Autónoma de Chapingo, Texcoco, México. Email: arteagar@correo.chapingo.mx

[4] PhD in Statistics from Colegio de Postgraduados. Affiliation: Universidad Autónoma de Chapingo, Texcoco, México. Email: mvazquezp@chapingo.mx

Filter (EnKF) (Evensen, 1994, 2009; Gillijns et al., 2006) has been widely used as a method of assimilation (Liu and Gupta, 2007; Maxwell et al., 2018; Sun et al., 2016), with little evaluation in forecasting flows. EnKF is an extension of the Discrete Kalman Filter (DKF) (Kalman, 1960) and a computationally less demanding alternative to the Extended Kalman Filter (EKF) for treating non-linear dynamic systems (Evensen, 1994, 2003). Among the applications of EnKF are streamflow forecasting in basins dominated by melting snow and ice (Abaza et al., 2015), evapotranspiration (Zou et al., 2017), and soil moisture (Brandhorst et al., 2017; Meng et al., 2017). Moreover, it has been evaluated while integrated with distributed hydrological models such as TopNet, Hydrotel, and MGB-IPH (Abaza et al., 2015; Clark et al., 2008; Quiroz et al., 2019).

Hydrological phenomena such as streamflow have a non-linear behavior (Bai et al., 2016; Xu et al., 2009), especially when there are sudden changes in river levels. For this reason, the use of non-linear algorithms for data assimilation favors the fit of forecasts (Brandhorst et al., 2017; Medina-González et al., 2015). In addition, systematic errors can be reduced by recursive updating based on each new available measurement (Clark et al., 2008; Maxwell et al., 2018).

According to Valdés et al. (1980) and Winkler et al. (2010), in hydrographic basins, different representative measurements and a point of interest have a dynamic relationship with the predominant physical and biological characteristics of the area. Based on this information, the behavior of a given phenomenon is modeled to obtain short-term forecasts. The Kalman filter enables the incorporation of registers from diverse sources, as well as continuous updates (Box et al., 2016; Welch and Bishop, 2006).

To determine whether the algorithms for identifying non-linear dynamic systems allow forecasting short-term streamflow (6 h), this study evaluates the fit of the series predicted by algorithms of the EnKF, the DKF, and the first-order autoregressive model with first order exogenous variable (ARX(1, I)), in flows measured at the Chapalagana station on the Huaynamota River. The Kalman Filter algorithms estimate the system dynamic states and correspond to the response function of the basin.

Materials and methods

This study was conducted in a tributary of the Huaynamota River, also known as the Chapalagana or Atengo River, located in northwestern México between the states of Durango, Nayarit, Zacatecas, and Jalisco (INEGI, 2010) (Figure 1), between -104°33'34,16" and -103°27'29,84" W and between 23°28'50,05" and 21°23'57,62" N, with an area of 12 075,7 km². The altitude varies from 219 to 3 147 masl. The concentration time is 39,88 h, the mean annual precipitation is 707 mm, and the mean annual temperature is 17,9 °C (SMN, 2019).
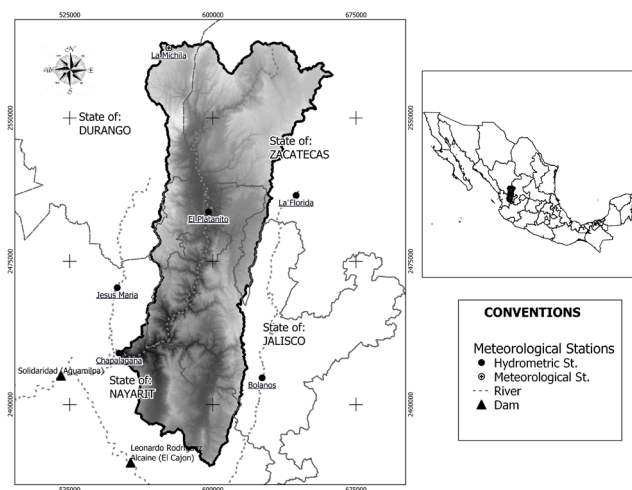
Figure 1. Location of the study area
Source: Authors

The Huaynamota River contributes to generating electricity. The Solidaridad dam (also known as Aguamilpa), located on the Lerma-Santiago River and geographically at 104°48'10,55" W and 21°50'22,74" N, produces 960 MW of electricity and has a maximum capacity of 5 540 million m³ of water (CONAGUA, 2008). The Huaynamota River discharges into the Santiago River, where the Aguamilpa dam is located, approximately 90 km upstream from the Pacific Ocean, into which the Santiago River empties on the coast of the Mexican state of Nayarit.

We implemented the EnKF (Evensen, 1994), DKF (Kalman, 1960), and ARX(1,1) (Bras and Rodríguez-Iturbe, 1985) algorithms. Forecasts were made at 1, 2, 3, 4, 5, and 6 h (L steps forward) of the flows at the Chapalagana station as a function of the flows at the Platanito station, located 100 km upstream from Chapalagana, as the exogenous variable. The hourly streamflow series between 9:00 hours on August 2 and 0:00 hours on September 28, 2017, were used, for a total of 1 360 registers supplied by Federal Electricity Comission (CFE).

EnKF, DKF, and ARX were implemented through R routines (R Core Team, 2021), which generate forecasts in six steps with DKF and ARX, and with 42 combinations between steps by set size in EnKF. Both EnKF and DKF were implemented to estimate the state vector corresponding to the response function of the basin, or Instantaneous Unitary Hydrograph (IUH) (Valdés et al., 1980). Values were estimated which correspond to the columns of the IUH. Multiplying these values by those of the measured series results in an estimation. In the three algorithms, the last observations of each series were considered (Valdés et al., 1980). The ARX model was recursively implemented based on a fraction of a series with 100 registers.

By means of the sensitivity analysis with 5, 10, 20, 30, 40, 50, and 100 members that were combined with the six steps, and based on the root mean square error (RMSE),

the adequate number of members in the EnKF sets was determined (Quiroz et al., 2019). White noise that is integrated in the EnKF members was generated with the mvtnorm package (Multivariant Normal and t Distributions) (Genz and Bretz, 2009). In the evaluated Kalman Filter algorithms, the Q variance was assumed to be constant (Simon, 2001) with a value of zero (Morales-Velázquez et al., 2014), and the R was assumed to have a near-zero value (0,01) in order to confer flexibility to the convergence of the algorithm (Welch and Bishop, 2006). With these values, the covariance matrices were created.

The fit reached by each algorithm was evaluated using the Nash-Sutcliffe coefficient (NS) (Nash and Sutcliffe, 1970) and the RMSE (Morales-Velázquez et al., 2014), as expressed by Equations (1) and (2). The assumed normality of errors was verified using graphs (González-Leiva et al., 2015).

$$NS = 1 - \frac{\sum_{i=1}^{i=n} (\hat{y}_i - y_i)^2}{\sum_{i=1}^{i=n} (\bar{y}_i - \hat{y}_i)^2} \qquad (1)$$

$$RMSE = \sqrt{\frac{\sum_{i=1}^{n} (\hat{y}_i - y_i)^2}{n}} \qquad (2)$$

where y_i is the forecasted data, y_i is the observed data, $\hat{y}_i$ is the average of the observed data, $\hat{y}_i$ is average of the forecasted data, and n is the amount of observations.

Ensemble Kalman Filter

To extend the functionality of the DKF (Kalman, 1960) and deal with non-linear dynamic systems, the EKF, among others, has been proposed (Jazwinski, 2007; Welch and Bishop, 2006), which includes the EnKF (Evensen, 1994, 2009). The EnKF emerges as an alternative to the EKF, which has a high computational demand (Evensen, 1994, 2009) and is a sub-optimal estimator that, via Monte Carlo simulations, estimates the statistical error (Evensen, 1994; Gillijns et al., 2006; Rafieeinasab et al., 2014). Errors should satisfy the normal distribution assumption and are estimated based on sets of q values.

The algorithm is based on two groups of equations: forecast and analysis (Figure 2). In this study, the cycle began with the forecast equations, using the random values that make up the first matrix x_{kai}, thus obtaining the first forecast via the measurement equation. The error matrices of the forecast were calculated against the new measurement, which is the input for the analysis equations, where the states are updated as new measurements are entered.

The h matrix is formed with the last register of two (n) hourly flow series of the Chapalagana and Platanitos stations. The uk parameter is absent because, in the upstream from the Chapalagana station, there are no structures (e.g., dams) that have a direct impact on streamflow. The errors v_k^i and v_k^i correspond to the noise contained by the process and the

measurement, respectively. They are assumed to be white noise, with a mean of zero and variance Q and R (Figure 2). The noise in the measurements is generated by adding q deviations with normal distribution to the measurement in k time.

In the second analysis equation, the component $y_k + v_k^i$ represents the noisy measurements, y_k is the measurement in time k, and the superscript i represents the number of members, i.e., random values under normal distribution that correspond to $i = 1, 2, \ldots, \ldots, q$. The adequate number of members in a set in hydrological studies is between 50 and 300 (Gillijns et al., 2006; Quiroz et al., 2019). The predicted value z_k is obtained by averaging the vector resulting from multiplying the h matrix and the x_{k-1}^{ai} and applying the measurement equation.

Discrete Kalman Filter

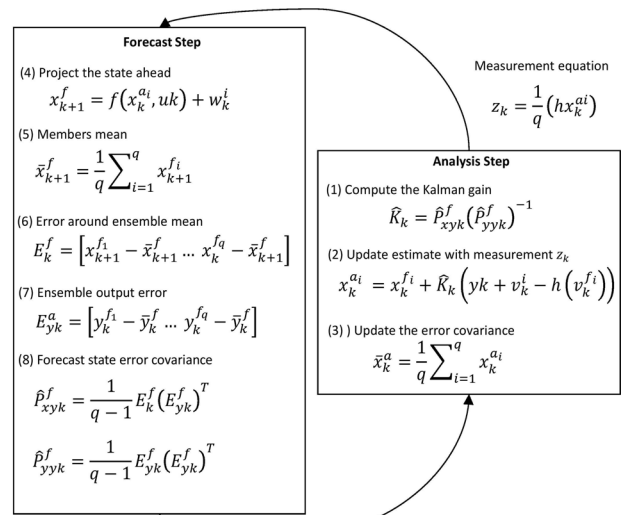The DKF is an optimal recursive estimator of states in linear dynamic systems (Kalman, 1960) (Figure 2).

Figure 2. EnKF algorithm
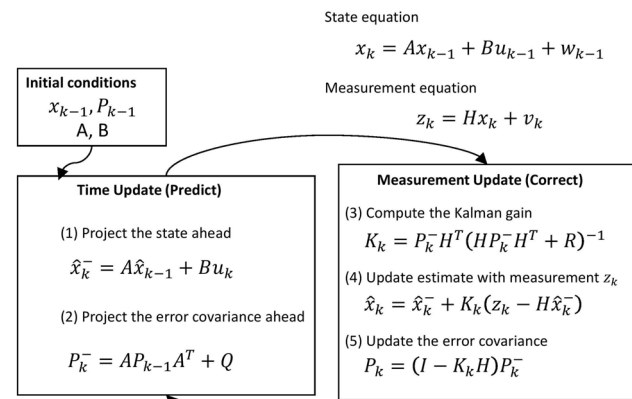**Source:** Gillijns et al. (2006)

Figure 3. DKF algorithm
Source: Welch and Bishop (2006)

The state equation has two (n) hourly flow series from the Chapalagana and Platanitos stations. The matrices A (n x n) and B (n x 1) relate the state at time $k - 1$ to the current state at time k. Like the EnKF, the control matrix B is not included, given that, in the upriver from the Chapalagana station, there are no structures that have a direct impact on streamflow. Matrix A is assumed constant throughout the process, and matrix H is composed of a vector row of $1 \times n$ that contains the last observation of each entry series. The predicted value z_k is obtained via the measurement equation by multiplying the H matrix by the state vector x_k (n x 1).

Implicit in the predicted value z_k is the measurement error w_{k-1}, and, likewise, the process error v_k is contained in the state equation. In both cases, the normality assumption must be satisfied.

The state and measurement equations maintain a cycle that is repeated indefinitely. At time $k - 1$, it makes the *a priori* estimation (forecast) of the states, and, at time k, they are updated (*a posteriori* estimation). The states are assumed to be the response function of the basin, and the *a posteriori* estimation corresponds to the forecast for time $k + 1$. This cycle is repeated indefinitely, predicting time $k + 1$ based on the H matrix and the state vector updated to time k.

First-order autoregressive model

One of the first approximations for the forecast is the first-order autoregressive model, which is based on the autocorrelation that occurs within the same series of data (Box *et al.*, 2016; Bras and Rodríguez-Iturbe, 1985). Algebraically, it is described as follows:

$$y_{k+1} = \sum_{i=0}^{na} \alpha_i y_{k-i} + \sum_{j=0}^{nb} \beta_j \gamma_{k-j} + e_{k+1} \quad (3)$$

where y_{k+1} is the predicted value, α_i and β_j are the model parameters, and y_k and γ_k correspond to the entry variable and the exogenous variable, respectively. The parameters are estimated by the method of least squares, which requires a series section of at least 50 registers (Box *et al.*, 2016; Shmueli and Lichtendahl, 2016). In the $ARX(na, nb)$ model, na and nb represent the autoregressive delays that are used in each variable.

Results and discussion

Forecasts with six-hour steps were made of the flows at the Chapalagana station. For the case of EnKF, seven set sizes were evaluated in order to estimate the error, which had 6, 10, 20, 30, 40, 50, and 100 members. Series with 1 360 registers were used, which included two main events.

As of 50 members per set, the EnKF algorithm showed a stable convergence for all steps. Consequently, under the conditions of this study, it is acceptable to use at least 50

members per set to have an adequate fit regarding the convergence of the algorithm and the stabilization of the error, aiming to minimize computational effort. As previously indicated, the results presented below have a base of 50 members per set. Table 1 presents the statistical indicators of fit for the observed series against the predicted one.
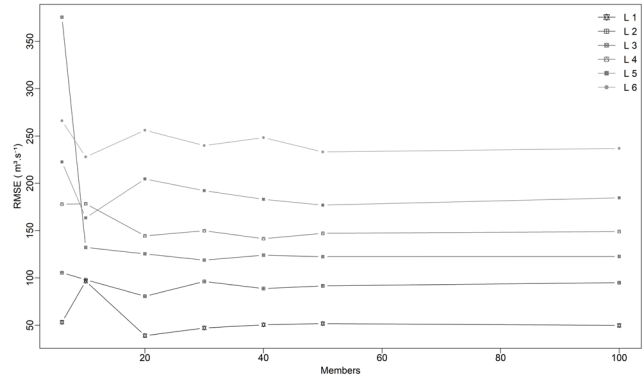
Figure 4. RMSE for different set sizes
Source: Authors

Table 1. Summary of statistics for application of EnKF, DKF, and ARX

Algorithm	Metric	L1	L2	L3	L4	L5	L6
DKF	RMSE	27,27	44,99	58,84	70,84	81,69	92,09
	Nash-Sutcliffe	0,99	0,96	0,94	0,91	0,88	0,85
	Mean	199,39	198,22	197,37	196,43	195,44	194,39
	SD	241,28	239,47	238,41	237,39	236,42	235,42
EnKF	RMSE	51,77	91,61	122,43	147,15	176,96	233,10
	Nash-Sutcliffe	0,95	0,85	0,74	0,62	0,45	0,05
	Mean	202,29	206,91	211,78	216,71	222,32	230,85
	SD	250,35	268,34	287,56	308,41	330,24	370,35
ARX(1,1)	RMSE	27,84	48,34	65,83	79,89	91,14	99,74
	Nash-Sutcliffe	0,99	0,96	0,92	0,89	0,86	0,83
	Mean	200,88	202,51	203,83	204,81	205,93	206,42
	SD	243,54	245,72	248,35	250,15	251,53	251,21

Note: RMSE: root mean square error; Nash-Sutcliffe: Nash-Sutcliffe index; Mean: Average. The mean and standard deviation (SD) of the observed series are 198,7 and 239,77, respectively.

Source: Authors

According to the statistical indicators in Table 1, the NS shows similarities between DKF and ARX, with values of 0,99 and 0,83 in steps one and six, respectively, while EnKF obtained 0,95 and 0,05 in steps one and six. According to the NS, the fit of all the steps is less with EnKF; in step one, it is 0,04 less, and there is a marked change up to step six, where the difference is around 0,78. The mean of the predicted series is more stable with DKF, followed by ARX and, finally, EnKF. EnKF and ARX show an upward trend in the mean value for each step, whereas DKF has a downward trend.

Despite the low fit values, the EnKF algorithm expressed the changes with a non-linear trend and showed better convergence on the observed series once it was updated with new measurements. DKF and ARX generated forecasts in which the displacement of the predicted series was accentuated against the observed series, similar to the persistent forecast method (Aguado-Rodríguez *et al.*, 2016;

Kavasseri and Seetharaman, 2009). This behavior is also noticeable in the work of Alvarado-Hernández *et al*. (2020), González-Leiva *et al*. (2015), and Morales-Velázquez *et al*. (2014).

In the flood that began at 810 h, EnKF assumed the abrupt change in flow and generated a forecast with a steeper slope than DKF and ARX. Also, in the flow descents between 870 and 900 h, EnKF converged more precisely on the observed series (Figure 5).
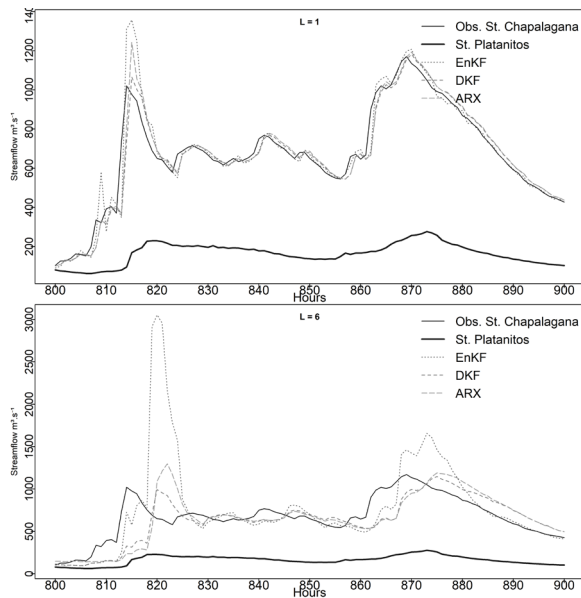
Figure 5. Observed flow and flows predicted with EnKF, DKF, and ARX (flood from 4/9/2017, 16:00 h, to 8/9/2017, 20:00 h)
Source: Authors

The DKF fits are similar to those obtained by Alvarado-Hernández *et al*. (2020), who used the same series and a model that integrates ARX and DKF. This model considers the delay between series to be one, whereas, in our study, it was updated dynamically throughout the series, favoring the fit at peaks and reducing the effect of displacement of the predicted series. EnKF, in its six steps, obtained lower fits due to overestimation or underestimation at the peaks, with the difference that it achieved a better fit in ascents and descents of the observed series. The EnKF algorithm obtained a better temporal fit at peaks and converged more precisely on the observed series when the trend persisted in a number of hours higher or equal to the evaluated step.

The forecast with EnKF showed overestimations relative to the observed series. This occurred because we treated the measurements as a non-linear phenomenon (Evensen, 1994, 2009), a situation that, in step one, allows for an acceptable fit in the entire series. However, in step six, broad overestimations may be found which can affect the quality of the forecast. As the forecast step increases, the frequency of overestimations increases because the new register that serves to update the states also breaks away, and there may be changes in the L interval that are not considered in the initial forecast. The dynamic incorporation of the delay time

between series (Meng *et al*., 2017) allows improving the fit, given that updating is performed with the equivalent event in the exogenous variable (Figure 6).
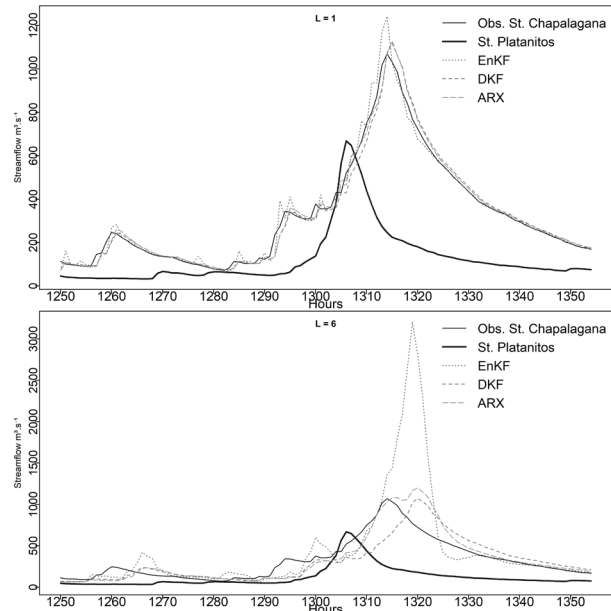
Figure 6. Observed flow and flows predicted with EnKF, DKF and ARX (flood from 23/09/17, 10:00 h, to 28/09/17, 00:00 h)
Source: Authors

The dispersion of the observed series against the predicted one was congruent with the NS index, highlighting the similarities between DKF and ARX. The difference exhibited by EnKF is due to the peaks associated with abrupt changes in flow. The EnKF algorithm tended to overestimate throughout the series, unlike DFK and ARX, which caused a slight tendency to underestimate. Step six with EnKF produced large overestimations that are reflected as isolated points above the diagonal in Figure 7.
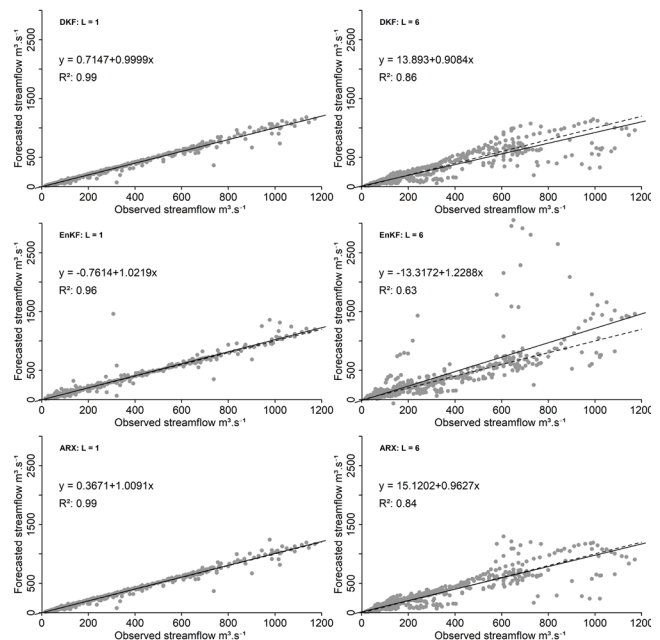
Figure 7. Observed *vs*. predicted flows
Source: Authors
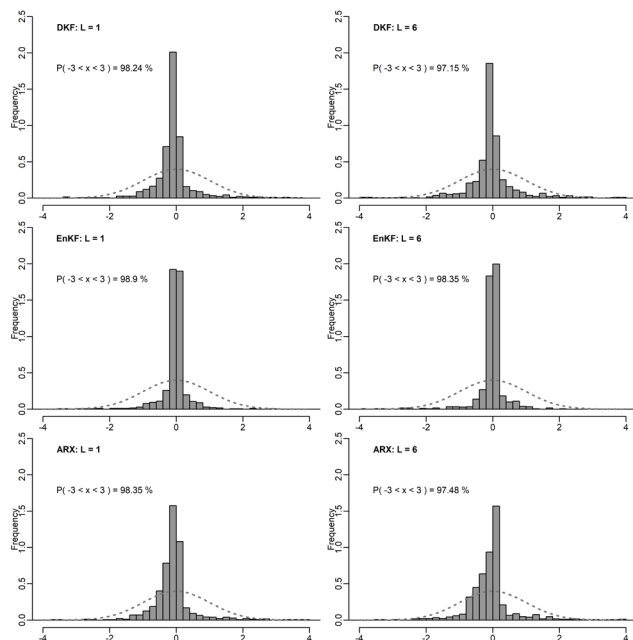
Figure 8. Histograms of residuals
Source: Authors

The standardized errors of the forecasts have a symmetrical distribution around zero (Figure 8) (Cryer and Chan, 2008; Martínez *et al.*, 2012; Wang *et al.*, 2017). According to Chatfield (2001), a behavior approaching normality is accepted. As shown in Figure 8, there is symmetry and higher concentration of registers in the central area of the Gauss bell curve. The proportion of registers between three standard deviations above and below the mean is more than 97%, and EnKF had the highest values in all steps.

As the steps of the forecast increase, the fit decreases, and overestimations and underestimations become more frequent for EnKF. Introducing coefficients that represent stationality and autocorrelation into the transference function can reduce the over-dimensioned estimations and achieve better fit.

Conclusions

The dynamic updating of delay time relative to the exogenous variable allowed improving the fit in the evaluated algorithms. The EnKF algorithm achieved a better convergence on the observed series but generated overestimations of greater magnitude as the step increased, which resulted in a lower degree of fit, as demonstrated with the Nash-Sutcliffe index. The potential of EnKF lies in its convergence and non-linear treatment of abrupt changes in flow. Basically, EnKF helps capture the non-linearity in some parts of the of the hydrograph and accurately represents the timing or times of occurrence of maximum flows, even though they are overestimated.

In future studies, the use of EnKF for streamflow forecasting can be a viable alternative when integrated with autocorrelation analysis, so that stationality and stationarity become part of the model, thus allowing to represent the

changes associated with daytime, nighttime, or the months of the year. Together, the quantity of registers for updating the states can be increased in order to enable the detection of changes in trends during the last registered hours.

To improve the fit of the forecast, it is important to advance in research with step sizes of several hours (*e.g.*, groups of six hours using the mean or maximum) in such a way that each step is equivalent to six hours and the forecast at six steps equals 36 hours.

Acknowledgements

References

Abaza, M., Anctil, F., Fortin, V., and Turcotte, R. (2015). Exploration of sequential streamflow assimilation in snow dominated watersheds. *Advances in Water Resources*, *86*, 414-424. https://doi.org/10.1016/j.advwatres.2015.10.008

Aguado-Rodríguez, J., Quevedo-Nolasco, A., Castro-Popoca, M., Arteaga-Ramírez, R., Vázquez-Peña, M., and Zamora-Morales, P. (2016). Predicción de variables meteorológicas por medio de modelos ARIMA. *Agrociencia*, *50*(1). http://www.scielo.org.mx/scielo.php?script=sci_arttext&pid=S1405-31952016000100001

Alvarado-Hernández, L., Ibáñez-Castillo, L., Ruiz-García, A., González-Leiva, F., and Vázquez-Peña, M. (2020). Pronóstico horario de caudales mediante filtro de kalman discreto en el Río Huaynamota, Nayarit, México. *Agrociencia*, *54*, 295-312. https://doi.org/10.47163/agrociencia.v54i3.1907

Bai, L., Chen, Z., Xu, J., and Li, W. (2016). Multi-scale response of runoff to climate fluctuation in the headwater region of Kaidu River in Xinjiang of China. *Theoretical and Applied Climatology*, *125*(3-4), 703-712. https://doi.org/10.1007/s00704-015-1539-2

Box, G., Jenkins, G., Reinsel, G., and Ljung, G. (2016). *Time series analysis: Forecasting and control* (5th ed.). Wiley.

Brandhorst, N., Erdal, D., and Neuweiler, I. (2017). Soil moisture prediction with the ensemble Kalman filter: Handling uncertainty of soil hydraulic parameters. *Advances in Water Resources*, *110*, 360-370. https://doi.org/10.1016/j.advwatres.2017.10.022

Bras, R., and Rodríguez-Iturbe, I. (1985). *Random functions and hydrology*. Addison-Wesley Publishing Company.

Chatfield, C. (2001). Prediction intervals for time-series forecasting. In J. S. Armstrong (Ed.), *A Handbook for Researchers and Practitioners* (vol. 30, pp. 475-494). Springer. https://doi.org/10.1007/978-0-306-47630-3

Clark, M. P., Rupp, D. E., Woods, R. A., Zheng, X., Ibbitt, R. P., Slater, A. G., Schmidt, J., and Uddstrom, M. J. (2008). Hydrological data assimilation with the ensemble Kalman filter: Use of streamflow observations to update states in a

distributed hydrological model. *Advances in Water Resources*, *31*(10), 1309-1324. https://doi.org/10.1016/j.advwatres.2008.06.005

CONAGUA (2008). *Estadisticas del agua en México*. SEMARNAT.

Cryer, J. D., and Chan, K.-S. (2008). *Time series analysis with applications in R* (2nd ed.). Springer. https://doi.org/10.1007/978-0-387-75959-3

Evensen, G. (1994). Sequential data assimilation with a nonlinear quasi-geostrophic model using Monte Carlo methods to forecast error statistics. *Journal of Geophysical Research*, *99*(C5), 10143. https://doi.org/10.1029/94jc00572

Evensen, G. (2003). The Ensemble Kalman Filter: Theoretical formulation and practical implementation. *Ocean Dynamics*, *53*(4), 343-367. https://doi.org/10.1007/s10236-003-0036-9

Evensen, G. (2009). *Data assimilation: The ensemble Kalman filter* (2nd ed.). Springer. https://doi.org/10.1007/978-3-642-03711-5

Field, C. B., Barros, V., Stocker, T. F., and Dahe, Q. (Eds.) (2012). *Managing the risks of extreme events and disasters to advance climate change adaptation*. Cambridge University Press. https://doi.org/10.1017/CBO9781139177245

Genz, A., and Bretz, F. (2009). *Computation of multivariate normal and t probabilities*. Springer. https://doi.org/10.1007/978-3-642-01689-9

Gillijns, S., Mendoza, O. B., Chandrasekar, J., De Moor, B. L. R., Bernstein, D. S., and Ridley, A. (2006, June 14-16). *What is the ensemble Kalman filter and how well does it work?* [Conference presentation]. 2006 American Control Conference, Minneapolis, MN, USA. https://doi.org/10.1109/ACC.2006.1657419

González-Leiva, F., Ibáñez-Castillo, L. A., Valdés, J. B., Vázquez-Peña, M. A., and Ruiz-García, A. (2015). Pronóstico de caudales con Filtro de Kalman Discreto en el río Turbio. *Tecnologia y Ciencias Del Agua*, *6*(4), 5-24. http://revistatyca.org.mx/ojs/index.php/tyca/article/view/1176

INEGI (2010). *Hidrografía*. https://www.inegi.org.mx/temas/hidrografia/default.html#Descargas

Jazwinski, A. H. (2007). *Stochastic processes and filtering theory*. Dover Publications.

Kalman, R. E. (1960). A new approach to linear filtering and prediction problems. *Journal of Basic Engineering*, *82*(Series D), 35-45. https://doi.org/10.1115/1.3662552

Kavasseri, R. G., and Seetharaman, K. (2009). Day-ahead wind speed forecasting using f-ARIMA models. *Renewable Energy*, *34*(5), 1388-1393. https://doi.org/10.1016/j.renene.2008.09.006

Liu, Y., and Gupta, H. V. (2007). Uncertainty in hydrologic modeling: Toward an integrated data assimilation framework. *Water Resources Research*, *43*(7), W07401. https://doi.org/10.1029/2006WR005756

Martínez, J., Domínguez, E., and Rivera, H. (2012). Uncertainty regarding instantaneous discharge obtained from stage-discharge rating curves built with low density discharge measurements. *Ingenieria e Investigación*, *32*(1), 30-35. https://revistas.unal.edu.co/index.php/ingeinv/article/view/28517

Maxwell, D. H., Jackson, B. M., and McGregor, J. (2018). Constraining the ensemble Kalman filter for improved streamflow forecasting. *Journal of Hydrology*, *560*, 127-140. https://doi.org/10.1016/j.jhydrol.2018.03.015

Medina-González, H., Hernández-Pereira, Y., Santiago-Piloto, A. B., and Lau Quan, A. (2015). Modelación de perfil de humedad de suelos empleando un filtro de Kalman de Monte Carlo. *Revista Ciencias Técnicas Agropecuarias*, *24*(2), 31-37. http://scielo.sld.cu/scielo.php?script=sci_arttext&pid=S2071-00542015000200005

Meng, S., Xie, X., and Liang, S. (2017). Assimilation of soil moisture and streamflow observations to improve flood forecasting with considering runoff routing lags. *Journal of Hydrology*, *550*, 568-579. https://doi.org/10.1016/j.jhydrol.2017.05.024

Morales-Velázquez, M. I., Aparicio, J., and Valdés, J. B. (2014). Pronóstico de avenidas utilizando el filtro de Kalman discreto. *Tecnologia y Ciencias Del Agua*, *5*(2), 85-110. http://www.scielo.org.mx/scielo.php?script=sci_arttext&pid=S2007-24222014000200006

Nash, J. E., and Sutcliffe, J. V. (1970). River flow forecasting through conceptual models part I — A discussion of principles. *Journal of Hydrology*, *10*(3), 282-290. https://doi.org/10.1016/0022-1694(70)90255-6

Quiroz, K., Collischonn, W., and de Paiva, R. C. D. (2019). Data assimilation using the ensemble Kalman filter in a distributed hydrological model on the Tocantins River, Brasil. *RBRH*, *24*, e14. https://doi.org/10.1590/2318-0331.241920180031

R Core Team. (2021). *R: A language and environment for statistical computing*. R Foundation for Statistical Computing. https://www.r-project.org/

Rafieeinasab, A., Seo, D. J., Lee, H., and Kim, S. (2014). Comparative evaluation of maximum likelihood ensemble filter and ensemble Kalman filter for real-time assimilation of streamflow data into operational hydrologic models. *Journal of Hydrology*, *519*(PD), 2663-2675. https://doi.org/10.1016/j.jhydrol.2014.06.052

Shmueli, G., and Lichtendahl, K. (2016). *Practical time series forecasting with R: A hands on guide*. Axelrod Schnall Publishers.

Simon, D. (2001, June). Kalman filtering. *Embedded Systems Programming*, 72-79. https://abel.math.harvard.edu/archive/116_fall_03/handouts/kalman.pdf

Singh, A., and Zommers, Z. (Eds.). (2014). *Reducing disaster: Early warning systems for climate change*. Springer. https://doi.org/10.1007/978-94-017-8598-3

Servicio Metereológico Nacional (SMN) (2019). *Sistema de información climática computarizada CLICOM*. Servicio Metereológico Nacional. http://clicom-mex.cicese.mx/malla/index.php

Sun, L., Seidou, O., Nistor, I., and Liu, K. (2016). Review of the Kalman-type hydrological data assimilation. *Hydrological Sciences Journal*, *61*(13), 2348-2366. https://doi.org/10.1080/02626667.2015.1127376

Valdés, J., Mejía, J., and Rodríguez-Iturbe, I. (1980). *Filtros de Kalman en la hidrología: predicción de descargas fluviales para la operación óptima de embalses. Informe Técnico No. 80-2*. https://n9.cl/hd6y9

Wang, S., Huang, G. H., Baetz, B. W., Cai, X. M., Ancell, B. C., and Fan, Y. R. (2017). Examining dynamic interactions among experimental factors influencing hydrologic data assimilation with the ensemble Kalman filter. *Journal of Hydrology*, *554*, 743-757. https://doi.org/10.1016/j.jhydrol.2017.09.052

Welch, G., and Bishop, G. (2006). *An introduction to the Kalman filter.* https://www.cs.unc.edu/~welch/media/pdf/kalman_intro.pdf

Winkler, R. D., Moore, R. D. D., Redding, T. E., Spittlehouse, D. L., Carlyle-Moses, D. E., and Smerdon, B. D. (2010). Hydrologic processes and watershed response. In R. Pike, T. Redding, R. Moore, R. Winkler, and K. Bladon (Eds.), *Compendium of forest hydrology and geomorphology in British Columbia* (pp. 133-178). B.C. Ministry of Forests and Range. https://www.for.gov.bc.ca/hfd/pubs/docs/lmh/Lmh66/Lmh66_ch06.pdf

Xu, J., Li, W., Ji, M., Lu, F., and Dong, S. (2009). A comprehensive approach to characterization of the nonlinearity of runoff in the headwaters of the Tarim River, western China. *Hydrological Processes*, *24*(2), 136-146. https://doi.org/10.1002/hyp.7484

Zou, L., Zhan, C., Xia, J., Wang, T., and Gippel, C. J. (2017). Implementation of evapotranspiration data assimilation with catchment scale distributed hydrological model via an ensemble Kalman Filter. *Journal of Hydrology*, *549*, 685-702. https://doi.org/10.1016/j.jhydrol.2017.04.036

Recent Trends in the Optimization of Renewable Distributed Generation: A Review

Tendencias recientes en la optimización de la generación distribuida renovable: una revisión

Vivek Saxena [1], Narendra Kumar [2], and Uma Nangia [3]

ABSTRACT

Distributed energy resources, or distributed generation (DG), are the mainstay of modern power systems aiming towards green energy generation via the effective integration of renewable energy sources. DG involvement in traditional power systems comprises the enhancement of power quality parameters, the utilization of renewable sources, cost optimization, and stable and reliable energy generation. The advantages of such a revolutionary approach can be achieved with the optimal sizing and allocation of DG by means of adequate optimization techniques, constraints, and optimized parameters. In this study, a comprehensive review of DG optimization is presented in light of recent developments, and a comparison is carried out based on the adopted optimization techniques, test system, enhanced parameters, and outcome evaluations.

Keywords: energy generation, distributed energy resources, renewable sources, optimization approach

RESUMEN

Los recursos energéticos distribuidos, o generación distribuida (GD), son el pilar de los sistemas energéticos modernos, que tienen como objetivo generar energía verde a través de la integración efectiva de fuentes de energía renovables. La participación de la GD en el sistema eléctrico tradicional abarca la mejora de los parámetros de calidad de la energía, la utilización de fuentes renovables, la optimización de costos y la generación de energía estable y confiable. Las ventajas de un enfoque tan revolucionario se pueden alcanzar asignando el tamaño y la ubicación óptimos de la GD mediante técnicas de optimización adecuadas, restricciones y parámetros optimizados. En este estudio se presenta una revisión completa de la optimización de GD en vista del desarrollo reciente, y se hace una comparación basada en las técnicas de optimización adoptadas, el sistema de prueba, los parámetros mejorados y las evaluaciones de resultados.

Palabras clave: generación de energía, recursos energéticos distribuidos, fuentes renovables, enfoque de optimización

Introduction

Distributed generation (DG) is different from the centralized generation of electrical energy, which is attributed to an approach that involves generation through small units situated near the end users. DG is also known as dispersed generation, embedded generation, or decentralized generation. Renewable and non-renewable energy resources can be utilized due to their technical, financial, and environmental advantages via the optimal establishing of DG. The qualities of electrical parameters that can be consigned in electrical power systems are real and reactive power losses, voltage stability, the tap setting of a transformer, power factor correction, reliability, fault level, and total harmonic reduction with the assimilation of DG.

Environmental pollution has been minimized by maximizing the use of renewable energy sources. Integrated generation models have been designed as an alternative to centralized generation, which demonstrate the potential of solar photovoltaic systems, wind power generation, biogas, and other natural energy sources. The emission level of hazardous pollutants can also be an objective parameter in a multi-objective function for DG allocation. The challenges of renewable energy amalgamation are the intermittent nature of energy sources, which are highly dependent on meteorological conditions and geographical structures (Saxena *et al.*, 2021).

[1] Research scholar, Department of Electrical Engineering, Delhi Technological University, Delhi, India. Assistant professor, Department of Electrical and Electronics Engineering, A.B.E.S. Engineering College, Ghaziabad, India. E-mail: vvksaxena1234@gmail.com

[3] Professor, Department of Electrical Engineering, Delhi Technological University, Delhi, India. E-mail: narendrakumar@dtu.ac.in

[4] Professor, Department of Electrical Engineering, Delhi Technological University, Delhi, India. E-mail: umanangia@dce.ac.in

Merits of DG planning

For optimal DG allocation, the objective function has been optimized by considering various constraints in order to determine the reliability, stability, and utility of the system. As per the desired level of operation, constraints such as load flow, voltage profile, line losses, transformer capacity, short circuit level, power quality, number, size, and capacity of DG may be a part of a single objective or multi-objective functions. As far as financial objectives are concerned, DG capital, operation, and maintenance costs have been considered for cost reduction and maximization of profit. In this process, the objective function includes revenue besides the expenditure, the penalty factor for constraints violations, the integrated cost parameters, and fixed and variable cost parameters.

The benefits of DG optimization are summarized in Figure 1. The planning of renewable DG in distribution networks has several advantages, and broad classifications are given as per the following highlights.

Technological benefits

DG integration in distribution networks reduces system losses and increases the efficacy, reliability, and optimal dispatch of the system. Moreover, the voltage profile and power factor are also simultaneously optimized with power loss minimization. The objective function may be single-objective or multi-objective and subjected to various equality and inequality constraints. Technological benefits are achieved after optimized DG allocation.
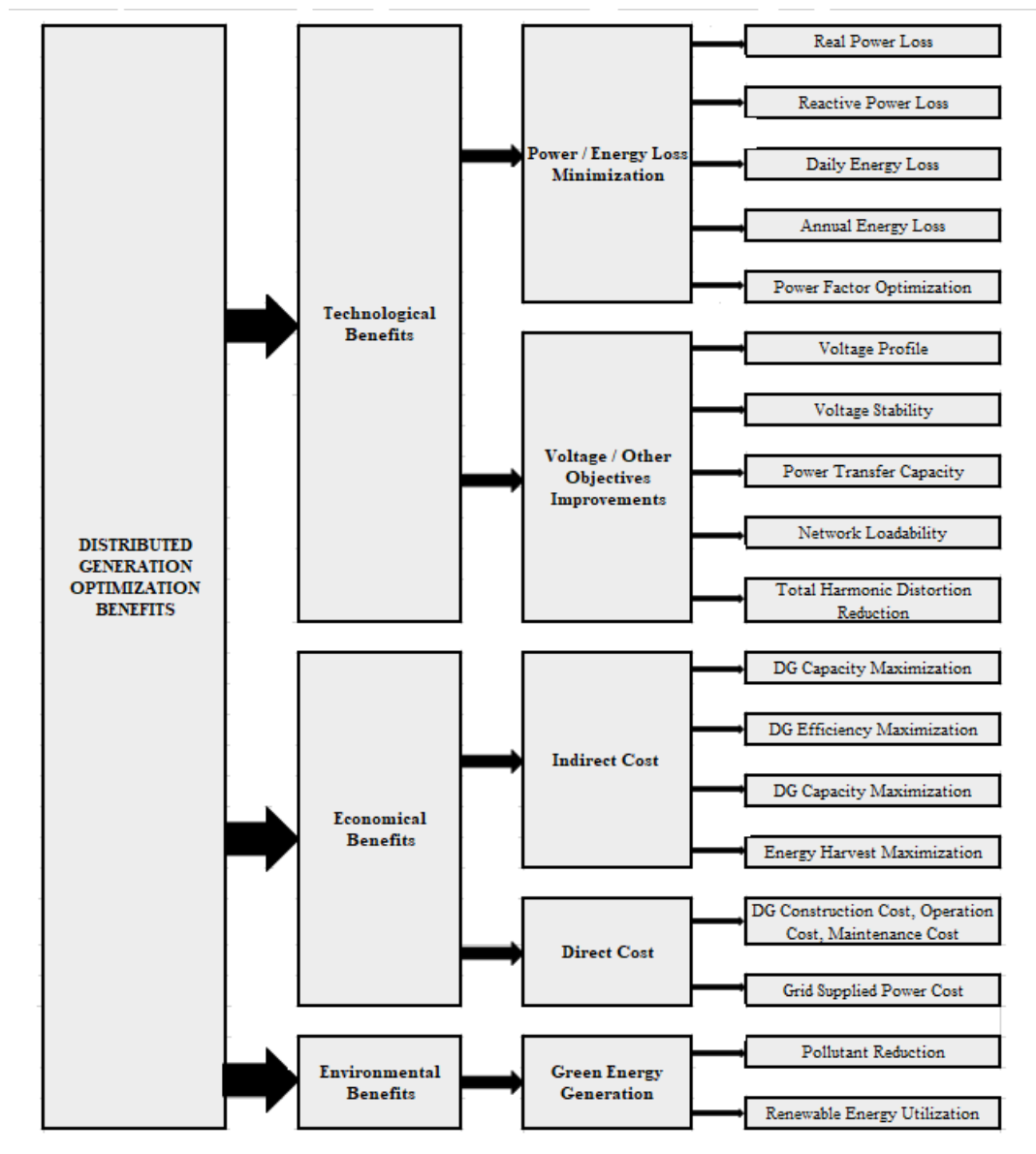
Figure 1. Benefits of DG optimization
Source: Authors

Economic benefits

The demand for electrical energy is increasing day by day, and it is not economic to expand centralized generation due to its various limitations. The incorporation of DG may lead down a path that is cost-effective and provides technological benefits, reducing energy losses and satisfying the energy demand through natural resources project DG as a futuristic approach. Capacity maximization and energy harvesting within the distribution network is also involved in financially optimized systems.

Environmental benefits

The high impact of renewable energy resources in the power network enlightens the pathway towards pollution-free, green energy generation. The maximization of extracted renewable energy is possible through the integration of DG in the distribution system.
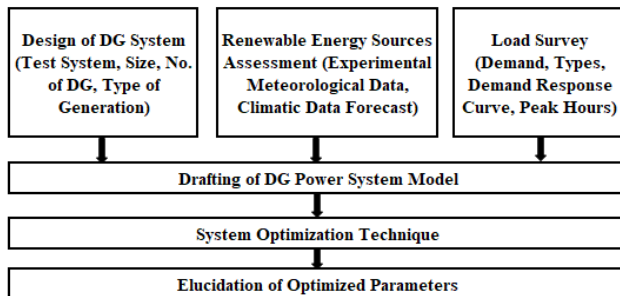
Figure 2. Framework for renewable DG planning
Source: Authors

The key segments of renewable energy-based DG planning are shown in Figure 2.

DG system design

Designing the DG system involves the selection of the energy generation category, the storage technique, and the bus system. Energy generation is broadly categorized based on renewable and non-renewable resources. Solar energy, wind energy, biomass energy, and fuel cells are the main renewable energy sources, whereas combustion is utilized in fossil fuel-based energy extraction (Allan *et al.*, 2015).

Despite the intermittent nature of renewable energy, there are numerous stable integrations of distributed energy generation and utilization, in addition to the incorporation of storage devices. Moreover, crop-based energy is also employed in DG.

The different types of bus planning can be categorized as follows:

Bus system with DC

The generated energy is delivered easily to DC load via a DC bus. However, inverter devices may be used to deliver energy to AC loads.

Bus system with AC

This architecture is used to directly supply AC loads through AC buses, while the DC demand is completed by using rectifiers.

Bus system with AC and DC

It is a more complex but highly efficient system to deliver AC and DC supply concurrently. Energy storage is also possible with the help of supply converters.

A categorization of renewable energy sources is presented in Figure 3 (DTI, 2007).
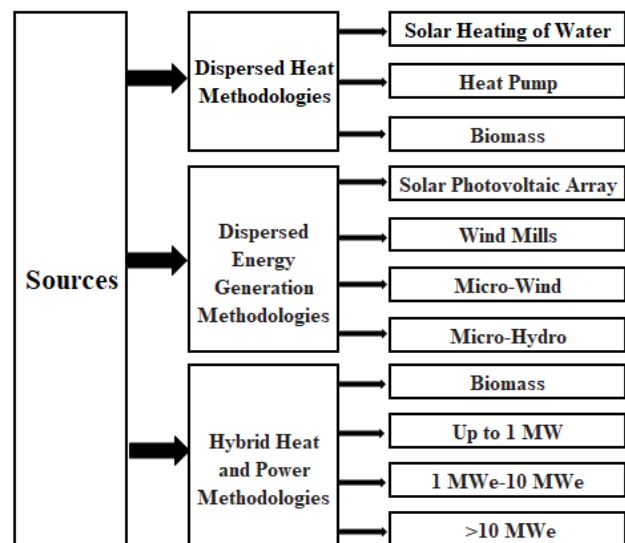
Figure 3. Categorization of renewable energy sources
Source: Authors

Renewable energy assessment

The assessment of renewable energy is a key component of DG implementation because of the intermittent nature of such resources in comparison with fossil fuel-based generation. To enhance the impact of green energy generation, it is necessary to prepare a framework of renewable energy-based DGs to neutralize the impact of intermittency. The weather conditions, topographical properties, experimental results, data records, soil grade, and seasonal variation are the most important parameters for the analysis involved in the elaboration of the renewable DG framework.

In this vein, biomass energy is dependent on atmospheric conditions, but storage of feedstock can provide continuous energy generation. In turn, wind and solar are unlimited sources of energy but have a high level of intermittency. It is a very difficult task to develop a model that can ensure uninterrupted energy generation.

The intermittency of wind and solar power can be reduced by the following methods (Theo *et al.*, 2017):

Experiential meteorological data

Experiential data of solar and wind function can be collected both directly and indirectly by means of visiting the site and consulting published research, meteorological laboratory records, relevant offices, and authorities. The measured metrological data related to solar energy are the irradiance level (hourly, daily, weekly, monthly, seasonal, and global), the intensity, and the power output. Moreover, the wind data collected are the hourly average, the monthly mean, the energy generated per day, and the frequency.

Climatic data forecast

It is necessary to forecast reliable metrological information, even in light of the following constraints, which may hamper the assessment:

- The proficiency and resources are limited in a particular area;

- low financial assistance limits the complete, highly accurate seasonal data observation; and

- the failure of an observational system may lead to the absence of regular data recording for a long period.

Load survey

Load demand analysis is mandatory for generation planning and utilization. The nature of the load may be continuous or discrete, while its measurement may be conducted in different time frames or seasons. It consists of analyzing the demand at low, medium, and high levels, and it varies from residential to industrial sectors. Studying the load curve from peak to valley and valley to peak is also required to maintain the consistency between demand and supply.

Optimized DG allocation

A predicted capacity-based solar power plant in an unbalanced power distribution model was recommended. The particle swarm optimization (PSO) technique was used to optimize the size and location to get the plant's capacity and determine its power capacity per day. The process started by modeling the varying load, followed by assuming an unbalanced distribution system, and concluded with the determination of the DG's probable capacity. The optimized parameters were compared to the absence of distributed generation (ADG) (Jana *et al.*, 2020).

A metaheuristic, hybrid-approach PSO coupled with a grey wolf optimization (PSOGWO) approach was implemented to enhance the voltage profile and optimize the real power losses. The photovoltaic and fuel cells and variable capacitor types were selected for the optimization process, and the results were significant for voltage profile improvement and real power losses reduction (Kumar *et al.*, 2020).

A simulation test was conducted on a physical 10 kV Chinese feeder for the execution of the cluster coordinated optimization (CCO) method, which exhibits a dual approach: determining voltage handling capacity of internal constellation reactive generators and employing constellation sovereign optimization. Moreover, complex circuits can be converted into an evident network based on essential observational information and Ohmic parameters, as well as autonomously evaluated for every cluster. The concept of this optimization basically involves choosing a fundamental load among two nearby nodes, and the effectiveness of its outcomes have been demonstrated in comparison with other optimization techniques such as centralized optimization (CO), multiplier-based distributed inter-cluster optimization (MBDICO), and cluster independent optimization (CIO) (Lu *et al.*, 2020).

Heuristic nature-inspired algorithms, namely dragonfly-particle swarm optimization (DFPSO) show prominent results in the enhancement of power losses and voltage profiles. Hybrid optimization techniques exhibit a dual approach: dragonfly for optimizing switching sequences and PSO for DG allocation in view of different scenarios of loss reduction (only active power, only kVAR, or complex power). The outcomes are impressive in comparison without those without DG reconfiguration (WRDG) (Rafi *et al.*, 2020).

It is necessary to optimize a mixed-integer nonlinear programming objective function to increase the penetration level of renewable energy sources in the distribution network. This objective function was solved with the help of a two-stage technique named coyote optimization algorithm (COA) at variable load levels to minimize the energy losses of the system. This methodology started with a load flow analysis, followed by determining the DG location, size, and loss reduction ratio (LRR). Furthermore, a methodology was examined for two types of cases: the IEEE 123-bus benchmark and the Tai power 123-bus system. The test results were compared with those of mixed-integer linear programming (MILP), genetic algorithm (GA), PSO, biogeography-based optimization, (BBO), and grey wolf optimization (GWO) (Chang *et al.*, 2020).

The challenges of voltage regulation and power losses were addressed in HV and MV distribution networks (DN) via generalized benders decomposition (GBD), and a simulation test was carried out in the Jinzhai distribution network of China. The effectiveness was examined with global centralized optimization (GCO) and independent optimization (IO). Crest voltage compensation was adopted in order to obtain enhanced results in a master-slave network with the increased precision of the LinDistFlow equation. Unlike other optimization techniques, this one facilitates the complete utilization of the voltage regulation capacity, which reduces energy losses during off-grid generation and yields good results in terms of cost-saving and computational calculation. A multi-objective function was disintegrated into a main universal problem and auxiliary problems in order to generate an iterative process (Chai *et al.*, 2020).

A DG management approach (DGMA) was proposed as a supervisor unit for controlling and optimizing the operations of multiple inverter modules in a power grid in order to operate simultaneously in different dispatch segments. The proposed supervisor unit allows independent and subsidiary services to enable various modes of operation: maximum real power, power factor improvement subjected to connection/disconnection authorization, constant reactive power, and active power (Santos *et al.*, 2020).

A two-stage data-driven distributed robust optimization (DDRORO) model was implemented to overcome the challenges of intermittency in renewable source integration given the lack of informative characteristics as compared to robust and stochastic optimization approaches. Green energy generation and profit maximization were accomplished by increasing the penetration level of renewable energy. Consequently, in comparison with the other stochastic optimization (SO) models, cost-saving reached 20% via the optimal sizing and allocation of DG (Fathabad *et al.*, 2020).

The PSO method was studied in a 22 kV distribution system (DS) in Thailand to reduce the system energy losses caused by the inappropriate allocation of DG. Additionally, the concept of load transfer was used, and, to this effect, the tie-switch location was identified through this nature-inspired optimization algorithm. A comparison of results demonstrated reduced energy losses and a voltage profile increase of 40,38 and 6,59%, respectively, which took 3,13 h (Karaaom *et al.*, 2020).

To enrich the generating capacity of DG and smoothen voltage fluctuations, reactive power optimization was modeled via the general algebraic modeling system approach (GAMSA), although the utilization capacity of DG was reduced. The recognized multi-objective function (considering the voltage variant, the real power losses, and the DG capacity) was converted into a single objective function, which was subjected to various constraints such as power balance, balanced node, line power, node voltage, DG output, and reactive power compensation. The variations in active power, reactive power, and node voltage irrespective of load demand were demonstrated in optimized results (Wang *et al.*, 2020).

Compared to the absence of DG optimization (WDG), the importance of DG planning and allocation was justified with the help of the PSO approach in view of its enormous advantages, which include improved voltage profiles, reliability, and power quality. This was carried out in the Basuki Rahmat Surabaya feeder by using a graphical user interface system. Voltage and current-based injection matrices were used for power flow analysis, and the particle swarm optimization technique was then demonstrated with suitable results (Saidah *et al.*, 2020).

Cost minimization and voltage regulation were achieved by trivial alteration using a moth search optimization technique called corrected moth search optimization (CMSO). A multi-

objective function was developed via the optimal placement of DG and shunt capacitors while concurrently optimizing and controlling the tap position of grid transformer. The results were also presented in comparison with other established optimization techniques such as the harmony search algorithm (HAS), the fireworks algorithm (FA), and the dynamic node priority list-genetic algorithm (DNPLGA) for the IEEE 33 and 118 test systems at different load conditions (peak, normal, and light) (Singh *et al.*, 2020).

A qualitative merging of genetic algorithm (GA) and ant colony optimization (ACO) resulted in a restructured algorithm dubbed genetic ant colony optimization (GACO), an approach that exhibited reduced energy losses and improved voltages. Load flow analysis was completed via the forward-backward method, and the newly developed technique was implemented with a faster convergence and free from local optima tracking. The results obtained were compared to those of renowned metaheuristic optimization techniques, which resulted in better voltage levels, average iterations (AI), reduced losses, and a faster convergence rate (Yang, 2020).

A multi-objective modified symbiotic organism search algorithm (MMSOSA) was executed for the optimization of the capacity and placement of renewable DG, with the purpose of achieving cost minimization (the cost of electricity for yearly purchases, the yearly expenditure, and the cost of operation), voltage regulation, and annual energy loss reduction at various load levels (constant, residential, commercial, and industrial) subjected to various constraints such as the power balance equation, the node voltage limit, and the DG capacity limit. Hourly demand variation and the total voltage deviation (TVD) curve were also significant for the improved results. Moreover, the results were quite impressive as compared to multi-objective symbiotic organism search (MOSOS) and the non-dominated sorting genetic algorithm-II (NDSGA) (Saha *et al.*, 2020).

The frequency regulation of a DG was carried out with the help of the moth swarm optimization technique, in which a series of PI-PD controllers were used through the incorporation of renewable energy-based sources (such as solar photovoltaic and wind power) and energy storage devices along with an electric vehicle. PI works in the primary stage and PD in the secondary one. Such a cascaded operation reduced the steady-state error of the system in comparison with conventional PID controllers, which may lead to an unstable transient response. For the execution in MATLAB and SIMULINK, the gain and time constant parameters of solar photovoltaic, wind power, fuel cell, and diesel engine generators, the electric vehicle, and the battery storage were taken as the nominal parameter of DG (Khamari *et al.*, 2020).

A battery storage architecture was proposed for the effective integration of distributed solar photovoltaic systems in order to avoid the intermittency of renewable energy sources. The flexibility of the grid, regardless

of faults (circuit scale fault, substation scale fault, and generation plant scale factor), has also been understood to cause disturbances. Numerous types of battery storage architectures were identified based on different types of working principles: In-building Distributed Storage Architecture, Circuit/Distribution Storage Architecture, Substation/Microgrid Storage Architecture, Generation Plant Storage Architecture, and Utility/Grid Storage Architecture. As an outcome, grid resilience was maximized by optimizing the combination of battery storage systems to increase the penetration level (PL) of renewable energy (Confrey et al., 2020).

A mathematical apprehension technique was proposed to enhance power and voltage quality via the amalgamation of DG in power distribution. This operation was carried out with the help of a flexible multi-level switch. The loading frequency and the power handling capability of the feeder were considered for the effective assimilation of DG through equalization. Moreover, a control framework for a PI controller and a steady-state converse model were developed in order to optimize the different modes of a flexible multi-level switch (Yu et al., 2020).

The coordinated scheduling of renewable DG with the constraints of a futuristic smart grid was presented, and such a combination was focused on sorting out the disturbance caused by the intermittency of renewable energy sources. Firstly, renewable virtual sources were considered for the procedural implementation, and then the obtained characteristics were simulated in order to design the framework of the strategy. The recommended model showed potential regarding the use of pumped storage energy in order to minimize the intermittency of renewable energy generation. Effective forecasting was achieved with source shedding with the purpose of maximizing profits (Dong et al., 2020).

A novel filter was used for the prediction of distributed solar power generation, in which the geographical proximity of the energy system affects the observations. Moreover, the intermittency in cloud formation and propagation was considered for the model at a resolution of 1 minute. This bi-level methodology consists of estimating PV power and measuring the lower frequency of the sampled data (Alam et al., 2020).

A dumping cost to evaluate soil contamination was proposed along with a new framework for delivering the electrical energy at a unitary power factor level in order to minimize distribution energy losses. Consequently, the cost required for power congestion management was also reduced, thus enhancing the level of futuristic smart city power projects (Parida et al., 2020).

The voltage regulation of a distribution system was improved with the use of solar PV DG as a reactive element that was independent from information exchange and feedback assessment. The backward/forward sweep algorithm was used while considering the irradiance level of solar energy and ambient temperature (Ammar et al., 2019).

The cost of acquiring land is increasing day by day for the installation of a solar PV system as DG. An appropriate method was recommended by the authors for solar PV installation so that land could be utilized in a better way. The unusable land near the railway track area, water storage land, and highways could be used while offering remuneration to the owner instead of purchasing new land. A geographic information system was also developed to get the details of such lands having the appropriate irradiation level of solar energy. (Asanov et al., 2019).

The increased risk power failure of renewable DG due to the intermittency of the climatological and atmospheric conditions has been highlighted with the proposal of an adaptive forecaster subgroup assortment strategy for enhancing the forecast. In this two-level approach, a binary genetic algorithm was used for selecting the characteristic, and a regression-based vector was applied to calculate the suitability level of the estimator. The accuracy was enhanced by 58,4% in comparison with the real prediction method (Eseye et al., 2019).

A case study of wind power generation in DG to meet the demand of rural America was analyzed. In this context, 2015 separates the pre-wind and the post-wind eras. A graphical presentation was included showing the variation in the development of residential, commercial, and industrial customers over the last five years of the span. Along with this, wind speed, atmospheric temperature, and load demand were also taken into account (Madala et al., 2019).

A simulation test was carried out to investigate the survival of wind power generation as distributed energy sources during the abnormal conditions of a power failure. A seven-scenario system (without DG, downstream, mid-way, upstream, and four types of wind power generation) was adopted to validate the results (Gumilar et al., 2019).

Due to the progression of large heat pump projects, many countries are required to advance in the traditional grid system, which offers the possibilities of renewable energy sources. For the effective integration of heat pumps with wind power generation in the distribution network, a mathematical model was presented with the purpose of maximizing profits and reducing costs (Cui et al., 2019).

Wind power generation in DG has been used for voltage profile enhancement, loss reduction, and ecological benefits in the distribution network. A power control curve optimization approach was adopted for the speed regulation of a windmill rotor. The optimized parameters were energy losses and voltage quality (Eltamaly et al., 2019).

A multi-objective function of DG size and allocation optimization was considered regarding the operating, capital, environmental, wind, and light abandonment costs,

which were subjected to voltage, current, equation flow, and DG capacity constraints. This was carried out with the implementation of the particle swarm optimization method in wind turbine, solar PV, and gas fueled micro turbine generators (Ma *et al.*, 2019).

The reliability of the radial distribution network could be increased by facilitating DG integration in the formation of multiple energy sources. PSO and the gravitational search algorithm (GSA) were used to obtain the optimal allocation of single and multiple DG. The reliability of the system was calculated in terms of numerous indices. The outcomes were evaluated in the IEEE 33-bus system for the various DG categories and compared to different metaheuristic approaches. The results were more significant in real and reactive power injection than in real power injection. The annual cost of energy losses (AELS) was better in comparison with GSA, PSO, the iterative algorithm (IA), and the krill herd algorithm (KHA) (Parihar *et al.*, 2021).

The optimal allocation and sizing of renewable energy-based DG could be found with the use of two different approaches in the same distribution network, namely the PSO and weighted-sum multi-objective (WSMO) approaches. The impact of optimal DG allocation was evaluated in the presence of harmonics distortion and validated in the IEEE 33-bus test system. In this strategy, a bi-level objective function was converted into a single objective function, and PSO was then applied. This approach demonstrated reduced energy losses, enhanced voltage profiles, and better reliability in the distorted distribution network. The results were compared with a GA, a multi-objective GA (MOGA), the analytical method (AM), and the backtracking search optimization algorithm (BSOA) (Parihar *et al.*, 2022).

Power quality parameters were also enhanced by incorporating a fuzzy logic controller (FLC) with hybrid optimization approaches. A hybrid optimization approach was proposed which integrates the features of the ant lion optimization algorithm (ALOA) and PSO. The multi-objective function was optimized in the presence of a training dataset offered by FLC, which resulted in optimized DG allocation. Such a process was evaluated in terms of load flow in the IEEE 33 test system. The results showed significant improvements stemming from the use of hybrid optimization techniques for different renewable energy-based power generators across a wide range of power factors. Said results were evaluated in comparison with those of ALOA and the proposed technique without FLC (Samala *et al.*, 2020b).

Another hybrid optimization approach was proposed by integrating the grasshopper optimization algorithm (GOA) and cuckoo search (CS) for the enhancement of various parameters of a distribution network in the presence of DG. This technique was evaluated in the IEEE 33 and 69 test systems under half load, full load, and overload conditions. The results were compared to those obtained via salp swarm optimization (SSO) and the lightning search algorithm (LSA) (Suresh *et al.*, 2020).

Comparative assessment

An comparative assessment of renewable DG optimization is given in Table 1. The analysis was carried out in terms of the DG optimization technique, the test system, the parameters evaluated, and the optimized outcomes. The Table provides an insight into the literature on DG allocation in distribution networks.

Research gap

After assessing the planning and optimization of renewable DG systems, it was concluded that the intermittency of renewable energy resources is not properly considered in order to establish a stable and reliable distribution system. The integration of energy storage systems and demand response schemes are also under-evaluated during optimal power dispatch. The utilization of energy storage devices can reduce the intermittent nature of natural resources, although the overall cost is increased. It is known that energy saving is also regarded as energy generation, so the end-user can shift their demand as per the demand response scheme. Load shifting from peak to valley hours enhances the quality of optimal power dispatch to reduce the system losses and imbalances between demand and supply. Consequently, battery storage and demand response integration are necessary for renewable DG planning in order to increase the impact of natural energy sources and coordination between distribution companies and consumers.

Conclusions

A comprehensive evaluation of recent trends in DG optimization is demonstrated in this paper, with its massive benefits subject to various constraints. These enormous benefits are associated with power quality, economic, and atmospheric parameters. The literature was reviewed based on optimization techniques, methodology, test system, optimized parameters, type of generation, enhanced outcomes, and compared approaches. The optimization techniques can be classified as classical, nature-inspired, and hybrid approaches depending on their methodology. Moreover, these techniques could be compared in terms of their convergence time, available literature, the dimensions of their objective function, and the complexity of their implementation. DG has the potential to exploit the dissemination of renewable energy sources in order to meet the present challenges as it contributes to safe environmental conditions. Moreover, the integration of a battery storage system can reduce the intermittency of renewable energy sources. Demand response is also an important aspect of the modern power grid. Renewable energy-based DG, battery storage, demand response, capacitor banks, and electric vehicles could be used for optimal power dispatch in distribution networks.

Table 1. A comparative analysis of DG optimization

Reference	Optimization technique	Test system	Evaluated parameters	Optimized results	Renewable DG	Non-renewable DG	Compared approaches	DG size (DGS)	DG location (DGL)	System losses (SL)	Voltage profile	Total cost (TC)	Calculation time (CT)	Fitness value (FV)	Power factor (pf)	Reliability
Lu et al. (2020)	CCO	IEEE 123	SL (MW)	0,8319	✓		CO, CI, MBDICO			✓	✓		✓			
			Vmax (p.u.)	1,05												
			CT	16,69												
Chang et al. (2020)	DFPSO	IEEE 33, DG=1	DGL	29	✓		WRDG	✓	✓	✓	✓					
			DGS (kW)	830												
			SL (kVA)	135,44 + j 83,69												
		IEEE 33, DG=2	DGL	29, 24												
			DGS (kW)	830, 340												
			SL (kVA)	118,40 + j 81,6												
		IEEE 33, DG=3	DGL	29, 24, 20												
			DGS (kW)	830, 340, 720												
			SL (kVA)	116,7 + j 80,44												
Chang et al. (2020)	COA	IEEE 123	SL (kW)	18,2081	✓		MILP, GA, PSO, BBO, GWO			✓	✓		✓	✓		
			LRR	77,01												
			V (p.u.)	0,9939 – 1,0023												
			FV	0,2299												
Chai et al. (2020)	GBD	HV and MV DN	SL (MW)	0,6877, 0,0273, 0,0463, 0,055	✓		GCO, IO			✓	✓	✓			✓	
			TC (Yuan)	333,1												
Santos et al. (2020)	DGMA	IEEE 13	SL, p.f.	Near to the reference vaue	✓					✓					✓	✓
Fathabad et al. 2020	DDDRO	IEEE 33	TC (K$)	17 015	✓		SO						✓			
Karaaom et al. (2020)	PSO	22 kV DS	SL (MWh)	36,38		✓	WDG			✓	✓					
			Vrise (p.u.)	0,97												

Reference	Optimization technique	Test system	Evaluated parameters	Optimized results	Renewable DG	Non-renewable DG	Compared approaches	DG size (DGS)	DG location (DGL)	System losses (SL)	Voltage profile	Total cost (TC)	Calculation time (CT)	Fitness value (FV)	Power factor (pf)	Reliability
Wang *et al.* (2020)	GAMSA	IEEE 33	DGL	4, 5, 6, 11, 25	✓		WDG		✓	✓	✓					✓
Saidah *et al.* (2020)	PSO	IEEE 33	DGL	25		✓	WDG	✓	✓	✓	✓					
			DGS (MVA)	9.5												
			SL (kW)	1.56												
Singh *et al.* (2020)	CMSO	IEEE 33	DGL	13, 25, 30	✓		HAS, FA, DNPLGA	✓	✓	✓	✓	✓				
			DGS (MW / MVAr)	1,459, 0,987, 1,795												
			PL	60.65%												
			SL (MW)	0,1964												
			TC (USD)	64820												
		IEEE 118	DGL	33, 38, 52, 71, 80, 96, 109												
			DGS (MW / MVAr)	2,910, 3,225, 2,677, 4,414, 2,276, 2,159, 4,642												
			SL (MW)	1,4622												
			TC (USD)	478 229												
Yang (2020)	GACO	IEEE 33	SL / kW	139,4715		✓	ACO, GA			✓	✓		✓			
			AI	17,4												
Saha *et al.* (2020)	MMSOSA	IEEE 69	DGL	24, 26, 62	✓		MOSOS, NDSGA	✓	✓	✓	✓	✓				
			DGS (kW)	540,250, 1 325,5												
			SL (kWh)	299 850												
			TC ($)	783 670												
			TVD	5 666												
Parihar *et al.* (2022)	WSMO, PSO	IEEE-33	DGS (kW)	2 588,4	✓		AM, MOGA, BSOA, GA	✓	✓	✓	✓	✓				✓
			DGL	6												
			Improved V %	4,18												
			PDG cost ($/Hr)	52,01												
			AELS ($)	54 499,46												

Reference	Optimization technique	Test system	Evaluated parameters	Optimized results	Renewable DG	Non-renewable DG	Compared approaches	DG size (DGS)	DG location (DGL)	System losses (SL)	Voltage profile	Total cost (TC)	Calculation time (CT)	Fitness value (FV)	Power factor (pf)	Reliability
Parihar et al. (2021)	PSO & GSA	IEEE 33, DG=1 (Injects P)	DGS (kW)	2 605	✓		IA, GSA, PSO, KHA etc.	✓	✓	✓	✓	✓				✓
			DGL	6												
			improved V %	4.35												
			AELS ($)	52 597												
		IEEE 33, DG=3 (Injects P & Q)	DGS (kW)	3 150												
			DGL	6												
			improved V %	6,19												
			AELS ($)	76 774,6												
		IEEE 33, DG=3 (Injects P & Q)	DGS (kW)	859,2, 1 031,6, 605,3												
			DGL	24, 30, 14												
			Improved V %	10,07												
			AELS ($)	101 477,8												
Samala et al. (2020b)	ALOA+PSO+FLC	IEEE-33 (PV=2, u.p.f)	DGS (kW)	385, 2 154	✓		PSO, ALOP+PSO	✓	✓	✓	✓	✓	✓		✓	
			DGL	32, 7												
			TC ($)	12 062												
		IEEE-33 (WT=2, u.p.f)	DGS (kW)	951, 696												
			DGL	31, 17												
			TC ($)	8 496												
		IEEE-33 (PV=2, p.f.=0,85 lag.)	DGS (kW + KVAr)	924 + j1223, 665 + j710												
			DGL	32, 14												
			TC ($)	8 037												
		IEEE-33 (WT=2, p.f.=0,85 lag.)	DGS (kW + KVAr)	993 + j1667, 606 + j913												
			DGL	8, 30												
			TC ($)	8 038												
Samala et al. (2020a)	ALOA+PSO	IEEE-33	DGL	5, 17, 31	✓	✓	ALOA, GSA	✓	✓	✓	✓		✓			✓
			DGS (MW)	0,4571, 0,2478, 0,9987												
			SL (MVA)	1,5257												

Reference	Optimization technique	Test system	Evaluated parameters	Optimized results	Renewable DG	Non-renewable DG	Compared approaches	DG size (DGS)	DG location (DGL)	System losses (SL)	Voltage profile	Total cost (TC)	Calculation time (CT)	Fitness value (FV)	Power factor (pf)	Reliability
Suresh et al. (2020)	GOA+CS	IEEE-33, half load	DGL	2	✓		SSO, LSA, GA	✓	✓	✓	✓	✓	✓	✓		✓
			DGS (kW)	1 716												
		IEEE-33, full load	DGL	24												
			DGS (kW)	926,99												
		IEEE-33, 150% load	DGL	24												
			DGS (kW)	926,99												
		IEEE-69, half load	DGL	17												
			DGS (kW)	1930,7												
		IEEE-69, full load	DGL	6												
			DGS (kW)	1990,7												
		IEEE-69, 150% load	DGL	12												
			DGS (kW)	1890,6												
Jana et al. (2020)	PSO	IEEE 34	DGS (kW)	58,928	✓		ADG	✓	✓	✓	✓					
Kumar et al. (2020)	PSOGWO	IEEE 33	DGL	6	✓		ADG	✓	✓	✓	✓					
			DGS (MW)	2,576												
			SL (kW)	103,966												
		IEEE 33	DGL	30		✓										
			DGS (MVAr)	1,25												
			SL (kW)	143,6												
		IEEE 69	DGL	61	✓											
			DGS (MW)	1,869												
			SL (kW)	83,9013												
		IEEE 69	DGL	61		✓										
			DGS (MVAr)	1,328												
			SL (kW)	152,4												

Source: Authors

References

Alam, S. S., Florita, A. R., and Hodge, B. (2020). Distributed PV generation estimation using multi-rate and event-driven Kalman kriging filter. *IET Smart Grid, 3*(4), 538-46. https://doi.org/10.1049/iet-stg.2018.0246

Allan, G., Eromenko, I., Gilmartin, M., Kockar, I., and McGregor, P. (2015). The economics of distributed energy generation: A literature review. *Renewable and Sustainable Energy Reviews, 42*, 543-556. https://doi.org/10.1016/j.rser.2014.07.064

Ammar, M., and Sharaf, A. M. (2019). Optimized use of PV distributed generation in voltage regulation: A probabilistic formulation. *IEEE Transactions on Industrial Informatics, 15*(1), 247-256. https://doi.org/10.1109/TII.2018.2829188

Asanov, I., Loktionov, E., and Sharaborova E. (2019, March 25-29). *Evaluation of potential distributed solar generation at right-of-way land of infrastructure objects* [Conference presentation]. 2019 International Conference on Industrial Engineering, Applications and Manufacturing (ICIEAM), Sochi, Russia. https://doi.org/10.1109/ICIEAM.2019.8742979

Chai, Y., Guo, L., Wang, C., and Y. Liu. (2020). Hierarchical distributed voltage optimization method for HV and MV distribution networks. *IEEE Transactions on Smart Grid, 11*(2), 968-980. https://doi.org/10.1109/TSG.2019.2928701

Chang, G. W., and N. Cong Chinh. (2020). Coyote optimization algorithm-based approach for strategic planning of photovoltaic distributed generation. *IEEE Access, 8*, 36180-36190. https://doi.org/10.1109/ACCESS.2020.2975107

Confrey, J., Etemadi, A. H., and Eveleigh, T. J. (2020). Energy storage system architecture optimization for grid resilience with high penetration of distributed photovoltaic generation. *IEEE Systems Journal, 14*(1), 1135-1146. https://doi.org/10.1109/JSYST.2019.2918273

Cui, Q., Bai, X., and Dong, W. (2019). Collaborative planning of distributed wind power generation and distribution network with large-scale heat pumps. *CSEE Journal of Power and Energy System, 5*(3), 335-347. https://doi.org/10.1109/JSYST.2019.2918273

Dong, H., Li, S., and Z. Tian. (2020). Coordinated scheduled strategy for distributed generation considering uncertainties in smart grids. *IEEE Access, 8*, 86171-86179. https://doi.org/10.1109/ACCESS.2020.2992342

DTI (2007). *Review of distributed generation. A joint Government/Ofgem report*. https://www.ofgem.gov.uk/publications/review-distributed-generation-joint-governmentofgem-report

Eltamaly, A. M., Mohamed, Y. S., and Elghaffar, A. N. A. (2019, April 15-17). *Analyzing of wind distributed generation configuration in active distribution network* [Conference presentation]. 2019 8th International Conference on Modeling Simulation and Applied Optimization (ICMSAO), Manama, Bahrain. https://doi.org/10.1109/ICMSAO.2019.8880291

Eseye, A. T., Lehtonen, M., and Millar, R. J. (2019). Adaptive predictor subset selection strategy for enhanced forecasting of distributed PV power generation. *IEEE Access, 7*, 90652-90665. https://doi.org/10.1109/ACCESS.2019.2926826

Fathabad, A. M., Cheng, J., Pan, K., and Qiu, F. (2020). Data-driven planning for renewable distributed generation in distribution systems. *IEEE Transactions on Power Systems, 35*(6), 4357-4368. https://doi.org/10.1109/TPWRS.2020.3001235

Gumilar, L., Habibi, M. A., and Nugroho, W. S. (2020, February 20). *Analysis of short circuit on four types wind power plants as distributed generation* [Conference presentation]. 2020 International Conference on Smart Technology and Applications (ICoSTA), Surabaya, Indonesia. https://doi.org/10.1109/ICoSTA48221.2020.1570599089

Jana, C., Bala, M. J., and Goswami, S. K. (2020). *Finding of the probable size and location of distributed generation in unbalanced distribution system with demand uncertainty* [Conference presentation]. 2020 IEEE Calcutta Conference (CALCON), Kolkata, India. https://doi.org/10.1109/CALCON49167.2020.9106559

Karaaom, C., Jirapong, P., and Tantrapon, K. (2020, March, 4-6). *Optimal allocation of tie switch in distribution systems for energy loss reduction using particle swarm optimization* [Conference presentation]. 2020 8th International Electrical Engineering Congress (iEECON), Chiang Mai, Thailand. https://doi.org/10.1109/iEECON48109.2020.229528

Khamari, D., Sahu, R. K., and Panda, S. (2020, January 3-5). *Moth Swarm Algorithm based cascade PI-PD controller for frequency regulation of distributed power generation system with electric vehicle* [Conference presentation]. 2020 First International Conference on Power, Control and Computing Technologies (ICPC2T), Raipur, India. https://doi.org/10.1109/ICPC2T48082.2020.907149

Kumar, K., Ramswaroop, R., Yadav, L. K., and Joshi, P. (2020, February 28 – March 1). *Optimal planning of distributed generation using hybrid metaheuristic approach* [Conference presentation]. 2020 IEEE 9th Power India International Conference (PIICON), Sonepat, India. https://doi.org/10.1109/PIICON49524.2020.9112955

Lu, H., Y. Chai, Y., J. Hao, J., and Chen, X. (2020). Network simplification-based cluster coordinated optimization method for distributed PVs with inadequate measurement. *IEEE Access, 8*, 65283-65293. https://doi.org/10.1109/ACCESS.2020.2984709

Ma, Q., Zhang, Y., and Wen, Y. (2019, December 1-4). *Research on optimization for siting and sizing of distributed generation considering wind and light abandonment and environment cost* [Conference presentation]. 2019 IEEE PES Asia-Pacific Power and Energy Engineering Conference (APPEEC), Macao, China. https://doi.org/10.1109/APPEEC45492.2019.8994588

Madala, S., Ramaekers, T., and Herink, A. (2019, April 28 – May 1). *The story of a rural public power district – Before and after distribution grid conneceted wind power generation* [Conference presentation]. 2019 IEEE Rural Electric Power Conference (REPC), Bloomington, MN, USA. https://doi.org/10.1109/REPC.2019.00018

Mahmoud, H. A., and Rama, K. (2017). A review of the optimal allocation of distributed generation: Object, constraints, methods, and algorithms. *Renewable and Sustainable Energy Reviews, 75*, 293-312. https://doi.org/10.1016/j.rser.2016.10.071

Parida, A., Choudhury, S., and Chatterjee, D. (2020, February 28 – March 1). *Optimal solar PV based distributed generation system suitable for cost-effective energy supply* [Conference presentation]. 2020 IEEE 9th Power India International Conference (PIICON), Sonepat, India. https://doi.org/10.1109/PIICON49524.2020.9113018

Parihar S. S., and Malik M. (2021). Optimal allocation of multiple DGs in RDS using PSO and its impact on system reliability. *Electronics and Energetics, 34*(2), 219-237. https://doi.org/10.2298/FUEE2102219P

Parihar S. S., and Malik M. (2022). Analysing the impact of optimally allocated solar PV-based DG in harmonics polluted distribution network. *Sustainable Energy Technologies and Assessments, 49*, 101784. https://doi.org/10.1016/j.seta.2021.101784

Rafi, V., and Dhal, P. K. (2020, January 20-22). *Loss minimization based distributed generator placement at radial distributed system using hybrid optimization technique* [Conference presentation]. 2020 International Conference on Computer Communication and Informatics (ICCCI), Coimbatore, India. https://doi.org/10.1109/ICCCI48352.2020.9104145

Saha, S., and Mukherjee, V. (2020, February 28 – March 1). *A novel meta-heuristic for optimal allocation of distributed generation in balanced distribution network considering hour-*

ly load variation [Conference presentation]. 2020 IEEE 9th Power India International Conference (PIICON), Sonepat, India. https://doi.org/10.1109/PIICON49524.2020.9113054

Saidah, and Masrufun M. (2020, February 20). *Optimization of DG placement and size using PSO based on GUI* [Conference presentation]. 2020 International Conference on Smart Technology and Applications (ICoSTA), Surabaya, Indonesia. https://doi.org/10.1109/ICoSTA48221.2020.1570615982

Samala, R. K., and Kotapuri, M. R. (2020a). Distributed generation allocation in distribution system using particle swarm optimization based ant-lion. *International Journal of Control and Automation, 13*, 414-426. http://sersc.org/journals/index.php/IJCA/article/view/6004

Samala, R. K., and Kotapuri, M. R. (2020b). Optimal allocation of multiple photo-voltaic and/or wind-turbine based distributed generations in radial distribution system using hybrid technique with fuzzy logic controller. *SN Applied Sciences, 2*, 191. https://doi.org/10.1007/s42452-020-1957-3

Santos, L. N., Sousa, G. G., Salvatti, G. A., Carati, E. G., da Costa, J. P., Cardoso, R., Stein, C. M. O., and, Nadal, Z. L. I. (2020, February 26-28). *A distributed generation manager with support for distributed network operator commands* [Conference presentation]. 2020 IEEE International Conference on Industrial Technology (ICIT), Buenos Aires, Argentina. https://doi.org/10.1109/ICIT45562.2020.9067315

Saxena, V., Kumar, N., and Nangia, U. (2021, February 11-13). *Smart grid: A sustainable smart approach* [Conference presentation]. 2020 3rd International Conference on Computational & Experimental Methods in Mechanical Engineering ICCEMME (2021), Uttar Pradesh, India.

Singh, P., Bishnoi, S. K., and Meena, N. K. (2020). Moth search optimization for optimal DERs integration in conjunction to OLTC tap operations in distribution systems. *IEEE Systems Journal, 14*(1), 880-888. https://doi.org/10.1109/JSYST.2019.2911534

Suresh, M. C. V., and Edward J. B. (2020). A hybrid algorithm based optimal placement of DG units for loss reduction in the distribution system. *Applied Soft Computing, 91*, 106191. https://doi.org/10.1016/j.asoc.2020.106191

Wang, Z., Liu, H., and Li, J. (2020, June 4-7). *Reactive power planning in distribution network considering the consumption capacity of distributed generation* [Conference presentation]. 2020 5th Asia Conference on Power and Electrical Engineering (ACPEE), Chengdu, China. https://doi.org/10.1109/ACPEE48638.2020.9136183

Yang, J. (2020, March 18-20). *Research on optimized reconfiguration of distributed distribution network based on ant colony optimization algorithm* [Conference presentation]. 2020 International Conference on Computer Engineering and Application (ICCEA), Guangzhou, China. https://doi.org/10.1109/ICCEA50009.2020.00012

Yu, C., Zhang, G., and Peng, B. (2020, June 4-7). *Feeder power flow control strategy for flexible multi-state switch with joint access to the distributed generation* [Conference presentation]. 2020 5th Asia Conference on Power and Electrical Engineering (ACPEE), Chengdu, China. https://doi.org/10.1109/ACPEE48638.2020.9136556

Emulating Textures Using Vibrotactile Technology: HaptTech System and its Adaptation to a Commercial Kinesthetic Interface

Emulando texturas usando tecnología vibrotáctil: sistema HaptTech y su adaptación a una interfaz cinestésica comercial

Mauricio Santís-Chaves[1], Juan C. Franco-Mesa[2], José F. Zapata-Berruecos[3], Jonathan A. Hernández-Calle[4], Sergio A. Salinas[5], and Vera Z. Pérez-Ariza[6]

ABSTRACT

This article presents the development and testing of a tactile interface prototype, HaptTech, that applies vibrotactile stimulation patterns to the fingertip, as well as an analysis of its performance when coupled to the commercial kinesthetic interface Novint Falcon. Its applicability in digital entertainment expects to improve the level of immersion into virtual reality scenarios. In the first experiment, a group of 75 subjects compared three different vibration stimuli that emulated different textures. They evaluated the stimuli on a 1 to 10 scale, where 1 means 'non-perceivable differences' and 10 means 'entirely differentiable'. The obtained mean values were 9 (textures 1 and 3), 8,29 (textures 1 and 2), and 7,43 (textures 2 and 3), indicating HaptTech's capability to reproduce differentiable stimuli. In the second experiment, 31 subjects evaluated the coupling between HaptTech and Novint Falcon. They perceived differences when the HaptTech system was activated in the context of a comparison between kinesthetic and vibrotactile plus kinesthetic stimuli. In the third experiment, the subjects evaluated the similarity between the perceived stimuli on the hand and a visualized texture pattern in a virtual environment. The resulting median values were 8, 8, and 9 for textures 1, 2, and 3, respectively, which demonstrate that the subjects perceived a high correspondence for each one.

Keywords: tactile Interface, kinesthetic Interface, vibrotactile reproducer, interface coupling, level of immersion

RESUMEN

Este artículo presenta el desarrollo y pruebas de un prototipo de interfaz táctil, HaptTech, que aplica al dedo patrones de estímulo vibrotáctil, así como un análisis de su desempeño cuando se acopla con la interfaz cinestésica comercial Novint Falcon. Su aplicabilidad en el entretenimiento digital espera mejorar el nivel de inmersión en escenarios de realidad virtual. En el primer experimento, un grupo de 75 personas comparó tres estímulos de vibración que emulaban diferentes texturas. Evaluaron el estímulo en una escala de 1 a 10, donde 1 significa 'diferencias no perceptibles' diferencias y 10 significa 'completamente diferenciables'. Los promedios fueron 9 (texturas 1 y 3), 8,29 (texturas 1 y 2) y 7,43 (texturas 2 y 3), indicando la capacidad del HaptTech de reproducir estímulos diferenciables. En el segundo experimento, 31 sujetos evaluaron el acople entre HaptTech y Novint Falcon. Los participantes percibieron diferencias cuando el sistema HaptTech se activaba en el contexto de una comparación entre estímulos cinestésicos y estímulos cinestésicos y vibrotáctiles. En el tercer experimento, los sujetos evaluaron la similitud entre el estímulo percibido en la mano y un patrón de textura visualizado en un ambiente virtual. Las medianas resultantes fueron 8, 8 y 9 para las texturas 1, 2, y 3 respectivamente, lo cual demuestra que los sujetos percibieron una alta correspondencia para cada una.

Palabras clave: interfaz táctil, interfaz cinestésica, reproductor vibrotáctil, acople de interfaces, nivel de inmersión

[1] BSc Electronic Engineering, Universidad Pontificia Bolivariana, Colombia. M.Sc. Engineering, Universidad Pontificia Bolivariana, Colombia. mauricio.santis@upb.edu.co

[2] BSc Electronic Engineering, Universidad Pontificia Bolivariana, Colombia. M.Sc. student in Engineering, Universidad Pontificia Bolivariana, Colombia. Email: juan.franco@upb.edu.co

[3] MD, Universidad de Antioquia. Colombia. Clinical neurologist, Universidad CES. Colombia. MSc. Applied Mathematics, Universidad EAFIT. Colombia. PhD, Medical Sciences, Universidad Pontificia Bolivariana. Colombia. Email: jose.zapata@neurologico.org.co

[4] Psychologist, Universidad de Antioquia, Colombia. M.Sc. Epidemiology, Universidad CES, Colombia. Email: andres.epi2016@gmail.com

[5] MSc Electronics and Telecommunications, Universidad del Cauca, Colombia. BSc Electronic Engineering, Universidad Industrial de Santander, Colombia. Email: sergio.salinas@upb.edu.co

[6] PhD, in Engineering, Universidad Pontificia Bolivariana. Colombia. B.Sc Electronic Engineering, Universidad Pontificia Bolivariana. Colombia. Email: vera.perez@upb.edu.co

Introduction

Touch is the sense that obtains information from physical objects using haptic exploratory activities (Bremner and Spence, 2017). This sense has nerve receptors distributed in the skin, transferring different types of energy stimuli to nerve impulses.

Some examples are thermal energy detected by thermoreceptors or mechanical energy detected by mechanoreceptors. Mechanoreceptors detect skin stimuli such as vibration, stretch, pressure, and texture (Fox, 2014; French and Torkkeli, 2009). Vibration stimuli can be detected in a range from 8 to 400 Hz (Griffin, 2012). Skin also contains nociceptors, which generate a biological alert when they detect damaging or potentially damaging stimuli. Another receptor type is the proprioceptor, located in muscles and tendons, which indicates the location of the body and other objects. This kind of receptor is related to kinesthesia (Proske and Gandevia, 2012).

Analogously, haptic interfaces (HI) are elements or devices that stimulate receptors related to touch. HI are divided into tactile and kinesthetic interfaces to replicate essential tangible and subjection characteristics of real objects, respectively. Both types of stimuli are necessary for reproducing the sensation of contact and manipulation of an object inside a virtual or a remote environment (Golledge et al., 2006; O'Malley and Gupta, 2008).

Some studies show a trend that involves combining both interface types to complement their effects (Fontana et al., 2012; Hoshi et al., 2010; Pacchierotti et al., 2013; Yang, 2013; MIRALab, 2021), producing greater realism and immersion for the user inside the virtual environment. This immersive experience makes it an ideal technology to be applied in digital entertainment systems (DES).

DES are digital devices that allow people to enjoy different forms of entertainment, such as music, cinema, radio, games, and gambling, converging on digital media and platforms. DES usually involve electronic devices such as smartphones, DVD recorders and players, MP3 players, game consoles (Sadiku et al., 2017), computers, and others. One part of digital entertainment refers to playing digital interactive games on different kinds of electronic media (Tan and Jansz, 2008).

Currently, some DES use virtual reality (VR). In these types of systems, mainly visual and auditory cues help create immersion, and the use of tactile displays contributes to the manipulation of virtual objects (Pacchierotti et al., 2017; Villa-Salazar et al., 2020). The closer the system stimuli are to the perception of the human senses, the higher the immersion potential. This means matching multimodal information channels to the user's head and body (Rosa et al., 2016).

Hardware devices used with DES and virtual reality such as joysticks or cellphones typically use vibration cues to generate alerts or indicate actions, as is the case of gunshots or explosions. Furthermore, some developments use vibration to produce touch sensations. The interaction consists of feeling the presence of an object by means of a vibration stimulus (CybergloveSystems, 2019; Kim et al., 2017). Usually, haptic stimulations do not consider the surface texture in a DES.

However, it is possible to perceive the surface texture through vibration stimuli based on when a finger touches and explores a texturized surface. This action produces vibrations in the skin that are transduced by mechanoreceptors (Bensmaïa and Hollins, 2003).

This paper describes the development of a vibrotactile device called HaptTech, which is designed to generate tactile stimuli for textures in virtual objects. The device is coupled with Novint Falcon, a kinesthetic interface. This system complements the user's kinesthetic perception in order to increase the perceived degree of realism regarding the interaction with a virtual object by reproducing the feel of its surface texture on the user's hand.

The proof of concept is carried out with the addition of a vibrotactile texture reproducer mounted on the fingertip to a force-kinesthetic commercial interface coupled to the palm. This development aims to improve the realism of touch sensation when a user interacts with a virtual object in a DES, where the user can differentiate between surface textures by touch.

This paper is organized as follows: the *Prototype description* section describes the design criteria and the development of the vibrotactile reproducer, the Novint Falcon interface and its coupling with the vibrotactile reproducer, and the virtual environment utilized; the *Methodology* section describes the test applied to the subjects; the *Results* section contains the obtained results for each experiment conducted, as well as their interpretation; the *Discussion* section delves into the contribution of this work; and the *Conclusions* section presents our final remarks, along with proposals for future work.

Prototype description

This section describes the design criteria, the development of the vibrotactile reproducer, the Novint Falcon interface and its coupling with the vibrotactile reproducer, and the virtual environment utilized.

Design criteria for a texture reproducer vibrotactile system

The design parameters of the texture reproducer are as follows. Vibration is the stimulus to be used since it is innocuous and, at the adequate frequency, it stimulates the Pacinian corpuscles, which transmit the sensation of texture. The vibration actuator has a reduced size, low power consumption, and operates within the skin perception range.

The actuator case should be made from a lightweight material, inoffensive to contact with the skin. The control and driver circuit must be of reduced size. The expected result is a compact and portable device with the appropriate resistance to support the movements of the participant's hand during testing.

Considering these parameters, the outcome is a robust, compact, and portable device, with an appropriate resistance to support the weight and movements of the subject's limbs undergoing the tests.

Development of the texture reproducer vibrotactile system

As per these requirements, Figure 1 illustrates the proposed hardware design of the vibrotactile texture reproducer system. It utilizes a microcontroller system (CPU). The device receives the commands from a computer via USB input and is activated when the surface of an object is touched. The CPU sends the appropriate signal pattern to the driver device, delivering the current and voltage levels to the actuator in order to generate the appropriate vibrotactile stimuli.
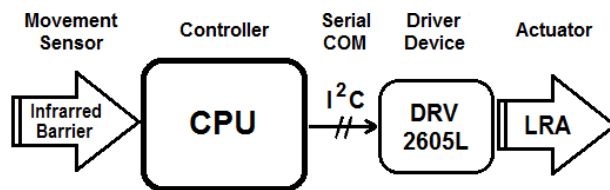
Figure 1. Block diagram of the design of the vibrotactile texture reproducer system
Source: Authors

The actuator is a low-consumption vibration motor (Linear Resonant Actuator, LRA), with an operation frequency of 175 ± 1 Hz, oscillating at frequencies close to this value like a voice coil speaker, and it is controlled by a low-voltage haptic driver (DRV2605L) for LRAs. The vibrotactile stimuli are homogeneously transferred from the LRA to the user's finger, using a thimble made from a hypoallergenic resistant polymer. Figure 2 shows the selected devices in the vibrotactile fingertip actuator.

To create the three levels of roughness in the texture using vibration, the total amplitude range of the actuator output was divided by three. To this effect, the DRV driver was used in open-loop LRA drive mode through internally generated PWM, programming the driver to generate an electrical signal in order to stimulate the actuator in the appropriate proportion in each case. For instance, a 33% driver activation induces 33% of the maximum possible amplitude, which is related to a low roughness sensation. In the same way, a 66% activation corresponds to a medium level of roughness and 100% to a high level of roughness. A preliminary study verified that said percentage levels simulate the perception of roughness (Santís *et al.*, 2016).

Description of the Novint Falcon interface

Figure 3 shows the kinesthetic interface Novint Falcon®. It is composed of a grip, an arm, a body, and a base. The grip translates the force feedback to the user's hand, and it contains the control buttons. This device communicates with a personal computer (PC) via a USB port.

(a)   (b)
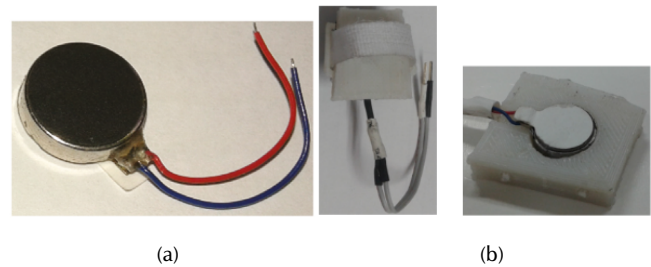
Figure 2. Assembly components of HaptTech: (a) LRA, (b) thimble-shaped actuator
Source: Authors

Figure 3. Kinesthetic interface Novint Falcon
Source: Authors

Coupling with the Novint Falcon interface

The grip was adjusted to monitor the force feedback on the palm. The grip connects with a piece embedded in a glove, which holds the thimble (Figure 4).

(a)   (b)

Figure 4. a) Grip adaptation of the kinesthetic interface, b) coupling between HaptTech and the Novint Falcon interface
Source: Authors

Developing the virtual environment

A software application synchronizes the interaction between the Novint Falcon and the HaptTech tactile interface in order to create an increased sensation of immersion in the virtual environment on a PC screen. The application simulates interaction with a virtual cube through the control movements of the Novint Falcon. When the cube is virtually manipulated, force and tactile stimuli are transmitted to the user's hand.

The application used the C++ language and other computer graphic tools. The OpenGL library was useful for rendering the objects, as well as other complementary tools such as FreeGLUT for Windows (Freeglut, 2019), and GLEW for light distribution or shading on the objects (Glew, 2019).

Methodology

The selected design was quasi-experimental because it provided high-level evidence without randomization (Bärnighausen *et al.*, 2017).

Three experiments were performed on the aforementioned device, evaluating the texture reproducer vibrotactile system and its coupling with the Novint Falcon interface.

The institutional Ethics Committee approved the study. The participants signed an informed consent document before testing and later received instructions on how to execute the experiment, as well as on the appropriate hand position for a correct evaluation of the interface. The researchers read scripted instructions in order to guarantee that each participant received the same information to perform the tests.

The exclusion criteria included a review of hand skin conditions that affect sensitivity (*e.g.*, scars, burns, traumas), diabetes, neurological or immunological diseases, any surgery or neurological condition that affects hand sensitivity, the exposure to toxic substances, and the prolonged use of medication or stimulants.

Experiment 1. Discrimination of vibrotactile stimuli

A group of participants aged 18 to 60 assessed three textures simulated by the vibrotactile HaptTech system. The sample size of 60 subjects was obtained using the GPower 3.1 software, with Power=80, a basis of Effect=0,4, Measurement=3, and Confidence=95%. The sample was acquired using non-probabilistic sampling, maintaining heterogeneity in 77 participants who participated in the experiments, before excluding two of them. To meet the inclusion and exclusion criteria, a physician evaluated the skin condition and neurological response of the upper limbs at the beginning and end of the test.

The test participants were not associated with the project to avoid bias in the sample selection and result detection, and the order of applied stimuli was random (Álvarez and Álvarez, 2009; Glantz, 2006).

To evaluate the tactile interface's capability to reproduce differentiable stimuli on the subjects, three stimuli were classified as low-, medium-, and high-intensity. The 75 participants underwent the vibrotactile response perception experiment, indicating, on a scale from 1 to 10, the degree to which they perceived a difference between the stimuli, where 1 meant that there was no perceivable difference and 10 that they were completely different. There were three experiments: the first experiment compared textures 1 and 2, the second compared textures 2 and 3, and the third compared textures 1 and 3. Researchers asked each participant to make exploratory circles and zigzag movements on the two surfaces for comparison in each experiment. Afterwards, the participants were asked to rate the degree of difference between the textures.

Experiment 2. Comparison between kinesthetic and vibrotactile plus kinesthetic stimuli

For experiment 2, 31 people aged 18 to 60 were suitable to participate. One person who did not meet the inclusion criteria was excluded. A small sample size (less than 30) would skew the variables, but, as the sample size increases, the variables tend to take on a normal distribution (Delice, 2010). At the beginning and at the end of the experiment, a physician evaluated the same criteria mentioned in experiment 1.

In this experiment, the users wore the glove containing the HaptTech system coupled with the Novint Falcon kinesthetic interface. The subjects manipulated the coupled HaptTech-Novint interface's grip while interacting with a small sphere and cube in a virtual environment (Figure 5).
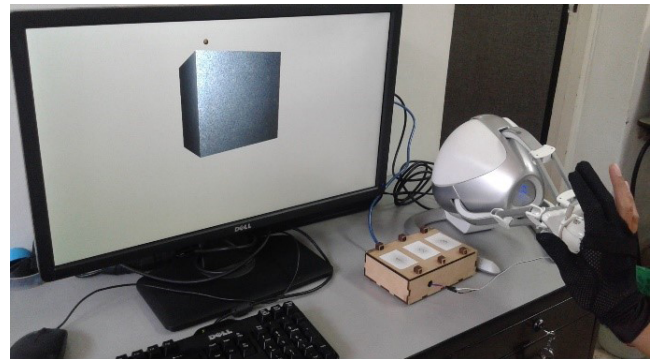
Figure 5. Scenario for experiment 3, including kinesthetic and vibrotactile stimuli
Source: Authors

The virtual cube randomly displayed three different surface textures (Figure 6). The user switched between the three different surfaces by pressing a selector button on the grip. In the first part of the experiment, the vibrotactile stimuli were deactivated, thus, the user only perceived the kinesthetic stimuli generated by the Novint Falcon Interface.

(a)   (c)   (b)
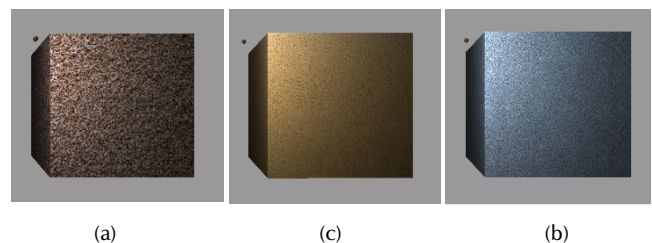
Figure 6. Textures for user interaction: a) surface texture 1, b) surface texture 2, c) surface texture 3
Source: Authors

In the second part of the experiment, the vibrotactile stimuli were activated in the HaptTech device, and the user perceived the kinesthetic and tactile stimuli simultaneously.

Each subject then completed a survey assessing whether there was any perceived difference between the two parts of the experiment.

Experiment 3. Comparison between perceived and visualized stimuli

The same 31 participants of experiment 2 participated in experiment 3. Using the glove, the users manipulated the small virtual sphere with the HaptTech-Novint Falcon interface to touch the surface of the virtual cube.

Figure 5 shows that the exploration of the cube's surface was carried out naturally, with an open hand and outstretched fingers. This time, the user assessed the level of realism regarding the perceived sensation of the visualized surface on the palm and finger by assigning a score from 1 to 10; 1 indicated that there was no relationship between the visualized surface and the sensation on the hand, and 10 indicated a strong relationship between the visualized surface and the perceived sensation. The users randomly interacted with the same three surfaces.

Data analysis

In experiment 1, the descriptive measures of the differences between textures were calculated. The Kolmogorov-Smirnov Test for Normality (N>50), whose null hypothesis is that the variable has a normal distribution, showed a result of less than 0,05, indicating an uneven distribution. The Friedman test was implemented to evaluate significant differences between texture comparisons. This test's null hypothesis is that all median values are the same, which is rejected if at least one median is different, with a significance value of less than 0,05.

In experiment 2, a dichotomic scale (yes/no) was used to examine the frequencies of the answers after the second part of the experiment.

In experiment 3, descriptive statistics for the coupling test determined how users felt about the interactions with the system, looking for trends in the data distribution and the statistical values. Additionally, the Shapiro-Wilk Test for Normality was applied (N<50), whose null hypothesis is that the variable has a normal distribution. This is rejected if the significance value is less than 0,05. The Friedman test also evaluated the significant differences between the level of realism with regard to the perceived sensation on the palm and finger according to the virtual surface. In this test, the null hypothesis is the same as in experiment 1.

Results

This section presents the results of the three experiments.

Vibrotactile stimuli on the fingertip

Figure 7 shows the discrimination percentage for the participants of experiment 1, which valued the difference between each texture pair. The obtained results show a tendency towards a high valuation regarding texture differentiability. Considering that the rounded lowest

average was 7 (Table 1), the ratings were considered to be high from this number. A low percentage of subjects gave a low score (1, 2, 3) for the three comparisons. The subjects reported the highest score (7, 8, 9, and 10) for the comparison of textures 1 and 3, which was followed by textures 1 and 2.

Percentage of Differentiation
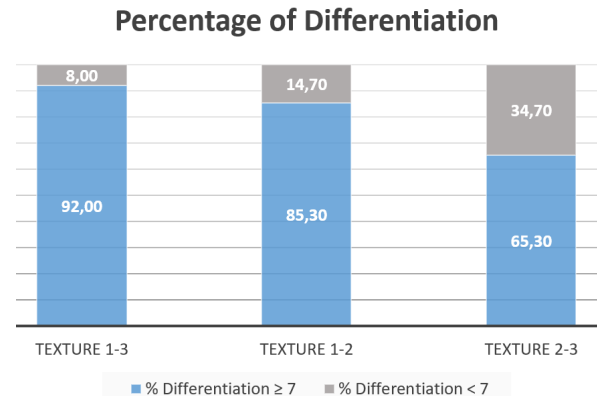
Figure 7. Percentage of individuals who assigned scores below and above 7
Source: Authors

Table 1 summarizes the descriptive measures of the discrimination results. It is clear that the highest mean was attributed to texture comparison 1-3, while the lowest average for texture comparison 2-3. In general, the median values between texture comparisons are in the upper extreme, which confirms the tendency towards a high differentiability.

Table 1. Descriptive measures of collected data

	Texture 1-2	Texture 2-3	Texture 1-3
minimum	3	2	3
maximum	10	10	10
mean (s)*	8,29 (1,807)	7,43 (2,035)	9 (1,644)
median (IR)**	8 (2)	8 (3)	10 (1)
asymmetry	-1,59	-0,36	-2,1

* s: Standard Deviation; ** Interquartile Range

Source: Authors

A negative symmetry is evident in the valuation distribution. Nevertheless, the Kolmogorov-Smirnov test was applied to examine the normality of the data. The result obtained was the rejection of the null hypothesis. The results were the following: textures 1-2 (KS=0,222; p=0,000), textures 2-3 (KS=0,131; p=0,003), and textures 1-3 (KS=0,302; p=0,000).

Table 2 shows the significant difference values between the three textures according to the Friedman test. There is at least one difference in one of the textures (p<0,05). This result confirms that the comparison between textures 1 and 3 has the greatest differentiability. In addition, its median value is the highest.

Table 2. Results for Friedman test 1

N	75
Chi-square	30,791
DF	2
P-value	0,000

Source: Authors

Coupling tests between the vibrotactile and the kinesthetic interfaces

Figure 5 also shows the virtual environment, the virtual object, and both the kinesthetic and tactile interfaces. In this environment, a subject manipulated a rigid cube with fixed dimensions, whose surface texture image displayed three different textures (Figure 6).

The results of experiment 2 were subjective; all participants (100%) reported a difference between the two parts of the experiment.

Table 3 shows a part of the descriptive analysis for the results of experiment 3. The data have a negative symmetry. Moreover, the median values are in the upper extreme, thus confirming the tendency to a high level of realism regarding the perceived sensation on the palm and finger according to the visualized surface.

Table 3. Descriptive statistics of the coupling test

	Coupling of Kinesthetic Interface with:		
	Textures 1-2	*Textures 2-3*	*Textures 1-3*
minimum	5	3	4
maximum	10	10	10
mean (s)*	7,54 (1,88)	7,29 (2,25)	8,097 (1,95)
median (IR)**	8 (2)	8 (3)	9 (3)
asymmetry	-1,59	-0,36	-2,1

* s: Standard Deviation; ** Interquartile Range

Source: Authors

The results obtained from experiment 3 are summarized in a box and whiskers diagram (Figure 8). The median value of the subjects' ratings for the degree of correspondence between the sensation and the visual image was 8 for textures 1 and 2 and 9 for texture 3, thus indicating that the perception of realism was closer to the maximum possible value. According to Figure 8, most of the data for texture 1 were concentrated between 7 and 9; for texture 2, the data were concentrated between 6 and 9; and, for texture 3, the scores were concentrated between 7 and 10. In light of the high values of the medians, it is considered that a high perception of realism was achieved in each texture.

The Shapiro-Wilk test confirmed that the data does not have a normal distribution. The results were the following: texture 1 (SW=0,906; p=0,010), texture 2 (SW=0,909; p= 0,013), and texture 3 (SW=0,848; p= 0,000).

The Friedman test showed no significant differences (p>0,05) between the three realism comparisons (Table 4).
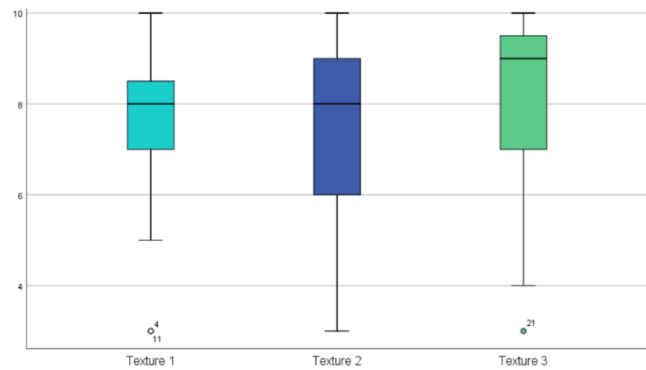
Figure 8. Box and whiskers diagram for the evaluation of each tactile stimulus coupled with the kinesthetic interface
Source: Authors

Table 4. Results for Friedman test 3

N	75
Chi-square	4,980
DF	2
P-value	0,083

Source: Authors

Discussion

The main contribution of this work was testing the performance of a low-cost vibrotactile system attachable to the Novint Falcon interface by means of physically reproducing three virtual textures. The system has some characteristics that improve the level of immersion into a virtual environment, which a DES can take advantage of in order to enhance interactivity.

Three fundamental elements support the above: a) the vibrotactile system HaptTech reproduces three different stimuli and is incorporable to a DES; b) there is an increased level of immersion regarding texture perception with the inclusion of a vibrotactile stimulus to the Novint Falcon kinesthetic interface; and c) there is a high correspondence between the vibrotactile pattern presented to the subjects and the texture displayed.

A review of the state of the art shows a representative European project that simulates the touch of virtual textiles. This system, Haptex, uses tactile and kinesthetic actuators with several contact points in every finger. These actuators, developed independently, are bulky, and the system is not easily transportable (MIRALab, 2021; Haptex, 2021). HaptTech adapted a tactile actuator to a commercial kinesthetic system, in which the vibration stimulus acts on the contact area of the fingertip. The main features of this system are its simplicity, safety, and portability.

Vibrotactile texture reproduction incorporable to a digital entertainment system

Regarding the HaptTech vibrotactile stimuli reproduction system, there are three stimuli varying in surface roughness, differentiable enough from each other, to be used in a DES. This was verified by conducting differentiability tests on 75 people and finding that a percentage higher than 65% of the sample considered the differentiability to be greater than 7 in all pairs of textures (on a 1-10 perception scale). For the best texture pair comparison, 92% of the population agreed with this level of differentiability (Figure 7).

The vibration stimuli received by the subjects are within the perception range of the skin and activate mechanoreceptors (Chouvardas *et al.*, 2008). These receptors detect the variations in the applied stimulus.

DES could include a texture reproduction module, which would create a higher level of immersion for the user by differentiating object textures in virtual environments used in commercial or serious games.

These vibrotactile systems are safe, portable, and energy-efficient, which makes them useful for game applications, in addition to adding a tactile complement for interacting with texturized objects.

Only three texture stimuli were used in the tests for this study, but future research should use more. The degree of vibration intensity and its relationship with surface roughness in the three texture stimuli confirmed a relationship of differentiability. It is possible to improve tactile simulation, achieving a higher resolution by including additional stimuli to the vibration. However, this augmented effect may not be necessary for digital entertainment applications.

Increased level of immersion

As for the increase in the level of immersion when perceiving textures, by adding the device for reproducing vibrotactile stimuli to the kinesthetic stimulation provided by the Novint Falcon interface, a 100% differentiation (present *vs.* absent stimulus) was achieved in 31 participants.

By including tactile feedback in a VR environment while the participants interact with virtual objects, the mechanoreceptors are also activated, which favors immersion. The importance of this complement is that it can generate more complex interactions that are different from just identifying boundaries or obstacles in VR, as is the case of recognizing different texturized objects.

The coupling reproduces the texture perception directly on the fingertip, unlike other devices with pen-like grips (Culbertson and Kuchenbecker, 2017b; Ujitoko *et al.*, 2019). These indirectly transfer the sensation of the surface to the hand.

The physical coupling of the vibrotactile reproducer is non-invasive. The electronic coupling was carried out through programming routines that synchronized the texture stimuli when the virtual object was touched, thus enhancing the level of immersion.

High correspondence between vibrotactile patterns and visualized textures

A high correspondence between vibrotactile patterns applied to the subject and the virtual surface textures makes for a more realistic perception (Culbertson and Kuchenbecker, 2017a). The test performed to assess perception correspondence yielded results with high medians. Based on the Box and Whiskers diagram (Figure 8), the data are mostly located at the upper end, indicating that users perceive a relationship between what they see with what they feel.

The above is useful for applications that require permanent correspondence between visual and manual perception, *e.g.,* palpation procedures or others that involve texture identification.

Two possible phenomena can explain the instances of less coincidence: a) concerning vision and haptics in material perception, the disparity between the mental image that the person formed when observing the texture that formed when they received the tactile stimulus (Baumgartner *et al.*, 2013; Klatzky and Lederman, 2010); and b), the prolonged use of vibrotactile actuators, which could block the user's discernability because this actuator only stimulates one type of tactile receptor (Pacinian, *i.e.,* a Phasic type or of fast adaptation), and this receptor can be saturated or adapt when a stimulus is applied too often (Fox, 2014).

Conclusions

This research described the development of a vibrotactile device to generate surface texture stimuli while coupled with the Novint Falcon kinesthetic interface.

By testing the low-cost vibrotactile reproducer, HaptTech, which reproduces three textures while coupled to the interface, results were found which favor the level of realism of the perceived sensation, which suggests that the device could help increase the level of immersion in a VR environment, in addition to being useful in a DES.

Current applications of interactive digital entertainment do not feature texture differentiation, although they use vibrotactile actuators, commonly for contact, in order to indicate the presence of an object or signal an action such as a gunshot or bursts.

The addition of tactile feedback generates stimuli that activate mechanoreceptors, which could also improve the immersion and complement the visual sensation produced by the DES.

Vibrotactile stimulation has no risks or side effects. However, prolonged vibrotactile stimulation can block the perception of the same stimulus.

Complementing kinesthetic perception and visual feedback is suitable for application in a DES, especially for VR, serious games for rehabilitation, or training. Further studies on the differentiation of more than three textures would improve performance in different applications.

Future work

Future research could change the vibration component to a piezoelectric element, which maintains a reduced size and weight but generates high-resolution stimuli. Furthermore, testing could be conducted for greater degrees of realism by coupling the stimuli with other complementary stimuli (*e.g.,* electro-cutaneous or electro-capacitive), while adapting the findings of previous research. A greater degree of realism means that the virtual stimulus simulates the real stimuli more closely.

More tests are necessary, with the addition of other textures for differentiation while discerning the influence of the visual texture expectation produced in the user. It is also necessary to implement a method to convert the roughness of a surface into a quantified, digitalized vibrotactile signal.

Finally, future applications of the HaptTech device to a DES may benefit from an additional hardware device that simultaneously manages the interaction with the virtual environment using both the texture reproducer and the Novint Falcon interface.

Acknowledgements

References

Álvarez, F., and Álvarez, A. (2009). *Auditoría médica y epidemiología* (1st ed.). Ecoe Ediciones.

Baumgartner, E., Wiebel, C. B., and Gegenfurtner, K. R. (2013). Visual and haptic representations of material properties. *Multisensory Research*, 26(5), 429-455. https://doi.org/10.1163/22134808-00002429

Bärnighausen, T., Tugwell, P., Røttingen, J. A., Shemilt, I., Rockers, P., Geldsetzer, P., Lavis, J., Grimshaw, J., Daniels, K., Brown, A., Bor, J., Tanner, J., Rashidian, A., Barreto, M., Vollmer, S., and Atun, R. (2017). Quasi-experimental study designs series–Paper 4: Uses and value. *Journal of Clinical Epidemiology, 89*, 21-29. https://doi.org/10.1016/j.jclinepi.2017.03.012

Bensmaïa, S. J., and Hollins, M. (2003). The vibrations of texture. *Somatosensory & Motor Research, 20*(1), 33-43. https://doi.org/10.1080/0899022031000083825

Bremner, A. J., and Spence, C. (2017). The development of tactile perception. In J. B. Benson (Ed.), *Advances in Child Development and Behavior* (vol. 52, pp. 227-268). Elsevier. https://doi.org/10.1016/bs.acdb.2016.12.002

Chouvardas, V. G., Miliou, A. N., and Hatalis, M. K. (2008). Tactile displays: Overview and recent advances. *Displays, 29*(3), 185-194. https://doi.org/10.1016/j.displa.2007.07.003

Culbertson, H., and Kuchenbecker, K. J. (2017a). Importance of matching physical friction, hardness, and texture in creating realistic haptic virtual surfaces. *IEEE Transactions on Haptics, 10*(1), 63-74. https://doi.org/10.1109/TOH.2016.2598751

Culbertson, H., and Kuchenbecker, K. J. (2017b). Ungrounded haptic augmented reality system for displaying roughness and friction. *IEEE/ASME Transactions on Mechatronics, 22*(4), 1839-1849. https://doi.org/10.1109/TMECH.2017.2700467

CybergloveSystems (2019). *Cybertouch.* http://www.cyberglovesystems.com/cybertouch/

Delice, A. (2010). The sampling issues in quantitative research. *Educational Sciences: Theory & Practices, 10*(4), 2001-2018. https://eric.ed.gov/?id=EJ919871

Fontana, M., Ruffaldi, E., Salasedo, F., and Bergamasco, M. (2012). On the integration of tactile and force feedback. In A. El Saddik (Ed.), *Haptics Rendering and Applications* (pp. 47-75). https://doi.org/10.5772/25446

Fox, S. I. (2014). *Fisiología humana* (13th ed.). McGraw Hill Education.

Freeglut (2019). *The free OpenGL utility toolkit*. http://freeglut.sourceforge.net

French, A. S., and Torkkeli, P. H. (2009). Mechanoreceptors. In L. R. Squire (Ed.), *Encyclopedia of Neuroscience* (pp. 689-695). Academic Press. https://doi.org/doi.org/10.1016/B978-008045046-9.01921-5

Glantz, S. A. (2006). *Bioestadística*. McGraw-Hill Interamericana.

Glew (2019). *The OpenGL Extension Wrangler Library*. http://glew.sourceforge.net

Golledge, R. G., Rice, M. T., and Jacobson, R. D. (2006). Multimodal interfaces for representing and accessing geospatial information. In S. Rana and J. Sharma (Eds.) *Frontiers of Geographic Information Technology* (pp. 181-208). Springer https://doi.org/10.1007/3-540-31305-2_9

Griffin, M. J. (2012). Vibraciones. In M. J. Griffin (Ed.), *Enciclopedia de Salud y Seguridad en el Trabajo en la OIT* (vol. II, p. 18). https://www.insst.es/documents/94886/162520/Capítulo+50.+Vibraciones

Haptex (2021). *The Haptex project*. https://n9.cl/ex9xu

Hoshi, T., Takahashi, M., Iwamoto, T., and Shinoda, H. (2010). Noncontact tactile display based on radiation pressure of airborne ultrasound. *IEEE Transactions on Haptics, 3*(3), 155-165. https://doi.org/10.1109/TOH.2010.4

Kim, M., Jeon, C., and Kim, J. (2017). A study on immersion and presence of a portable hand haptic system for immersive virtual reality. *Sensors, 17*(5), 1141. https://doi.org/10.3390/s17051141

Klatzky, R. L., and Lederman, S. J. (2010). Multisensory texture perception. In M. J. Naumer and J. Kaiser (Eds.), *Multisensory Object Perception in the Primate Brain* (pp. 211-230). Springer. https://doi.org/10.1007/978-1-4419-5615-6

MIRALab (2021). *MIRALab – CUI – University of Geneva*. https://n9.cl/dgamj

O'Malley, M., and Gupta, A. (2008). Haptic interfaces. In P. Kortum (Ed.), *HCI Beyond the GUI: Design for Haptic, Design for Haptic, Speech, Olfatory and Other Nontraditional Interfaces* (1st ed., pp. 25-73). Morgan Kaufmann. http://dx.doi.org/10.1016/B978-0-12-374017-5.00002-X

Pacchierotti, C., Sinclair, S., Solazzi, M., Frisoli, A., Hayward, V., and Prattichizzo, D. (2017). Wearable haptic systems for the fingertip and the hand: Taxonomy, review, and perspectives. *IEEE Transactions on Haptics, 10*(4), 580-600. https://doi.org/10.1109/TOH.2017.2689006

Pacchierotti, C., Tirmizi, A., Bianchini, G., and Prattichizzo, D. (2013, November 3-7). *Improving transparency in passive teleoperation by combining cutaneous and kinesthetic force feedback* [Conference presentation]. 2013 IEEE/RSJ International Conference on Intelligent Robots and Systems, Tokyo, Japan. https://doi.org/10.1109/IROS.2013.6697072

Proske, U., and Gandevia, S. C. (2012). The proprioceptive senses: Their roles in signaling body shape, body position and movement, and muscle force historical background. *Physiological Reviews, 92*(4), 1651-1697. https://doi.org/10.1152/physrev.00048.2011

Rosa, P. J., Morais, D., Gamito, P., Oliveira, J., and Saraiva, T. (2016). The immersive virtual reality experience: A typology of users revealed through multiple correspondence analysis combined with cluster analysis technique. *Cyberpsychology, Behavior, and Social Networking, 19*(3), 209-216. https://doi.org/10.1089/cyber.2015.0130

Sadiku, M. N. O., Shadare, A. E., and Musa, S. M. (2017). Digital Entertainment 1, 2. *International Journals of Advanced Research in Computer Science and Software Engineering, 7*(8), 62-63. https://www.researchgate.net/publication/326085524_Digital_Entertainment

Santís, M., Jaramillo, D., and Pérez, V. Z. (2016, October 26-28). *Vibrotactile system for the replication of textures* [Conference presentation]. VII Latin American Congress on Biomedical Engineering CLAIB 2016, Bucaramanga, Colombia. https://doi.org/10.1007/978-981-10-4086-3_129

Tan, E. S., and Jansz, J. (2008). The game experience. In H. F. N. Schifferstein and P. Hekkert (Eds.) *Product Experience* (pp. 531-556). https://doi.org/10.1016/B978-008045089-6.50026-5

Ujitoko, Y., Ban, Y., and Hirota, K. (2019). Modulating fine roughness perception of vibrotactile textured surface using pseudo-haptic effect. *IEEE Transactions on Visualization and Computer Graphics, 25*(5), 1981-1990. https://doi.org/10.1109/TVCG.2019.2898820

Villa-Salazar, D. S., Pacchierotti, C., de Tinguy de la Girouliere, X., Maciel, A., and Marchal, M. (2020). Altering the stiffness, friction, and shape perception of tangible objects in virtual reality using wearable haptics. *IEEE Transactions on Haptics, 13*(1), 167-174. https://doi.org/10.1109/TOH.2020.2967389

Yang, Y. (2013). *Design and control of an integrated haptic interface for touch screen applications* [Doctoral thesis, Université Lille]. http://goo.gl/9J8s4R

Assessment of the Wind Power Potential in the Gulf of Urabá, Department of Antioquia

Evaluación del potencial de energía eólica en el Golfo de Urabá, departamento de Antioquia

Juan C. Pineda-Ortiz[1] Ana Barona-Mejía[2] Ainhoa Rubio-Clemente[3], and Edwin L. Chica-Arrieta[4]

ABSTRACT

In this work, an estimation of the wind resource potential was calculated using the Weibull method in the Gulf of Urabá, where wind velocities reach significant and more uniform values. Particularly, this potential was calculated at the coordinates 8,713280° latitude and -77,075274° longitude, where the power density varies between 33,59 and 128,39 W/m2 throughout the year. Based on the guidelines established by the International Electrotechnical Commission (IEC) and the power curves of commercial wind turbines, the installation of 875 offshore-type wind turbines in the Gulf of Urabá was determined to generate monthly and annual averages of electrical energy of 522 982,66 MWh and 6 275,79 GWh, respectively. The wind potential of the selected point represented 8,72% of the electrical energy demanded in Colombia during 2019, which was around 71,93 TWh. Therefore, the use of the wind resource in this area might contribute to the development of the national policy related to the utilization of non-conventional sources of renewable energy (NCSRE), guaranteeing energy security and the reduction of greenhouse gas emissions. However, the incorporation of NCSRE in the national energy matrix poses challenges in the flexibility of the energy system network, which must be solved to ensure the reliability of the system.

Keywords: wind energy, energy density, wind turbine, energy potential, flexible systems

RESUMEN

En este trabajo se realizó una estimación del potencial del recurso eólico usando el método de Weibull en el Golfo de Urabá, donde las velocidades del viento alcanzan valores significativos y más uniformes. Particularmente, este potencial se calculó en las coordenadas 8,713280° de latitud y -77,075274° de longitud, donde la densidad de potencia varía entre 33,59 y 128,39 W/m2 a lo largo del año. A partir de las pautas establecidas por la Comisión Electrotécnica Internacional (IEC) y las curvas de potencia de aerogeneradores comerciales, se logró determinar que la instalación de 875 aerogeneradores tipo offshore en el Golfo de Urabá podría llegar a generar promedios de energía eléctrica mensual y anual de 522 982,66 MWh y 6 275,79 GWh, respectivamente. El potencial eólico del punto seleccionado representa el 8,72 % de la energía eléctrica requerida en Colombia durante el año 2019, la cual fue alrededor de 71,93 TWh. Por lo tanto, el aprovechamiento del recurso eólico de esta zona puede llegar a contribuir al desarrollo de la política nacional relacionada con el uso de fuentes no convencionales de energía renovable (FNCER), garantizando la seguridad energética y la reducción de las emisiones de gases de efecto invernadero. Sin embargo, la incorporación de las FNCER en la matriz energética nacional genera desafíos en la flexibilidad de la red del sistema de energía, los cuales deben ser resueltos para asegurar la confiabilidad del sistema.

Palabras clave: energía eólica, densidad de energía, turbina eólica, potencial energético, sistemas flexibles

Introduction

Knowing the current situation of Colombia with regard to the available energy resources and the need to supply an energy basket that tends to increase over time, with rates ranging between 1,50 and 4,10% (Cortés and Londoño, 2017), the electrical energy demand would theoretically become greater than the supply of the electrical energy in 2021 (Ministerio de Minas y Energía - Unidad de Planeación Minero Energética, 2017). In this regard, the development of versatile and flexible energy systems that can guarantee energy availability is required. One option that may be useful is the integration of energies from renewable sources to the National Interconnected System (NIS).

In line with the above, the Colombian energy plan contemplates the diversification of the energy matrix with

[1] Master's student in mechanical engineering, Universidad de Antioquia, Colombia. Affiliation: Grupo de Investigación Energía Alternativa-GEA, Department of Engineering, Universidad de Antioquia, Medellín, Colombia. Email: juan.pineda2@udea.edu.co

[2] Mechanical Engineering student. Universidad de Antioquia, Colombia. Affiliation: Grupo de Investigación Energía Alternativa-GEA, Department of Engineering, Universidad de Antioquia, Medellín, Colombia. Email: ana.barona@udea.edu.co

[3] PhD in Environmental Engineering. Universidad de Antioquia, Colombia. Affiliation: Grupo de Investigación Energía Alternativa-GEA, Department of Engineering, Universidad de Antioquia, Medellín, Colombia. Email: ainhoa.rubioc@udea.edu.co

[4] PhD in Engineering. Universidad de Valladolid, España. Affiliation: Grupo de Investigación Energía Alternativa-GEA, Department of Engineering, Universidad de Antioquia, Medellín, Colombia. Email: edwin.chica@udea.edu.co

renewable energy resources, ensuring a timely, reliable, safe, and efficient supply to the entire society and, in turn, contributing to the reduction of greenhouse gas emissions and the mitigation of the climate change. In the country, despite the fact that there are capabilities for generating electricity from non-conventional sources of renewable energy (NCSRE), mainly systems that take advantage of wind and solar energy, the interest of the national government is to increase the participation of NCSRE in the energy matrix in order to improve the resilience to climate variability events such as El Niño phenomenon and the natural cyclical periods of rains and droughts (Rueda-Bayona *et al.*, 2019; Gómez-Navarro and Ribó-Pérez 2018). For this purpose, the Ministry of Mines and Energy (MME) of Colombia, through Resolutions 40590, 40591, and 40725 of 2019, put the Mining and Energy Planning Unit (UPME) in charge of carrying out the implementation and execution of the auction of long-term energy contracts CLPE No. 02-2019, in which only generation projects from NCSRE could participate.

According to the aforementioned auction reports, the total energy allocated was 10 186,00 MWh/day out of the 12 050,50 MWh/day of the target demand, and responsibility was assigned to seven companies generating energy with eight NCSRE projects, out of which five were wind projects and three were solar. 17,39 and 82,61% of the total assigned energy corresponded to the generation from photovoltaic solar energy and wind energy, respectively. A maximum sale price of $110,00/kWh is expected. After the inclusion of the new NCSRE projects, in 2022, the country will go from less than 60 MW to more than 2 250 MW of the installed capacity in renewable energy. Currently, Colombia has an installed wind capacity of 19,50 MW through the Jepírachi project. However, given the fact that the Energy and Gas Regulation Commission (CREG) issued Resolution 060 of June 20th, 2019, by which the operating regulations for solar and wind energy projects were modified, the Jepírachi project was found to not comply with the new quality specifications. Under this scenario, in January 2020, the project suspended the delivery of energy to the NIS. Nevertheless, in July 2020, Jepírachi resumed its operation because Empresas Públicas de Medellín (EPM) issued a requirement to the National Government for enabling the project to continue generating energy temporarily until the end of the park's useful life, which is estimated to be in 2023.

Considering that, in Colombia, 15,00%, of the energy will be expected to come from NCSRE to provide flexibility and complementarity to the NIS by 2030, the identification of potential sites where generation projects could be developed is of utmost importance in order to contribute to the mitigation of the risks related to deficits in the energy basket. Even though the Colombian wind resource is not characterized by being one of the best ones in terms of energy density, the wind resource available in certain areas located in the department of La Guajira, as well as in a large portion of the Caribbean region, in the department of Norte de Santander,

and in the coastal strips can be adequately used to increase the installed capacity of the country with regard to renewable energy. In the case of La Guajira, trade winds have average velocities close to 9,00 m/s and a prevailing east-westward direction (Rueda-Bayona *et al.*, 2019; Gómez-Navarro and Ribó-Pérez, 2018). Although the department of Antioquia has lower wind velocities, it can be also attractive to increase the installed capacity, taking into account that it has the necessary electrical infrastructure to distribute the produced energy to the consumption centers. Therefore, this work aims to determine the potentially available wind energy in the department of Antioquia, specifically in the Gulf of Urabá, in order for it to be used in the generation of electricity. In this regard, by involving non-conventional sources, the risk of an energy deficit, as foreseen in the projections made by the UPME, would be mitigated.

In the literature, there are different approaches to study the wind energy potential of a specific area, such as the wind atlas analysis and application programs, as well as Rayleigh and Weibull distributions. However, the most used method for assessing the wind energy potential is the Weibull distribution of wind speed data studied within multiple temporal scales (Chandel *et al.*, 2014; Solyali *et al.*, 2016; Dayal *et al.*, 2021; Mohamadi *et al.*, 2021). This assessment is an imperative step in the prediction of the annual electrical energy production from the wind energy in potential areas in order to verify whether there are enough wind resources within the area to justify further site-specific investigations, determine initial feasibility and cash flow projections, and obtain representative data for estimating the performance and/or the economic viability of the selected wind turbines.

For this reason, in this study, the wind energy potential of the Gulf of Urabá is assessed using the Weibull method, particularly at a specific location in the maritime area, by utilizing detailed wind variables such as the direction, speed, availability, and continuity of the wind resource.

Methods and materials

Wind velocity distribution

The wind is an intermittent renewable resource (both geographically and temporally), *i.e.*, it fluctuates due to weather patterns and cloud presence, and it cycles from day to night depending on many factors. Among them, it is important to note that the wind velocity varies with altitude and is a function of the nature of the soil over which the air masses move (Nedaei *et al.*, 2018; Li *et al.*, 2016; Ohunakin, 2011; Boopathi *et al.*, 2021). Consequently, the production of electricity is variable and does not follow the same pattern as the demand. For example, in the case of wind energy, electricity generation is sometimes higher at night, when the demand for electricity is lower. Therefore, the incorporation of these systems requires the development of auxiliary systems of energy use and/or storage.

Depending on the intensity and periodicity of the wind, the technical and economic feasibility of using wind energy to generate electricity can be estimated. Some locations are not profitable enough for the development of an electric power generation project with the available wind resource (Nedaei *et al.*, 2018; Li *et al.*, 2016). In this regard, the development of a technical and economic study is of utmost importance in order to evaluate whether the projects are competitive in comparison with conventional generation sources. In this regard, choosing a proper site for the installation of wind farms must be conducted. In many cases, potential installation sites are often located in remote areas, far from large consumption centers. Thus, transmission lines must be built to transport electricity from the wind farm to the consumption centers, a situation that can result in increased production costs and financial infeasibility for the generation project.

Even though there are initiatives by entities, such as the UPME and the Institute for Hydrology, Meteorology, and Environmental Studies (IDEAM) in Colombia to provide information on the characterization of the wind resource as a first approximation for investors interested in its use, few public studies detailing this resource and other NCSRE that can help plan its adequate applicability are reported. In line with this, this research evaluates potential sites in the department of Antioquia, where electricity generation projects can be developed from the wind potential.

The ideal cut-in wind velocity of wind turbines is typically between 3,00 and 4,00 m/s. Nevertheless, a nominal wind velocity (rated wind velocity) is required for the turbine to generate electricity at its own maximum or nominal capacity. This velocity ranges from 10,00 to 15,00 m/s. Finally, at the cut-out wind velocity, which is in the order of 25,00 m/s, the turbine turns off to avoid damage. When the cutting velocity is exceeded, the controllers place the blade in the flag position to enable the wind to pass through and brake the rotor hub. The wind generally has to return to a much lower velocity –the so-called cut-back wind velocity in wind turbines– for a certain time before the turbine restarts. This velocity is about 20,00 m/s (Abdulgalil *et al.*, 2019; Tummala *et al.*, 2016). The change of the power output of a wind turbine along with the wind velocity is represented in Figure 1.

To initially identify potential sites in Antioquia, the wind velocity maps made available by IDEAM identify the areas with average wind velocities equal to or greater than 5,00 m/s, where wind turbines could be installed in order to transform the wind kinetic energy into rotational mechanical energy and, subsequently, into electrical energy (Siabato-Benavides, 2018). Thus, the annual average distribution of wind velocities in the department of Antioquia, according to the IDEAM interactive atlas, is illustrated in Figure 2. As it can be observed in said Figure, there is only one area in Antioquia where the annual average velocities exceed 5,00 m/s, and it is located in the coastal and maritime zone of the Urabá region.
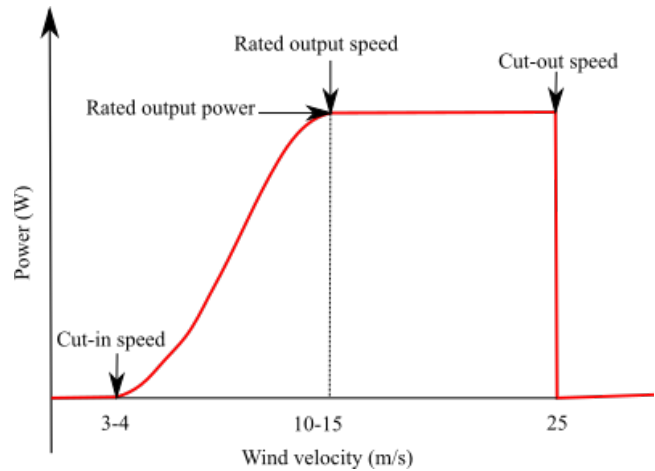
Figure 1. Characteristic power curve of a wind turbine
Source: Authors
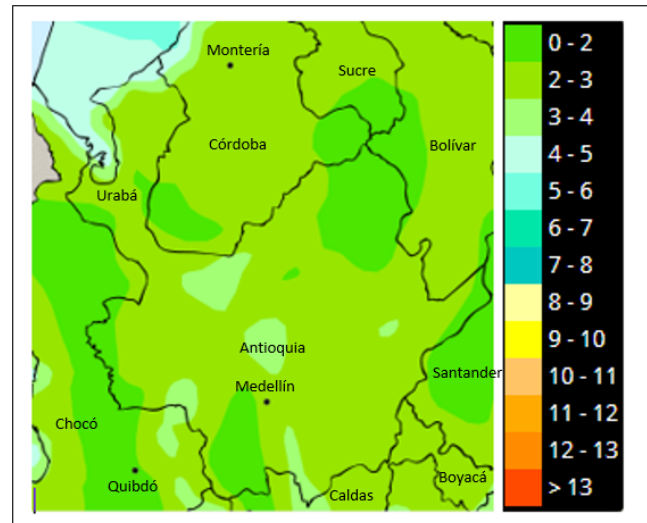
Figure 2. Map representing the annual average of the wind velocity distribution (m/s) in the department of Antioquia for 2015
Source: Gómez-Navarro and Ribó-Pérez (2018)

The area value of this region estimated using Google Earth Pro software is 7 684 338 660,59 m². In Figure 3, the annual average velocities are found to vary between 7,00 and 8,00 m/s in some locations of the coastal region, whereas these velocities are ranged between 8,00 and 9,00 m/s in other areas. The same can be observed for the maritime zone.

In order to carry out a more accurate estimation of the wind resource in the coastal and maritime areas of Antioquia, wind data generated by a meteorological station are necessary, preferably from a long period of time (greater than 1 year). These data must include at least the wind direction and velocity (Nagababu *et al.*, 2015). To determine the wind resource, a point (P) very close to the coast was selected in the area of interest, as shown in Figure 3. In the current case, the P coordinates were 8,713280° latitude and -77,075274° longitude.
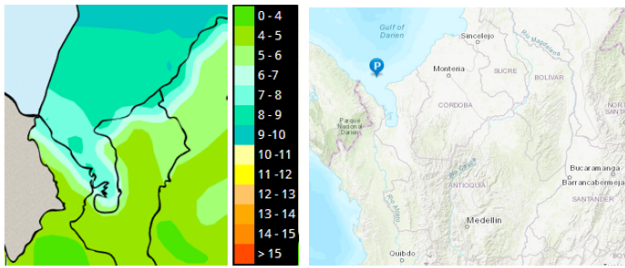
Figure 3. Map representing the annual average of the wind velocity distributions (m/s) at 100 m of altitude in the area of interest for 2015
Source: Gómez-Navarro and Ribó-Pérez (2018)

Since no meteorological stations are installed at the selected point, the information published by NASA (Prediction of Worldwide Energy Resource) was used to evaluate the wind resource. This information source reports a large database of meteorological parameters such as wind velocity, temperature, and radiation, among others. In this database, from the location of the site, it is possible to obtain the maximum, mean, and minimum wind velocities. In Tables 1 and 2, the monthly average of the mean daily wind velocities at altitude values of 10,00 and 50,00 m at the selected point are correspondingly compiled. The monthly average wind velocity ($\bar{v}$) can be estimated with Equation (1).

$$\bar{v} = \frac{1}{N}\sum_{i=1}^{N} v_i \qquad (1)$$

where N is the data number, and v_i refers to the recorded data of the daily average wind velocity. It is highlighted that the wind velocity is measured as an international meteorological standard at an altitude of 10,00 m (Ohunakin, 2011). To estimate the wind resource at the selected point, a statistical analysis of the wind velocity data from the last 10 years was carried out (between 2010 and 2019). From the database, the daily average maximum and minimum velocity values at the indicated altitudes were obtained.

The wind velocity, as previously mentioned, depends on the altitude and the nature of the soil over which the air masses are moving. The wind velocity variation can be represented by Equation (2) (Ali *et al.*, 2017; Manwell *et al.*, 2010; Gul *et al.*, 2019):

$$\frac{V_2}{V_1} = \left[\frac{h_2}{h_1}\right]^{á} \qquad (2)$$

where $V_1 < V_2$ represents the wind velocities at altitudes $h_1 < h_2$, respectively. In turn, α is an exponent that depends on the average surface roughness and the average atmospheric stability in the considered location. This parameter can take a value between 0,08 and 0,12 for smooth surfaces (ice, snow, sea, lagoons, *etc.*); between 0,13 and 0,16 for a slightly uneven terrain and grazing and cultivating areas; in the range from 0,20 to 0,23 for a rough terrain, forests, and sparsely inhabited areas; and between 0,25 and 0,40 for an uneven terrain (Ali *et al.*,

Table 1. Monthly average of the daily mean velocity (m/s) at an altitude of 10,00 m

Year	Jan	Feb	Mar	Apr	May	Jun	Jul	Aug	Sep	Oct	Nov	Dec
2010	3,66	3,30	3,49	2,84	2,19	1,92	1,94	1,94	2,09	2,12	2,28	3,24
2011	3,09	3,48	3,70	3,09	2,11	1,78	1,85	1,73	1,91	2,33	2,18	2,87
2012	3,46	3,54	3,81	2,33	1,95	1,76	1,78	1,76	1,84	2,42	2,32	2,56
2013	3,54	3,73	3,94	3,04	2,28	1,71	1,70	1,74	1,73	1,73	2,12	2,53
2014	3,31	3,67	3,68	2,97	2,22	1,70	1,76	1,88	1,63	1,74	2,15	2,69
2015	3,76	3,77	3,91	2,81	2,32	1,83	1,96	1,85	1,79	1,88	2,06	2,22
2016	3,48	4,47	3,64	3,36	1,85	1,72	1,81	1,68	1,78	1,96	2,09	2,56
2017	3,39	3,47	3,65	2,76	1,83	1,85	1,72	1,71	1,62	1,76	2,44	2,88
2018	2,80	3,84	3,99	2,91	1,90	1,75	1,67	1,64	1,71	1,73	2,30	3,18
2019	3,95	3,67	4,22	3,24	1,82	1,71	1,71	1,65	1,78	1,76	2,26	2,75

Source: Authors

Table 2. Monthly average of the daily mean velocity (m/s) at an altitude of 50,00 m

Year	Jan	Feb	Mar	Apr	May	Jun	Jul	Aug	Sep	Oct	Nov	Dec
2009	4,64	5,45	5,46	4,37	2,51	2,40	2,41	2,50	2,38	2,37	2,96	3,58
2010	4,76	4,26	4,56	3,71	2,91	2,54	2,60	2,60	2,80	2,84	3,03	4,27
2011	4,07	4,54	4,80	4,04	2,76	2,37	2,47	2,27	2,53	3,08	2,92	3,79
2012	4,51	4,58	4,93	3,05	2,56	2,30	2,36	2,32	2,40	3,24	3,05	3,38
2013	4,61	4,83	5,15	3,98	3,03	2,25	2,20	2,30	2,31	2,28	2,80	3,32
2014	4,30	4,72	4,71	3,79	2,91	2,24	2,29	2,46	2,15	2,30	2,83	3,53
2015	4,90	4,90	5,03	3,64	3,05	2,40	2,60	2,45	2,35	2,49	2,72	2,91
2016	4,54	5,81	4,67	4,39	2,44	2,26	2,38	2,18	2,34	2,61	2,81	3,39
2017	4,41	4,49	4,75	3,62	2,44	2,26	2,28	2,26	2,14	2,33	3,22	3,79
2018	3,68	4,99	5,16	3,78	2,48	2,32	2,23	2,12	2,25	2,33	3,08	4,18
2019	5,13	4,74	5,45	4,22	2,41	2,29	2,43	2,43	2,37	2,34	3,02	3,64

Source: Authors

2017; Manwell et al., 2010). From the available data for the minimum, mean, and maximum velocity at 10 and 50 m in the NASA database and using Equation (2), α was estimated for each pair of daily records. From the data reported at 50,00 m (minimum, mean, and maximum velocity) and the previously determined α, the wind velocity was estimated at 100,00 m at the point of interest. Table 3 shows the $\bar{v}$ values of the records corresponding to the daily minimum, mean, and maximum velocity at 100,00 m of altitude. Table 3 also details the standard deviation (σ) of the data set, which can be obtained using Equation (3) (Fazelpour et al., 2015).

$$\acute{\sigma}^2 = \frac{1}{N-1} \sum_{i=1}^{N} \left(v_i - \bar{v} \right)^2 \tag{3}$$

In order to estimate the wind potential at the site of interest, a classification of recorded velocities was performed according to the frequency in which they occurred from 2009 to 2019. The data were classified by intervals, so that they start at values whose velocities were between 0,00 and 1,00 m/s and are followed by velocities between 1,00 and 2,00 m/s. The sequence continues to be increased by 1,00 m/s until velocities greater than 9,00 m/s are finally acquired. This was required to improve the characterization of the data and determine the optimal wind frequency for power generation.

The classification of the frequencies of the daily wind velocities (minimum, mean, and maximum) at 100,00 m is presented in Table 4. The average data corresponding to the minimum, mean, and maximum velocities were 2,25, 3,67,

and 5,05 m/s, with σ values of 1,71, 1,45, and 1,33 m/s, respectively. Finally, the average of the data set (minimum, mean, and maximum velocities) was 3,66 m/s, with a σ value of 1,89 m/s.

It should be noted that the frequency $f(x_i)$ of a measure x_i is the ratio between the number of observations (w_i) and the total number of measures or records (N). $f(x_i)$ can be calculated using Equation (4). The cumulative frequency $F(x_i)$ is defined as the sum of the frequencies from k=1 to i. $F(x_i)$ can be determined using Equation (5).

$$f\left(x_i \right) = \frac{w_i}{N} * 100 \tag{4}$$

$$F\left(x_i \right) = \sum_{k=1}^{i} f\left(x_i \right) \tag{5}$$

When analyzing Table 4, velocities of less than 3,00 m/s are observed to be only 37,53% of the analyzed data, which means that the remaining 62,47% of the data exceeds 3,00 m/s. 61,29% of the data show velocities from 3,00 to 8,00 m/s, with 1,18% of velocities exceeding 8,00 m/s. Beyond 3,00 or 4,00 m/s, depending on the turbine manufacturer, the wind has enough strength to overcome the internal friction of the wind turbine and, consequently, to deliver power to the grid. This means that the wind turbine would be delivering electrical power to the grid for more than 62,47% of the time analyzed.

Table 3. Monthly average of the daily wind velocity (m/s) data set (minimum, mean and maximum) at an altitude of 100,00 m

Year	Parameter	Jan	Feb	Mar	Apr	May	Jun	Jul	Aug	Sep	Oct	Nov	Dec
2009	$\bar{v}$	5,32	4,76	5,10	4,13	3,24	2,86	2,92	2,87	3,08	3,15	3,41	4,75
	σ	1,62	1,76	1,77	1,63	1,50	1,54	1,46	1,29	1,35	1,35	1,74	1,55
2010	$\bar{v}$	4,54	5,06	5,38	4,55	3,10	2,67	2,72	2,52	2,81	3,42	3,27	4,24
	σ	1,47	1,37	1,72	1,65	1,50	1,55	1,61	1,36	1,42	1,59	1,22	1,69
2011	$\bar{v}$	5,04	5,10	5,55	3,43	2,93	2,64	2,63	2,64	2,67	3,63	3,48	3,79
	σ	1,36	1,41	1,40	1,57	1,47	1,53	1,51	1,48	1,52	1,75	1,83	1,58
2012	$\bar{v}$	5,13	5,39	5,80	4,52	3,40	2,53	2,56	2,58	2,60	2,53	3,19	3,75
	σ	1,56	1,71	1,78	1,58	1,69	1,51	1,56	1,41	1,23	1,40	1,42	1,66
2013	$\bar{v}$	4,75	5,28	5,20	4,20	3,22	2,46	2,57	2,74	2,47	2,59	3,17	3,97
	σ	1,56	1,35	1,46	1,63	1,58	1,46	1,63	1,47	1,35	1,34	1,65	1,66
2014	$\bar{v}$	5,54	5,54	5,56	4,04	3,41	2,68	2,90	2,69	2,65	2,76	3,07	3,22
	σ	1,55	1,57	1,34	2,04	1,48	1,46	1,49	1,45	1,46	1,32	1,57	1,48
2015	$\bar{v}$	5,06	6,53	5,15	4,94	2,74	2,58	2,68	2,48	2,59	2,89	3,14	3,77
	σ	1,52	1,39	1,42	1,92	1,38	1,49	1,53	1,45	1,42	1,34	1,41	1,61
2016	$\bar{v}$	5,00	4,97	5,28	4,05	2,72	2,80	2,58	2,53	2,45	2,63	3,59	4,30
	σ	1,77	1,79	1,40	2,19	1,47	1,52	1,55	1,44	1,37	1,49	1,41	1,54
2017	$\bar{v}$	4,12	5,61	5,78	4,19	2,78	2,67	2,54	2,44	2,56	2,61	3,43	4,65
	σ	1,63	1,47	1,33	1,69	1,53	1,40	1,51	1,47	1,43	1,52	1,38	1,46
2018	$\bar{v}$	5,77	5,32	6,14	4,71	2,69	2,59	2,72	2,41	2,67	2,55	3,38	4,09
	σ	1,50	1,68	1,51	1,38	1,48	1,47	1,65	1,52	1,40	1,36	1,51	1,43
2019	$\bar{v}$	5,32	4,76	5,10	4,13	3,24	2,86	2,92	2,87	3,08	3,15	3,41	4,75
	σ	1,62	1,76	1,77	1,63	1,50	1,54	1,46	1,29	1,35	1,35	1,74	1,55

Source: Authors

Table 4. Velocity classification at 100,00 m

Lower limit (m/s)	Upper limit (m/s)	Observations w_i	Relative frequency (%) $f(x_i)$	Cumulative frequency	Cumulative relative frequency (%) $F(x_i)$
Less or equal	1,00	1 124	10,26	1 124	10,26
1,00	2,00	1 144	10,44	2 268	20,70
2,00	3,00	1 844	16,83	4 112	37,53
3,00	4,00	1 948	17,78	6 060	55,31
4,00	5,00	2 301	21,00	8 361	76,31
5,00	6,00	1 379	12,59	9 740	88,90
6,00	7,00	755	6,89	10 495	95,79
7,00	8,00	332	3,03	10 827	98,82
8,00	9,00	111	1,01	10 938	99,84
Greater	9,00	18	0,16	10 956	100,00
Total data (N)		**10 956**			

Source: Authors

In order to determine the wind potential, it is more relevant to establish a continuous mathematical function of wind velocity frequencies, rather than to use a table of discrete values such as the ones shown in Table 4 (Nedaei *et al.*, 2018; Li *et al.*, 2016; Wais, 2017). Therefore, if $f(v)$ is a function representing the probability that the wind velocity is within an interval between v and $v + dv$, the area under the probability function $f(v)$ is the unit and can be determined using Equation (6).

$$\int_0^\infty f(v)\,dv = 1 \tag{6}$$

On the other hand, the probability that the wind velocity was between v_0 and v_1 is given by the expression described by Equation (7).

$$P(v_0 \le v \le v_1) = \int_{v_0}^{v_1} f(v)\,dv \tag{7}$$

When N is large and a measurement has been made in the time interval Δt, the time at which the wind is blowing at a velocity between v_0 and v_1 can be calculated via Equation (8).

$$t = N * \Delta t * P(v_0 \le v \le v_1) \tag{8}$$

To estimate the variation of the mean wind velocity for a large period of time, the cumulative distribution function or wind duration curve was used. This function provides information on the probability that the velocity (v) exceeds a limit value for a given period of time (Nedaei *et al.*, 2018; Wais, 2017). In the literature, there are several functions f(v) that can be used to describe the frequency of the wind velocity distribution. Among these functions, the most commonly used ones are the Rayleigh and Weibull functions (Wais, 2017; El Khchine *et al.*, 2019). Therefore, to estimate the wind potential, the parameters of the Weibull distribution equation must be determined, which are the c scale (m/s) and the k-shape parameters. The c value represents the average wind velocity at the site of study. In turn, the k value

indicates the degree of dispersion of the records. With the referred parameters, the frequency by which a given velocity is obtained can be calculated using Equation (9) (Nagababu *et al.*, 2015; Wais, 2017; El Khchine *et al.*, 2019). For the following equations, the mathematical models by Manwell *et al.* (2010) and Fazelpour *et al.* (2015) were used.

$$f(v) = \left(\frac{k}{c}\right)\left(\frac{v}{c}\right)^{k-1} e^{\left(-\left(\frac{v}{c}\right)^k\right)} \tag{9}$$

The variables $\bar{v}$ and σ of the dataset can be calculated using Equations (10) and (11), respectively.

$$\bar{v} = \int_0^\infty v f(v)\,dv = c\Gamma\left(1 + \frac{1}{k}\right) \tag{10}$$

$$\acute{o}^2 = \int_0^\infty (v - \bar{v})^2 f(v)\,dv = c^2\left[\tilde{A}\left(1 + \frac{2}{k}\right) - \tilde{A}^2\left(1 + \frac{2}{k}\right)\right] \tag{11}$$

The variable $\Gamma(x)$ is known as the gamma function and is defined by Equation (12).

$$\Gamma(x) = \int_0^\infty e^{-u} u^{x-1}\,du \tag{12}$$

$\Gamma(x)$ can be numerically determined through the series showed in Equation (13).

$$\Gamma(x) = \left(\sqrt{2\pi x}\right)\left(x^{x-1}\right)\left(e^{-x}\right)\left(1 + \frac{1}{12x} + \frac{1}{288x^2} - \frac{139}{51840x^3} + \cdots\right) \tag{13}$$

From Equation (10), the c parameter can be estimated using Equation (14).

$$c = \frac{\bar{v}}{\tilde{A}\left(1 + \frac{1}{k}\right)} \tag{14}$$

Similarly, the parameter k can be predicted by Equation (15).

$$k = \left(\frac{\acute{o}}{\overline{v}}\right)^{-1.086} \tag{15}$$

On the other hand, the cumulative distribution function ($F(v)$) may be calculated using Equation (16).

$$F(v) = \int_0^v f(v)\, dv \tag{16}$$

Therefore, the probability that v is within the interval defined by v_0 and v_1 is given by Equation (17).

$$P(v_0 \le v \le v_1) = \int_{v_0}^{v_1} f(v)\, dv = e^{\left(-\left(\frac{v_0}{c}\right)^k\right)} - e^{\left(-\left(\frac{v_1}{c}\right)^k\right)} \tag{17}$$

Finally, $F(v)$ can be calculated via Equation (18).

$$F(v) = \int_0^v f(v)\, dv = 1 - e^{\left(-\left(\frac{v}{c}\right)^k\right)} \tag{18}$$

The values of the k and c parameters must be obtained from the wind measurements taken at the wind turbine installation site. To estimate the k and c parameters of the Weibull equation, a nonlinear adjustment was made from the set of wind velocity data (minimum, mean, and maximum) to an altitude of 100,00 m. From the nonlinear adjustment, the c parameter was obtained to be equal to 4,51 m/s. In turn, the k parameter turned out to be equal to 2,19. The frequencies and the Weibull function for the data from the minimum, mean, and maximum velocities at 10,00 m/s between 2010 and 2019 are represented in Figure 4.
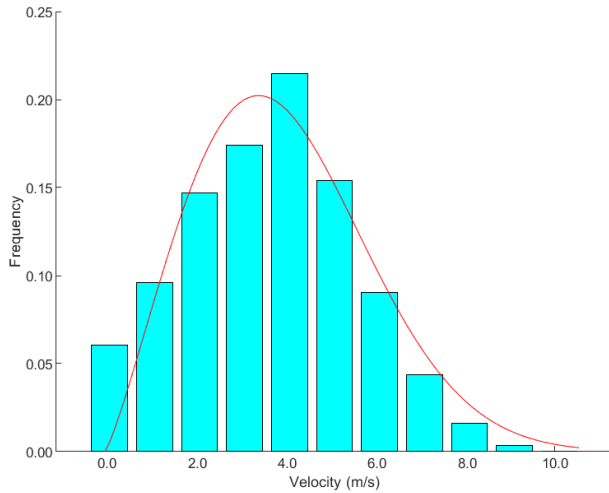

Figure 4. Weibull distribution of wind velocity data at a height of 100 m
Source: Authors

The wind distribution function for the study area that is represented by Equation (19) was defined with the parameters found.

$$f(v) = \left(\frac{2.1701}{4.5241}\right)\left(\frac{v}{4.5241}\right)^{2.1701-1} e^{\left(-\left(\frac{v}{4.5241}\right)^{2.1701}\right)} \tag{19}$$

Equation (19) allows calculating the occurrence probability of wind velocities higher or lower than a given velocity. For example, Equation (18) enables the determination of the probability that a reference velocity (v_i) will occur. Equation (20) was used to determine the velocities higher than v_i.

$$F_i(v \ge v_i) = e^{\left(-\left(\frac{v_i}{c}\right)^k\right)} \tag{20}$$

In this regard, the reference values ranging from 0,00 to a maximum of 12,00 m/s were selected for the entire set of wind velocity intervals, which were taken as reference, also using Equation (21). Thus, the probability of obtaining wind velocities greater than v_i could be determined. These results are presented in Table 5. According to said Table, the probability of having velocities equal to or greater than 3,00 m/s, which is the minimum velocity required for wind turbine start-up, was found to be 66,36%.

When this probability was multiplied by 8 760,00 (annual hours), the equivalent hours were obtained, which corresponded to the number of hours in which the velocity of 3,00 m/s is exceeded within a year. In the studied site, these hours were equal to 5 813,14 h.

The most likely wind velocity (V_{mp}), expressed in m/s, can be determined by using the Weibull k and c parameters. This velocity is the most common for a given wind probability distribution, and it can be expressed via Equation (21) (Jamil, 1994).

$$V_{mp} = c\left(1 - \frac{1}{k}\right)^{\frac{1}{k}} \tag{21}$$

In addition, the velocity with the highest energy production from the Weibull distribution can be determined through Equation (22) (Jamil, 1994).

$$V_{max,\, E} = c\left(1 + \frac{2}{k}\right)^{\frac{1}{k}} \tag{22}$$

Table 5. Probabilities of obtaining wind velocities greater that the reference value (v_i)

v_i	0,00	1,00	2,00	3,00	4,00	5,00	6,00	7,00	8,00	9,00	10.0	11,00	12,00
$F_i(v \ge v_i)$	100,00	96,29	84,36	66,36	46,51	28,87	15,80	7,59	3,19	1,17	0,37	0,10	0,02

Source: Authors

Power density

The wind potential at a site can be broadly characterized by the average wind velocity. However, the available power density in the wind provides a proper indicator of the wind power potential of the place of interest. The power density is proportional to the product of the air density and the cube of the average wind velocity (Nedaei et al., 2018; Nagababu et al., 2015; Wais, 2017). By using the general power equation, which is labeled in this paper a Equation (23), the available power density (P/A) can be determined as expressed in Equation (24).

$$P = \frac{1}{2}\rho A V^3 \tag{23}$$

$$\frac{P}{A} = \frac{1}{2}\rho V^3 \tag{24}$$

where ρ refers to the air density at the place of study, which depends on the pressure and the temperature; the cross-section A is πR^2 (m²); and R is the radius of the wind turbine blades (m). In turn, V is the average wind velocity (m/s) of the application site. The power density can also be determined from the Weibull distribution via Equation (25) (Jamil, 1994).

$$\frac{P}{A} = \int_0^\infty \frac{1}{2}\rho v^3 f(v)dV = \frac{1}{2}\rho c^3 \Gamma\left(1+\frac{3}{k}\right) \tag{25}$$

The average wind power density (WPD) for a wind velocity dataset can be calculated using Equation (26) (Fazelpour et al., 2015).

$$WPD = \frac{\sum_{i=1}^n \frac{1}{2}\rho v_i^3}{N} \tag{26}$$

Once the power density is calculated, the energy density for a desired duration (T) is determined through Equation (27).

$$\frac{E}{A} = \frac{1}{2}\rho c^3 \Gamma\left(1+\frac{3}{k}\right)T \tag{27}$$

For calculations, an air density at sea level is assumed, with an average temperature of 15 ˚C and an atmospheric pressure of 1 atm (1,23 kg/m³) (Arrambide et al., 2019).

Table 6 contains the analysis of the wind potential of the selected site in the department of Antioquia. The k-values obtained from the nonlinear fit of the Weibull distribution are observed to range from 1,50 to 4,17 with an average of 2,63, while the c-scale parameter ranges from 3,55 m/s to 6,11 m/s, with an average of 4,45 m/s. Comparing the mean values of k and c with respect to the k and c values obtained from the nonlinear fit of the dataset results in an error of 20,08 and 1,43% for k and c, respectively.

Figure 5 shows the values of the annual average wind power density in the area of interest. The power distribution turned out to be greater than the one found through analyzing the selected point data, annually varying between 33,59 and 128,39 W/m². This difference was due to the distribution of the power density presented in Figure 5, where the data correspond to an altitude of 80,00 m for 2015. In the same year and for an altitude of 80,00 m, the annual average velocity reported was between 7,00 and 8,00 m/s depending on the source from which Figure 5 was extracted. Additionally, only the year 2015 was analyzed, although a longer period of time was considered during the data analysis. According to the categorization of the wind resource informed by Ambrosini et al. (1992), the wind resource potential is between marginal and poor for the analyzed data. In Ambrosini et al. (1992), the resource is considered to be poor and marginal when $P/A < 100,00$ W/m² and 100,00 W/m² $< P/A < 300,00$ W/m², respectively. In turn, the resource is good

Table 6. Wind potential at an altitude of 100,00

Month	Weibull distribution k	c (m/s)	Maximum velocity V_{max} (m/s)	$\bar{v}$ (m/s) Eq. (1)	σ Eq. (3)	k Eq. (12)	c (m/s) Eq. (11)	V_{mp} (m/s) Eq. (18)	$V_{max,E}$ (m/s) Eq. (19)	WPD (W/m²) Eq. (23)	P/A (W/m²) Eq. (22)	E/A $\left(\frac{kWh}{m^2 month}\right)$ Eq. (24)
January	3,85	5,60	9,49	5,03	1,62	3,43	5,59	5,07	6,41	101,24	102,68	76,39
February	3,84	5,95	10,53	5,36	1,62	3,67	5,94	5,45	6,69	119,69	120,58	81,61
March	4,17	6,11	9,63	5,49	1,55	3,96	6,06	5,67	6,77	124,93	128,39	95,52
April	2,79	5,08	9,61	4,28	1,78	2,59	4,82	4,20	6,33	72,41	86,38	62,19
May	2,16	3,82	7,97	3,02	1,53	2,09	3,41	2,80	5,25	29,85	43,22	32,16
June	1,68	3,55	6,96	2,65	1,49	1,87	2,98	2,35	5,25	22,28	39,47	28,42
July	1,50	3,65	6,69	2,68	1,55	1,81	3,01	2,35	5,51	23,66	44,53	33,13
August	1,77	3,66	5,98	2,59	1,44	1,89	2,92	2,46	5,34	20,29	42,21	30,39
September	2,04	3,46	7,02	2,66	1,40	2,01	2,99	2,45	4,88	20,97	33,59	24,18
October	2,19	3,65	8,57	2,88	1,49	2,04	3,25	2,63	5,11	26,52	38,89	28,94
November	2,47	4,03	8,08	3,31	1,53	2,32	3,74	3,16	5,26	36,26	46,49	33,48
December	3,06	4,83	7,83	4,05	1,62	2,71	4,56	4,07	5,92	59,33	72,38	53,85

Source: Authors

when 300,00 W/m² < P / A < 700,00 W/m² and excellent when P / A >700,00 W/m². For a better wind resource estimation, making a systematic collection of wind data at the site where a possible wind farm can be installed is required. Hence, the installation of weather station towers at several points in the area of interest is necessary.

During the analysis of the wind potential, identifying the dominant directions of the wind is also relevant for establishing the correct location of the wind turbine, since it must be placed at a site where there is a minimal number of obstacles in said directions. The annual wind direction in the area of interest is depicted in Figure 6. As it can be seen in the Figure, the predominant wind direction is the northeast (NE) in the coastal region outside the Gulf of Urabá. When there is indeed a predominant wind direction, a distribution in aligned rows with cross-sectional separation between turbines from 3 to 5 times the rotor diameter and from 5 to 9 times the rotor diameter in the direction of the dominant wind is recommended.
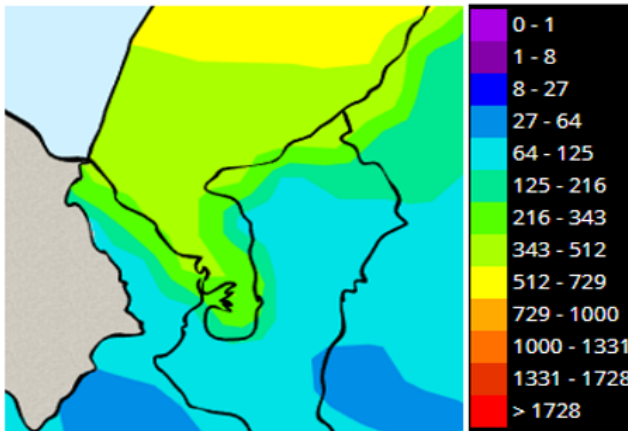

Figure 5. Map representing the annual average of the wind power density distribution (W/m²) at an altitude of 80 m in the area of interest for 2015
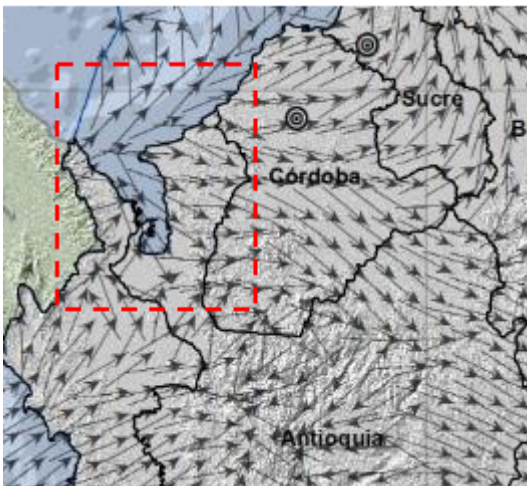**Source:** IDEAM (2019)

Figure 6. Annual wind direction in the area of interest for 2015
Source: IDEAM (2019)

Results and discussion

Wind turbines to take advantage of the wind resource

Type of wind turbine: The different types or classes of wind turbines, in terms of wind velocity and turbulence parameters, are defined in the IEC 61400-1 international standard (Sirnivas *et al.*, 2014; Roach *et al.*, 2020). In this regard, the wind turbine class is established according to the reference velocity, which can be determined via Equation (28). It is highlighted that the class of the turbine determines its suitability for the normal wind conditions of the site where it will be installed.

$$V_{ref} = \frac{V_{prom}}{0.2} \qquad (28)$$

where V_{avg} is the annual average wind velocity in the area intended for exploiting the wind resource. In Table 7, the different wind turbine classes according to the IEC 61400-1 international standard are presented (Sirnivas *et al.*, 2014; Roach *et al.*, 2020).

Table 7. Classes of wind turbines according to the IEC 61400-1 international standard

Wind turbine class	I	II	III	S
V_{ref} (m/s)	50,00	42,50	37,50	
V_{avg} (m/s)	10,00	8,50	7,50	
A I_{ref} (-)		0,16		Values specified by the designer
B I_{ref} (-)		0,14		
C I_{ref} (-)		0,12		

Source: IEC 61400-1 international standard (Sirnivas *et al.*, 2014; Roach *et al.*, 2020).

In Table 7, A, B, and C correspond to the categories for upper, mean, and lower turbulences, respectively. In turn, I_{ref} is the expected value for the turbulence intensity at 15,00 m/s. The AI design class is stronger, and the IIIC design class is weaker. By finding the right design according to the wind conditions at the site of interest, the wind turbine selection process is facilitated by limiting the number of possible turbine models. Selecting an incorrect wind turbine design class could increase the costs of generation projects. For example, the selection of a design class that is too weak leads to an increase of the turbine failure risk by decreasing the service life. On the other hand, when a design class that is too strong is selected, it may result in higher capital costs and lower economic project feasibility. Classes I, II, and III are not intended to cover marine (offshore)

installations or wind conditions experienced in tropical storms such as hurricanes, cyclones, and typhoons if the generic parameters of the design classes are exceeded. These conditions may require a class S, user-defined wind turbine design that allows for unique conditions. The IEC standards for the design of fixed offshore wind turbines at the bottom and for floating turbines are IEC 61400-3-1 and IEC 61400-3-2, respectively (Sirnivas *et al.*, 2014; Roach *et al.*, 2020).

The turbulence index (I) is defined as the ratio between the mean sample velocity and the standard deviation of the sample. This index allows defining the variation in wind velocity in a relatively short time. It can be calculated as described in Equation (29).

$$I = \frac{\acute{o}}{v} \qquad (29)$$

Table 8 presents the wind turbine class to be used in the area of interest according to the monthly average velocities. For the selection, as the average velocities range from 2,59 to 5,49 m/s, the highest value corresponding to March was taken in order to ensure that the wind turbine supports the most critical turbulence conditions.

Table 8. Selected wind turbine class

Areas of interest	Average velocity at an altitude of 100,00 m (m/s)	Reference velocity (m/s)	Wind turbine class according to IEC 61400-1
Sea area	5,49	27,46	III

Source: Authors

For velocities lower than 13 m/s, wind turbines from the manufacturer GAMESA, a worldwide technology leader in the wind industry and a pioneer in offshore wind turbine production, tend to be more efficient than those from NORDEX (Rueda-Bayona *et al.*, 2019). Therefore, for this study, the wind turbine models from GAMESA were considered. It is noteworthy that, in the portfolio provided by GAMESA, only generators for class I as described in IEC 61400-1 are presented. Thus, the class III generator, which had been previously defined for the maritime zone, was replaced with a class I generator. Note that this change was not a problem since a wind turbine designed to operate under class I conditions was used instead of one intended for class III conditions. Additionally, the conditions established for the design of class I wind turbines are considered to be more aggressive than those established for class III. The selected wind turbine model was the SWT-6.0-154. The main technical characteristics of said wind turbine are listed in Table 9.

The selected wind turbines can be installed in zone 1, which is detailed in Figure 7. The Figure shows the values of the transversal distances and the wind direction where installation would be attainable.

Following the recommendations of the separation distances of the wind turbines in the predominant transversal and wind directions, the number of offshore wind turbines that could be installed at the site is presented in Table 10. From the analysis, the installation of 2 187 offshore wind turbines in the area is found to be feasible. Since the area is an air and sea traffic zone, 40,00% of the possible amount of turbines to be installed was assumed, thus resulting in a total of 875 wind turbines.

In Table 11 and for a wind turbine swept area (A) of 18 626,50 m², the energy that could be generated with a wind turbine is presented, which is equivalent to 10 808 218,27 kWh/year.

Table 9. Technical characteristics of the selected wind turbine

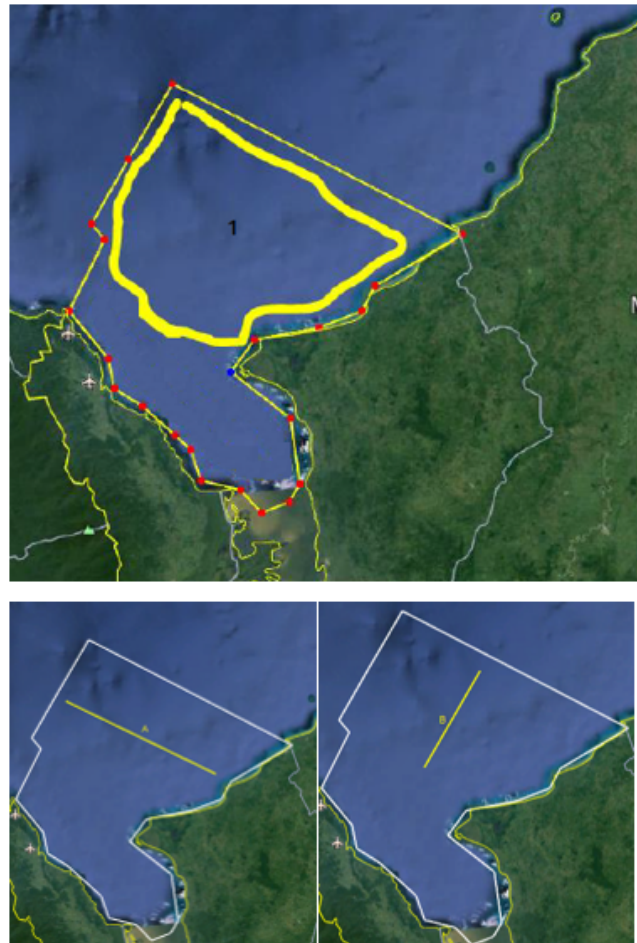| Description	Model SWT-6.0-154
Nominal Power	6 MW
Rotor diameter	154,00 m
Swept area	18 626,50 m²
Frequency	--
Blades length	--
Tower height	Dependent on the location

Source: Authors

Figure 7. Available area to install wind turbines
Source: Authors

Table 10. Analysis of the number of wind turbines to be installed

Area	A: Transversal distance (m)	B Distance in the direction of the dominant wind (m)	Rotor diameter (m)	Recommended transversal separation distance (m)	Separation distance in the recommended dominant wind direction (m)	Number of wind turbines installed in the transversal direction	Number of wind turbines in the direction of the dominant wind	Total amount of wind turbines
1	62 810,00	37 779,00	154,00	770,00	1 386,00	81	27	2 187

Source: Authors

In Table 11 and for a wind turbine swept area (*A*) of 18 626,50 m², the energy that could be generated with a wind turbine is presented, which is equivalent to 10 808 218,27 kWh/year. In this regard, if 875 wind turbines are installed, the energy that could be produced is equivalent to 9 457,19 GWh/year. Nevertheless, since the probability of having wind velocities greater than 3,00 m/s is 66,36%, as detailed in Table 5, the energy that can be generated with the wind turbines per year and on a monthly basis would be equal to 7 172 333,64 kWh/year and 597 694,47 kWh/month, respectively. Therefore, the energy that could be produced with the 875 wind turbines would only be equal to 6 275,79 GWh/year. Knowing the amount of wind turbines and the nominal power, if the turbines operate at the rated capacity, the value of the power generated could be obtained. For the 875 units of SWT-6.0-154 wind turbines (offshore), the power would be 5,25 MW or 45,99 GWh/year. To generate the same amount of energy that is produced in one year with the available resource (6 275,79 GWh/year), the selected wind turbine model would have to work 1 195,39 h at the rated capacity. According to the annual report for 2019 presented by XM, a firm specialized in the management of real-time systems, the electricity demand in Colombia was around 71,93 TWh/year. Thus, the potential of the site in the Gulf of Urabá would be around 8,72% of the national demand value in 2019. On the other hand, according to the same report for 2019, the demand for electricity in Antioquia was around 9 409 GWh/year, so the potential of the site in the Gulf of Urabá is about 66,7% the value of the energy demand in the department of Antioquia.

Table 11. Ideal available energy in a wind turbine

Month	E/A (kWh/m²/month) Equation (24)	E (kWh/month)
January	76,39	1 422 926,98
February	81,61	1 520 118,21
March	95,52	1 779 201,69
April	62,19	1 158 326,33
May	32,16	598 972,45
June	28,42	529 316,78
July	33,13	617 036,43
August	30,39	566 139,52
September	24,18	450 437,27
October	28,94	539 039,82
November	33,48	623 596,69
December	53,85	1 003 106,09
Monthly average		**900 684,86**
Total		**10 808 218,27**

Source: Authors

Flexible energy systems based on the wind resource in the department of Antioquia

In many developing countries such as Colombia, energy system networks are traditionally structured and designed to effectively regulate the effects of uncertainty and variability in terms of energy demand and resource availability (Babatunde *et al.*, 2020). In order to transform the current generation system into another one where NCSRE have higher participation, it is necessary to increase the flexibility requirements in the power system grid, given that the incorporation of more variable energy resources, such as wind and solar energy, is not predictable due to their intermittent and variable nature, which is due to climatic conditions. Both solar and wind energies have three main common characteristics: variability, uncertainty, and location dependence. These have effects on distribution and transmission networks. Increasing the flexibility of the grid for the integration of large amounts of energy from NCSRE leads to some technical and economic challenges that must be solved in order to ensure the satisfaction of the energy demand and the stability of the energy system (voltage and frequency regulation). System flexibility means increasing the capacity of an energy system to reliably and cost-effectively manage the demand, supply variability, and uncertainty across all relevant timelines (Babatunde *et al.*, 2020; Akrami *et al.*, 2019; Alexopoulos *et al.*, 2021; Ebrahimi *et al.*, 2022).

Power system networks achieve flexibility by using thermal power plants (gas turbines) that can be quickly connected and disconnected. The integration of NCSRE in the country requires strengthening distribution and transmission facilities, as well as developing auxiliary energy harvesting or storage systems. Currently, hydroelectric pumping systems, thermal storage, and compressed air energy storage can be named among the most common examples of large-scale energy storage technologies (Kougias and Szabó, 2017). In turn, on a decentralized scale, super-capacitors, batteries, electrolysis, flywheels, and fuel cells are some of the available energy accumulators (Ogbonnaya *et al.*, 2019).

The energy potential at the analyzed site is considerable, which is due to the fact that, in the maritime area of the Gulf of Urabá, there is a large area in which offshore wind turbines could be installed. Nevertheless, given the energy fluctuations at the installation site, when a high energy production in the area occurs, surplus energy could be

generated. For this reason, the following alternatives are proposed as flexible energy systems to prevent the energy excess from being lost or compromising the stability of the grid:

- Harnessing the energy surplus to desalinate seawater and bring drinking water to communities around the area of interest. On average, the specific energy consumption including water pre-treatment and post-treatment processes can be between 3,50 and 4,50 kWh/m^3 (Kim *et al.*, 2019) for a water desalination plant with a properly installed technology.

- Because there are large hydroelectric plants in Antioquia, the NCSRE excess could be stored through the development of pumping plants. The excess energy can be used to generate hydrogen by means of electrolysis and provide it to the local industry. Additionally, the generated hydrogen can be converted into synthetic natural gas through the methanation process (power to gas) before providing it to the grid (Mazza *et al.*, 2020).

- If electric mobility becomes more prevalent in the future, the storage possibilities within home systems could increase the chances of flexible demand (Pilpola *et al.*, 2019).

Flexible energy systems can be useful in overcoming the challenges related to NCSRE penetration into the country's generation system in the future. In Colombia, it is important to improve the energy transmission and distribution systems, as well as to increase the storage capacity and manage the demand in order to ensure a sustainable future with regard to energy. Several research questions can be defined: To what extent could different flexibility measures be used in a cost-effective way to integrate large-scale wind power in developing countries? How does the existence of hydroelectric plants affect wind integration? What is the appropriate combination of different flexibility technologies for wind power integration? Could the combination of gas and power or heat and power form a barrier to a cost-effective wind power integration?

Conclusion

To assess the wind resource at the site with coordinates 8,713280° latitude and -77,075274° longitude, the Prediction of Worldwide Energy Resource NASA database was used, which includes meteorological data for a long period of time. Data analysis reveals poor to marginal wind potential. The energy potential annually ranged from 24,18 to 95,52 kWh/m^2/month with a predominant NE direction. The average velocity of the analyzed dataset was 3,86 m/s. The maximum velocity recorded during the observed period (2009 to 2019) was 10,53 m/s at a 100,00 m altitude. Given the conditions of the site and the nominal capacity of the selected wind turbines, the equipment was seen to operate most of the time under

conditions below the nominal design, and, therefore, the energy potential produced would be actually lower. The energy that could be produced out of the installation of 875 SWT-6.0-154 wind turbines (offshore) would be equal to 6 275,79 GWh/year.

For the economic feasibility study, carrying out a comprehensive analysis of wind potential from the weather information collected on the installation site over a long period of time is recommended. To this effect, installing measurement towers with the proper instrumentation is crucial. In addition, further analysis considering the oceanic crust and its conditions for the installation of offshore wind turbines is required, so that more accurate results can be obtained according to the approximate number of this type of wind turbines that could be installed.

It is important to advance in the development of flexible network systems to adequately support the operation of the distribution system in the event of large penetrations of NCSRE into the national energy matrix. Power to heat and power to gas, energy stores (mechanical, electrochemical, and electromagnetic energy storage), and smart charging of electric vehicles are main flexibility technologies to integrate wind power into energy system networks.

Acknowledgements

References

Abdulgalil, M. A., Khalid, M., and Alismail, F. (2019). Optimizing a distributed wind-storage system under critical uncertainties using Benders decomposition. *IEEE Access, 7*, 77951-77963. https://doi.org/10.1109/ACCESS.2019.2922619

Akrami, A., Doostizadeh, M., and Aminifar, F. (2019). Power system flexibility: an overview of emergence to evolution. *Journal of Modern Power Systems and Clean Energy, 7*(5), 987-1007. https://doi.org/10.1007/s40565-019-0527-4

Alexopoulos, D. K., Anastasiadis, A. G., Vokas, G. A., Kaminaris, S. D., and Psomopoulos, C. S. (2021). A review of flexibility options for high RES penetration in power systems—Focusing the Greek case. *Energy Reports, 7*, 33-50. https://doi.org/10.1016/j.egyr.2021.09.050

Ali, S., Lee, S. M., and Jang, C. M. (2017). Techno-economic assessment of wind energy potential at three locations in South Korea using long-term measured wind data. *Energies, 10*(9), 1442. https://doi.org/10.3390/en10091442

Ambrosini, G., Benato, B., Garavaso, C., Botta, G., Cenerini, M., Comand, D., and Stork, C. (1992). Wind energy potential in Emilia Romagna, Italy. *Journal of Wind Engineering and Industrial Aerodynamics, 39*(1-3), 211-220. https://doi.org/10.1016/0167-6105(92)90547-N

Arrambide, I., Zubia, I., and Madariaga, A. (2019). Critical review of offshore wind turbine energy production and site potential assessment. *Electric Power Systems Research, 167*, 39-47. https://doi.org/10.1016/j.epsr.2018.10.016

Babatunde, O. M., Munda, J. L., and Hamam, Y. (2020). Power system flexibility: a review. *Energy Reports, 6*, 101-106. https://doi.org/10.1016/j.egyr.2019.11.048

Boopathi, K., Kushwaha, R., Balaraman, K., Bastin, J., Kanagavel, P., and Prasad, D. R. (2021). Assessment of wind power potential in the coastal region of Tamil Nadu, India. *Ocean Engineering, 219*, 108356. https://doi.org/10.1016/j.oceaneng.2020.108356

Cortés, S., and Londoño, A. A. (2017). Energías renovables en Colombia: una aproximación desde la economía. *Revista Ciencias Estratégicas, 25*(38), 375-390. https://doi.org/rces.v25n38.a7

Chandel, S. S., Ramasamy, P., and Murthy, K. S. R. (2014). Wind power potential assessment of 12 locations in western Himalayan region of India. *Renewable and Sustainable Energy Reviews, 39*, 530-545. https://doi.org/10.1016/j.rser.2014.07.050

Dayal, K. K., Cater, J. E., Kingan, M. J., Bellon, G. D., and Sharma, R. N. (2021). Wind resource assessment and energy potential of selected locations in Fiji. *Renewable Energy, 172*, 219-237. https://doi.org/10.1016/j.renene.2021.03.034

Ebrahimi, H., Yazdaninejadi, A., and Golshannavaz, S. (2022). Demand response programs in power systems with energy storage system-coordinated wind energy sources: A security-constrained problem. *Journal of Cleaner Production, 335*, 130342. https://doi.org/10.1016/j.jclepro.2021.130342

El Khchine, Y., Sriti, M., and Elyamani, N. E. E. K. (2019). Evaluation of wind energy potential and trends in Morocco. *Heliyon, 5*(6), e01830. https://doi.org/10.1016/j.heliyon.2019.e01830

Fazelpour, F., Soltani, N., and Rosen, M. A. (2015). Wind resource assessment and wind power potential for the city of Ardabil, Iran. *International Journal of Energy and Environmental Engineering, 6*(4), 431-438. https://doi.org/10.1007/s40095-014-0139-8

Gómez-Navarro, T., and Ribó-Pérez, D. (2018). Assessing the obstacles to the participation of renewable energy sources in the electricity market of Colombia. *Renewable and Sustainable Energy Reviews, 90*, 131-141. https://doi.org/10.1016/j.rser.2018.03.015

Gul, M., Tai, N., Huang, W., Nadeem, M. H., and Yu, M. (2019). Assessment of wind power potential and economic analysis at Hyderabad in Pakistan: powering to local communities using wind power. *Sustainability, 11*(5), 1391. https://doi.org/10.3390/su11051391

Instituto de Hidrología, Meteorología y Estudios Ambientales (IDEAM) (2019). *Atlas Interactivo - Vientos - IDEAM*. http://atlas.ideam.gov.co/visorAtlasVientos.html

Jamil, M. (1994). Wind power statistics and evaluation of wind energy density. *Wind Engineering, 18*(5), 227-240. http://www.jstor.org/stable/43749549

Kim, J., Park, K., Yang, D., and Hong, S. (2019). A comprehensive review of energy consumption of seawater reverse osmosis desalination plants. *Applied Energy, 254*, 113652. https://doi.org/10.1016/j.apenergy.2019.113652

Kougias, I., and Szabó, S. (2017). Pumped hydroelectric storage utilization assessment: forerunner of renewable energy integration or Trojan horse? *Energy, 140*, 318-329. https://doi.org/10.1016/j.energy.2017.08.106

Li, C., Liu, Y., Li, G., Li, J., Zhu, D., Jia, W., and Zhai, X. (2016). Evaluation of wind energy resource and wind turbine characteristics at two locations in China. *Technology in Society, 47*, 121-128. https://doi.org/10.1016/j.techsoc.2016.09.003

Manwell, J. F., McGowan, J. G., and Rogers, A. L. (2010). *Wind energy explained: Theory, design and application*. John Wiley & Sons.

Mazza, A., Salomone, F., Arrigo, F., Bensaid, S., Bompard, E., and Chicco, G. (2020). Impact of power-to-gas on distribution systems with large renewable energy penetration. *Energy Conversion and Management: X, 7*, 100053. https://doi.org/10.1016/j.ecmx.2020.100053

Ministerio de Minas y Energía - Unidad de Planeación Minero-Energética (2017). *Informe de Rendición de Cuentas UPME 2016-2017*. MMyE-UPME.

Mohamadi, H., Saeedi, A., Firoozi, Z., Zangabadi, S. S., and Veisi, S. (2021). Assessment of wind energy potential and economic evaluation of four wind turbine models for the east of Iran. *Heliyon, 7*(6), e07234. https://doi.org/10.1016/j.heliyon.2021.e07234

Nagababu, G., Bavishi, D., Kachhwaha, S. S., and Savsani, V. (2015). Evaluation of wind resource in selected locations in Gujarat. *Energy Procedia, 79*, 212-219. https://doi.org/10.1016/j.egypro.2015.11.467

Nedaei, M., Assareh, E., and Walsh, P. R. (2018). A comprehensive evaluation of the wind resource characteristics to investigate the short term penetration of regional wind power based on different probability statistical methods. *Renewable Energy, 128*(A), 362-374. https://doi.org/10.1016/j.renene.2018.05.077

Ogbonnaya, C., Abeykoon, C., Damo, U. M., and Turan, A. (2019). The current and emerging renewable energy technologies for power generation in Nigeria: A review. *Thermal Science and Engineering Progress, 13*, 100390. https://doi.org/10.1016/j.tsep.2019.100390

Ohunakin, O. S. (2011). Wind resource evaluation in six selected high altitude locations in Nigeria. *Renewable Energy, 36*(12), 3273-3281. https://doi.org/10.1016/j.renene.2011.04.026

Pilpola, S., and Lund, P. D. (2019). Different flexibility options for better system integration of wind power. *Energy Strategy Reviews, 26*, 100368. https://doi.org/10.1016/j.esr.2019.100368

Siabato-Benavides, R. (2018). *Identificación de proyectos con potencial de generación de energía eólica como complemento a otras fuentes de generación eléctrica en el departamento de Boyacá*. Universidad Nacional de Colombia. https://repositorio.unal.edu.co/handle/unal/63745

Sirnivas, S., Musial, W., Bailey, B., and Filippelli, M. (2014). *Assessment of offshore wind system design, safety, and operation standards (No. NREL/TP-5000-60573)*. National Renewable Energy Lab.

Solyali, D., Altunç, M., Tolun, S., and Aslan, Z. (2016). Wind resource assessment of Northern Cyprus. *Renewable and Sustainable Energy Reviews, 55*, 180-187. https://doi.org/10.1016/j.rser.2015.10.123

Roach, S., Park, S. M., Gaertner, E., Manwell, J., and Lackner, M. (2020). Application of the new IEC international design standard for offshore wind turbines to a reference site in the Massachusetts offshore wind energy area. *Journal of Physics: Conference Series, 1452*, 012038. https://doi.org/10.1088/1742-6596/1452/1/012038

Rueda-Bayona, J. G., Guzmán, A., Eras, J. J. C., Silva-Casarín, R., Bastidas-Arteaga, E., and Horrillo-Caraballo, J. (2019). Renewables energies in Colombia and the opportunity for the offshore wind technology. *Journal of Cleaner Production, 220*, 529-543. https://doi.org/10.1016/j.jclepro.2019.02.174

Tummala, A., Velamati, R. K., Sinha, D. K., Indraja, V., and Krishna, V. H. (2016). A review on small scale wind turbines. *Renewable and Sustainable Energy Reviews, 56*, 1351-137. https://doi.org/10.1016/j.rser.2015.12.027

Wais, P. (2017). A review of Weibull functions in wind sector. *Renewable and Sustainable Energy Reviews, 70*, 1099-1107. https://doi.org/10.1016/j.rser.2016.12.014

Effect of Temperature on a Vortex Reactor for Hydrodynamic Cavitation

Efecto de la temperatura en un reactor vórtice para cavitación hidrodinámica

Octavio A. González-Estrada [1], Mauricio A. Rojas-Nova [2], and Germán González-Silva [3]

ABSTRACT

The oil and gas sector has recently shown an interest in hydrodynamic cavitation for oil enhancement, as it allows reducing transportation and refinement costs. This work presents a fluid-dynamic study of Colombian oil at different temperatures passing through a vortex reactor. First, an experimental design was elaborated, establishing the temperature and quantity of the injected hydrogen donor as factors and the final viscosity of oil as the response. Then, a numerical model was developed in the Ansys Fluent software using multiphase models, where the required properties of the fluid were obtained via laboratory tests and the Aspen HYSYS software. The results obtained from numerical experimentation were analyzed, and it was observed that the final viscosity was less affected by the temperature than by the hydrogen donor. Moreover, numerical modeling showed an exponential relation between vapor generation and temperature. The experimental and numerical data were compared, and it was found that the temperatures established in the experimental design were not high enough to generate a significant amount of vapor, which is why the decrease in viscosity was lower.

Keywords: computational fluid dynamics, hydrodynamic cavitation, heavy crude oil

RESUMEN

Últimamente, el sector de petróleo y gas ha mostrado interés en la cavitación hidrodinámica para la mejora del petróleo, ya que esta permite reducir los costos de transporte y refinamiento. Este trabajo presenta un estudio fluidodinámico de petróleo colombiano a diferentes temperaturas mientras pasa por un reactor vórtice. Primero se realizó un diseño experimental, estableciendo la temperatura y la cantidad de donante de hidrógeno inyectado como factores y la viscosidad final del aceite como respuesta. Luego se desarrolló un modelo numérico en el software Ansys Fluent utilizando modelos multifase, donde se obtuvieron las propiedades requeridas del fluido mediante pruebas de laboratorio y el software Aspen HYSYS. Se analizaron los resultados de la experimentación numérica y se observó que la viscosidad final se vio menos afectada por la temperatura que por el donante de hidrógeno. Asimismo, el modelado numérico mostró una relación exponencial entre la generación de vapor y la temperatura. Se compararon los datos experimentales y numéricos, y se encontró que las temperaturas establecidas en el diseño experimental no eran lo suficientemente altas para generar una cantidad significativa de vapor, por lo que la reducción de la viscosidad fue menor.

Palabras clave: mecánica de fluidos computacional, cavitación hidrodinámica, petróleo crudo pesado

Introduction

Cavitation is the physical phenomenon that occurs in a fluid when vapor cavities are formed due to a pressure drop, which can be generated by a sudden decrease in the flow cross-sectional area. When designing an experiment that involves cavitation, parameters such as velocity, temperature, and the geometry through which the fluid passes must be considered (Barona-Mejía *et al.*, 2021; Šarc *et al.*, 2017).

Mathematical models can simulate cavitation by describing the phase change and behavior of the bubble. One of the most commonly used models is the Singhal method, also known as the full cavitation model, since it describes the formation and transport of the bubble, the turbulent fluctuations, and the magnitude of non-condensable gases (Singhal *et al.*, 2002). Another widely known model is the

[1] Mechanical and manufacturing engineer, Universidad Autónoma de Manizales, Colombia. MSc, PhD in Mechanical and Materials Engineering, Universitat Politècnica de València, Spain. Affiliation: Associate professor, School of Mechanical Engineering, Universidad Industrial de Santander, Colombia. Email: agonzale@uis.edu.co

[2] Mechanical engineer, Universidad Industrial de Santander. Affiliation: School of Mechanical Engineering, Universidad Industrial de Santander, Colombia.Email: andrsnov@gmail.com

[3] Chemical engineer, Universidad Nacional de Colombia, Manizales, Colombia. MSc, PhD in Chemical Engineering, Universidade Estadual de Campinas, Brazil. Affiliation: Associate professor, School of Petroleum Engineering, Universidad Industrial de Santander, Colombia. Email: germangs@uis.edu.co

Schnerr-Sauer method, which is a combination of the VOF (Volume of Fluid) technique and a prediction of bubble growth and collapse (Sauer and Schnerr, 2000).

One of the parameters that affects cavitation is temperature, which has been studied in different ways, be it to determine erosion in solids (Dular, 2015) or to study bubble dynamics (Petkovšek and Dular, 2013). Moreover, the thermal effect has been studied in hydrodynamic cavitation reactors used for water cleaning (Ge *et al.*, 2022; Sun *et al.*, 2018). Another parameter is the geometry through which the fluid passes, among which Venturi tubes are the most common (Shi *et al.*, 2019). Given its basic configuration, this geometry has been used to test different turbulence models (Nouri *et al.*, 2010) or to compare experimental and computational data (Cappa *et al.*, 2014).

Additionally, during the hydrodynamic cavitation process for oil upgrading, a hydrogen donor such as gasoline (Yang *et al.*, 2013) needs to be added in order to avoid the reorganization of the free radicals in heavier molecules during the implosion of bubbles, thus preventing the crude from becoming even more viscous (Askarian *et al.*, 2017).

The oil and gas sector has different applications for the use of cavitation within crude refining processes, *e.g.*, enhanced recovery, de-metallization, viscosity reduction, desulfurization, and upgrading (Avvaru *et al.*, 2018). In terms of upgrading, hydrodynamic and acoustic cavitation are the most attractive from an industrial point of view (Montes *et al.*, 2018; Olaya-Escobar *et al.*, 2020; Sawarkar, 2019). Consequently, projects have focused on making this process profitable. However, a number of design parameters must be considered, which means that further research is needed (Gogate and Pandit, 2000). In this sense, several works have shown that vortex reactors using hydrodynamic cavitation are more energy-efficient for oil upgrading in comparison with thermal cracking and acoustic cavitation (Quan *et al.*, 2011; Sawarkar, 2019; Senthil Kumar *et al.*, 2000).

The purpose of this study is to evaluate the effect of temperature on a vortex reactor for hydrodynamic cavitation. The fluid of study is heavy crude oil, and the evaluation is carried out experimentally and numerically by using Ansys Fluent.

Materials and methods

The methodology was divided into two parts: the first one consists of the experimentation process in the vortex reactor; and the second one is the computational fluid dynamics analysis performed in the Ansys Fluent software.

Experimental design

The effect of temperature was determined via a two-factor, three-level experimental design. The factors evaluated were the temperature and the percentage of injected hydrogen donor, and the response variable was the final viscosity when the crude had already undergone the hydrodynamic cavitation process. All tests were performed with a crude flow rate of 12 GPM.

The data employed are shown in Table. 1. The initial viscosity was measured before the oil was introduced into the vortex reactor. The initial viscosity was not measured in the presence of hydrogen. Overall, there was a decrease in viscosity as the temperature increased. However, it was much lower when compared to that generated by an increase in the percentage of the injected hydrogen donor. A statistical analysis was conducted in the Minitab software for a detailed assessment of the effect of each factor.
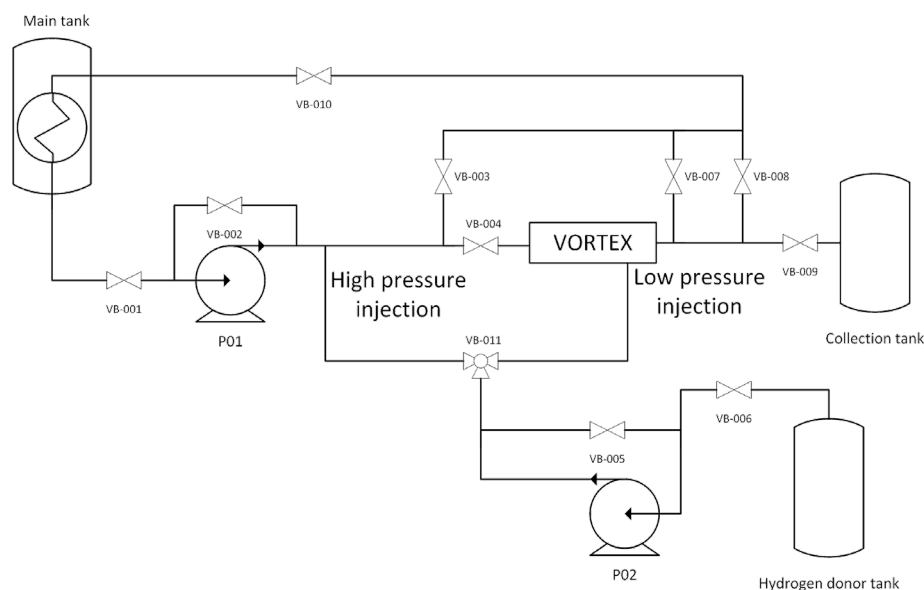

Figure 1. Diagram of the vortex reactor system
Source: Authors

The tests were run in the vortex reactor owned by the Energy Rap Vortex Services company (Quiroga *et al.*, 2021)**.** shows the complete system that made the reactor functional. It is composed of the pumping subsystem; the piping subsystem; the storage subsystem, which can elevate the oil temperature to 180 °F; the control subsystem; and the vortex reactor. The hydrogen donor can be injected into the oil with high or low pressure. In this case, the latter was employed. Note that the phenomena of mixing and vapor generation were not studied independently. It was assumed that these two conditions affect the performance of the vortex reactor (Quiroga *et al.*, 2021).

Table. 1 Results obtained from the experimental design

Iter	Hydrogen donor [%]	Temperature [°F]	Initial Viscosity [cP]	Final Viscosity [cP]	Viscosity reduction [%]
1	2	92	740	710	4,054
2	2	140	740	702	5,135
3	2	180	740	692	6,486
4	3	94	740	464	37,297
5	3	141	740	463	37,432
6	3	180	740	452	38,919
7	4	93	740	342	53,784
8	4	141	740	335	54,730
9	4	180	740	331	55,270

Source: Authors

Cavitation model

Modeling cavitation in the vortex reactor allowed studying the fluid-dynamic behavior of the oil. The parameter of interest in the numerical model was vapor generation, which is a consequence of the cavitation process.

The selection of numerical models was carried out by reviewing the works of several authors (Moll *et al.*, 2011, 2012; Salvador and Frankel, 2004; Darbandi and Sadeghi, 2009), who simulated the behavior of a cavitating fluid in injectors. This research is based on a widely recognized experimental study in this field (Nurick, 1976).

The turbulence model used was the K-Epsilon Realizable with Standard Wall Functions because the viscous effects near the wall were not relevant. As there is cavitation, there is a two-phase flow. For this reason, a mixture model was chosen in conjunction with the Schnerr-Sauer method in order to model the formation of bubbles. Since the behavior and evolution of bubbles is not a concern in this project, the model was run in a steady state.

The geometry used corresponds to the volume of fluid extracted from the vortex reactor, which is shown with the corresponding scale in Figure 2. The inlet and outlet domains for the boundary conditions are indicated in the isometric view in Figure 2a. Detailed geometric dimensions are not provided for patent protection purposes.

The values established as boundary conditions for each numerical model are shown in Figure 2a, where the first three were taken from the experimental stage. Furthermore, two models with pressure values corresponding to higher temperatures were added, which were obtained through a mathematical correlation. Finally, the walls were treated with the conditions of non-slip and zero flow.

Table 2. Boundary conditions for each numerical model

Model	Inlet pressure [psi]	Outlet pressure [psi]
1	360	14
2	335	14
3	325	14
4	308,6	14
5	293	14

Source: Authors

A mesh independence study was conducted in order to find the appropriate element size. Overall, five meshes were employed which had between 1 179 758 and 8 474 211 elements. Finally, a mesh with 6 764 078 first-order elements was selected. The skewness, orthogonal quality, and aspect ratio were evaluated, and they are shown in Table 3. Note that the quality of the mesh is enough to achieve a good accuracy and avoid high discretization errors.

Table 3. Quality parameters of the selected mesh

Parameter	Minimum value	Maximum value	Average value
Aspect ratio	1,002	29,267	2,661
Skewness	8,832E-9	0,799	0,166
Orthogonal quality	0,2	1	0,857

Source: Authors

The numerical results were evaluated using various guidelines related to the validation and verification of computational fluid dynamics simulations (Freitas, 2002). To define the models, prior characterization of the oil in the liquid and vapor phase was necessary. To find the required properties, the Aspen HYSYS software was used in conjunction with the data obtained from the following tests:

- ASTM D445 for viscosity (2021)
- ASTM D1298 for API gravity (2017)
- ASTM D86 for a distillation curve (2020)
- PVT analysis

Figure 3 shows the configuration used in Aspen HYSYS. It has an oil stream whose properties were obtained using the previous tests, a control valve to throttle the fluid and generate two phases, and a flash drum to independently obtain the properties of vapor and liquid.

Once the configuration was set, five different conditions were established on the crude stream, which are shown
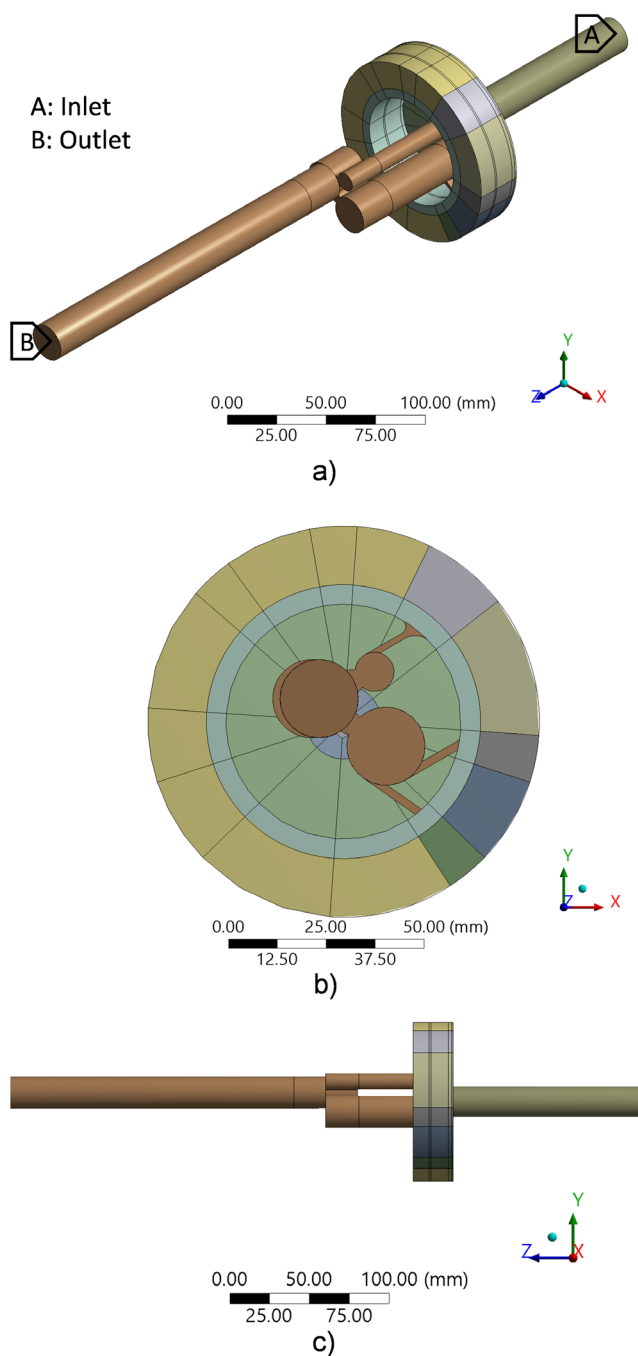
A: Inlet
B: Outlet

a)

b)

c)

Figure 2. Volume of fluid extracted from the vortex reactor: a) isometric view with inlet and outlet domains, b) front view, c) side view
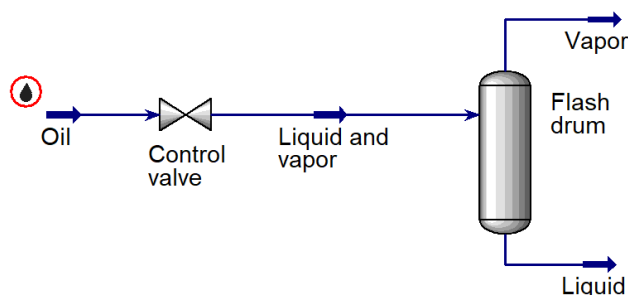**Source:** Authors

Figure 3. Aspen HYSYS configuration for oil characterization
Source: Authors

in Table 4. The first three conditions are the values used in the experimental stage, when a 2% hydrogen donor was injected. Additionally, two conditions were added, with higher temperatures to evaluate the behavior of the vapor fraction.

Table 4. Oil stream conditions used in Aspen HYSYS

Condition	Temperature [°F]	Pressure [psi]
1	92	360
2	140	335
3	180	325
4	250	308,6
5	350	293

Source: Authors

Results

Statistical analysis of experimental data

The data obtained through the experimental design was evaluated using Minitab. The individual effects of each variable on the final viscosity were entered, and a statistical analysis was performed.

The Pareto chart of standardized effects can be seen in Figure 4. When the bar of one of the factors crosses the dotted line with a value of 2,8, it can be considered to be statistically significant. In this case, both the temperature and the injected hydrogen donor crossed it. Nevertheless, the donor did it to a greater extent, which means that it has a greater effect on the final viscosity.
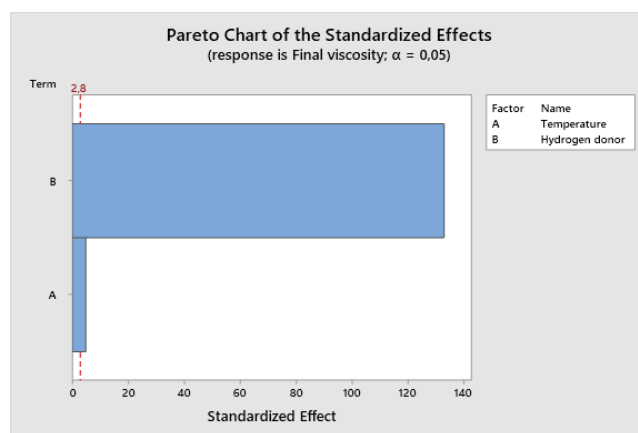
Figure 4. Pareto chart of standardized effects
Source: Authors

Moreover, the main effects of the levels of each factor on the viscosity can be seen in Figure 5. The temperature showed an almost horizontal line at the different levels, which means that its effect on the final viscosity is low. On the contrary, the hydrogen donor presented inclined lines at its different levels, which suggests that there is a considerable effect on the response variable.

Vapor generated from cavitation

The generated vapor was the variable of interest in the model because, with it, the effect of temperature on cavitation can be observed. Figure 6 shows the vapor fraction isosurfaces at the different analysis temperatures, except for 92 °F, since there was no vapor. Note that there is an increase in vapor generation as the temperature rises. In total, four different zones were found and marked with a number.

Figure 5. Main effects plot
Source: Authors

Vapor generated from cavitation

The generated vapor was the variable of interest in the model because, with it, the effect of temperature on cavitation can be observed. Figure 6 shows the vapor fraction isosurfaces at the different analysis temperatures, except for 92 °F, since there was no vapor. Note that there is an increase in vapor generation as the temperature rises. In total, four different zones were found and marked with a number.
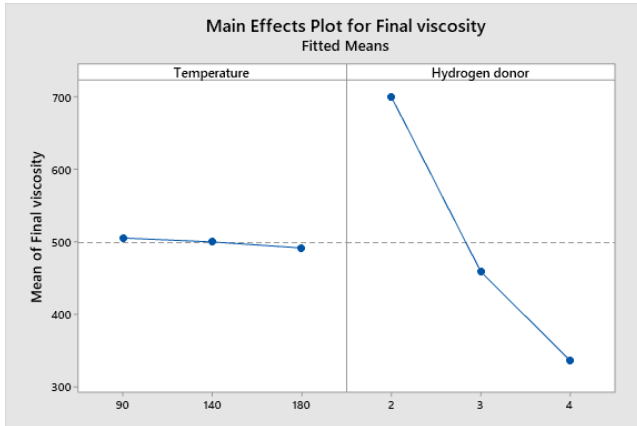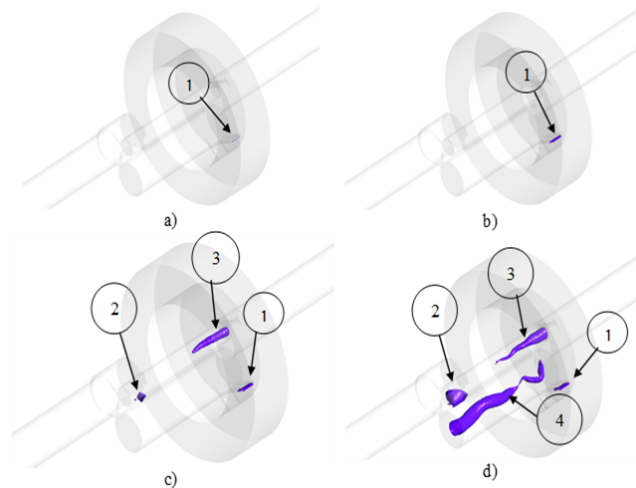

Figure 6. Vapor fraction isosurfaces at 140 °F (a), 180 °F (b), 250 °F (c), and 350 °F (d)
Source: Authors

Zone 1 occurs when there is a sudden reduction in the cross-sectional area and an abrupt change in the flow direction. This leads to a separation of the boundary layer

from the walls and causes what is known as *vena contracta*, from which a recirculation zone is formed. Here, the static pressure can be lower than the vapor pressure, thus producing cavitation (Payri *et al.*, 2005). This phenomenon is usually studied in injector nozzles (Sou *et al.*, 2014). Likewise, in zone 2, a similar type of cavitation is generated since the flow is abruptly diverted.

Zones 3 and 4 correspond to cavitation generated by a vortex. Vapor is formed in its center, since there is a zone of low pressure because of the centrifugal force created by the rotation of the fluid. This phenomenon occurs mainly in the suction tubes of Francis turbines (Brennen, 1995).

The total vapor volume generated was obtained from the numerical models and was plotted as a function of temperature, as shown in Figure 6. At 92 °F, no vapor has yet formed, and, as the temperature rises, the amount of steam increases exponentially. The maximum value was 1,507 cm³ at 350 °F. By contrasting the graph with the isosurfaces of Figure 7, the increase in vapor volume can be related to the aforementioned zones, thus implying that the vortices contribute the greatest amount.
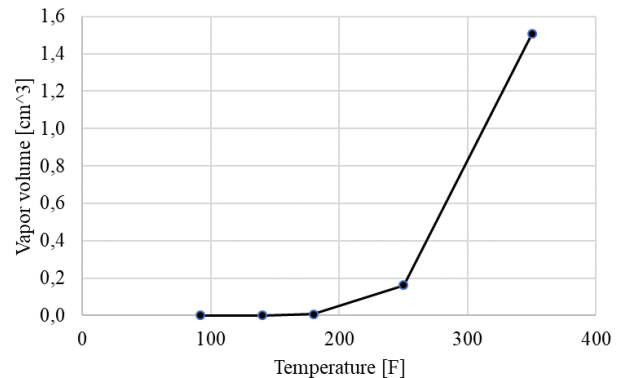
Figure 7. Variation of the vapor volume with temperature
Source: Authors

Conclusions

The experimentally obtained data showed that the increase in the fluid temperature during the tests did not have a considerable effect on the final viscosity of the oil. On the contrary, the increase of the injected hydrogen donor did achieve a high final reduction. This could be verified in the Pareto chart of standardized effects and the slopes of the main effects plot.

The Aspen HYSYS software, along with the ASTM D445, ASTM D1298, and ASTM D86 tests as well as the PVT analysis allowed completely characterizing the oil. The software proved to be a useful tool for obtaining the properties of the oil necessary to develop the numerical model in Fluent.

Using computational fluid dynamics, the behavior of the oil through the vortex reactor at different operating temperatures

was modeled. It was found that, in the range from 92 to 180 °F, the vapor volume did not exceed 0,00685 cm³. However, at 350 °F, the vapor volume increased significantly to 1,507 cm³. By observing the isosurfaces, it was found that the sudden increase is due to cavitation in the vortices.

From the data obtained both experimentally and numerically, it is concluded that the temperatures employed in the tests were very low to have an effect on the final viscosity of the oil. Therefore, it is recommended to increase the power in the storage tank's resistance in order to reach higher temperatures. In addition, a feasibility analysis must be conducted since this change represents costs that could not be offset in the reduction of viscosity of the oil.

Acknowledgments

References

Askarian, M., Vatani, A., and Edalat, M. (2017). Heavy oil upgrading via hydrodynamic cavitation in the presence of an appropriate hydrogen donor. *Journal of Petroleum Science and Engineering*, *151*, 55-61. https://doi.org/10.1016/j.petrol.2017.01.037

Avvaru, B., Venkateswaran, N., Uppara, P., Iyengar, S. B., and Katti, S. S. (2018). Current knowledge and potential applications of cavitation technologies for the petroleum industry. *Ultrasonics Sonochemistry*, *42*, 493-507. https://doi.org/10.1016/j.ultsonch.2017.12.010

ASTM International. (2017). *ASTM D1298-12b: Standard test method for density, relative density, or API gravity of crude petroleum and liquid petroleum products by hydrometer method*. ASTM International.

ASTM International. (2020). *ASTM D86-20b: Standard test method for distillation of petroleum products and liquid fuels at atmospheric pressure*. ASTM International.

ASTM International. (2021). *ASTM D445-21: Standard test method for kinematic viscosity of transparent and opaque liquids (and calculation of dynamic viscosity)*. ASTM International.

Barona-Mejía, A. S., Gómez-Díaz, S., Aguilar-Bedoya, J., Rubio-Clemente, A., and Chica-Arrieta, E. L. (2021). Cavitación en perfiles hidrodinámicos para turbinas hidrocinéticas. *Revista UIS Ingenierías*, *20*(2), 85-96. https://doi.org/10.18273/revuin.v20n2-2021008

Brennen, C. E. (1995). *Cavitation and bubble dynamics*. Oxford University Press. https://doi.org/10.1017/CBO9781107338760

Cappa, E. F., Moll, F., Coussirat-Núñez, M., Gandolfo, E., Fontanals-García, A., and Guardo-Zabaleta, A. (2014). Estudio de sensibilidad de parámetros de modelos en flujos cavitantes en régimen no estacionario. *Mecánica Computacional*, *XXXII*(2), 93-107. https://cimec.org.ar/ojs/index.php/mc/article/view/4620

Darbandi, M., and Sadeghi, H. (2009). A study on flow through an orifice with prediction of cavitation and hydraulic flip. *Proceedings of the ASME Fluids Engineering Division Summer Conference 2009, FEDSM2009*, *2*, 381-386. https://doi.org/10.1115/FEDSM2009-78448

Dular, M. (2015). Hydrodynamic cavitation damage in water at elevated temperatures. *Wear*, *346-347*, 78-86. https://doi.org/10.1016/j.wear.2015.11.007

Freitas, C. J. (2002). The issue of numerical uncertainty. *Applied Mathematical Modelling*, *26*(2), 237-248. https://doi.org/10.1016/S0307-904X(01)00058-0

Ge, M., Zhang, G., Petkovšek, M., Long, K., and Coutier-Delgosha, O. (2022). Intensity and regimes changing of hydrodynamic cavitation considering temperature effects. *Journal of Cleaner Production*, *338*, 130470. https://doi.org/10.1016/j.jclepro.2022.130470

Gogate, P. R., and Pandit, A. B. (2000). Engineering design methods for cavitation reactors II: Hydrodynamic cavitation. *AIChE Journal*, *46*, 1641-1649. https://doi.org/10.1002/aic.690460815

Moll, F., Manuele, D., Coussirat-Núñez, M., Cappa, E., Gandolfo, E., Guardo-Zabaleta, A., and Fontanals-García, A. (2012). Optimización de un banco de ensayos de cavitación mediante fluidodinámica computacional. *Mecánica Computacional*, *XXXI*, 3661-3676. https://upcommons.upc.edu/bitstream/handle/2117/17056/Mecanica%20Computacional%20XXXI%20(2012)%203661%20-%203676.pdf

Moll, F., Manuele, D. E., Coussirat-Núñez, M. G., Guardo-Zabaleta, A., and Fontanals-García, A. (2011). Caracterización del tipo de cavitación mediante CFD. *Mecánica Computacional*, *XXX*, 435-450. https://upcommons.upc.edu/bitstream/handle/2117/15553/Mecanica%20Computacional%20XXX%20(2011)%20435%20-%20450.pdf

Montes, D., Cortés, F. B., and Franco, C. A. (2018). Reduction of heavy oil viscosity through ultrasound cavitation assisted by NiO nanocrystals-functionalized SiO₂ nanoparticles. *DYNA*, *85*(207), 153-160. https://doi.org/10.15446/dyna.v85n207.71804

Nouri, N. M., Mirsaeedi, S. M. H., and Moghimi, M. (2010). Large eddy simulation of natural cavitating flows in Venturi-type sections. *Proceedings of the Institution of Mechanical Engineers, Part C: Journal of Mechanical Engineering Science*, *225*, 369-381. https://doi.org/10.1243/09544062JMES2036

Nurick, W. H. (1976). Orifice cavitation and its effect on spray mixing. *Journal of Fluids Engineering*, *98*(2), 681-687. https://doi.org/10.1115/1.3448785

Olaya-Escobar, D. R., Quintana-Jiménez, L. A., González-Jiménez, E. E., and Olaya-Escobar, E. S. (2020). Ultrasound applied in the reduction of viscosity of heavy crude oil. *Revista Facultad de Ingeniería*, *29*(54), e11528. https://doi.org/10.19053/01211129.v29.n54.2020.11528

Payri, R., García, J. M., Salvador, F. J., and Gimeno, J. (2005). Using spray momentum flux measurements to understand the influence of diesel nozzle geometry on spray characteristics. *Fuel*, *84*(5), 551-561. https://doi.org/10.1016/j.fuel.2004.10.009

Petkovšek, M., and Dular, M. (2013). IR measurements of the thermodynamic effects in cavitating flow. *International Journal of Heat and Fluid Flow*, *44*, 756-763. https://doi.org/10.1016/j.ijheatfluidflow.2013.10.005

Quan, K. M., Avvaru, B., and Pandit, A. B. (2011). Measurement and interpretation of cavitation noise in a hybrid hydrodynamic cavitating device. *AIChE Journal*, *57*(4), 861-871. https://doi.org/10.1002/aic.12323

Quiroga, R., González-Estrada, O. A., and González-Silva, G. (2021). Efecto de la temperatura en la fracción de vapor del crudo pesado en el reactor Vortex de cavitación hidrodinámica mediante CFD. *Ciencia en Desarrollo*, *12*(2), 57-65. https://doi.org/10.19053/01217488.v12.n2.2021.13418

Salvador, G. P., and Frankel, S. H. (2004, June 28-July 1). *Numerical modeling of cavitation using fluent: Validation and parametric studies* [Conference presentation]. 34th AIAA Fluid Dynamics Conference and Exhibit, Portland, OR, USA. https://doi.org/10.2514/6.2004-2642

Šarc, A., Stepišnik-Perdih, T., Petkovšek, M., and Dular, M. (2017). The issue of cavitation number value in studies of water treatment by hydrodynamic cavitation. *Ultrasonics Sonochemistry*, *34*, 51-59. https://doi.org/10.1016/j.ultsonch.2016.05.020

Sauer, J., and Schnerr, G. H. (2000). *Unsteady cavitating flow - A new cavitation model based on a modified front capturing method and bubble dynamics* [Conference presentation]. 2000 ASME Fluids Engineering Summer Conference, Boston, MA, USA. https://publikationen.bibliothek.kit.edu/27552000

Sawarkar, A. N. (2019). Cavitation induced upgrading of heavy oil and bottom-of-the-barrel: A review. *Ultrasonics Sonochemistry*, *58*, 104690. https://doi.org/10.1016/j.ultsonch.2019.104690

Senthil Kumar, P., Siva Kumar, M., and Pandit, A. B. (2000). Experimental quantification of chemical effects of hydrodynamic cavitation. *Chemical Engineering Science*, *55*(9), 1633-1639. https://doi.org/10.1016/S0009-2509(99)00435-2

Shi, H., Li, M., Nikrityuk, P., and Liu, Q. (2019). Experimental and numerical study of cavitation flows in venturi tubes: From CFD to an empirical model. *Chemical Engineering Science*, *207*, 672-687. https://doi.org/10.1016/j.ces.2019.07.004

Singhal, A. K., Athavale, M. M., Li, H., and Jiang, Y. (2002). Mathematical basis and validation of the full cavitation model. *Journal of Fuids Engineering, 12*(3), 617-624. https://doi.org/10.1115/1.1486223

Sou, A., Biçer, B., and Tomiyama, A. (2014). Numerical simulation of incipient cavitation flow in a nozzle of fuel injector. *Computers and Fluids*, *103*, 42-48. https://doi.org/10.1016/j.compfluid.2014.07.011

Sun, X., Park, J. J., Kim, H. S., Lee, S. H., Seong, S. J., Om, A. S., and Yoon, J. Y. (2018). Experimental investigation of the thermal and disinfection performances of a novel hydrodynamic cavitation reactor. *Ultrasonics Sonochemistry*, *49*, 13-23. https://doi.org/10.1016/j.ultsonch.2018.02.039

Yang, Z., Zhang, C., Gu, S., Han, P., and Lu, X. (2013). Upgrading vacuum residuum by combined sonication and treatment with a hydrogen donor. *Chemistry and Technology of Fuels and Oils*, *48*(6), 426-435. https://doi.org/10.1007/s10553-013-0391-2

Energy and Exergy Analysis in a Centrifugal Pump Driven by a Diesel Engine Using Soybean Biodiesel and Mixtures with Diesel

Análisis de energía y exergía en una bomba centrífuga accionada por un motor diésel con biodiésel de soya y mezclas con diésel

Roberto Guimarães Pereira [1], Ivenio Moreira da Silva [2], and Juan M. Pardal [3]

ABSTRACT

In this study, soybean biodiesel and mixtures with diesel are used as fuel in a diesel engine that drives a centrifugal pump. The consumption useful work rate, the reversible work rate, and the efficiency of the second law of thermodynamics were calculated by means of energetic and exergetic analyses. The soybean biodiesel was produced using ethanol with a proportion of 33% v/v and the catalyst NaOH (1%), thus obtaining a yield of 90,63%. The fuels used were pure diesel (B0); 25% soybean biodiesel and 75% diesel (B25); 50% soybean biodiesel and 50% diesel (B50); 75% soybean biodiesel and 25% diesel (B75); and soybean biodiesel (B100). The density and kinematic viscosity were within the limits established by the National Petroleum, Natural Gas, and Biofuels Agency. A value of 39 017 kJ.kg^{-1} was obtained for the highest heating value of the soybean biodiesel (B100). A 32,05% maximum second-law efficiency was obtained in the case of soybean biodiesel at maximum pump speed and at 9,2 m³/h. The B50 fuel obtained a 29,78% maximum second-law efficiency when the centrifugal pump operated at 2 733 rpm and at a maximum flow rate.

Keywords: soybean biodiesel, centrifugal pump, energy, exergy, sustainability

RESUMEN

En este estudio se utilizan el biodiésel de soya y mezclas con diésel como combustible en un motor diésel que impulsa una bomba centrífuga. La tasa de trabajo útil de consumo, la tasa de trabajo reversible y la eficiencia de la segunda ley de la termodinámica se calcularon mediante análisis energético y exergético. El biodiésel de soya se produjo utilizando etanol en la proporción de 33 % v/v y el catalizador NaOH (1 %), obteniendo un rendimiento de 90,63 %. Los combustibles utilizados fueron diésel (B0); 25 % de biodiésel de soya y 75 % de diésel (B25); 50 % biodiésel de soya y 50 % de diésel (B50); 75 % de biodiésel de soya y 25 % de diésel (B75); y biodiésel de soya (B100). La densidad y la viscosidad cinemática estuvieron dentro de los límites establecidos por la Agencia Nacional de Petróleo, Gas Natural y Biocombustibles. Se obtuvo un valor de 39 017 kJ.kg^{-1} para el mayor poder calorífico del biodiésel de soya (B100). Se obtuvo 32,05 % de eficiencia máxima de la segunda ley en el caso del biodiésel de soya a la máxima velocidad de bombeo y a 9,2 m³/h. El combustible B50 obtuvo 29,78 % de eficiencia máxima de la segunda ley cuando la bomba centrífuga operó a 2 733 rpm y al caudal máximo.

Palabras clave: biodiésel de soja, bomba centrífuga, energía, exergía, sustentabilidad

Introduction

Several countries have been using biodiesel to replace fossil fuels. Biodiesel is produced from different renewable sources such as cotton, soybean, castor bean, sunflower, coconut, and palm, in addition to beef tallow and micro algae. It can be used in conventional engines without modifications, considering that its physicochemical properties are similar to those of diesel. The use of biodiesel in engines promotes a reduction in emissions of particulate matter and polluting gases (carbon monoxide, sulfur oxides, and hydrocarbons), and it also promotes the recycling of CO_2 (Pereira *et al*., 2017a, 2017b, 2014, 2012, 2007; Demirbas, 2009; Fajardo *et al*., 2010).

Soybean is one of the most important crops in the agroindustry around the world. It is a raw material that can be used for oil extraction and biofuel production. The oil content of soybean (*Glycine max* L., Merrill) is around 25%.

Pure soybean biodiesel has been used in engines, as well as in combination with diesel (Pereira *et al*., 2007, 2011; Ozener *et al*., 2014), as its use in energy generation contributes to sustainability and cleaner production.

[1] Fluminense Federal University, TEM/PGMEC/PGEB, Rua Passo da Pátria 156, CEP 24210-240, Niterói - RJ, Brazil. E-mail: temrobe@vm.uff.br

[2] Fluminense Federal University, TER, Rua Passo da Pátria, 156, CEP: 24210-240, Niterói, RJ, Brazil. E-mail: ivenio@vm.uff.br

[3] Fluminense Federal University, TEM/PGMEC, Rua Passo da Pátria, 156, CEP: 24210-240, Niterói, RJ, Brazil. E-mail: juanpardal@id.uff.br

Agriculture is an important component in a country's economy. In irrigation processes, the use of centrifugal pumps driven by diesel cycle engines is common, especially in places without a power network. The use of biodiesel to replace diesel has economic and socio-environmental advantages, since biodiesel is a renewable fuel. Thus, in view of the importance of using combustion engines to drive pumps, the use of soybean biodiesel and its mixtures with diesel in a centrifugal pump driven by a diesel engine was studied in this work. This system was coupled to an instrumented hydraulic circuit in order to carry out energy and exergy analyses.

Biodiesel in Brazil

The use of biodiesel is regulated in several countries; it is necessary to meet several technical specifications for use in engines. For example, in the USA, the ASTM D6751 (ASTM International, 2020) standard is used, as well as the EN 14214 (European Standards, 2012) in the European Union and, in the case of Brazil, the properties of biodiesel must meet the specifications of the National Petroleum, Natural Gas, and Biofuels Agency (ANP) detailed in Resolution No. 45 from August 25th, 2014.

Brazil has been leading in the worldwide production of biodiesel since 2008 (Pereira and Lameira, 2013). According to ANP data, Brazil produced 482 304 m³ of biodiesel in February 2020, with soybean oil representing 68,85% of the total raw materials used for biodiesel production, followed by beef tallow with 10,99%. In 2019, Brazil produced 5 899 483 m³ of biodiesel (ANP, 2020).

In February 2020, there were 51 biodiesel plants operating in Brazil which were authorized by the ANP. This corresponds to 25 918,26 m³.day⁻¹ of the total authorized capacity (ANP, 2020), with soybean oil being the main raw material for biodiesel production.

The main fuel used in Brazil's buses and trucks is diesel, which is largely imported. In order to reduce this dependence, biodiesel is emerging as an alternative for use in diesel engines.

In 2005, the diesel sold in Brazil started to be combined with 2% of biodiesel. This percentage increased to 3% in the period from July 2008 to the first half of 2009, and it increased to 4% in July 1st, remaining constant until the end of 2009. In January 2010, the replacement percentage became 5%. 7% was implemented in November 2014, increasing to 10% in March 2016 (Law 13263) (Presidência da República, 2016). Since September 1st, 2019, the addition of biodiesel to diesel is between 11 and 15% (B11 to B15) as per the ANP (Corrêa, 2019).

Thus, this study deals with the use of soybean biodiesel and mixtures with diesel in a diesel engine that drives a centrifugal pump.

Soybean production

Soybean production has grown worldwide. In 2010, the world production was around 265×10^6 ton in a harvested area of 103×10^6 ha, while, in 2018, the world production was 349×10^6 ton in 125×10^6 ha (FAO, 2020).

In 2018, 118×10^6 ton of soybean were produced in Brazil –thus making it the second largest producer– in a harvested area of $34,77 \times 10^6$ ha, corresponding to the second largest harvested area in the world. The yield was 3,39 ton.ha⁻¹, which is the fifth in the world (FAO, 2020).

Energy and exergy analysis

The energy conservation principle, also known as the first law of thermodynamics, is related to the various forms of energy transformation and the amount of energy involved in the processes, regardless of the quality of said energy (Kanoğlu *et al.*, 2012).

The second law of thermodynamics is of great importance in engineering, given that, in addition to identifying the direction of the process, it makes it possible to determine the quality and degradation degree of energy (Kanoğlu *et al.*, 2012). Pereira and Silva (2019) have discussed the topic of exergy analysis.

Energy and exergy analyses in a centrifugal pump driven by a diesel engine

For the energy analysis, a control volume was considered, which covered the centrifugal pump driven by a diesel engine with input and output mass (Macedo, 2013; Silva, 2014). The energy balance applied to a process for control volume (steady state flow process) was used, as shown in Equation (1):

$$\dot{Q} - \dot{W} + \sum \dot{m}_{in}\left(h_{in} + \left(V_{in^2}/2\right) + gz_{in}\right)$$
$$- \sum \dot{m}_{out}\left(h_{out} + \left(V_{out^2}/2\right) + gz_{out}\right) = 0 \tag{1}$$

The consumption useful work rate ($\dot{W}_u$) under single current, $\dot{Q} = 0$, uniform properties, and not considering kinetic and potential energy variations, becomes a function of the difference regarding enthalpy between the initial state 1 (at the input of the pump) and the final state 2 (at the output of the pump), which is given by Equation (2):

$$\dot{W}_u = \dot{m}\left(h_2 - h_1\right) \tag{2}$$

The exergy term (X_{heat}) was neglected, considering the pump to be an adiabatic device. To obtain an expression for the reversible work rate ($\dot{W}_{rev}$), the destroyed exergy ($X_{destroyed}$) was made zero. The reversible work rate is given by Equation

(3) in terms of the specific exergies in a steady state and with uniform properties.

$$\dot{W}_{rev} = \dot{m}\left(\psi_2 - \psi_1\right) \quad (3)$$

Where:

$$\psi_2 = \left(h_2 - h_0\right) - T_0\left(s_2 - s_0\right) + \left(V_2^2 / 2\right) + gz_2 \quad (4)$$

$$\psi_1 = \left(h_1 - h_0\right) - T_0\left(s_1 - s_0\right) + \left(V_1^2 / 2\right) + gz_1 \quad (5)$$

The reversible work rate ($\dot{W}_{rev}$) is given by Equation (6), which does not consider kinetic and potential energy variations:

$$\dot{W}_{rev} = \dot{m}\left(\left(h_2 - h_1\right) - T_0\left(s_2 - s_1\right)\right) \quad (6)$$

$\dot{W}_{rev}$ represents the minimum power consumed by the pump.

The second-law efficiency (η_{II}) is the ratio between the minimum power (reversible work rate) and the real power (consumption useful work rate) for devices that consume power:

$$\eta_{II} = \dot{W}_{rev} / \dot{W}_u = \left(\psi_2 - \psi_1\right) / \left(h_2 - h_1\right) \quad (7)$$

By measuring the pressure and temperature parameters at the pump inlet and outlet, it is possible to determine h_1 and h_2, as well as s_1 and s_2, in order to obtain the reversible work rate ($\dot{W}_{rev}$), the consumption useful work rate ($\dot{W}_u$), and the second-law efficiency (η_{II}).

Methodology

Production and characterization of soybean biodiesel

Soybean biodiesel production was carried out using ethanol anhydrous PA 99,7% and NaOH as a catalyst. The soybean oil used in the biodiesel production process was obtained from the national market. The experiments were conducted in batches of 100 mL of oil. An ultrasound was used in the process, as detailed by Silva (2014). Ethanol was used instead of methanol for the transesterification reaction because it is inherently safer and produced from renewable sources such as sugar cane in Brazil.

The soybean biodiesel produced was identified and stored in amber glass bottles with a capacity of 1 L, remaining in a light-free and airy place.

The mixtures were conditioned in amber-colored bottles and labeled as follows: B0 (diesel), B25 (soybean biodiesel 25% and diesel 75%), B50 (soybean biodiesel 50% and diesel 50%), B75 (soybean biodiesel 75% and diesel 25%), and B100 (soybean biodiesel).

The soybean-biodiesel mixtures were characterized, determining the following properties: kinematic viscosity (ASTM D445), density (ASTM D4052), cloud point (ASTM D2500), pour point (ASTM D97), and higher heating value (ASTM D4809) (ASTM International, 2017a, 2017b, 2018a, 2018b, 2021).

Energy and exergy analyses

By measuring the pressure and temperature parameters at the pump inlet and outlet, it is possible to determine the values of enthalpy and entropy in order to obtain the reversible work rate ($\dot{W}_{rev}$), the consumption useful work rate ($\dot{W}_u$), and the second-law efficiency (η_{II}). Figure 1 shows the experimental apparatus used in the tests.
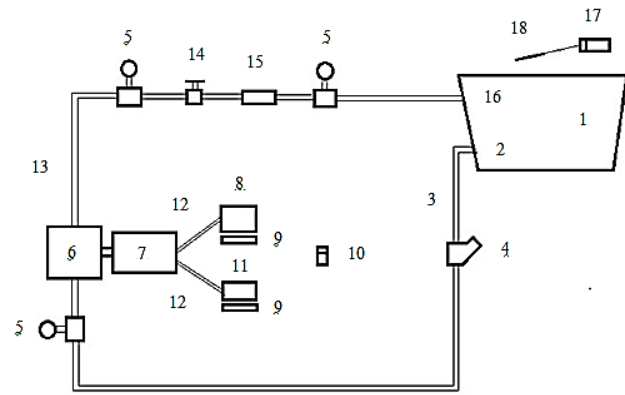
1) reservoir; 2) suction; 3) suction tube; 4) Y filter; 5) pressure gauge; 6) centrifugal pump; 7) diesel engine; 8) fuel reservoir; 9) digital scale; 10) thermometer (room temperature); 11) reservoir of returning fuel; 12) hose; 13) discharge tube; 14) globe valve; 15) flow meter; 16) discharge; 17) thermometer; 18) pt 100 sensor

Figure 1. Experimental apparatus
Source: Authors

The centrifugal pump used in the experiments was manufactured by Lintec and has a maximum flow rate of 36 m³/h, a maximum head of 26 m, and a maximum suction head of 8 m.

The diesel cycle engine used in the experiments was also manufactured by Lintec. It has a maximum speed of 3 300 rpm, and it is a four-stroke and direct injection engine with an air-cooling system, a displacement volume of 0,211 L, a maximum output of 2,8 kW, a fuel capacity of 2,5 L, and a weight of 32 kg.

A centesimal precision thermometer (Instrutherm, Model THR-080) was used to measure the suction and discharge temperatures of the fluid. A digital thermometer (Hikari, model HK - T 220) with decimal precision was used to measure the room temperature (T_0).

The suction and discharge pressures were determined using Bourdon-type pressure gauges with a measuring range of

0-40 kPa (0-400 mbar) in the suction line and from 0-392,27 kPa (0-4 kgf/cm²) in the discharge line.

The flow rate was obtained using an InControl digital meter, model PRO 1000.

The SteamTab software was used to obtain the values of entropy and enthalpy from the measured pressure and temperature values at the inlet and outlet of the centrifugal pump.

Centrifugal pump at maximum speed

With the speed of the centrifugal pump kept at 3 300 rpm (maximum speed) and the globe valve restricted to six positions, the following parameters were measured: the suction and discharge temperatures, the room temperature, and the pressures at the suction manometer and in the two manometers positioned before and after the globe.

Centrifugal pump at the maximum flow rate

With the maximum opening of the globe valve (maximum flow rate) and while changing the pump speed, the following parameters were measured: the suction and discharge temperatures, the room temperature, the pressures at the suction manometer and in the two manometers positioned before and after the globe valve.

Results and discussion

Soybean biodiesel production

A yield of 90,63% was obtained for the soybean biodiesel.

Properties of diesel-soybean biodiesel blends

Table 1 shows the properties of the diesel-soybean biodiesel blends.

Table 1. Properties of diesel-soybean biodiesel blends

Properties	Diesel (B0)	B25	B50	B75	Soybean biodiesel (B100)
Viscosity at 40⁰C (mm².s⁻¹)	2,545	3,195	3,504	3,909	4,312
Density at 20⁰C (kg.L⁻¹)	0,83217	0,84203	0,85522	0,86715	0,87984
Cloud point (⁰C)	-2,7	1,2	1,9	3,2	3,7
Pour point (⁰C)	-6,9	-4,9	-4,5	-3,1	-2,2
Higher heating value (kJ.kg⁻¹)	45 280	-	-	-	39 017

Source: Authors

The expanded uncertainty in the measurements is as follows: density = ± 0,00008 kg.L⁻¹; viscosity = ±0,006 mm².s⁻¹; cloud point = ±1,5 ˚C; and pour point = ± 1,8 ˚C (Abreu, 2010; Santo Filho, 2010).

As shown in Table 1, the viscosity of soybean biodiesel at 40 ˚C (4,312 mm².s⁻¹) is kept within the limits established by the ANP (3-6 mm².s⁻¹ at 40 ˚C). The density of soybean biodiesel at 20 ˚C (0,87984 kg. L⁻¹) is also within the limits established by the ANP (0,850-0,900 kg.L⁻¹ at 20 ˚C). It is more viscous than diesel, and increasing the biodiesel percentage in the diesel mixture leads to an increase in viscosity. This tendency was also reported by Mejía *et al*. (2013) and Geller *et al*. (2008).

The pour point of the diesel-soybean biodiesel blends varies from -6,9 to -2,2 ˚C, indicating favorable conditions for use in winter conditions.

The diesel has a higher heating value (45 280 kJ.kg⁻¹), whereas soybean biodiesel has 39 017 kJ.kg⁻¹. The use of diesel-soybean biodiesel blends in the motor pump set showed a good behavior; no anomaly was observed.

Energy and exergy analyses

Centrifugal pump at the maximum speed

The consumption useful work rate and the reversible work rate at the maximum pump speed (3 300 rpm) for the diesel-soybean biodiesel mixtures are shown in Figures 2 and 3. The lower consumption useful work rate and reversible work rate occur under the lower flow rate conditions.
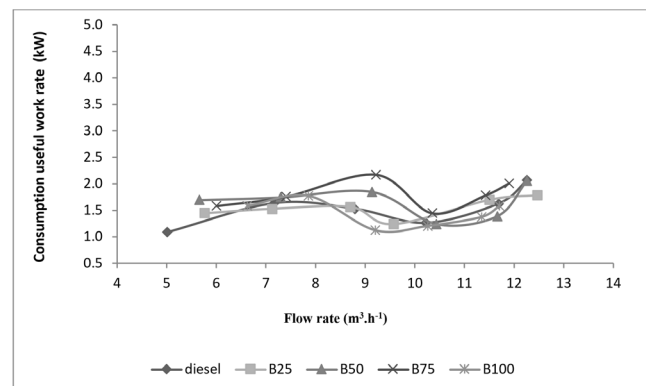

Figure 2. Consumption useful work rate *vs*. flow rate (maximum pump speed)
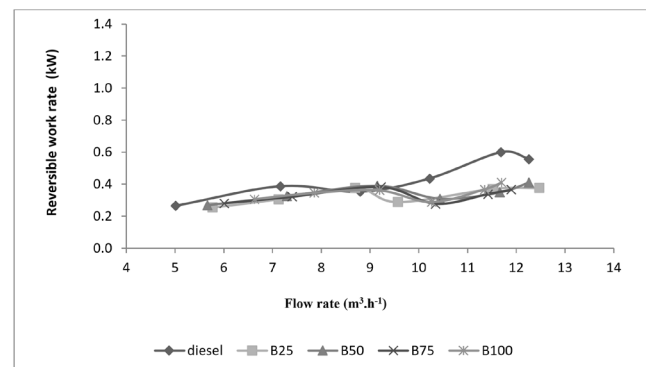**Source:** Authors

Figure 3. Reversible work rate *vs*. flow rate (maximum pump speed)
Source: Authors

The consumption useful work rate and the reversible work rate at maximum flow rate for the diesel-soybean biodiesel mixtures are shown in Figures 4 and 5. The lower consumption useful work rate and reversible work rate occur at the lower speed conditions.
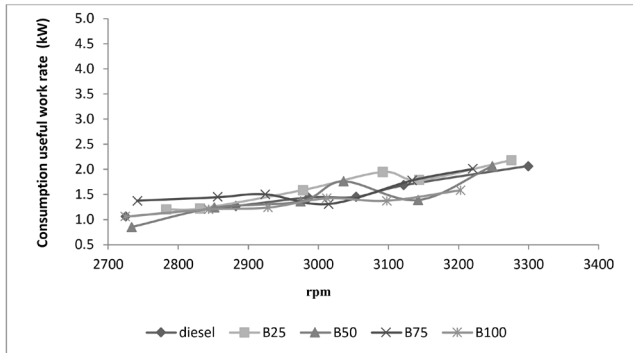

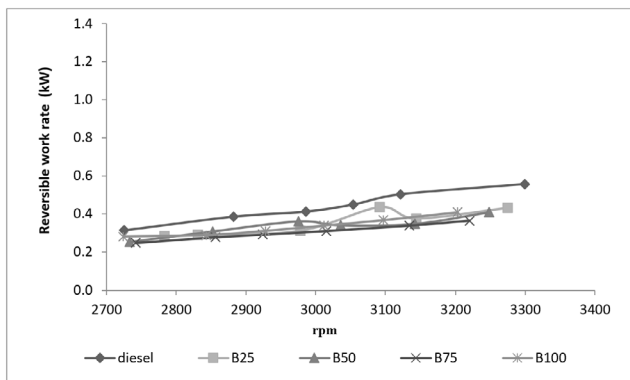**Figure 4.** Consumption useful work rate *vs.* speed (maximum pump flow rate)
Source: Authors

Figure 5. Reversible work rate *vs.* speed (maximum pump flow rate)
Source: Authors

Second-law efficiency

The behavior of the second-law efficiency is shown in Figure 6 as a function of the flow rate at maximum pump speed for diesel, diesel-soybean biodiesel mixtures, and soybean biodiesel. The efficiency ranges from 15,80% (B50 at 5,66 m³/h) to 36,82% (diesel at 11,69 m³/h). In the case of soybean biodiesel (B100), the efficiency ranges from 19,29%, at 6,63 m³/h to 32,05%, at 9,2 m³/h. The maximum second-law efficiency (25,02%) for the mixtures of soybean biodiesel with diesel occurs for B50 at 11,66 m³/h. The average second-law efficiency value for all fuels used in the centrifugal pump at maximum pump speed (3 300 rpm) was 22,64%.

The behavior of the second-law efficiency as a function of pump speed at maximum flow rate is shown in Figure 7 for diesel, diesel-soybean biodiesel mixtures, and soybean biodiesel. The efficiency ranges from 17,98% (B75 at 2 742 rpm) to 30,93% (diesel at 3 054 rpm). In the case of soybean biodiesel (B100), the efficiency ranges from 23,81% at 3 012 rpm to 26,69% at 3 097 rpm. The maximum second-law efficiency (29,78%) for the mixtures of soybean biodiesel with diesel was obtained by B50 at 2 733 rpm. At the

maximum flow rate, the average second-law efficiency value for all fuels used in the centrifugal pump was 24,03%.

For comparison, an exergetic efficiency value of 33% was found in the case of soybean oil used in a compression ignition engine at 1 800 rpm (Nieto Garzón *et al.*, 2015).
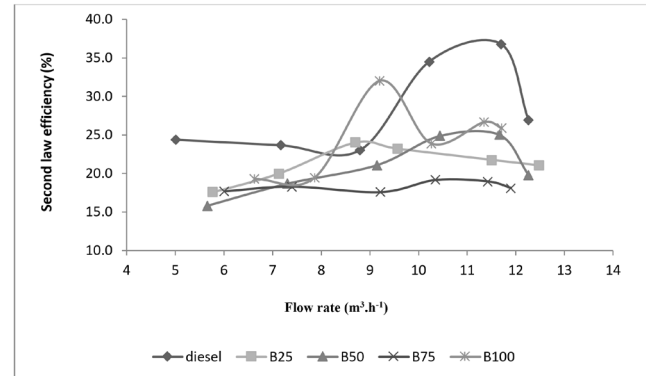
Figure 6. Second-law efficiency *vs.* flow rate (maximum pump speed)
Source: Authors
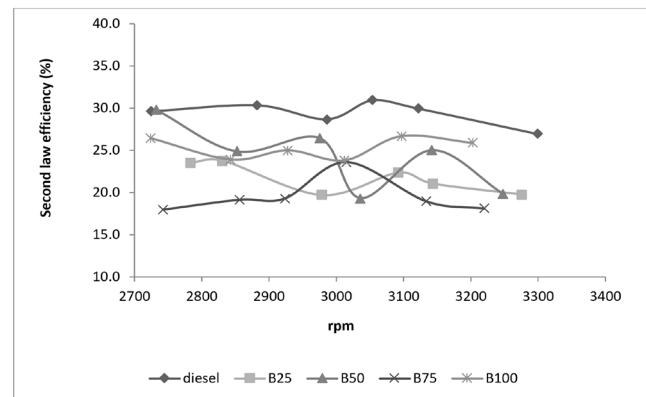
Figure 7. Second law efficiency *vs.* speed (maximum pump flow rate)
Source: Authors

Table 2 shows the average second-law efficiency value ($\bar{\eta}_{II}$) for all fuels at different flow rates, at maximum pump speed, and at different pump speeds at maximum flow rate.

Table 2. $\bar{\eta}_{II}$ for all fuels

FUEL	$\bar{\eta}_{II}$ (%) (different flow rates, at maximum pump speed)	$\bar{\eta}_{II}$ (%) (different pump speeds, at maximum flow rate)
DIESEL (B0)	28,23	29,41
B25	21,27	21,70
B50	20,87	24,22
B75	18,30	19,53
B100	24,54	25,29

Source: Authors

According to Table 2, it can be pointed out that the average second-law efficiency value was the highest in the case of diesel fuel. For the other fuels, the maximum value of

$\bar{\eta}_{II}$ was obtained with B100, which corresponds to a 100% substitution of diesel by a renewable fuel (soybean biodiesel).

Conclusions

The extracted oil from soybean constitutes a potential raw material for biodiesel production.

A centrifugal pump can be driven by a diesel engine operating with soybean biodiesel and different mixtures of soybean biodiesel with pure diesel.

The maximum second-law efficiency (32,05%) was obtained for B100 at maximum pump speed and at the flow rate of 9,2 m³/h. This optimal condition corresponds to a 100% substitution of diesel by a renewable fuel (soybean biodiesel).

For different flow rate and pump speed conditions, using the B50 fuel is recommended, given that it showed the best average second-law efficiency for the mixtures of diesel and soybean biodiesel.

Acknowledgments

Compliance with ethical standard, conflict of interest

The authors declare that they have no conflict of interest.

References

Abreu, F. L. B. (2010). *Power generation and analysis of emissions in stationary engine using biodiesel, blends of biodiesel and blends of biodiesel containing additive, produced via ethylic route and its characterization* [Doctoral thesis, Universidade Federal Fluminense].

ANP (2014). *Especificação do biodiesel*. https://www.gov.br/anp/pt-br/assuntos/producao-e-fornecimento-de-biocombustiveis/biodiesel/especificacao-do-biodiesel

ASTM International (2017a). *Standard test method for cloud point of petroleum products and liquid fuels* (*ASTM D2500-17a*). https://webstore.ansi.org/Standards/ASTM/ASTM-D250017a

ASTM International (2017b). *Standard test method for pour point of petroleum products*. (*ASTM D97-17b*). https://www.astm.org/d0097-17b.html

ASTM International (2018a). *Standard test method for density, relative density, and api gravity of liquids by digital density meter* (ASTM D4052-18a). https://webstore.ansi.org/Search/Find?in=1&st=ASTM+D4052

ASTM International (2018b). *Standard test method for heat of combustion of liquid hydrocarbon fuels by bomb calorimeter* (*precision method*) (*ASTM D4809-18*). https://webstore.ansi.org/Standards/ASTM/ASTMD480918

ASTM International (2020). *Standard specification for biodiesel fuel blend stock* (*b100*) *for middle distillate fuels* (*ASTM D6751-20a*). https://www.astm.org/d6751-20a.html

ASTM International (2021). *Standard test method for kinematic viscosity of transparent and opaque liquids* (*and calculation of dynamic viscosity*) (*ASTM D445-21e1*). https://www.astm.org/d0445-21e01.html

National Petroleum, Natural Gas, and Biofuels Agency (ANP) (2020). *Informações de mercado*. http://www.anp.gov.br/producao-de-biocombustiveis/biodiesel/informacoes-de--mercado

Demirbas, A. (2009). Biofuels securing the planet's future energy needs. *Energy Conversion and Management, 50*(9), 2239-2249. https://doi.org/10.1016/j.enconman.2009.05.010

Corrêa, D. (2019, August 6). ANP aprova aumento do percentual de adição de biodiesel ao óleo diesel. *Agência Brasil*. https://agenciabrasil.ebc.com.br/economia/noticia/2019-08/anp-aprova-aumento-do-percentual-de-adicao-de-biodiesel-ao-oleo-diesel

European Standards (2012). *Liquid petroleum products. Fatty acid methyl esters* (*FAME*) *for use in diesel engines and heating applications. Requirements and test methods*. (BS EN 14214:2012+A2:2019). https://www.en-standard.eu/bs-en-14214-2012-a2-2019-liquid-petroleum-products-fatty-acid-methyl-esters-fame-for-use-in-diesel-engines-and-heating-applications-requirements-and-test-methods/?gclid=EAIaIQobChMI6pm_37zk9gIVdMqzCh1uxw24EAAYASAAEgKt4fD_BwE

Fajardo, C. A. G., León, I. D. O., and Vargas, F. E. S. (2010). Evaluating the effect of temperature on biodiesel production from castor oil. *Ingeniería e Investigación, 30*(2), 52-61. https://doi.org/10.15446/ing.investig.v30n2.15733

Food and Agriculture Organization of the United Nations (FAO) (2020). *FAOSTAT*. https://www.fao.org/faostat/en/#data/QCL

Geller, D. P., Adams, T. T., Goodrum, J. W., and Pendergrass, J. (2008). Storage stability of poultry fat and diesel fuel mixtures: Specific gravity and viscosity. *Fuel, 87*, 92-102. https://doi.org/10.1016/j.fuel.2007.03.043

Kanoğlu, M., Çengel, Y. A., and Dinçer, I. (2012). *Efficiency evaluation of energy systems*. Springer. https://doi.org/10.1007/978-1-4614-2242-6_2

Macedo, T. O. (2013). *Methodology for experimental exergetic evaluation of a pump driven by a diesel engine, operating with standard diesel and biodiesel* [Master's thesis, Universidade Federal Fluminense].

Mejía, J. D., Salgado, N., and Orrego, C. E. (2013). Effect of blends of diesel and palm-castor biodiesels on viscosity, cloud point and flash point. *Industrial Crops and Products, 43*, 791-797. https://doi.org/10.1016/j.indcrop.2012.08.026

Nieto-Garzón, N. A., Oliveira, A. A. M., Hartmann, R. M., and Bazzo, E. (2015) Experimental and thermodynamic analysis of a compression ignition engine operating with straight soybean oil. *Journal of the Brazilian Society of Mechanical Sciences and Engineering, 37*, 1467-1478. https://doi.org/10.1007/s40430-014-0287-z

Özener, O., Yüksek, L., Ergenç, A. T., and Özkan, M. (2014). Effects of soybean biodiesel on a DI diesel engine performance, emission and combustion characteristics. *Fuel, 115*, 875-883. https://doi.org/10.1016/j.fuel.2012.10.081

Pereira, R. G., and Silva, I. M. (2019). Energy and exergy analysis of a centrifugal pump driven by a diesel engine operating with passion fruit biodiesel and mixtures with diesel. *Revista Ibero-americana de Ciências Ambientais, 10*(1), 262-273. https://doi.org/10.6008/CBPC2179-6858.2019.001.0022

Pereira, R. G., Tulcan, O. E. P., Lameira, V. J., Santo Filho, D. M. E., and Andrade, E. T. (2011). Use of soybean oil in energy generation. In D. Krezhova (Ed.), *Recent trends for enhancing the diversity and quality of soybean* (pp. 301-320). Intech Open Access Publisher.

Pereira, R. G., Tulcan, O. E. P., and Fellows, C. E. (2017a). Engine performance: biofuels versus petrofuels. In M. R. Riazi and D. Chiaramonti (Eds.), *Biofuels Production and Processing Technology* (1st ed., pp. 596-586). CRC Press Taylor & Francis Group. https://doi.org/10.1201/9781315155067-20

Pereira, R. G., Tulcan, O. E. P., Fellows, C. E., and Braz, A. J. L. (2017b). Energy generation and exhaust emissions analysis in a stationary engine using palm biodiesel, palm oil and diesel, *International Journal of Oil, Gas and Coal Technology*, *16*(4), 402-421. https://doi.org/10.1504/IJOGCT.2017.10008349

Pereira, R. G., Tulcan, O. E. P., Fellows, C. E., Silva, I. M., Santo Filho, D. M. E., Lameira, V. J., and Quelhas, O. L. G. (2014). Energy generation using coconut biodiesel and coconut oil in a stationary engine. *International Journal of Oil, Gas and Coal Technology*, *7*(4), 450-473. https://doi.org/10.1504/IJOGCT.2014.062165

Pereira, R. G., Tulcan, O. E. P., Fellows, C. E., Lameira, V. J., Quelhas, O. L. G., Aguiar, M. E., and Santo Filho, D. M. E. (2012). Sustainability and mitigation of greenhouse gases using ethyl beef tallow biodiesel in energy generation. *Journal of Cleaner Production, 29*(30), 269-276. https://doi.org/10.1016/j.jclepro.2012.01.007

Pereira, R. G., Oliveira, C. D., Oliveira, J. L., Oliveira, P. C. P., Fellows, C. E., and Piamba, O. E. (2007). Exhaust emissions and electric energy generation in a stationary engine using blends of diesel and soybean biodiesel. *Renewable Energy, 32*(14), 2453-2460. https://doi.org/10.1016/j.renene.2006.05.007

Pereira, R. G., and Lameira, V. J. (2013). Production and consumption of biodiesel and ethanol: A comparison, from 2000 to 2010. *Journal of Materials Science and Engineering B, 3*(10), 677-682. https://doi.org/10.17265/2161-6221/2013.10.007

Presidência da República (2016). *Lei no. 13 263, de 23 de março de 2016.* http://www.planalto.gov.br/ccivil_03/_ato2015-2018/2016/lei/l13263.htm

Santo Filho, D. M. E. (2010). *Metrology applied to analysis of biodiesel* [Doctoral thesis, Universidade Federal Fluminense].

Silva, I. M. (2014). *Power generation and exergy analysis in a motor-pump set using biodiesel produced through transesterification by ultrasound* [Doctoral thesis, Universidade Federal Fluminense].

A Survey of Virtualization Technologies: Towards a New Taxonomic Proposal

Una revisión de las tecnologías de virtualización: hacia una nueva propuesta taxonómica

Luis E. Sepúlveda-Rodríguez[1], Julio C. Chavarro-Porras[2], John A. Sanabria-Ordoñez[3], Harold E. Castro[4], and Jeanna Matthews[5]

ABSTRACT

At present, there is a proliferation of virtualization technologies (VTs), which are part of the basic and underlying infrastructure of popular cloud computing. Those interested in VTs are faced with a non-unified volume of information and various approaches to modes of operation, classification structures, and the performance implications of these technologies. This makes it difficult to decide which type of VT is appropriate for a particular context. Therefore, this paper reviews the state of the art on VT taxonomic models. Methodologically, a literature review is carried out to identify VT classification models, recognizing their features and weaknesses. With this in mind, a new taxonomy of virtualization technologies is proposed, which responds to the weaknesses identified in the analyzed schemes. The new VT taxonomy combines the Abstraction Level and Virtual Machine Type approaches, providing the reader with a means to visualize VTs. In doing so, the reader can locate the level of abstraction at which each VT is developed, in addition to the type of machine projected, whether it is a complete system or an execution environment for processes. The proposed taxonomy can be used in the academic environment to facilitate teaching processes or in the business environment to facilitate decision-making when implementing VTs.

Keywords: container, taxonomy, virtualization, virtual machine, virtualization technologies

RESUMEN

En la actualidad existe una proliferación de tecnologías de virtualización (VTs), las cuales constituyen una parte de la infraestructura fundamental y subyacente al tan popular cloud computing. Los interesados en las VTs se enfrentan a un volumen de información no unificada y con enfoques diversos acerca de los modos de operación, estructuras de clasificación e implicaciones del desempeño de estas tecnologías. Esto hace difícil decidir sobre el tipo de VT adecuado para un contexto particular. Por lo anterior, este trabajo realiza una revisión del estado del arte acerca de los modelos taxonómicos de las VTs. Metodológicamente, se realiza una revisión de la literatura para identificar modelos de clasificación de las VTs, reconociendo sus características y debilidades. Considerando lo anterior, se propone una nueva taxonomía de las tecnologías de virtualización, que responde a las debilidades identificadas en los esquemas analizados. La nueva taxonomía de VTs combina los enfoques de Nivel de Abstracción y Tipo de Máquina Virtual, proporcionando al lector un medio para visualizar las VTs. Al hacerlo, el lector puede ubicar el nivel de abstracción en el que se desarrolla cada VT, además del tipo de máquina proyectada, ya sea un sistema completo o un entorno de ejecución para procesos. La taxonomía propuesta puede ser utilizada en el ámbito académico para facilitar los procesos de enseñanza o en el ámbito empresarial para favorecer la toma de decisiones a la hora de implementar VTs.

Palabras clave: contenedor, máquina virtual, taxonomía, tecnologías de virtualización

---

[1] Systems and computing engineer. MSc in Open Software. Affiliation: PhD student in Engineering with emphasis on Computer Science, Universidad Tecnológica de Pereira, Pereira, Colombia. Professor at Universidad del Quindío. Armenia, Colombia. Email: lesepulveda@uniquindio.edu.co

[2] Systems engineer. PhD in Engineering, Universidad del Valle, Cali, Colombia. Affiliation: Universidad Tecnológica de Pereira, Colombia. Email: jchavar@utp.edu.co

[3] Systems engineer. PhD in Computer Information Science and Engineering, Universidad de Puerto Rico. Affiliation: Universidad del Valle, Cali, Colombia. Email: john.sanabria@correounivalle.edu.co

[4] Systems and computing engineer. PhD in Computer Science, Institut National Polytechnique de Grenoble (INPG), Grenoble, France. Affiliation: Computing and Systems Engineering Department, Universidad de los Andes, Bogotá, Colombia. Email: hcastro@uniandes.edu.co

[5] Mathematics and Computer Science, BS PhD in Computer Science, University of California, Berkeley, CA, USA. Affiliation: Department of Computer Science, Clarkson University, Potsdam, NY, USA. Email: jnm@clarkson.edu

Introduction

In recent years Virtualization Technology (VT) has been used to obtain benefits such as isolation, resource splitting, consolidation, security, migration, and ease of management (Varasteh and Goudarzi, 2017). VT builds an abstraction of applications and hardware in a virtual view (AbdElRahem *et al.*, 2016). This virtual view can be different from the physical

view of computing resources (Stallings, 2015). In addition, Silberschatz et al. (2014) note that VT allows an operating systems (OS) to run as an application within another OS.

VT includes emulation, which refers to the fact that there are differences between the physical and logical architectures used by virtualized processes. Thus, a virtual machine (VM) could use the same host architecture, a different emulated architecture, or a hybrid. In addition, the processes could use a physical architecture with modifications in order to make virtualization easier (paravirtualization).

VT allows creating one or several environments, i.e., many computers can look like a single large resource (resource aggregation) or, conversely, a single computer is considered as several instances of itself (resource splitting) (Hoopes, 2009; Silberschatz et al., 2014).

Unfortunately, the x86 computer architecture, despite being one of the most widely adopted architectures in the world, cannot be completely virtualized (Adams and Agesen, 2006). However, this situation can be solved through mechanisms and VT approaches that act at different levels of abstraction. The abstraction levels where VT takes place are the instruction set level, the hardware abstraction level (HAL), the OS level, the user library interface level, and the application level (Nanda and Chiueh, 2005).

The concept of virtualization was formalized in Goldberg's thesis (1973) and published in other works (Goldberg, 1974; Popek and Goldberg, 1974). In these studies, VMs were defined as "an efficient and isolated duplicate of the real machine" (Goldberg, 1973, p. 12). In later works, the term VM was expanded to include other kinds of virtualization, including applications at user level such as libraries, system calls, interfaces/services, system configurations, processes, and state files (Nanda and Chiueh, 2005).

The term virtual machine monitor (VMM) was also established by Popek and Goldberg (1974). It is a software layer that supports infrastructure using the resources of a lower level to create multiple independent and isolated VMs (Cafaro and Aloisio, 2011; Nanda and Chiueh, 2005). Similarly, Stallings (2015) determined that a VMM acts as an intermediary between the real machine and VMs. VMMs are also called hypervisors (Hoopes, 2009).

VT also brings financial benefits regarding returns on investment and reductions in the total cost of ownership of computer systems hardware (AbdElRahem et al., 2016). Moreover, VT uses less energy, which is related to the so-called green computing (Jing et al., 2013; Ranjith et al., 2017; Thathera et al., 2015) and plays an essential role in safeguarding the environment. Other goals of VT include increasing the scalability and availability of computing environments, as well as improving the administrative and security structures of the existing computational infrastructure (Hui and Seok, 2014; Kusnetzky, 2011).

Kampert (2010) indicates that the benefits of VTs have revolutionized data centers in the last two decades and have motivated the development of many variations to suit different use cases. In response, several attempts have been made in the academic literature to establish classification schemes for these variations of VT.

This paper reviews VT classification schemes and proposes a new taxonomy that responds to several identified weaknesses. This taxonomy improves and unifies the previous works in the classification of VTs in three ways: first, it combines and unifies approaches that consider the VM type with those that consider the level of abstraction; second, it updates classification approaches to include examples of VTs that have emerged more recently; third, it introduces a taxonomic key diagram based on our unified classification, which can guide the selection of VTs in either academic or production environments.

The remainder of this document comprises the following sections: VT classification schemes, The need for a new taxonomy, Proposal for a virtual machine taxonomy, Taxonomic key diagram, and Conclusions.

VT classification schemes

This section presents the results of a literature review by means of a systematic process of combined database search and manual reference tracking using the Snowball technique (Samireh and Claes, 2012). In this way, 12 classification schemes for VTs were identified, and their characteristics were highlighted. A paragraph is added at the end of each case which highlights the strengths and weaknesses of the classification scheme.

VT taxonomy by Nanda and Chiueh

Nanda and Chiueh (2005) classified VTs according to the following five levels of abstraction of a computer system.

Instruction set architecture (ISA) level

VTs emulate an ISA, allowing VMs to run as if they were running on hardware. When the ISA offered by this layer differs from the real ISA, this is called emulation.

- **Hardware Abstraction Layer (HAL)**: VTs use the same ISA as the host. Here, it is possible to perform independent OS installations, and its applications run as if they were executed in a real environment.

- **Operating System**: VTs work through an OS module to provide a virtualized system call interface.

- **Library Level**: User-level libraries control the communication between the applications and the rest of the system. VTs allow implementation as an Application Binary Interface (ABI) or an Application Programming Interface (API).

- **Programming Language Level**: VTs implement the virtualization layer as an application that can create a simplex or complex VM.

Although Nanda and Chiueh (2005) establish a way to classify VTs, they do not consider virtualization types at the same level of abstraction. Besides, it is necessary to include some VTs that have emerged in recent years.
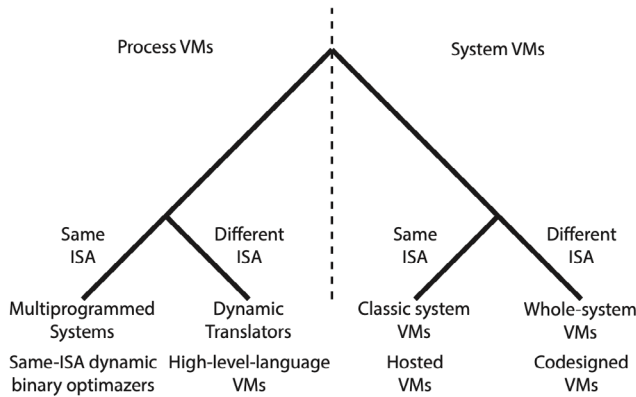
VM taxonomy by Smith and Nair

Figure 1. VM taxonomy proposed by Smith and Nair in 2005
Source: Smith and Nair (2005)

Smith and Nair (2005) presented a taxonomy with two main categories: Process VMs and System VMs. Furthermore, these categories divide VTs according to whether the ISA supported in the VM is the same as the underlying hardware (Figure 1).

Process VMs

This category describes an environment in the ABI interface or at the API level. It is called a *Multiprogrammed System* when it uses the same ISA; otherwise, it is called *Dynamic Emulator* or *Binary Translator*. The subcategories are described below:

- **Multiprogrammed Systems** are multiprogramming OSs that implement the management of timeshare access to the available underlying hardware resources. These systems use the same ISA and can handle multiple user processes 'simultaneously'. The OS delivers an individual VM for each user process that runs concurrently. One implementation in this context involves dynamic binary optimizers using the same ISA from the host system.

- **Dynamic Emulators** use process VMs to support compiled binary programs for an ISA different from the underlying hardware. This condition implies executing an emulation effort performed through interpretation, which can be relatively slow. However, this situation can be compensated when a software cache is implemented in order to deal with the overload.

System VMs

These are characterized by hosting one or several complete and independent OSs running simultaneously on the same hardware of the host computer, which results from the intermediation performed by the VMM. The subcategories of the system VMs are described below:

- **Classic System VMs** use the VMM and execute it directly on the bare hardware without an underlying OS. Thus, the VMM has real access to hardware resources and serves as an intermediary between the guest OSs and the hardware itself. In this case, the VMs are called *Hosted VMs*.

- **Whole-system VMs** provide virtualization of a complete environment, but guest systems use an ISA different from those used in the underlying hardware, unlike the previous category. In this case, the VMs are called *Codesigned VMs*.

Smith and Nair's study (2005) can be considered an essential basis for classifying VTs that provide a virtual environment for a complete system or processes. However, this work does not contemplate what was established by Nanda and Chiueh (2005) regarding the levels of abstraction. Another important aspect is that this classification model does not have a high degree of detail; it uses very general descriptions, without even including specific technologies. It is essential to consider that this study was carried out in 2005 and does not include subsequently developed technologies.

Virtualization taxonomy by the SCOPE Alliance

The SCOPE Alliance (2008) proposed an extension of the work carried out by Smith and Nair in 2005. The proposal includes more branching of the main categories and more examples of VTs (Figure 2).

This classification places type I and type II hypervisors as distinctions of the Classic OS VM model of System VMs that support the same ISA as the underlying hardware.
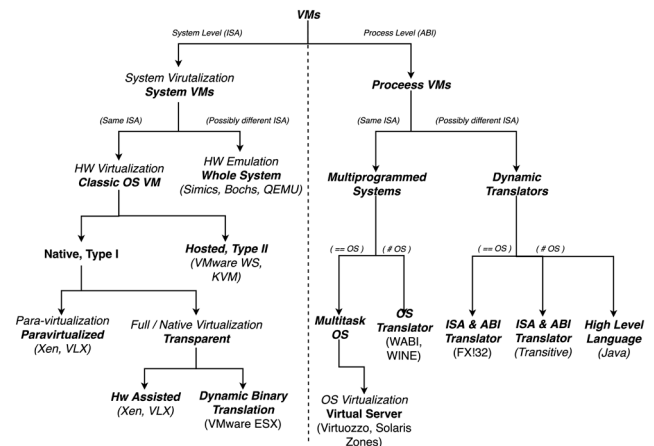

Figure 2. Virtualization taxonomy by the SCOPE Alliance
Source: SCOPE Alliance (2008)

Regarding the Process VMs category, this classification distinguishes between a Multiprogrammed System and Dynamic Translators. Multiprogrammed Systems are further classified depending on whether the OS provided by the underlying system is the same as the OS used by the application. If it uses the same OS, the category is called *Multitask OS*, which contains OS Virtualization. If the OS is different, it is called *OS Translator*. When the processes are based on a different ISA, they are called *Dynamic Translators*. Finally, if the VMs use the same OS, they are called *ISA & ABI Translators*; otherwise, they are called *High-level Language*.

Although the SCOPE Alliance's study (2008) contributes to complementing the taxonomy of VTs, the research does not contemplate aspects such as the levels of abstraction indicated by Nanda and Chiueh (2005). This situation gives rise to problems of conceptual inference, in which, for example, type I and type II hypervisors are perceived to be at the same level of abstraction. Additionally, according to the date of publication of the study, it is necessary to expand concepts and update VTs that have emerged in recent years.

Taxonomy of VTs by Kampert

Kampert (2010) presented his taxonomy of VTs using different virtualization techniques. This taxonomy uses the unified modeling language, as shown in Figure 3, where all elements are classes. For example, the class Domain is a superclass of the classes Server, Application, Desktop, Storage, and Network.

Kampert's taxonomy (2010) aims to cover the domains in a complete way in which the concept of virtualization takes place, including storage and network virtualization not seen in previous taxonomies. However, this taxonomy itself does not offer the level of granularity necessary to identify VTs in each of the specified domains.
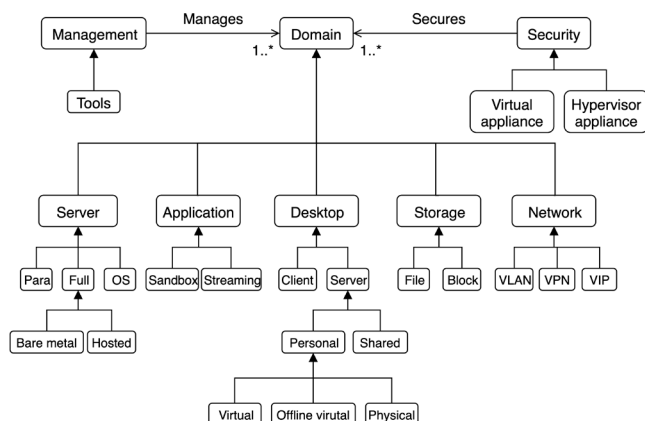

Figure 3. VT taxonomy by Pual Kampert
Source: Kampert (2010)

Virtualization model by Kusnetzky

Kusnetzky's virtualization model (2011) is composed of seven parts, five distributed in layers, and two arranged

parallel to the layers above Kampert (2010). Each part is briefly described below:

- **Access virtualization**: Many users share the same system.

- **Application virtualization**: Many applications run transparently on different OSs and hardware platforms.

- **Processing virtualization** allows the division or aggregation of resources.

- **Network virtualization** presents a logical view of the physical network elements.

- **Storage virtualization** hides the location and type of physical storage devices in which applications store their data.

- **Security for virtual environment** controls the access to the various elements of virtual media in order to protect them from unauthorized actions.

- **Management of the virtual environment** controls the available physical resources and the generated virtual environments.
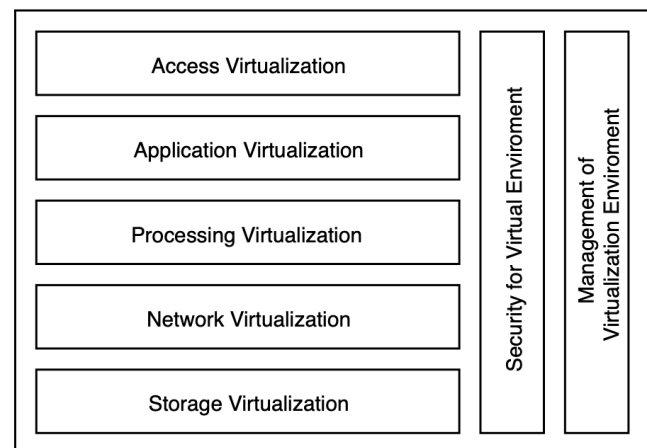
Figure 4. Kusnetzky's model of virtualization
Source: Kusnetzky (2011)

Kusnetzky presents a way to include categories for a range of virtualizable computational resources but does not provide details about the existing VTs in each layer of the model. In addition, the model does not differentiate between technologies of the same layer. For example, in Processing Virtualization, there is no evidence of a difference between the types of VMs present in type I or type II hypervisors.

Taxonomy of VTs by Pessolani

Pessolani *et al*. (2012) proposed their taxonomy of VTs with five main categories: 1) Hardware or System Virtualization, 2) Para-virtualization, 3) Virtualization based on OS, 4)

Virtualization at the Process or Application level, and 5) Virtualization of OS. Additionally, the main categories include subcategories that suggest a level of abstraction (Figure 5). These main categories are described below:

Figure 5. Taxonomy of VTs proposed by Pessolani *et al.*
Source: Pessolani *et al.* (2012)

- **Hardware or System Virtualization** puts the type I hypervisor on top of the hardware with its VMs and their respective guest OSs.

- **Paravirtualization** distributes its elements to Hardware or System Virtualization, but the guest OS is modified to be aware that it is virtualized.
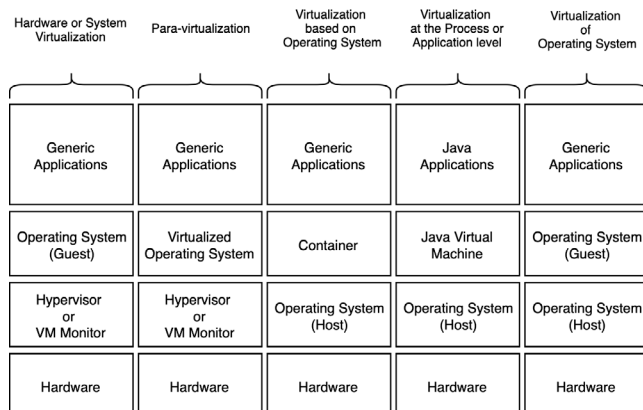
- **Virtualization based on OS** is founded on using independent workspaces called *containers*, which are based on the host OS.

- **Virtualization at the Process or Application level** uses an application on the host OS to provide a VM that allows the execution of processes based on it.

- **Virtualization of OS** needs a host OS to carry out the functions of a hypervisor in order to support the guest OSs, which in turn have their own completely independent applications.

Pessolani's taxonomy (2012) does not explicitly consider the levels of abstraction to which these technologies apply. In addition, it focuses only on the conceptual elements, leaving specific examples aside, nor does it establish a way to divide types of VMs within each main category.

Taxonomy of virtualization concepts by Pék

Pék *et al.* published a taxonomy of virtualization concepts in 2013. This work extends the studies by Smith and Nair (2005) an the SCOPE Alliance (2008) (Figure 6).

This taxonomy adds elements and several components, such as in the Hosted category, equivalent to type II hypervisors from the study by the SCOPE Alliance (2008). It also includes the Paravirtualization subcategory.
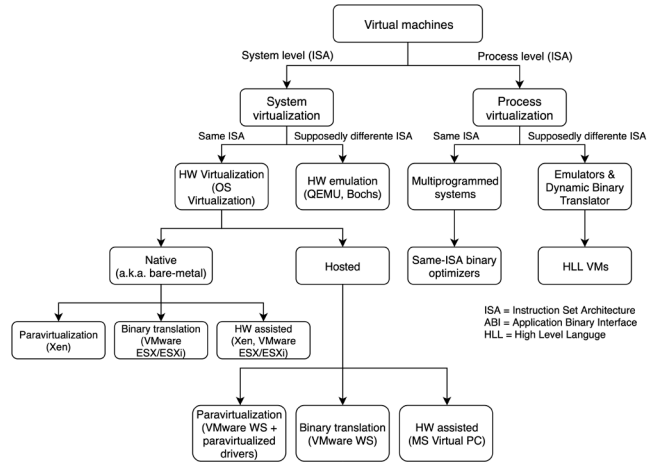
Figure 6. Taxonomy of virtualization concepts by Pék *et al.*
Source: Pék *et al.* (2013)

Although the study by Pék *et al.* (2013) presents an extension to some previous works, this taxonomy leaves a gap in the search for the details of VT categorization, since they do not contemplate the levels of abstraction at which VTs are implemented.

Taxonomy of virtualization by Ameen
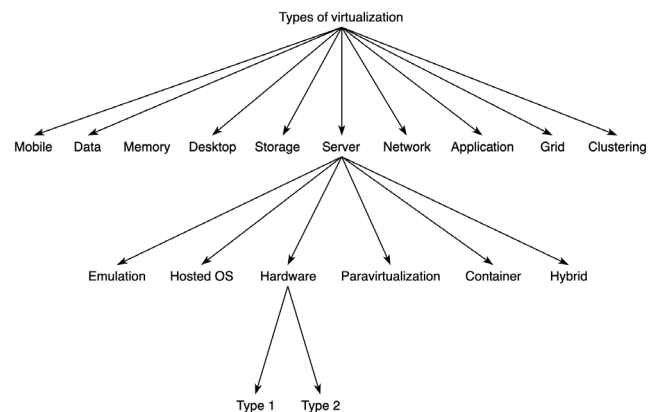
Figure 7. Taxonomy of virtualization by Ameen and Hamo
Source: Ameen and Hamo (2013)

Ameen and Hamo presented a taxonomy with three levels in 2013. (Figure 7). The first level contains the following ten categories:

- **Mobile** software that is embedded on a mobile phone to decouple the applications and data from the underlying hardware (VMware, 2022).

- **Data** abstracts the source of individual data items and provides a common data access layer for different data access methods such as SQL, XML, JDBC, File access, MQ, JMS, *etc.* (Mann, 2006).

- **Memory** adds an extra level of address translation to give each VM the illusion of having zero memory address space, as real hardware provides (Waldspurger, 2002).

- **Desktop** is the ability to display a graphical desktop from one computer system on another computer (von Hagen, 2008).

- **Storage** creates logical abstractions of physical storage systems (B. Li *et al.*, 2005).

- **Server** is a type of virtualization that allows running many OSs both in isolation and independence.

- **Network** provides an abstraction layer that can decouple the physical network equipment from the delivered business services over the network (Annapareddy, 2011).

- **Application** allows the user to run the application using local resources without installing the application in his system completely (Annapareddy, 2011; White and Pilbeam, 2010).

- **Grid** provides a way to abstract multiple physical servers from the application they are running (Mann, 2006).

- **Clustering** causes several locally connected physical systems to appear to the application and end-users as a single processing resource (Mann, 2006).

- The following describes the virtualization types at the second level of the taxonomy, which are derived from the Server category, as indicated by Ameen and Hamo (2013):

- **Emulation** is a virtualization method in which you can create a complete hardware architecture in software (Ameen and Hamo, 2013).

- **Hosted OS** uses software-only. The hypervisor is over an OS (Ameen and Hamo, 2013; von Hagen, 2008).

- **Hardware** the hypervisor is assisted by processor hardware such as AMD-V or Intel VT-x processor virtualization technologies (von Hagen, 2008).

- **Paravirtualization,** according to Ameen and Hamo (2013, p. 7), is "a technique in which the guest OS includes modified (para-virtualized) I/O drivers for the hardware".

- **Container** is a kernel-layer abstraction and refers to techniques in which the abstraction technology is built directly into the OS kernel rather than having a separate hypervisor layer (Ameen and Hamo, 2013; Q. Lin *et al.*, 2012).

- **Hybrid** is a combination of Full Virtualization and Paravirtualization that uses input/output (I/O) acceleration techniques (White and Pilbeam, 2010).

At the third level of the taxonomy are the type I and type II hypervisor categories derived from Server/Hardware.

Ameen and Hamo's taxonomy (2013) is closely related to the works by Kampert (2010) and Kusnetzky (2011). Furthermore, it presents a classification scheme through a three-level hierarchical structure. However, although this graphical representation is interesting, it is unbalanced, since it focuses only on detailing the Server category.

Taxonomy of VTs by Abdulhamid

Abdulhamid *et al.* (2014) presented a taxonomy focused on cloud computing (Abdekhoda *et al.*, 2019; Fareghzadeh *et al.*, 2019) and based on the work by Sahoo *et al.* (2010), which includes categories such as Full Virtualization, OS-Layer Virtualization, Hardware-Layer Virtualization, Paravirtualization, Application Virtualization, Resource virtualization, and Storage virtualization. In addition, this work adds the Grid Virtualization and Cloud Virtualization categories (Figure 8).
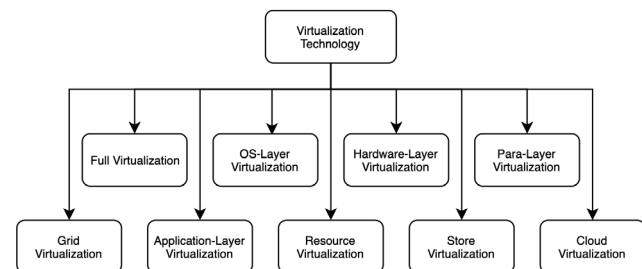
Figure 8. Taxonomy of VTs by Abdulhamid
Source: Abdulhamid *et al*. (2014)

Some categories have already been described. Below is a brief description of the new ones.

- **Grid Virtualization** focuses on the virtualization of grid resources either for a virtual organization (VO) or for a Virtual Organization Cluster (Abdulhamid *et al.*, 2014).

- **Cloud Virtualization** or **Cloud Computing** (Sehgal and Bhatt, 2018) enables on-demand provisioning of virtual resources through the Web, as well as applying the concept of pay-per-use. In this category, the VTs form cloud computing services, provisioning virtual resources to customers on demand. (Abdulhamid *et al.*, 2014; Aceto *et al.*, 2013).

Although the taxonomy by Abdulhamid *et al*. (2014) shows two levels, only one level can be observed which comprises its nine categories from a hierarchical perspective. On the other hand, the description of each category lacks details and examples of VTs.

Types of VMs by Li

X.-F. Li (2016) presented his work with four types of VMs:

- **Type 1**: The Full ISA VM allows full ISA-level emulation or virtualization. The OS and its applications can run on top of the VM as a real machine (X.-F. Li, 2016).

- **Type 2**: The ABI VM allows ABI-level emulation of the processes in the guest OS. These applications can run in conjunction with native ABI applications (X.-F. Li, 2016).

- **Type 3**: The Virtual ISA VM provides a runtime engine for applications encoded in the virtual ISA to run on it (X.-F. Li, 2016).

- **Type 4**: The Language VM gives a runtime engine that runs programs written in a guest language (source). The runtime engine needs to interpret or translate the program.

Although the study by X.-F. Li (2016) presented a four-type classification scheme, it does not indicate a hierarchical structure that clarifies how they relate. It also does not have a supporting graph to facilitate understanding. This work does not contemplate many of the categories indicated in other previously presented taxonomies.

Taxonomy of VMs by Bugnion

Bugnion (2017) presented a structure with two levels that shows the concepts related to VMs. The first level is related to abstraction, and it includes the following categories: Language-based VM, System-level VM, and Lightweight VM. The second level is related to the platform, and it includes two categories derived from System-level VM, which are called *Machine Simulator* and *Hypervisor*. The latter is divided into Bare-metal Hypervisor (type I) and Hosted Hypervisor (type II) (Figure 9).
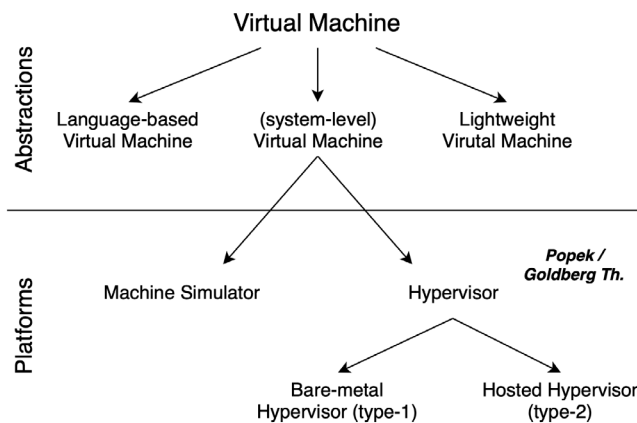

Figure 9. Taxonomy of VMs and the platforms that run them presented by Bugnion
Source: Bugnion et al. (2017)

- **Language-based VM** refers to any managed language runtime environment such as the Java VM, Microsoft Common Language Runtime, and JavaScript engines embedded in browsers.

- **Lightweight VM** refers to software mechanisms to ensure that applications run directly on the processor as securely isolated from other environments and the underlying OS.

- **System-level VM** refers to the computer environment that resembles the hardware of a computer, so that the VM can run an OS and its applications in complete isolation from the other VMs and the rest of the environment. This category includes two Hypervisor types (type I and type II).

Bugnion's work (2017) is less a taxonomy than a book focusing on the core architectural support provided by hardware to run VMs efficiently.

The need for a new taxonomy

The taxonomies described above have many elements that contribute to the classification of VTs. However, in each of these classification schemes, some aspects that need improvement have been identified. Each scheme offers a taxonomic approach, such as a) Abstraction Level, b) Type of VM, and c) Virtualization Domains. Table 1 summarizes the classification schemes analyzed in this paper by author, year, and taxonomic approach, which were published between 2005 and 2017. It is worth noting that we found no taxonomies published between 2018 and 2021.

The Type of VM is the most popular approach, as demonstrated by CS2, CS3, CS6, and ACS7. On the other hand, CS4 and CS5 take a different perspective; their objective is to consider, in a general way, the largest number of technological domains in which it is possible to carry out virtualization processes, hence the name Virtualization Domain. Some taxonomies have a dual approach; for example, CS8 and CS9 combine the Type of VM with the Virtualization Domain, and CS11 combines the Type of VM with the Abstraction Level. Lastly, CS1 and CS10 consider the Abstraction Level approach as fundamental for the categorization of VTs. These differences in viewing VTs can confuse the community interested in this field when reading different authors.

Table 1. Summary of classification schemes

Classification Schemes (CS)		
ID	*Author(s)*	*Taxonomy approach*
CS1	Nanda and Chiueh (2005)	Abstraction Level
CS2	Smith and Nair (2005)	Type of VM
CS3	SCOPE Alliance (2008)	Type of VM
CS4	Kampert (2010)	Virtualization Domain
CS5	Kusnetzky (2011)	Virtualization Domain
CS6	Pessolani et al. (2012)	Type of VM
CS7	Pék et al. (2013)	Type of VM
CS8	Ameen and Hamo (2013)	Type of VM and Virtualization Domain
CS9	Abdulhamid et al. (2014)	Type of VM and Virtualization Domain
CS11	X.-F. Li (2016)	Abstraction Level
CS12	Bugnion (2017)	Type of VM and Abstraction Level

Source: Authors

Therefore, there is a need for a new taxonomy that provides a unified, organized, and current view of VTs. Therefore, this paper makes the following contributions:

- A review of the literature with the identification, analysis, and comparison of 12 classification VT schemes (Table 1).

- A proposal for a new VM taxonomy. This work identified, expanded, and combined different studies, offering a single view of multiple concepts such as the Types of VMs and their corresponding Abstraction Level. The taxonomy includes examples of older VTs in order to provide a reference factor to those who have some knowledge about them. It also includes examples of new VTs that have gained wide recognition in the industry and academia, such as those related to containers. The taxonomy is also intended to be an instrument to support the pedagogical processes within the academic community with interests in VTs (Figure 10).

- A taxonomic key diagram that facilitates the visualization of the technological ecosystem that surrounds this topic and consequently helps the academic and industrial community in the decision-making processes regarding the selection of VTs (Figure 11).

Proposal for a virtual machine taxonomy

This section presents a new taxonomic proposal for virtualization technologies. This taxonomy considers the 12 studies reviewed in this research, but it focuses mainly on studies such as CS1, CS2, CS3, CS7, and CS11 (Figure 10). The proposal presents an innovative contribution that integrates the Abstraction Level and Type of VM taxonomic approaches. In addition, it contributes by extending the examples of VTs, which are placed in the diagram representing the new taxonomy. The first approach considers the layers of the classical architecture of a computer system and makes it possible to visualize the VTs according to the level of abstraction they occupy at the time of execution. The second approach considers the types of virtual machines, be it complete systems or execution environments for processes. The description of the taxonomy is shown below, making a cross-analysis between the two approaches.

Approach 1: abstraction layers

The first approach of this taxonomy uses the abstraction layers in a computer system, such as the Hardware Abstraction Layer (HAL), the Operating System (OS), the Application Binary Interface (ABI), the Application Programming Interface (API), Type I/Type II Hypervisors, and Libraries. In Figure 10, the labels located on the left side indicate the abstraction level, and they are the title of rectangular structures with horizontal distribution in the taxonomy. With these layers, the taxonomy makes it possible to locate

VTs depending on the level at which they take place. Thus, the reader can quickly infer aspects such as the dependence or not of an underlying OS, as well as determine the number of intermediaries involved in the virtualization process. Furthermore, this information allows inferring the possible performance of these technologies. The abstraction layers are described below from bottom to top.

Hardware Abstraction Layer (HAL)

HAL includes those VTs that are placed directly on top of the hardware. This arrangement is also known as *BareMetal* and is identified by the absence of intermediaries between the VMs and the underlying hardware, suggesting a higher performance for the set of VTs placed here. This layer contains the category called *Type I Hypervisor* and can have several types of VTs.

Operating System (OS)

This layer contains the sublayers Application Binary Interface (ABI) and Application Programming Interface (API). In the ABI sublayer, the VTs use the OS as an intermediary to access the underlying hardware. The virtualization is carried by OS calls and uses Dynamic Binary Translation, Type II Hypervisors, or Libraries. This situation suggests that the VTs may present degradation in performance due to intermediation costs between the different environments. VTs implement virtualization based on high-level languages, offering portability in the API sublayer, as APIs support multiple hardware and software platforms. However, this sublayer has considerable degradation given the multiple interpreters between the VTs and the hardware functions.

Approach 2: Type of VM

The second approach of this taxonomy considers VTs according to their type: System VMs or Process VMs. System VMs contain a whole OS (guest OS) within their virtual environment. On the other hand, Process VMs use the host OS as an intermediary between the virtual environment and the actual hardware.

System VMs

This type of virtualization has two categories. The first is *Classic System VMs* and is characterized by the fact that the host and guest OSs have the same ISA. The second category is Whole-System VMs and is characterized by the host OS and guest OS having a different ISA.

- **Classic System VMs**: This category is known as *Hardware Virtualization* and includes two subcategories: the first one is Native VMs, and the second one is Hosted VMs. It is important to note that each subcategory takes place at different levels of abstraction.

  - **Native VMs**: This VT is also known as *Type I Hypervisor* and corresponds to the HAL abstraction

level. It uses a software layer directly on top of the hardware. It also presents a subdivision, as shown below:

- **Transparent** indicates that the OS inside the VM is unaware of its virtualization state and is divided into the following types:

  - **Hardware-Assisted** virtualization involves the use of physical components to facilitate the management of VMs. Examples of this are: KVM (2021), Microsoft Hyper-V (Jason *et al.*, 2009; Syrewicze and Siddaway, 2018), Xen (Xen Cambridge, 2022), VLX (Armand and Gien, 2009), and VMware ESX/ESXi (Z. Li, 2021; VMware, 2022).

  - **Dynamic Binary Translation** implies that the Type I Hypervisor catches and inspects the code of each guest OS request to convert it into a proper request towards the underlying hardware, *e.g.,* VMware ESX/ESXi (Z. Li, 2021; VMware, 2022) and XtratuM (Wessman *et al.*, 2021; Xtratum, 2022) .

  - **Para-virtualized** is also known as *Operating System-Assisted Virtualization* and refers to efficient communication between the guest OS and the hypervisor. This implies modifying the guest OS to be aware of virtualization and to take advantage of that condition. Examples of this are: Xen (Barham *et al.*, 2003; Matthews *et al.*, 2008; Xen Cambridge, 2022; Xen Project, 2022), VLX (Armand and Gien, 2009), KVM (Abeni and Faggioli, 2020; KVM, 2021), and VMware VMI (VMware, 2022).

- **Hosted VMs**: This subcategory is also known as *Type 2 Hypervisors,* corresponds to the ABI abstraction level, and uses a layer of software on a Host OS. It presents the same subdivision and functions of the **Native VMs** category, so only examples of VTs will be listed below.

  - **Transparent**

    - **Hardware-Assisted**: VMware Workstation/ Fusion (VMware, 2022), Parallels Desktop (Parallels, 2021), and Oracle VirtualBox (Oracle, 2021b).

    - **Dynamic Binary Translation**: VMware Workstation/Fusion (VMware, 2022; Z. Li, 2021), Microsoft Virtual PC (Honeycutt, 2003), Plex86 (2021), Parallels Desktop (Parallels, 2021), and Oracle VirtualBox (Oracle, 2021b).

- **Para-virtualized**: VMware Workstation, with the addition of the corresponding para-virtualization driver to the network in the guest OS (El-Anani, 2021; VMware, 2022).

- **Whole system VMs**: This category is called *Hardware Emulation* and presents an ISA different from the underlying hardware. It takes place at the API abstraction level, evidencing a preexisting OS on which emulation can occur. The subcategory is called *Dynamic Binary Translation* and features VTs such as QEMU (Díaz *et al.*, 2021; QEMU, 2021), Simcs (Magnusson *et al.*, 2002), Bochs (Bochs, 2021), Rosetta (Apple Inc, 2009), and BIRD (Nanda *et al.*, 2006).

Process VMs

This type of virtualization also has the same two categories as System VMs, depending on whether the host OS and guest OS have the same ISA. When the ISA is the same, the category is called *Multiprogrammed Systems*; otherwise, the category is called *Dynamic Translators*. Both categories are located at the OS layer.

- **Multi-programmed systems**: In this category, the VTs share the OS among many processes, generating independent execution spaces for each one. This generates the illusion that, for a moment, a process is an exclusive executor in the system. This category is then divided into two, depending on whether there is an OS. When the same OS is projecting, the category is called *Multitasking OS*; otherwise, it is called *OS Translators*.

  - **Multitasking OS** is divided into Operating System Virtualization and Same-ISA Dynamic Binary Optimizer.

    - **Operating System Virtualization** happens at the ABI abstraction level and uses system calls for interaction with the underlying hardware. It uses the preexisting OS, and it allows generating independent workspaces for the processes. This type of virtualization is booming and is often known as *lightweight virtualization*, *container-based*, or simply *containers* (Tfrifonov, 2018). For example: FreeBSD Jails (Biederman, 2006; Kamp and Watson, 2000) (Ryding and Johansson, 2020) , Solaris Zones/Containers (Oracle, 2021a), OpenVZ (2021), Linux-VServer (Linux-VServer, 2018), AIX Workload Partitions WPAR (Gibson, 2007), Parallels Virtuozzo Containers (Virtuozzo, 2022), Denali (Whitaker *et al.*, 2002), Google Native Client (Yee *et al.*, 2009), Vx32 (Ford and Cox, 2008), User-Mode Linux (Dike, 2006; User-Mode Linux, 2022), Minix Over Linux (Pessolani and Jara, 2011), Ensim (2022), LXC (Canonical Ltd., 2021), Docker (Docker, 2022; Ryding and Johansson,

2020), and Singularity (Chang *et al.*, 2021; Sylabs.io, 2022).

- **Same-ISA Dynamic Binary Optimizers** are translators implemented in software that perform optimized translations of binary code with an equal ISA. Their operation is transparent, and even the system's native binaries can be optimized. An example of this is the Dynamo project (Bala *et al.*, 2011).

- **Operating System Translators** allow the execution of applications built for OSs different

from the system host, *e.g.*, WINE (Jones *et al.*, 2018; Wine, 2022), WABI (Oracle, 2018), Lxrun (2022), Visual MainWin (Fisher *et al.*, 2006), and Vcuda (Balis *et al.*, 2021; S. Lin *et al.*, 2009).

- **Dynamic Translators**: Dynamic ISA translators can support processes that use the same host OS, *e.g.*, FX!32 (Chernoff *et al.*, 1998). It can also be the case of dynamic ISA translations for processes that use a different OS than the host, such as Transitive (eWeek, 2008; IBM, 2008). For the above cases, the translation occurs at the Library level. It can also be the case of dynamic
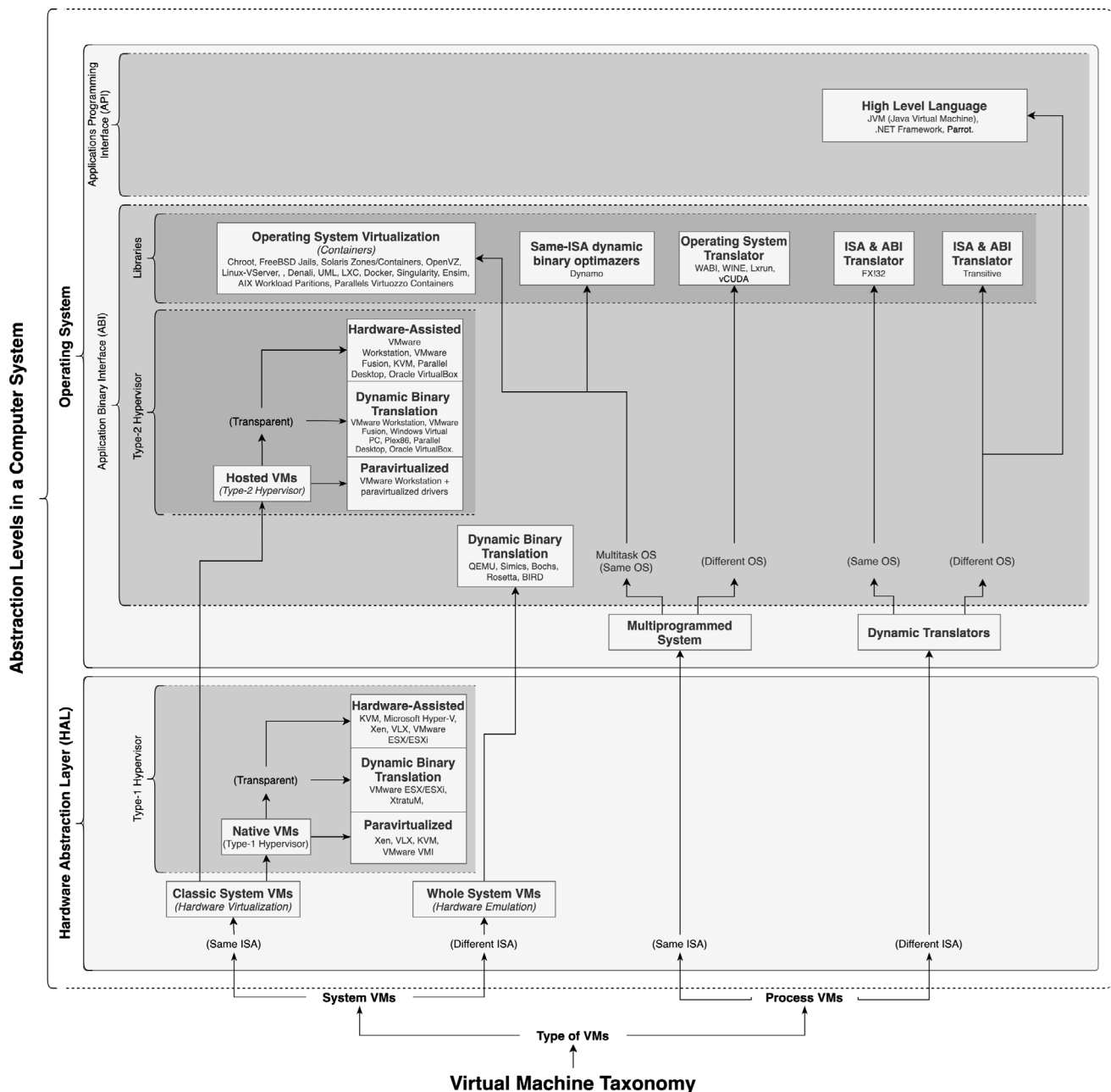

Figure 10. Proposal for a new virtual machine taxonomy
Source: Authors.

ISA translators for processes using a different OS and acting through high-level languages such as Java Virtual Machine (JVM) (Lindholm *et al.*, 1997; Beronić *et al.*, 2021), the Microsoft .NET common language infrastructure (CLI) (Thai and Lam, 2003), and Parrot (2022).

Taxonomic key diagram

This work also proposes a taxonomic key diagram to guide decision-making about the technologies related to VMs, as indicated in the proposed taxonomy (Figure 11). The diagram uses a set of questions, which, depending on each possible answer, establishes a path that leads to identifying a VT defined in the aforementioned taxonomy. For example, the diagram can be used by asking the question 'Do you need to virtualize the entire system or just some of its processes?' If the complete system needs to be virtualized, the following question will inquire about the specific need. If the desired virtual system needs an ISA different from the underlying hardware, the answer from the taxonomic key is the Dynamic Binary Translation category, *e.g.*, QEMU, Simics, and Bochs.

Conclusions

A review of literature on the different classification schemes for virtualization technologies proposed since 2005. These schemes have been introduced using a timeline that has allowed the identification of the following taxonomic approaches: Abstraction Level, Virtual Machine Type, and Virtualization Domains.

When performing the analysis of each classification scheme, it was possible to identify weaknesses. These include the presence of a single taxonomic approach in each scheme and the lack of topicality considering the date of publication, as well as the absence of the details on the inclusion of technologies.

The proposed taxonomy responds to the needs identified in the analyzed classification schemes. As a result, the proposal combines the Abstraction Level and Virtual Machine Type approaches, giving the reader a means of visualizing the virtualization technologies relating to virtual machines. By doing so, the reader is always aware of the level of abstraction at which each technology takes place, in
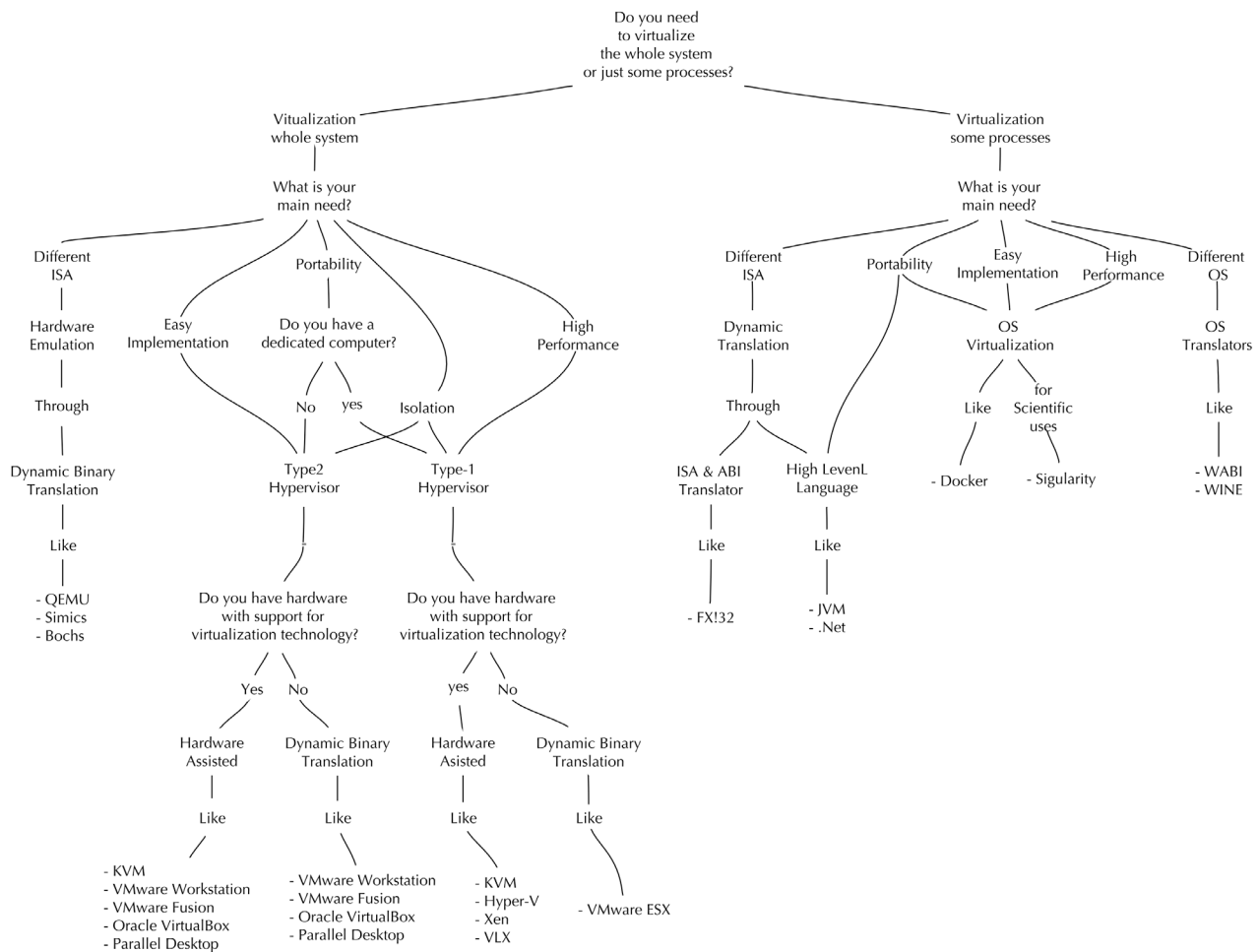

Figure 11. Taxonomic key diagram to select VTs
Source: Authors

addition to the type of machine projected, be it a complete system or an execution environment for processes.

The proposed taxonomy can be used in academic contexts to facilitate teaching and learning or in the business field to favor decision-making when implementing technologies related to virtual machines.

The taxonomy allows for the classification of VTs present in more than one conceptual branch, as these tools evolve, meeting the needs of more than one approach by themselves or using extensions.

Finally, a taxonomic key diagram has been created for use by the industry in order to aid the selection of virtualization technologies.

References

Abdekhoda, M., Asadi, Z., and Nadrian, H. (2019). Cloud computing services adoption among higher education faculties: Development of a standardized questionnaire. *Education and Information Technologies, 25*(1), 175-191. https://doi.org/10.1007/s10639-019-09932-0

AbdElRahem, O., Bahaa-Eldin, A. M., and Taha, A. (2016, December 20-21). *Virtualization security: A survey* [Conference presentation]. 2016 11th International Conference on Computer Engineering & Systems (ICCES), Cairo, Egypt. https://doi.org/10.1109/ICCES.2016.7821971

Abdulhamid, S. M., Latiff, M. S. A., and Bashir, M. B. (2014). On-demand grid provisioning using cloud infrastructures and related virtualization tools: A survey and taxonomy. *arXiv preprint*. https://doi.org/10.48550/arXiv.1402.0696

Abeni, L., and Faggioli, D. (2020). Using Xen and KVM as real-time hypervisors. *Journal of Systems Architecture, 106*, 101709. https://doi.org/10.1016/j.sysarc.2020.101709

Aceto, G., Botta, A., de Donato, W., and Pescapè, A. (2013). Cloud monitoring: A survey. *Computer Networks, 57*(9), 2093-2115. https://doi.org/10.1016/j.comnet.2013.04.001

Adams, K., and Agesen, O. (2006). A comparison of software and hardware techniques for x86 virtualization. *ACM SIGARCH Computer Architecture News, 34*(5), 2-13. https://doi.org/10.1145/1168919.1168860

Ameen, R. Y., and Hamo, A. Y. (2013). Survey of server virtualization. *arXiv preprint*. https://doi.org/10.48550/arXiv.1304.3557

Annapareddy, N. D. R. (2011). *An approach to storage virtualization*. Texas A & M University-Kingsville.

Apple Inc. (2009). *Universal binary programming guidelines*. https://web.archive.org/web/20120327121744/http://developer.apple.com/legacy/mac/library/documentation/MacOSX/Conceptual/universal_binary/universal_binary.pdf

Armand, F., and Gien, M. (2009, January 10-13). *A practical look at micro-kernels and virtual machine monitors* [Conference presentation]. 2009 6th IEEE Consumer Communications and Networking Conference, Las Vegas, NV, USA.. https://doi.org/10.1109/CCNC.2009.4784874

Bala, V., Duesterwald, E., and Banerjia, S. (2011). Dy-namo: a transparent dynamic optimization system. *ACM SIGPLAN Notices, 46*(4), 41-52. https://doi.org/10.1145/1988042.1988044

Balis, B., Antonelli, L., Bracciali, A., Gruber, T., Hyun-Wook, J., Kuhn, M., Scott, S., Unat, D., Wyrzykowski, R., and Eiling, N. (2021, August 24-25). *An open-source virtualization layer for CUDA applications* [Conference presentation]. Euro-par 2020: Parallel Processing, Warsaw, Poland.

Barham, P., Dragovic, B., Fraser, K., Hand, S., Harris, T., Ho, A., Neugebauer, R., Pratt, I., and Warfield, A. (2003). Xen and the art of virtualization. In ACM (Eds.), *Proceedings of the Nineteenth ACM Symposium on Operating Systems Principles* (pp. 164-177). ACM. https://doi.org/10.1145/945445.945462

Beronić, D., Pufek, P., Mihaljević, B., and Radovan, A. (2021). *On analyzing virtual threads – A structured concurrency model for scalable applications on the JVM* [Conference presentation]. 2021 44th International Convention on Information, Communication and Electronic Technology (MIPRO). Opatija, Croatia. https://doi.org/10.23919/MIPRO52101.2021.9596855

Biederman, E. W. (2006). *Multiple instances of the Global Linux Namespaces* [Conference presentation]. Linux Symposium, Ottawa, Ontario, Canada.

Bochs (2021). *bochs. The cross Platform IA-32 Emulator*. https://bochs.sourceforge.io

Bugnion, E., Nieh, J., Tsafrir, D., and Martonosi, M. (2017). *Hardware and software support for virtualization*. Morgan & Claypool. https://doi.org/10.2200/S00754ED1V01Y201701CAC038

Cafaro, M., and Aloisio, G. (2011). Grids, clouds, and virtualization. In M. Cafaro and G. Aloisio (Eds.), *Grids, Clouds and Virtualization* (pp. 1-21). Springer.

Canonical Ltd. (2021). *Container and virtualization tools*. https://linuxcontainers.org

Chang, Y. T. S., Heistand, S., Hood, R., and Jin, H. (2021, November 14). *Feasibility of running singularity containers with hybrid MPI on NASA high-end computing resources* [Conference presentation]. 2021 3rd International Workshop on Containers and New Orchestration Paradigms for Isolated Environments in HPC (CANOPIE-HPC), St. Louis, MO, USA. https://doi.org/10.1109/CANOPIEHPC54579.2021.00007

Chernoff, A., Herdeg, M., Hookway, R., Reeve, C., Rubin, N., Tye, T., Bharadwaj Yadavalli, S., and Yates, J. (1998). FX! 32: A profile-directed binary translator. *IEEE Micro, 18*(2), 56-64. https://doi.org/10.1109/40.671403

Díaz, E., Mateos, R., Bueno, E. J., and Nieto, R. (2021). Enabling parallelized-QEMU for hardware/software co-simulation virtual platforms. *Electronics, 10*(6), 759. https://doi.org/10.3390/electronics10060759

Dike, J. (2006). *User mode linux* (vol. 2). Prentice Hall Englewood Cliffs.

Docker (2022). *Docker*. https://www.docker.com

El-Anani, B. R. (2021). *Server virtualization: Para- and full virtualization: XenServer vs. KVM*. https://www.theseus.fi/handle/10024/507277

Ensim (2022). *Ensim*. http://www.ensim.com

eWeek. (2008). *IBM acquiring transitive to increase virtualization capabilities of power systems*. https://www.eweek.com/virtualization/ibm-acquiring-transitive-to-increase-virtualization-capabilities-of-power-systems/

Fareghzadeh, N., Seyyedi, M. A., and Mohsenzadeh, M. (2019). Toward holistic performance management in clouds: taxonomy, challenges and opportunities. *Journal of Supercomputing, 75*(1), 272-313. http://doi.org/10.1007/s11227-018-2679-9

Fisher, M., Sharma, S., Lai, R., and Moroney, L. (2006). *Java EE and .NET interoperability: Integration strategies, patterns, and best practices*. Prentice Hall Professional.

Ford, B., and Cox, R. (2008). *Vx32: Lightweight User-level Sandboxing on the x86* [Conference presentation]. USENIX Annual Technical Conference. https://www.usenix.org/legacy/events/usenix08/tech/full_papers/ford/ford.pdf

Gibson, C. (2007). WPAR Power AIX workload partition explained. *IBM Systems Magazine*. http://www.ibmsystemsmag.com/opensystems/december07/coverstory/18606p1.aspx

Goldberg, R. P. (1973). *Architectural principles for virtual computer systems*. Defense Technical Information Center.

Goldberg, R. P. (1974). Survey of virtual machine research. *Computer, 7*(6), 34-45. https://doi.org/10.1109/MC.1974.6323581

Honeycutt, J. (2003). *Microsoft virtual PC 2004 technical overview*. Microsoft.

Hoopes, J. (2009). *Virtualization for security: Including sandboxing, disaster recovery, high availability, forensic analysis, and honeypotting*. Syngress.

Hui, L. Y., and Seok, K. H. (2014). A study of savings of power consumption and server space through integrated virtualization of UNIX servers. *International Journal of Software Engineering and Its Applications, 8*(5), 219-230. http://dx.doi.org/10.14257/ijseia.2014.8.5.17

IBM (2008). *Transitive*. https://www-03.ibm.com/press/us/en/pressrelease/26106.wss

Jason, K., Velte, A., and Velte, T. (2009). *Microsoft virtualization with Hyper-V*. McGraw-Hill, Inc.

Jing, S.-Y., Ali, S., She, K., and Zhong, Y. (2013). State-of-the-art research study for green cloud computing. *The Journal of Supercomputing, 65*(1), 445-468. https://doi.org/10.1007/s11227-011-0722-1

Jones, M., Kepner, J., Orchard, B., Reuther, A., Arcand, W., Bestor, D., Bergeron, B., Byun, C., Gadepally, V., Houle, M., Hubbell, M., Klein, A., Milechin, L., Mullen, J., Prout, A., Rosa, A., Samsi, S., Yee, C., and Michaleas, P. (2018, September 25-27). *Interactive launch of 16,000 Microsoft Windows Instances on a supercomputer* [Conference presentation]. 2018 IEEE High Performance extreme Computing Conference (HPEC), Waltham, MA, USA. https://doi.org/10.1109/HPEC.2018.8547782

Kamp, P.-H., and Watson, R. N. (2000). *Jails: Confining the omnipotent root* [Conference presentation]. 2nd International SANE Conference. https://papers.freebsd.org/2000/phk-jails/

Kampert, P. (2010). *A taxonomy of virtualization technologies*. [Master's thesis, Delft University of Technology]. https://d1rkab7tlqy5f1.cloudfront.net/TBM/Over%20faculteit/Afdelingen/Engineering%20Systems%20and%20Services/People/Professors%20emeriti/Jan%20van%20den%20Berg/MasterPhdThesis/Masters_Thesis_Paulus_Kampert_August_2010-2.pdf

Kusnetzky, D. (2011). *Virtualization: A manager's guide*. O'Reilly Media, Inc.

KVM (2021). *Kernel Virtual Machine*. https://www.linux-kvm.org

Li, B., Shu, J., and Zheng, W. (2005). Design and implementation of a storage virtualization system based on SCSI target simulator in SAN. *Tsinghua Science and Technology, 10*(1), 122-127. https://doi.org/10.1016/S1007-0214(05)70018-3

Li, X.-F. (2016). *Advanced design and implementation of virtual machines*. CRC Press.

Li, Z. (2021, November 12-14). *Comparison between common virtualization solutions: VMware Workstation, Hyper-V and Docker* [Conference presentation]. 2021 IEEE 3rd International Conference on Frontiers Technology of Information and Computer (ICFTIC), Greenville, SC, USA. https://doi.org/10.1109/ICFTIC54370.2021.9647226

Lin, Q., Qi, Z., Wu, J., Dong, Y., and Guan, H. (2012). Optimizing virtual machines using hybrid virtualization. *Journal of Systems and Software, 85*(11), 2593-2603. https://doi.org/10.1016/j.jss.2012.05.093

Lin, S., Hao, C., and Jianhua, S. (2009, May 23-29). *vCUDA: GPU accelerated high performance computing in virtual machines* [Conference presentation]. 2009 IEEE International Symposium on Parallel & Distributed Processing, Rome, Italy. https://doi.org/10.1109/IPDPS.2009.5161020

Lindholm, T., Yellin, F., Bracha, G., and Buckley, A. (1997). *The Java virtual machine specification*. Addison-Wesley.

Linux-VServer (2018). *Linux-VServer*. http://www.linux-vserver.org

Lxrun (2022, 2008/03/09). *Official lxrun web site*. https://web.archive.org/web/20151025205205/http://www.ugcs.caltech.edu/~steven/lxrun/

Magnusson, P. S., Christensson, M., Eskilson, J., Forsgren, D., Hallberg, G., Hogberg, J., Larsson, F., Moested, A., and Werner, B. (2002). Simics: A full system simulation platform. *Computer, 35*(2), 50-58. https://doi.org/10.1109/2.982916

Mann, A. (2006). *Virtualization 101: Technologies, benefits, and challenges*. Enterprise Management Associates, Inc.

Matthews, J. N., Dow, E. M., Deshane, T., Hu, W., Bongio, J., Wilbur, P. F., and Johnson, B. (2008). *Running Xen: A hands-on guide to the art of virtualization*. Prentice Hall PTR.

Nanda, S., and Chiueh, T.-C. (2005). *A survey on virtualization technologies*. Stony Brook University. http://comet.lehman.cuny.edu/cocchi/CMP464/papers/VirtualizationSurveyTR179.pdf

Nanda, S., Li, W., Lam, L.-C., and Chiueh, T.-C. (2006). *BIRD: Binary interpretation using runtime disassembly* [Conference presentation]. 2006 International Symposium on Code Generation and Optimization, New York, NY, USA. https://doi.org/10.1109/CGO.2006.6

OpenVZ (2021). *OpenVZ*. https://openvz.org

Oracle (2018). *WABI* https://docs.oracle.com/cd/E19957-01/802-6306/802-6306.pdf

Oracle (2021a). *Oracle Solaris Zones*. https://docs.oracle.com/cd/E18440_01/doc.111/e18415/chapter_zones.htm#OPCUG426

Oracle (2021b). *Oracle Virtual Box*. https://www.oracle.com/virtualization/virtualbox/.

Parallels (2021). *Parallels*. https://www.parallels.com

Parrot (2022). *Parrot*. http://www.parrot.org

Pék, G., Buttyán, L., and Bencsáth, B. (2013). A survey of security issues in hardware virtualization. *ACM Computing Surveys (CSUR), 45*(3), 40. https://doi.org/10.1145/2480741.2480757

Pessolani, P., and Jara, O. (2011, November 7-11). *Minix over Linux: A user-space multiserver operating system* [Conference presentation]. 2011 Brazilian Symposium on Computing System Engineering, Florianopolis, Brazil. https://doi.org/10.1109/SBESC.2011.17

Pessolani, P., Gonnet, S. M., Tinetti, F. G., and Cortes, T. (2012). *Sistema de virtualización con recursos distribuidos* [Conference presentation]. XIV Workshop de Investigadores en Ciencias de la Computación. http://sedici.unlp.edu.ar/handle/10915/18375

Plex86 (2021). *The new Plex86, x86 Virtual Machine Project*. http://plex86.sourceforge.net

Popek, G. J., and Goldberg, R. P. (1974). Formal requirements for virtualizable third generation architectures. *Communications of the ACM, 17*(7), 412-421. https://doi.org/10.1145/361011.361073

QEMU (2021). *QEMU, the FAST! processor emulator*. https://www.qemu.org

Ranjith, D., Tamizharasi, G. S., and Balamurugan, B. (2017, April 20-22). *A survey on current trends to future trends in green computing* [Conference presentation]. 2017 International Conference of Electronics, Communication and Aerospace Technology (ICECA), Coimbatore, India. https://doi.org/10.1109/ICECA.2017.8203616

Ryding, C., and Johansson, R. (2020). *Jails vs Docker: A performance comparison of different container technologies* [Undergraduate thesis, Mid Sweden University]. http://urn.kb.se/resolve?urn=urn:nbn:se:miun:diva-39517

Sahoo, J., Mohapatra, S., and Lath, R. (2010, April 23-25). *Virtualization: A survey on concepts, taxonomy and associated security issues* [Conference presentation]. 2010 Second International Conference on Computer and Network Technology, Bangkok, Thailand. https://doi.org/10.1109/ICCNT.2010.49

Samireh, J., and Claes, W. (2012). *Systematic literature studies: database searches vs. backward snowballing* [Conference presentation]. ACM-IEEE International Symposium on Empirical Software Engineering and Measurement, Lund, Sweden. https://doi.org/10.1145/2372251.2372257

SCOPE Alliance (2008). *Virtualization: State of the art*. https://profsandhu.com/cs6393_s14/SCOPE-Virtualization-StateofTheArt-Version-1.0.pdf

Sehgal, N. K., and Bhatt, P. C. (2018). *Cloud computing*. Springer.

Silberschatz, A., Galvin, P. B., and Gagne, G. (2014). *Operating system concepts essentials*. John Wiley & Sons, Inc.

Smith, J. E., and Nair, R. (2005). The architecture of virtual machines. *Computer, 38*(5), 32-38. https://doi.org/10.1109/MC.2005.173

Stallings, W. (2015). *Operating systems: Internals and design principles* (9th ed.). Pearson.

Sylabs.io (2022). *Sylabs.io Singularity*. https://www.sylabs.io

Syrewicze, A., and Siddaway, R. (2018). *Pro Microsoft Hyper-V 2019: Practical guidance and hands-on labs*. Apress.

Tfrifonov, D. V., Hristo. (2018). Virtualization and containerization systems for Big Data. *Fundamental Science and Applications, 24*, 129-132. Thai, T. L., and Lam, H. (2003). *.NET framework essentials*. O'Reilly Media, Inc.

Thathera, H., Shashi, H., and Rajput, D. S. (2015). Green computing: An earth friendly system. *International Journal of Science and Research, 8*(4), 25540-25550 https://research.vit.ac.in/publication/green-computing-an-earth-friendly-system

User-Mode Linux (2022). *The user-mode Linux Kernel home page*. http://user-mode-linux.sourceforge.net

Varasteh, A., and Goudarzi, M. (2017). Server consolidation techniques in virtualized data centers: A survey. *IEEE Systems Journal, 11*(2), 772-783. https://doi.org/10.1109/JSYST.2015.2458273

Virtuozzo (2022). *Virtuozzo*. https://www.virtuozzo.com

VMware (2022). *VMware*. http://www.vmware.com

von Hagen, W. (2008). *Professional Xen virtualization*. John Wiley & Sons, Inc.

Waldspurger, C. A. (2002). Memory resource management in VMware ESX server. *ACM SIGOPS Operating Systems Review, 36*(SI), 181-194. https://doi.org/10.1145/844128.844146

Wessman, N. J., Malatesta, F., Andersson, J., Gomez, P., Masmano, M., Nicolau, V., Rhun, J. L., Cabo, G., Bas, F., Lorenzo, R., Sala, O., Trilla, D., and Abella, J. (2021, August 23-27). *De-RISC: The first RISC-V space-grade platform for safety-critical systems* [Conference presentation]. 2021 IEEE Space Computing Conference (SCC), Laurel, MD, USA. https://doi.org/10.1109/SCC49971.2021.00010

Whitaker, A., Shaw, M., and Gribble, S. D. (2002). *Denali: Lightweight virtual machines for distributed and networked applications*. http://web.cs.ucla.edu/~miodrag/cs259-security/whitaker02denali.pdf

White, J., and Pilbeam, A. (2010). A survey of virtualization technologies with performance testing. *arXiv preprint*. https://doi.org/10.48550/arXiv.1010.3233

Wine (2022). *Wine*. https://www.winehq.org

Xen Cambridge (2022). *Xen Cambridge. The virtual machine monitor*. https://www.cl.cam.ac.uk/research/srg/netos/projects/archive/xen/

Xen Project (2022). *Xen Project Website*. https://www.xenproject.org

Xtratum (2022). *Xtratum*. http://www.xtratum.org

Yee, B., Sehr, D., Dardyk, G., Chen, J. B., Muth, R., Ormandy, T., Okasaka, S., Narula, N., and Fullagar, N. (2009). *Native client: A sandbox for portable, untrusted x86 native code* [Conference presentation]. 2009 30th IEEE Symposium on Security and Privacy, Oakland, CA, USA. https://doi.org/10.1109/SP.2009.25

Instructions for Authors

The Editorial Committee reserves the copyright to printing any material and its total or partial reproduction, as well as the right to accept submitted material or reject it. It also reserves the right to make any editorial modification which it thinks fit. In such event, the author of the submitted material will receive the evaluators' recommendations in writing. If an author accepts them, the revised (or rewritten) article must be submitted with the suggested changes having been made by the date on the date set by the journal in order to guarantee its publication in the scheduled issue.

The process to be followed for publishing an article in the journal

The article must be uploaded into the journal's OJS website (see the guidelines for article submission in the Authors guide section in our website http://www.revistas.unal.edu.co/index.php/ ingeinv/article/view/59291/56815). Any manuscript must be submitted using journal's template (with a maximum length of six pages) and must be accompanied by the license agreement, addressed to the journal's editor, Prof. Andrés Pavas, stating that all authors involved in the work in question agree to its submission for consideration in the *Ingeniería e Investigación*.

Article and License templates are available on:

http://www.revistas.unal.edu.co/index.php/ingeinv/index

Once an article has been received by the journal, the corresponding author will be notified via Email and the peerreview process will begin. Following this evaluation, authors will then be informed whether their article has been accepted or not. If accepted, authors must deal with the respective corrections recommended by the evaluators and the Editorial Committee's final decision –if the article is to be published.

Content

All articles considered by the committee for possible publication in the *Ingeniería e Investigación* must consist of the following parts:

- Title, abstract and keywords must be written in Spanish and English. The title must clearly explain the contents of the article in question, it must be written in normal title form, and it must be preferably brief. The abstract should contain around 200 words in Spanish and English, in addition to the methods and materials used, results obtained, and conclusions drawn.

- An introduction must be given. It must describe the article's general purpose, including its main objective, referring to any previous work and the scope of the current article.

- Conclusions must be drawn. This section must provide the implications of the results found and their relationship to the proposed objective.

- Bibliographical references must be given (an explanation and example of how to set them out is given later on).

- Acknowledgements (optional). These should be brief and mention any essential support received for carrying out the work being reported.

- Appendix (optional).

Scientific and technological research articles must also include:

- Experimental development. This must be written giving sufficient details for the subject to be fully understood by readers, including the descriptions of any procedures involved.

- Results. These must give a clear explanation and interpretation of the findings. If necessary, a brief, focused discussion may be provided with regard to the way in which results can be interpreted.

It is required that the bibliographical references for all articles be included at the end of the article, given in alphabetical order of first authors' surnames, and mentioned in the text, and since May 2014, authors are required use the American Psychological Association (APA) style for citation and references:

- Articles published in journals:

Author, A. A., Author, B. B., and Author, C. C. (year). Article title. *Journal Title, volume number* (issue number), page numbers.

Del Sasso, L. A., Bey, L. G., and Renzel, D. (1958). Low-scale flight ballistic measurements for guided missiles. *Journal of the Aeronautical Sciences, 15*(10), 605-608.

Author, A. A., and Author, B. B. (year). Article title. *Journal Title, volume number* (issue number), page numbers. http://www. xxxxxxxxxxxxxxxx

Gaona, P. A. (2014). Information visualization: A proposal to improve search and access digital resources in repositories. *Ingeniería e Investigación*, *34*(1), 83-89. http://www.revistas. unal.edu.co/index.php/ingeinv/article/ view/39449

- Books:

Author, A. A., and Author, B. B. (year). Title of work. Publisher.

Turner, M. J., Martin, H. C., and Leible, R. C. (1964). Further development and applications of the stiffness method, Matrix Methods of Structural Analysis. Macmillan Co.

- Conference papers and symposium contributions:

Author, A. A., and Author, A. A. (year). *Title* [Conference presentation]. Name of conference, City, State, Country. http:// xxxxxxxxxxxxxxx

- Theses or undergraduate projects:

Author, A. A., and Author, A. A. (year). *Title* [Type of thesis, University]. http://xxxxxxxxxxxxxxx

Further information can be obtained by:

Contacting the Editorial Team (Email: revii_bog@unal.edu.co) or Prof. Andrés Pavas (Editor-in-Chief. Email: fapavasm@unal. edu.co)

The office of the journal *Ingeniería e Investigación* is located at: Ciudad Universitaria, Facultad de Ingeniería, Edificio CADE. Telefax: (57-1) 3165000 Ext. 13674. Bogotá - Colombia.